An Investigation of Low-Temperature Combustion Front Propagation Mechanisms

By

Matthew K. Blessinger

A dissertation submitted in partial fulfillment of

the requirements for the degree of

Doctor of Philosophy

(Mechanical Engineering)

at the

UNIVERSITY OF WISCONSIN-MADISON

2015

Date of final oral examination: 7/21/2015

The dissertation is approved by the following members of the Final Oral Committee:

Jaal B. Ghandhi, Professor, Mechanical Engineering
Christopher J. Rutland, Professor, Mechanical Engineering
David A. Rothamer, Associate Professor, Mechanical Engineering
Sage L. Kokjohn, Assistant Professor, Mechanical Engineering
Mark Saffman, Professor, Physics

Abstract

The combustion propagation mechanism of homogeneous charge compression ignition (HCCI) combustion was investigated using planar laser Rayleigh scattering thermometry. The experiments were performed in a small-bore, high-speed engine with Bowditch-style optical access uniformly fueled by ethylene and dimethyl ether. Image processing was seriously hindered by striations induced by beam steering, which made image processing difficult and whole sets of high-pressure HCCI data unusable. Beam steering was still an issue at lower system pressure, but a local quantitative analysis could be performed by assuming that the high-intensity regions were reactants. Global calibration of the images to temperature was not possible because of the beam steering. Analysis of the raw image results showed that the background image correction heavily influenced the temperature calculation; a wide range of temperatures (realistic or not) could be achieved. The combustion front thickness measurements were shown, however, to be immune to background image correction and could be performed on either density or temperature calculated from the scattering measurements.

The HCCI images were analyzed for sharp intensity gradients that would provide the highest chance of seeing evidence of flame propagation. The HCCI measurements yielded temperatures lower than a comparable spark ignition (SI) condition, and the resulting temperature gradients had values up to 8 K/μm. The HCCI combustion front thicknesses ranged as low as 80 μm, which were comparable with the SI flame front thickness, to several millimeters (although these regions were not quantitatively investigated). The combustion front propagation speed was estimated for SI and HCCI conditions by acquiring two images spaced closely in time. The measurements relied on the presence of small particles in the field to correct

for the chamber fluid motion; the combustion-induced in-cylinder flow field was quite significant, and the combustion front speed measurements were, therefore, unreliable.

A transition between successive autoignition and flame propagation was not observed when investigating the dependency between the combustion speed and the temperature gradient as had been suggested in the literature, but the uncertainties in the measured temperature gradient and, especially, the combustion speeds did not permit a conclusive determination about the role of flame propagation in HCCI. Based on the fact that HCCI combustion front thicknesses comparable to those for SI combustion were observed, however, it can be concluded that the presence of flame propagation in HCCI combustion is a very real possibility.

Acknowledgements

I, first and foremost, would like to thank Professor Jaal Ghandhi for his patience, tireless efforts, and seemingly endless knowledge required to help me progress as a researcher. I will always look up to him as my friend and mentor. I also need to thank my fellow ERC graduate students, in particular Nick Neal, Mike Tess and the various student hourlies for all the help they gave me throughout the years. I would have never finished my project without them.

My deepest gratitude goes to my family as they have always supported me in all my endeavors. I have my father, Dave, to thank for inspiring my pursuance of higher education, and my mother, Nora, for providing the comfort and reassurance that only a mother can. Bendita la luz.

Table of Contents

Abstract i
Acknowledgements iii
List of Figures vii
List of Tables xiii
Chapter 1 - Introduction 1
Chapter 2 - Literature Review 5
2.1 Engine Combustion Modes 5
2.2 Homogeneous Charge Compression Ignition 7
2.3 Partially Premixed Combustion 10
2.4 Reactivity Controlled Compression Ignition 12
2.5 Combustion Front Propagation Mechanism Analysis 14
2.6 Methods for Measuring Combustion Front Characteristics 20
2.7 Rayleigh Scattering Background and Theory 24
2.8 Rayleigh Scattering Thermometry and Reaction Front Thickness Measurements 32
2.9 Rayleigh Scattering Cross Section 38
2.9.1 Index of Refraction 39
2.9.2 Temperature Dependence 39
2.9.3 Depolarization 40
2.10 Experimental Difficulties 42
Chapter 3 - Experimental Setup 46
3.1 Engine Setup 46
3.2 Fuels 51
3.2.1 Preliminary Considerations 51
3.2.2 Rayleigh Scattering Cross Section 52
3.2.3 Combustion Effects 54
3.3 Optical Setup 59
3.3.1 Laser 59
3.3.2 Imaging Optical Access 61
3.3.3 Laser-Access Plate 65
3.3.4 Filters 70
3.3.5 Cameras 72

Chapter 4 - Calculations 78
4.1 Simulations 78
4.1.1 Mechanism Validation 79
4.1.2 Ignition Delay 86
4.1.3 Laminar Flame Speed 88
4.2 Rayleigh Scattering Cross Section 90
4.2.1 Example Cross Sections 90
4.2.2 Combustion Correction 93
4.3 Image Acquisition 100
4.3.1 Dark Current and Read Noise Image 100
4.3.2 Room Light Image 101
4.3.3 Combustion Luminosity Image 101
4.3.4 Motored Image 102
4.3.5 Combustion Image 105
4.3.6 Background Image 109
4.4 Image and Data Analysis 111
4.4.1 Image Correction 111
4.4.2 Combustion Front Identification 113
4.4.3 Temperature 117
4.4.4 Combustion Front Thickness 122
4.4.5 Combustion Speed 124
4.5 Signal-to-Noise Ratio 127
4.6 Uncertainty Analysis 132
4.6.1 Temperature 132
4.6.2 Temperature Gradient 139
4.6.3 Combustion Front Thickness 139
4.6.4 Combustion Speed 142
Chapter 5 - Results 144
5.1 Operating Conditions 144
5.2 Imaging Summary 149
5.2.1 Image Collection Statistics 150
5.2.2 Single vs. Dual Imaging Uncertainty 151
5.2.3 Combustion Distributions 153

5.2.4 Combustion Temperature Analysis 156
5.3 Spark-Ignition Baseline 166
5.3.1 Combustion Temperature 166
5.3.2 Flame Thickness 167
5.3.3 Single vs. Dual Imaging 169
5.4 Temperature 173
5.5 Combustion Front Thickness 181
5.6 Temperature Gradient 186
5.7 Combustion Speed 188
5.8 Combustion Propagation Mechanism 193
Chapter 6 - Conclusions 198
6.1 Summary 198
6.2 Future Work 201
Chapter 7 - Abbreviations 202
Chapter 8 - References 203

List of Figures

Figure 2-1: Depiction of a laminar flame front structure. Adapted from Turns [10]. 6

Figure 2-2: Wave speed for various temperature length scales. Adapted from Chen et al. [49].. 16

Figure 2-3: Wave speed for various temperature fluctuations. Adapted from Hawkes et al. [50]. 16

Figure 2-4: Wave speed vs. temperature gradient extracted from 2-D DNS simulations. Adapted from Chen et al. [49]. 17

Figure 2-5: Reaction (gray) and diffusion (black) rates of H_2-air mixtures for imposed temperature gradients of 33, 200 and 467 K/mm, respectively. Adapted from Bansal and Im [52]. 18

Figure 2-6: Energy state changes of common optical laser-based measurements. Adapted from Ref. [91]. 25

Figure 2-7: Diagram of a propagating light wave with a particle emitting Rayleigh scattering. The lighter area corresponds to greater Rayleigh scattering intensity. The wavelength and molecule size are not to scale..... 27

Figure 2-8: Rayleigh scattering intensity vs. distance across a flame front propagating from right to left. An island of unburned mixture exists behind the flame front. Adapted from Smith [8]. . 33

Figure 2-9: Smith's definition of flame front thickness based on the mixture density. Adapted from Smith and Zhao [8,85]..... 36

Figure 2-10: Variation of the Rayleigh cross section and mixture mean molecular weight as a function of the reaction progress variable through a stoichiometric ethylene-air flame. Adapted from Namer and Schefer [97]. 37

Figure 3-1: Optical engine assembly. 48

Figure 3-2: Percent difference between reactant and product differential cross section as a function of equivalence ratio. Mixture species are obtained from ignition delay simulations at 800 K and 11 bar. 53

Figure 3-3: Ignition delay measurements of ethylene, gasoline surrogate and isooctane fuels scaled by oxygen concentration. The data were adapted from Refs. [127-130]. 56

Figure 3-4: Shock tube ignition delay measurements of stoichiometric DME/air and n-heptane/air mixtures. DME data were adapted from Pfahl et al. [132]. n-heptane data were adapted from Ciezki and Adomeit [133]. 57

Figure 3-5: Ignition delay of direct-injection DME and Diesel fuel in constant-volume vessels. 41 bar data were adapted from Wakai et al. [134]. 45 bar were data adapted from Yao et al. [135]. 58

Figure 3-6: 532 nm laser optical setup. The black lines indicate a shield that enclosed the optics. 60

Figure 3-7: SI full window piston crown. 62

Figure 3-8: HCCI small window piston crown. 62

Figure 3-9: Overhead view of the optical access layout. The imaging region, marked by the cross hatched area, is the overlapping region of the piston and head windows. The dashed lines indicate the largest piston and head window sizes. Dimensions are in millimeters. 63

Figure 3-10: Head window holder. 64

Figure 3-11: Cross sectional view of the HCCI piston crown and recessed head window. 64

Figure 3-12: Overhead cutaway view of the laser-access plate. Windows are shown in purple, and the green laser path's direction is indicated by the red arrow. The laser sheet avoids the injector/ spark plug hole..... 66

Figure 3-13: Incident light reflectance vs. angle of incidence in fused silica. The inset plot shows the reflectance is zero at Brewster's angle. 70

Figure 3-14: Filter transmission as a function of incident light wavelength for the three filters used. 71

Figure 3-15: Example step response function from the PI-MAX4 scanning knife edge test. The fit parameter Λ is shown with its 95% regression confidence interval..... 76

Figure 4-1: Comparison of stoichiometric 15 bar experimental ethylene ignition delay adapted from Kumar et al. [127] compared to simulations. 80

Figure 4-2: Comparison of stoichiometric 50 bar experimental ethylene ignition delay adapted from Kumar et al. [127] compared to simulations. 80

Figure 4-3: Ethylene flame speed comparison at 1 atm and 300 K. Experimental data were adapted from Jomaas et al. [149]. 81

Figure 4-4: Ethylene flame speed comparison at 5 atm and 300 K. Experimental data were adapted from Jomaas et al. [149]. 81

Figure 4-5: Ethylene flame speed comparison for 1 atm and 470 K. Experimental data were adapted from Kumar et al. [127]. 82

Figure 4-6: Ethylene flame speed simulation comparison for 11 bar and Φ=1 reactant conditions. 82

Figure 4-7: Comparison of stoichiometric DME ignition delay adapted from Pfahl et al. [132] and Li et al. [151] compared to simulations using the NUI DME mechanism. 83

Figure 4-8: Comparison of DME ignition delay at 23 bar adapted from Li et al. [151] compared to simulations using the NUI DME mechanism. 84

Figure 4-9: DME flame speed comparison at 5 atm and 298 K. Experimental data were adapted from de Vries et al. [152]. 85

Figure 4-10: DME flame speed comparison at 6 atm and 298 K. Experimental data were adapted from Qin and Ju [157]. 85

Figure 4-11: DME flame speed comparison at 10 atm and 298 K. Experimental data were adapted from de Vries et al. [152] and Qin and Ju [157]..... 86

Figure 4-12: Ethylene laminar flame speed calculations over tested thermodynamic conditions. Φ = 1.03. 89

Figure 4-13: Ethylene laminar flame speed calculations over tested thermodynamic conditions. Φ = 0.82. 89

Figure 4-14: DME laminar flame speed calculations over tested HCCI thermodynamic conditions. Φ = 0.6..... 90

Figure 4-15: Differential Rayleigh scattering cross section ratio for ethylene flame propagation simulations. Φ=1.03..... 95

Figure 4-16: Cross section ratio of ethylene flame propagation and ignition delay simulations. 800 K, 13 bar, Φ=1.03. 95

Figure 4-17: Differential Rayleigh scattering cross section using ignition delay simulations. The arrow indicates the modified reference condition..... 96

Figure 4-18: Apparent heat release rate for the HCCI experiments. The low-temperature oxidation coincides with the initial cross section decrease..... 96

Figure 4-19: Differential Rayleigh scattering cross section ratio using the post-LTO mixture cross section as the reference condition. The ignition delay simulation was performed at the LTO thermodynamic conditions..... 98

Figure 4-20: Differential Rayleigh scattering cross section ratio using flame propagation and ignition delay simulations for the HCCI condition 750 K, 10 bar..... 99

Figure 4-21: SI Rayleigh scattering motored image. The laser beam propagates from top to bottom. Different types of particle scatterers are indicated by the colored circles..... 104

Figure 4-22: Overhead view of the imaging area relative to the center of the cylinder. The recorded image is given by the rectangle around the imaging area. Dimensions are in millimeters. 104

Figure 4-23: Rayleigh scattering high-pressure motored image. The striations were caused by beam steering. 105

Figure 4-24: SI Rayleigh scattering combustion image. The flame front has several characteristics: smooth and rough curvature, sharp and shallow intensity (temperature) gradients, and inclusions..... 107

Figure 4-25: HCCI Rayleigh scattering combustion image. The combustion front locations are random with a variety of intensity gradients. Charge bleeding at the bottom of the image caused the saturated structure. 108

Figure 4-26: SI background image. The uniform, low-intensity field with few particles indicates the Rayleigh scattering images are free of hidden errant sources of intensity..... 110

Figure 4-27: Image processing methodology of a flare corrected Rayleigh scattering sub image. a) Rayleigh scattering image, b) beam steering corrected, c) median filtered..... 115

Figure 4-28: Contour identification methodology. a) threshold-identified contour, b) orthogonal lines fit to the identified contour, c) intensity ratio along the orthogonal lines 116

Figure 4-29: Error function fit to a single intensity ratio profile from Fig. 4-28c). a) The fit captures the gradient and end points well. b) Zoomed in section of the combustion front shows the noise in the raw data..... 118

Figure 4-30: Temperature gradient error as a function of the weighting function width. The shaded regions indicate the 95% confidence interval. 120

Figure 4-31: Unweighted (blue) and weighted (red) error function fits of an intensity ratio profile. The weighted fit captures the gradient. 120

Figure 4-32: Temperature profile calculated from the intensity ratio profiles in Fig. 4-29..... 121

Figure 4-33: Definition of the density-based combustion front thickness. 123

Figure 4-34: Mixture molecular mass ratio through combustion. The SI time scale was adjusted to fit. 123

Figure 4-35: First (a) and second (b) image of a tracked SI flame front identified by the red contour. The particles circled in green and blue were used to monitor in-cylinder motion. 125

Figure 4-36: Signal-to-noise ratio of the MicroMAX and PI-MAX4 for collected signal levels. 130

Figure 4-37: Signal-to-noise ratio of an SI image (Fig. 4-24). 131

Figure 4-38: Signal-to-noise ratio of an HCCI image (Fig. 4-25). 131

Figure 4-39: Raw (a) and fit (b) temperature plotted with its uncertainty for the profiles from Fig. 4-32. The measurement uncertainty is indicated by the shaded region. 134

Figure 4-40: Raw (a) and fit (b) density plotted with its uncertainty for the data in Fig. 4-32. The measurement uncertainty is indicated by the shaded region. 141

Figure 5-1: Pressure (a) and rate of heat release (b) plots of the three spark-ignition cases. The markers indicate the image timing. 146

Figure 5-2: Comparison of the nominal SI and HCCI pressure (a) and rate of heat release (b). The markers indicate the image timing. 147

Figure 5-3: Probability density of the cumulative heat release percent at image timing for the processed images. 149

Figure 5-4: Comparison of single and dual image HCCI temperature profiles (a) and their relative uncertainties (b). 152

Figure 5-5: Comparison of single and dual image SI temperature profiles (a) and their relative uncertainties (b). 153

Figure 5-6: Single-image nominal SI density-based combustion front thickness (a), temperature gradient (b) and product temperature (c) kernel density distributions. 154

Figure 5-7: Single-image HCCI density-based combustion front thickness (a), temperature gradient (b) and product temperature (c) kernel density distributions. 154

Figure 5-8: Constant pressure adiabatic flame temperature (a) and product to adiabatic flame temperature ratio (b) of the single-image nominal SI and HCCI cases. 156

Figure 5-9: Error function fit parameter as a function of additional flare correction for the single SI (a) and HCCI (b) profiles in Figs. 5-4a) and 5-5a). The shaded region is the measurement uncertainty..... 158

Figure 5-10: Product temperature as a function of additional flare correction for the single SI (a) and HCCI (b) profiles in Figs. 5-4a) and 5-5a). The shaded region is the measurement uncertainty..... 159

Figure 5-11: Temperature gradient as a function of additional flare correction for the single SI (a) and HCCI (b) profiles in Figs. 5-4a) and 5-5a). The shaded region is the measurement uncertainty..... 160

Figure 5-12: Required additional flare correction to achieve the adiabatic flame temperature for single SI and HCCI data sets. 161

Figure 5-13: Ratio of the flare correction to the Rayleigh scattering intensity in the reactants (*R*) and products (*P*) if the flare was corrected for single SI (a) and HCCI (b) data sets. 162

Figure 5-14: Single SI (a) and single HCCI (b) product temperature distributions for intensities measured far away from the combustion front and their respective profile and adiabatic flame temperature. 163

Figure 5-15: Temperature-based combustion front thickness as a function of additional flare correction for the single SI (a) and HCCI (b) profiles in Figs. 5-4a) and 5-5a). The shaded region is the measurement uncertainty..... 164

Figure 5-16: Density-based combustion front thickness as a function of additional flare correction for the single SI (a) and HCCI (b) profiles in Figs. 5-4a) and 5-5a). The shaded region is the measurement uncertainty..... 165

Figure 5-17: Product temperature (a) and constant-pressure adiabatic flame temperature (b) of the SI cases..... 167

Figure 5-18: Density-based flame thickness distribution (a) and uncertainty (b) for the SI conditions..... 168

Figure 5-19: Nominal SI density-based combustion front thickness (a), temperature gradient (b) and product temperature (c) for single (solid line) and dual (dashed line) image data sets. 170

Figure 5-20: Low-pressure SI density-based combustion front thickness (a), temperature gradient (b) and product temperature (c) for single (solid line) and dual (dashed line) image data sets.. 172

Figure 5-21: Lean SI density-based combustion front thickness (a), temperature gradient (b) and product temperature (c) for single (solid line) and dual (dashed line) image data sets. 172

Figure 5-22: HCCI density-based combustion front thickness (a), temperature gradient (b) and product temperature (c) for single (solid line) and dual (dashed line) image data sets. 173

Figure 5-23: Single-image nominal SI and single- and dual-image HCCI product temperature (a) and uncertainty (b) distributions. 174

Figure 5-24: Single HCCI image demonstrating partial combustion. Combustion contour 1 identifies partial combustion. The blue ellipse identifies another partial combustion location.. 175

Figure 5-25: Rayleigh scattering intensity (a) and temperature profiles (b) of the combustion front contours identified in Fig. 5-24. 177

Figure 5-26: Contour 1 temperature profiles indicated by the green lines in Fig. 5-24. 178

Figure 5-27: Raw and fitted tracked temperature profiles from the first to second image of a dual HCCI image pair. The raw profiles show the temperatures leveled off. 180

Figure 5-28: Dual-image nominal SI and single- and dual-image HCCI density-based combustion front thickness (a) and uncertainty (b) distributions. 182

Figure 5-29: Dual-image nominal SI and single- and dual-image HCCI temperature-based combustion front thickness (a) and uncertainty (b) distributions. 183

Figure 5-30: Density-based combustion front thickness distributions of the 1st and 2nd image of the tracked HCCI contour presented in Fig. 5-27. 185

Figure 5-31: Single-image nominal SI and single- and dual-image HCCI temperature gradient (a) and uncertainty (b) distributions. 187

Figure 5-32: Nominal SI and HCCI combustion speed probability distributions. 189

Figure 5-33: Nominal, low-pressure and lean SI combustion speed probability distributions... 189

Figure 5-34: Calculated laminar flame speed probability distributions..... 190

Figure 5-35: Diagram of an oblique combustion front (red lines) giving a greater measured displacement than a normal combustion front (black lines). The laser plane is marked by the green line. 191

Figure 5-36: Nominal SI measured flame speed vs. combustion front thickness. 191

Figure 5-37: Nominal SI (a) and HCCI (b) in-cylinder flow field velocity vectors. The color bar represents the number of contours per bin. The origin (zero flow field velocity) is given by the green asterisk. 192

Figure 5-38: HCCI combustion speed as a function of the temperature gradient. 194

Figure 5-39: Log-log plot of the HCCI combustion speed as a function of the temperature gradient. Two nonlinear least-squares curve fits (black and red lines) were applied to the data. 195

Figure 5-40: Ignition delay temperature sensitivity distributions of the single- and dual-image HCCI data. 197

Figure 5-41: Calculated HCCI combustion speed via Eqn. (2-2). 197

List of Tables

Table 3-1: Engine geometry. Crank angle timings are relative to TDC of compression..... 47

Table 3-2: Ignition delay studies of ethylene and gasoline surrogates. 55

Table 3-3: Individual and combined camera filter specifications. 71

Table 3-4: MicroMAX and PI-MAX4 camera specifications [143,144]..... 73

Table 3-5: Camera image resolution specifications with mean ± 1σ. 77

Table 4-1: Differential Rayleigh scattering cross section [cm^2/sr] of common combustion species at 532 nm..... 92

Table 4-2: Sample dark current-corrected intensities and their uncertainties..... 112

Table 4-3: Relative uncertainties of the reactant (reference condition) and product cross sections. 137

Table 4-4: Relative uncertainties of the reactant (reference condition) and product molecular weights. 141

Table 5-1: SI and HCCI engine operating conditions and nominal combustion parameters..... 145

Table 5-2: Image statistics summary listing the number of collected images, identified combustion front contours and calculated temperature profiles. 151

Table 5-3: Mean value ± 1σ for the temperature gradient, product temperature and density-based combustion front thickness for single-image nominal SI and HCCI data. 155

Chapter 1 - Introduction

It is presumed that in the future pollutant emission and fuel economy regulations will become stricter, therefore it is imperative to develop internal combustion engines that can meet the current standards and still retain room for improvement to meet future mandates. Currently, gasoline and diesel engines have been meeting the standards but with a decreasing capacity to reasonably meet the next iteration as advanced after-treatment solutions are already implemented. As such, advanced engine technologies are being pursued to improve efficiency while reducing engine-out emissions.

Gasoline engines have made rapid improvements in recent years through a contribution of advanced fuel injection hardware and boosting technology. Port fuel injection (PFI) has been, and still is, the mainstay for manufacturers, but to meet future standards manufacturers have started using direct injection hardware, giving rise to the gasoline spark-ignited (SI) direct-injection (DI) engine. The advanced strategies have led to increased thermal efficiency, but characteristic SI engine issues still persist: high unburned hydrocarbon (UHC) and nitric oxide (NOx) emissions [1]. In general the reliability of the combustion cycle has improved, but on occasion misfires and partial burns occur due to the rapid change in velocity and equivalence ratio in the spark channel resulting in elevated carbon monoxide (CO) and UHC emissions [2]. Therefore, typical SI engine aftertreatment is still required to control UHC, NOx, and CO emissions.

Diesel engine combustion is highly efficient as it operates unthrottled, globally lean, and with high compression ratios [3], and researchers have obtained high thermal efficiency while maintaining low carbon monoxide (CO) and UHC emissions [3]. Unfortunately, the nature of

conventional diesel combustion (CDC) lends itself to high NOx formation due to locally stoichiometric combustion, and to high levels of soot due to the structure of the lifted diffusion flame [4]. With the highly emission-constrained markets, conventional diesel engines are not viable without the addition of aftertreatment devices such as selective catalytic reduction (SCR) for NOx and a particulate filter (DPF) for soot. Implementation of these devices is not without drawbacks, though; the SCR requires a reducing fluid (urea) to be added at intervals, and the DPF requires regeneration, which is accomplished by running for periods with late-combustion and low-efficiency.

Regardless of the type of engine (spark-ignition or compression ignition), aftertreatment increases costs and complexity of the system, thereby giving a strong incentive to bypass the use of aftertreatment altogether by pursuing advanced combustion strategies that mitigate formation of pollutants in the cylinder while providing high thermal efficiency. In-cylinder combustion strategies that are able to achieve low engine-out emissions are generically referred to as low-temperature combustion (LTC). The basic goal is to utilize both high dilution levels to maintain low-temperatures and, consequentially, NOx formation, and mixtures lean enough to avoid soot formation. Both goals can be achieved by diluting with air, or in many cases, recirculated exhaust gas (EGR). LTC research has shown the ability to simultaneously achieve high thermal efficiency and low engine-out emissions [5-7].

While the results of initial LTC experiments have been promising, there is a general lack of understanding of the combustion mechanism; this knowledge is necessary to properly model and fully optimize the combustion strategy. For example, Smith [8] used Rayleigh scattering thermometry to show that the turbulent flame was a wrinkled laminar flame in gasoline spark ignition engines, and Dec [9] used planar laser-based imaging diagnostics to define the structure

of the lifted diffusion flame reaction zone, which was critical for his conceptual model of diesel combustion [4]. Similarly, it is crucial to the development of LTC strategies to understand the mechanism by which the combustion front propagates, whether it is by sequential autoignition, flame propagation, or a combination thereof. In general, LTC is thought to progress by sequential autoignition, but a conclusive demonstration does not exist.

The objective of the study is to determine the role of flame propagation and autoignition in the low-temperature combustion regime, which has lacked a fundamental understanding, in part, due to the unknown method of propagation. The experiment was carried out in a firing, optical internal combustion engine by means of planar laser Rayleigh scattering thermometry. The Rayleigh scattering thermometry images allowed the 2-D temperature field to be calculated so the temperature gradient across the combustion front could be determined. As discussed in Section 2.5, knowing the temperature gradient allows the classification of the combustion front. To assure complete agreement, the combustion front speed was determined by dual imaging in which a second image of the combustion front was taken shortly after the first image. Initially, spark-ignition experiments were used as a baseline to characterize the diagnostics and data processing techniques. Next, the one of the most prominent LTC regimes was investigated: homogeneous charge compression ignition (HCCI).

The implications of knowing the combustion mechanism include advanced engine design that takes full advantage of the combustion mode and more accurate computer models, which have proven crucial in the advancement of the internal combustion engine. It is well known that modeling, when accurate, quickly advances the technology in its field, as it yields quick, cost-effective research. Current models include or exclude flame propagation subroutines based on the goodness of fit to experimental data. This study intends to guide modelers with a definitive

answer to aid in the furthering of the LTC strategy to improve fuel economy and reduce engine-out emissions to meet regulations and reduce the need for aftertreatment.

Chapter 2 - Literature Review

This work addresses the combustion wave propagation mechanisms for various combustion regimes. It is, therefore, necessary to understand the different types of propagation that exist in an engine environment. The following sections provide brief overviews of the types of propagation mechanisms, as well as the methods for measuring and characterizing the combustion front. There are several different prominent LTC strategies: HCCI that was investigated in this study, partially premixed combustion (PPC) also known as partially premixed compression ignition (PPCI), and reactivity controlled compression ignition (RCCI). Although HCCI was the only LTC strategy investigated in this study, it is useful to understand the potential role of flame propagation in the other common LTC combustion modes. The following sections discuss each strategy and their pros and cons, as well as provide a literature review of the scarce research that has addressed the propagation mechanism. In this chapter, the theory of Rayleigh scattering is presented with the derivation of the governing equations. Building upon the basic theory, the use of Rayleigh scattering for temperature measurements and subsequent development of the thermometry equations are shown. Next the Rayleigh scattering cross section is rigorously reviewed, and finally experimental difficulties associated with Rayleigh scattering are discussed.

2.1 Engine Combustion Modes

Combustion can occur in a flame or non-flame mode (autoignition). A premixed flame is characterized by a self-propagating, thin reaction zone traveling at subsonic speeds, and is also known as a deflagration. Figure 2-1 illustrates the key components of the premixed flame

structure. The reaction zone can be thought of as two zones: the preheat zone and the reaction zone [10]. Thermal and molecular diffusion from the reaction zone into the preheat zone heats the unburned fuel-air mixture to initiate the fuel oxidation process. The majority of the heat release occurs in a thin region at the beginning of the reaction zone due to the formation of intermediate combustion species (radicals). The temperature greatly increases in the preheat zone resulting in a large temperature gradient, which, with the radicals, drives the aforementioned diffusion. The flame will propagate if the thermal and molecular diffusion from the reaction zone to the preheat zone continues, otherwise quenching occurs. Flame quenching occurs in engines due to heat transfer to the relatively cool cylinder wall and piston surface by preventing thermal decomposition of the fuel [11].

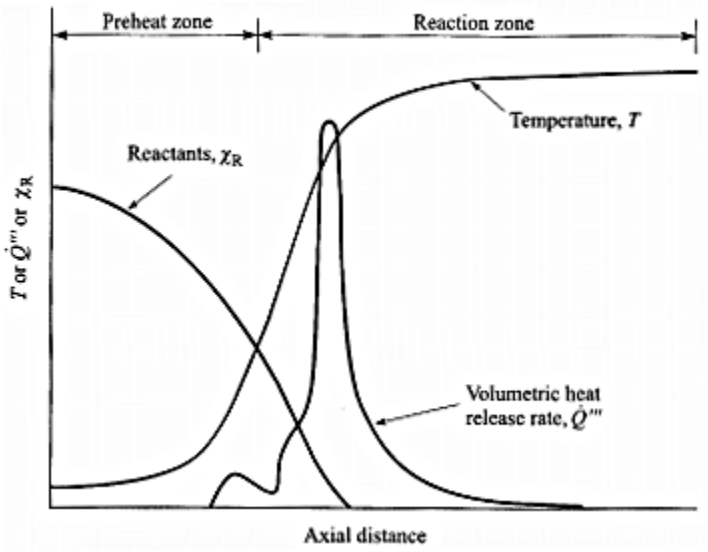

Figure 2-1: Depiction of a laminar flame front structure. Adapted from Turns [10].

Autoignition occurs when a fuel-air mixture reaches its ignition limit (temperature and pressure dependent) and spontaneously combusts without aid from an external ignition source. Because the combustion does not require an ignition source it can occur in multiple, independent

locations. Successive autoignition combustion fronts are characterized by adjacent locations combusting without the aid of heat conduction or radical species diffusion that happens with flame propagation. While thermal and molecular diffusion between adjacent autoignition sources occurs at a rate too low to affect front propagation, the combustion from one autoignition site increases the pressure and temperature (compression heating) of the system which results in adjacent sites reaching their ignition limit. Autoignition is not marked by a thin, propagating reaction zone like a flame owing to the combustion occurring in pockets. (Differentiating between flame fronts and autoignition fronts is discussed in Section 2.5.) With combustion occurring in multiple locations, the rate of heat release is rapid, leading to a short combustion event with high pressure rise rates. CDC relies on autoignition to initiate the combustion as there is no spark plug. Autoignition can occur in SI engines, i.e. knock, but is undesirable as SI engines are not mechanically designed to handle the rapid rate of heat release associated with autoignition events.

Supersonic combustion waves are referred to as detonations. Detonations normally occur in tubes where the expanding burned gases trapped at the closed end propel the flame front to speeds greater than the local speed of sound. Recently researchers have postulated that super-knock in the SI engine is a detonation event [12,13]. This study is solely concerned with flame propagation and autoignition events; detonations will not be encountered under the tested conditions.

2.2 Homogeneous Charge Compression Ignition

HCCI combustion uses an overall lean, premixed fuel-air mixture to achieve low-temperature combustion [14-17]. Similar to PFI, fuel preparation usually takes place upstream of the engine,

but fuel can also be early-cycle direct-injected to create the homogeneous mixture. Like most LTC strategies, the fuel-air mixture is compressed to high pressure and temperature and autoignites (compression ignition). Because the fuel-air mixture is homogeneously distributed in the cylinder, the whole chamber nearly simultaneously combusts; this causes the heat release duration to be short, and if phased properly near top dead center (TDC), a high thermal efficiency is attained. Many fuels have been used in HCCI research (e.g. n-heptane, iso-octane, ethanol), but low-reactivity fuels (e.g. gasoline) increase the efficiency as a higher compression ratio can be used. Additionally, by having a lean mixture no soot is formed, and, further, the temperature is low enough to produce low NO_x emissions.

HCCI is able to simultaneously achieve low emissions and high thermal efficiency, but it has its drawbacks. For instance, the combustion is kinetically controlled, and since the fuel is premixed, there is no direct control over the combustion phasing. The combustion phasing solely depends on the time-temperature history of the fuel-air mixture, so the intake charge temperature acts as the combustion phasing control. The thermal inertia of the engine results in a long time constant for changing the intake temperature, thus making it difficult to control combustion timing. The short combustion duration is also problematic when trying to use HCCI across a range of operating conditions. A high rate of heat release gives high in-cylinder pressure rise rates resulting in excessive combustion noise and structural issues. To minimize the risk of engine failure, the maximum load is limited such that HCCI cannot achieve the full load range of the engine.

Despite being one of the longest researched LTC combustion regimes, the exact mode of combustion propagation in HCCI remains an outstanding issue. The description of HCCI from optical studies has not changed an appreciable amount since the original publication in 1979

[14]. The combustion is seen to originate from multiple locations within the combustion chamber [18,19], and the combustion rapidly grows outward from these initiation sites. In principle, for a homogeneous mixture the entire charge would simultaneously ignite; single-zone detailed kinetic models show extremely short combustion durations, e.g. <2 crank angles [20]. In reality, while the combustion event is short, it typically takes ~5 crank angle degrees, which corresponds to <1 ms at road cruising speeds [21]. (Combustion in an SI engine takes on the order of 40-60 crank angle degrees [3], corresponding to a duration of ~6 ms.) Multi-zone models that simulate heat transfer to the cylinder walls, i.e. in-cylinder thermal gradients [19], can capture the combustion duration [22,23]. With HCCI's combustion event being much shorter than that of flame propagation, the mechanism of the propagation is assumed to be sequential autoignition.

Because autoignition has been widely accepted as the means of combustion, very little research has been performed to prove or disprove alternate theories. To date, the only research performed to prove an autoignition front existed was done by Hasegawa et al. [24], in which the authors used 2-D phosphor thermometry to map the temperature profile in a region of interest (ROI). The authors found ignition sources to have scales of 1-3 mm, making them too large for a flame front. The measurements were performed 27-10 ^{o}bTDC (crank angle degrees before TDC) where only approximately 7% of total heat release had occurred. At this point in the combustion event it is expected to be autoignition as there is no external ignition source. Additionally, the authors reported an image resolution of 180 μm. Based on Smith's research [8], SI engine flame thickness is approximately 200-300 μm; the flame thickness is expected to be less in a compression ignition engine as flame thickness is inversely proportional to pressure [10]. Typically 7-10 pixels are used to confidently resolve a length scale. Consequently for a flame, it

is estimated that a resolution of approximately 30 μm is required, making Haswegawa's optical arrangement inadequate to discern the existence of flame fronts.

While it is apparent that autoignition is a major contributor to the heat release, there are indications that flame propagation can exist. Spark assisted HCCI with spark timings of 55-25 ^{o}bTDC led to successful flame kernels and successive flame propagation with equivalence ratios as low as 0.33 [25]. Kaiser et al. [26] measured CO and CO_2 emissions as a function of equivalence ratio and found a transition point at $\Phi = 0.37$ where CO_2 was the dominant carbon emission for greater equivalence ratios and CO was prevailing for leaner mixtures. Kaiser cited Roberts et al. [27] who stated the conversion of CO to CO_2 is the main energy liberation mechanism for high temperature oxidation (i.e. flame propagation) whereas the formation of CO is the dominant energy liberation mechanism of autoignition. These examples of previous research demonstrate the possibility of flame propagation in HCCI conditions.

2.3 Partially Premixed Combustion

Similar to a diesel engine, PPC uses direct in-cylinder injection of the fuel. The goal is to extend the ignition delay enough such that the fuel-air mixture has mixed below the diesel sooting limit, $\Phi \approx 2$ [28,29] or the gasoline sooting limit, $\Phi \approx 1.5$ [30,31]. High amounts of dilution are used to keep the temperature, and consequently, the NO_x emissions low. The ignition delay can be extended by: (1) injecting early enough that the temperature is low and the fuel's ignition delay is long, (2) decreasing the oxygen concentration by using exhaust gas recirculation as the diluent [3], or (3) choosing a low reactivity fuel. There are many subtle variants of PPC, ranging from the use of diesel to gasoline and multiple injections [6,32-34], but the most promising implementation uses all three methods. When using gasoline as the fuel, nearly the full load

range of the engine can be achieved with acceptable noise levels [32-34]. The major drawback to gasoline PPC is that a narrow range of acceptable operating parameters exist for many conditions making control difficult [6].

PPC's propagation mechanism is less understood than HCCI because equivalence ratio stratification is present in addition to the thermal gradients due to evaporative cooling and wall heat transfer; the late-cycle injections create a highly stratified charge at the time of ignition. Because autoignition is the ignition source the propagation has been assumed to be sequential autoignition. The higher equivalence ratio regions approach conditions more conducive to flame propagation, but there are not any studies that have specifically addressed the existence of deflagrations in the PPC regime. Schmid et al. [35] used an optical engine to measure thermal soot radiation of diesel PPC for different nozzles and number of injections per cycle. The authors found that, depending on the configuration, high amounts of thermal soot radiation existed, indicating the presence of rich combustion. This rich, sooting diesel combustion is typical of a diffusion flame, and thus flame propagation.

Stratified-charge combustion also exists in recent wall- and spray-guided SIDI engines, in which late-cycle injections form a rich mixture at the spark plug to ensure stable flame kernel growth [1,2]. Combustion then proceeds by flame propagation from the rich regions to the leaner regions. The thermal and fuel stratifications are similar to PPC, suggesting flame propagation could exist in the PPC regime; however, due to the higher compression ratio of PPC engines, the in-cylinder pressure and temperature will be greater than in SI engines, decreasing the ignition delay [3]; a shorter ignition delay could indicate an autoignition front, as will be discussed in Section 2.5.

2.4 Reactivity Controlled Compression Ignition

RCCI is a relatively new LTC combustion strategy that utilizes two fuels to control the heat release rate (HRR) and combustion phasing. The simultaneous use of two fuels for emission control was first investigated by Inagaki et al. [36], but Reitz and co-workers [7,37-41] have developed the strategy with wide-spread success. A low-reactivity fuel (e.g. gasoline) is used to create a nearly homogeneous charge either through PFI or early-cycle DI. A high-reactivity fuel (e.g. diesel) is injected later in the compression stroke but still early enough to mix below soot and NO_x formation equivalence ratios, similar to PPC. Ignition takes place in regions of high reactivity and proceeds to low reactivity zones; the combustion duration is controlled by the spatial stratification of reactivity, where more mixing time decreases the stratification. Impressive results have been achieved over the full operating range of the engine using gasoline and diesel. The dual fuel strategy allows easy control of the combustion phasing, which is controlled by the local concentration of the high-reactivity fuel and the injection timing of the high-reactivity fuel. With the proper feedback, cycle-to-cycle control could be relatively easy to implement. As mentioned, the combustion duration is controlled by the reactivity gradient, which can be tailored to reduce pressure rise rates and decrease combustion noise. The drawback to RCCI lies in the need to have two separate fuels, but this is similar to needing a reductant fluid for an SCR system.

The combustion process of RCCI combustion shares many of the complications of PPC but with the added feature of a reactivity gradient introduced by the fuel composition. The ignition delay gradient, which controls the combustion progression, is affected by the equivalence ratio, fuel composition, and temperature. Computer models show combustion first ignites in the regions of high-reactivity (in spite of evaporative cooling) and the combustion

progresses along the reactivity gradient [7]; optical engine experiments have verified this behavior [42-44]. Depending on the high-reactivity fuel's injection timing and the injector's included angle, a core region can exist that will have conditions similar to that of HCCI, i.e. a region of purely low-reactivity fuel. The difference is that the core region is below the ignition limit, thus it requires either sequential autoignition or a deflagration to ignite the mixture.

The RCCI combustion process bears similarity to a diesel-piloted natural gas engine where a diesel injection near TDC is used as a strong ignition source for an overall lean natural gas mixture. In diesel-piloted combustion, the combustion is presumed to take place via a deflagration [45], but in RCCI combustion the role of flame propagation is unclear as only one study has experimentally addressed the question. Kokjohn [46] used laser ignition as a source for flame propagation. It was found that flame propagation could exist in RCCI conditions, as high-speed chemiluminescence showed luminous regions propagated away from the ignition spot. Flames did not propagate every cycle, but the probability of successful flame kernels increased with increasing equivalence ratio, suggesting the higher equivalence ratio regions are more likely to support flame propagation. The flame growth rate was also found to be similar to that of the autoignition reaction fronts further indicating flames could propagate from autoignition sites, but the two combustion fronts are not discernable with current optical measurements.

Kokjohn also modeled the iso-octane/n-heptane RCCI experiments and found that including the flame propagation mechanism had little effect on the results. (Both simulations captured the experiments well.) The author clarified that the results indicate the bulk of the combustion does not occur via flame propagation, but that it can still play a role on the local level as seen with the laser ignition experiments. Conversely, modeling results of natural gas/diesel RCCI required the addition of the same flame propagation model used by Kokjohn to

an autoignition model to correctly predict the experimental results indicating flame propagation is responsible for a nontrivial part of the heat release [47]. Both studies indicate flame propagation can exist in RCCI combustion, but the differing results indicate a need to fundamentally understand the mechanism by which the combustion propagates.

2.5 Combustion Front Propagation Mechanism Analysis

Owing to the interest in HCCI combustion, there have been several recent studies related to the mode of combustion propagation for mixtures that contain inhomogeneity in temperature and/or composition. The underpinning of all the work is the framework established by Zeldovich [48] who defined a set of propagation regimes based on the spatial distribution of ignition delay. Zeldovich proposed that a wave would travel at a speed s_{ig} of:

$$s_{ig} = \frac{1}{|\nabla \tau|} \tag{2-1}$$

where τ is the ignition delay; the nomenclature of Chen et al. [49-51] is used. For a mixture with a steep gradient in ignition delay, s_{ig} is very small, but in this case the combustion rate is constrained by the laminar flame speed s_L. That is, the wave does not propagate due to a successive autoignition front, but rather the front propagation is controlled by the diffusive-reactive balance of a premixed flame. For $c \gg s_{ig} > s_L$, where c is the local speed of sound, the front propagates at s_{ig}, which is still slow enough that the pressure waves equilibrate the pressure in the system. These two regimes are the most relevant to engine combustion, although detonations ($s_{ig} > c$) can occur as discussed in Section 2.1.

Chen and co-workers [49-51] have used one- and two-dimensional direct numerical simulation (DNS) to investigate combustion wave propagation in hydrogen-air mixtures with

initially non-uniform temperature fields; hot and cold spots were added at random with a fluctuation value of T' and characteristic length scale. The equivalence ratio, initial pressure and mean temperature were 0.1, 41 atm and 1070 K, respectively; these were derived from a 15:1 compression ratio engine with 1 atm and 400 K intake and are common to an engine operating in the HCCI regime. Knowing that the effect of temperature is a dominant contributor to ignition delay, the wave speed can be written in terms of the temperature gradient:

$$s_{ig} = \left|\frac{d\tau}{dT}\right|^{-1} \left|\frac{1}{\nabla \mathrm{T}}\right| \tag{2-2}$$

Chen et al. found that the effect of the non-uniform temperature depended on the integral length scale and fluctuation of the temperature field. Referring to Fig. 2-2 adapted from Chen et al. [49], small length scale disturbances had a long ignition delay which mixed out the initial temperature gradients resulting in homogeneous ignition, and thus combustion speeds greater than the deflagration speed. Thermal diffusion was found to be insignificant for large initial length scales as the ignition delay was short, and the combustion was governed by homogeneous ignition. An intermediate to these two limits, where a flame propagated, was found as can be seen by the 1.50 and 0.75 mm length scales having a front speed equal to the diffusive limit (laminar flame speed). Both small, due to mixing, and large length scales gave small temperature gradients yielding high front speeds, thereby agreeing with the inverse correlation of Zeldovich's proposal; the same is true for the intermediate scales with greater temperature gradients.

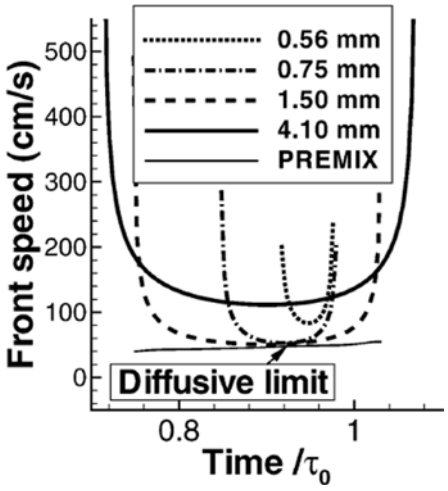

Figure 2-2: Wave speed for various temperature length scales. Adapted from Chen et al. [49].

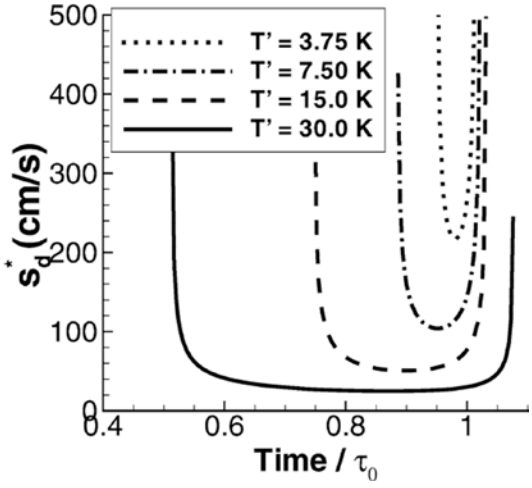

Figure 2-3: Wave speed for various temperature fluctuations. Adapted from Hawkes et al. [50].

The 2-D DNS studies were continued by Hawkes et al. [50] in which the temperature gradients were changed by varying the magnitude of the imposed temperature fluctuations. Increasing the magnitude for a fixed length scale increases the temperature gradient ($\Delta T = T'/\ell$). Keep in mind that temperature gradients are larger for flame propagation than autoignition as discussed in Section 2.1. The chosen, fixed length scale was shown to behave like the aforementioned intermediate length scales that yielded the smallest combustion front speed. Figure 2-3 shows that the largest temperature fluctuation reached a minimum limit. This agrees with the lower limit placed on Eqns. (2-1) and (2-2), and further shows that under HCCI conditions, the right combination of temperature gradient and length scale is indicative of a combustion front traveling at the laminar flame speed.

Chen et al. [49] sampled combustion fronts from the 2-D DNS results and plotted the wave speed against the temperature gradient. Figure 2-4 shows a power fit to the data with an exponent of -1.005 which is close to the expected value of -1 per Eqn. (2-2). Moreover, the inset figure shows the wave speed does not decrease indefinitely but, indeed, asymptotes to the

laminar flame speed $s_d/s_L = 1$; the crossover point is a temperature gradient of approximately 1800 K/mm. An examination of the reaction rate equations showed that the diffusive term was approximately 30% of the reactive term confirming the existence of flame propagation as opposed to autoignition fronts moving at the laminar flame speed, as radical species diffusion is a trait of flame propagation and not autoignition (see Section 2.1).

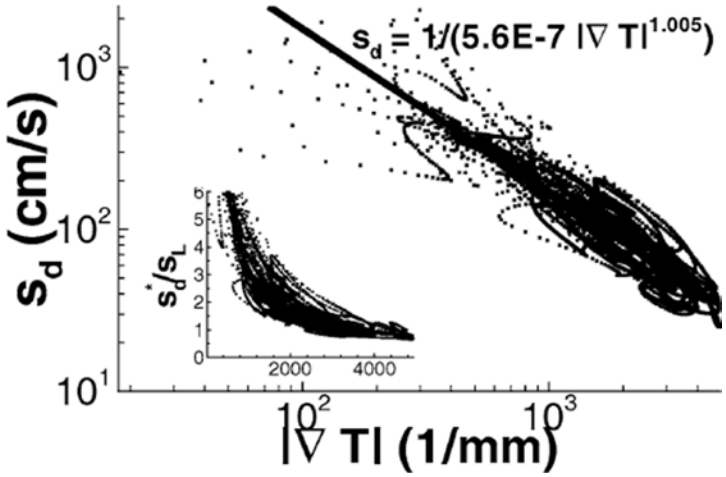

Figure 2-4: Wave speed vs. temperature gradient extracted from 2-D DNS simulations. Adapted from Chen et al. [49].

Recently Bansal and Im [52] investigated the combined effects of temperature and equivalence ratio inhomogeneity on the combustion rate for a hydrogen-air mixture with the same initial conditions as Chen et al (Φ = 0.1, T = 1070 K, P = 41 atm). Figure 2-5 shows the reaction (gray) and diffusion (black) rates of the HO_2 species front for increasing temperature gradients: 33, 200 and 467 K/mm, respectively. Cases Y and Z show a propagating front due to the significant diffusive term, which is absent in case X. As such, a Damköhler number based on the ratio of the positive peaks of reaction and diffusion rates of the HO_2 species was used to categorize the 2-D DNS simulations where a Damköhler *O*(1) is classified as flame propagation.

Cases with temperature gradients but homogenous fuel-air mixture showed flame propagation as previously shown by Chen et al. [49-51].

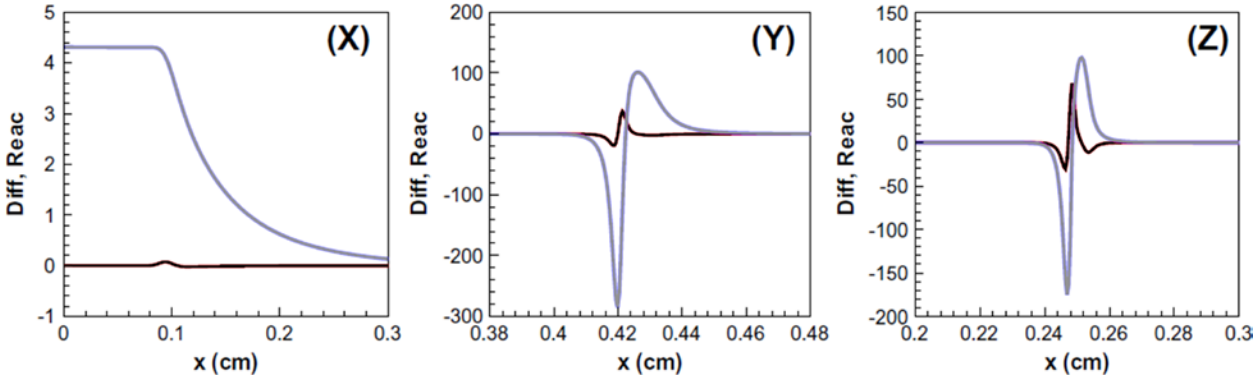

Figure 2-5: Reaction (gray) and diffusion (black) rates of H_2-air mixtures for imposed temperature gradients of 33, 200 and 467 K/mm, respectively. Adapted from Bansal and Im [52].

Thermal stratification of a more realistic engine fuel (n-heptane-air mixture) was investigated by Yoo et al. [53]. The authors chose mean temperatures within and outside the negative temperature coefficient (NTC) regime of n-heptane to assess the effects of single- and dual-stage ignition. A Damköhler number criterion for the diffusive limit yielded similar results to the earlier studies where a larger temperature fluctuation, regardless of the mean initial temperature, decreased the front speeds towards s_L showing the presence of flame propagation. Research therefore has shown that two vastly different fuels, hydrogen and n-heptane, agree with Zeldovich's proposal [48] that larger temperature gradients result in lower combustion speeds, which adds crucial robustness to the classification equation when one considers the wide range of engine fuels available.

Martz et al. [54] used a simplified 1-D approach to correlate front speeds and temperature profiles to the initial mixture temperature for HCCI of iso-octane. Results showed that a simple temperature criterion at the reaction front (the point separating the diffusion affected area from the chemical heat release) is suitable to differentiate between deflagration and ignition wave

propagation. The conclusion was supported by comparing the deflagration and chemical time scales; simulations where the chemical time scale was greater than the flame time scale had large temperature gradients and slow front speeds, whereas when the two time scales were within 5% of each other, the temperature gradient was smaller and the front speed increased fivefold. The authors did note the critical temperature is dependent on the fuel.

The simulations have yielded valuable information, but applying the DNS results to real engine flows reveals several differences between the two platforms. First, the temperature field in the engine is constantly changing prior to combustion. The relatively cold walls serve as a thermal energy sink during the compression stroke and during combustion. Therefore the effect of dissipation of the thermal gradients prior to combustion is less important than was seen in the DNS calculations; the heat transfer to the walls ensures thermal gradients always exist. Additionally, the Reynolds numbers (Re) in engine flows are higher than the values used in the DNS studies (Re = 51 in [52] and Re ≈ 200 in [53]). In an engine, the Reynolds number is on the order of 3000 assuming 1500 rpm, an integral length scale of 5 mm [55], and the turbulence intensity equal to one-half the mean piston speed. Parametric studies by Hawkes et al. [50] found that varying turbulent length scales, which changes the Reynolds number, resulted in the same temperature gradient (due to mixing during the ignition delay), the same combustion front speed, and the same amount of flame propagation. Consequently, the larger Reynolds number seen in engines is only expected to produce a larger range of scales [52].

As discussed in the above review, there are several proposed methods for categorizing the combustion propagation mechanism, thus it is essential to find the most robust method for an experimental environment. Defining a Damköhler number based on the reaction and diffusion rate of a species, like Bansal and Im [52] and Yoo et al. [53], is not allowable in an experiment

as only the total species concentration can be measured; the net production/consumption rate can be calculated from the total concentration, but the reaction and diffusion rates are not measurable nor discernable from the total concentration data. Also, using a simple temperature criterion at the base of the reaction front (Martz et al. [54]) is not practical as the temperature cutoff is a function of the fuel and the intake conditions. The temperature gradient relationship proposed by Zeldovich [48] and investigated by Chen and coworkers [49-51] promises to be a robust method because a temperature gradient will exist regardless of fuel composition, in-cylinder conditions, and propagation mechanism. The HCCI combustion regimes has temperature gradients induced by wall heat transfer making it an ideal candidate for application of Eqn. (2-2) as was previously done [49-51]. It Zeldovich's proposal were to be applied to PPC and RCCI, the effects of equivalence ratio and fuel composition (i.e. reactivity) on the ignition delay gradient would have to be quantified.

2.6 Methods for Measuring Combustion Front Characteristics

Using Zeldovich's proposal to determine the mode of propagation requires two pieces of information: the reacting front location and the temperature gradient. Several methods exist for identifying the reacting front such as planar laser-induced fluorescence (PLIF) of a tracer species added to the fuel [56-58], PLIF of an intermediate or equilibrium combustion species [56,57,59], Mie scattering [60,61], and Rayleigh scattering [8]. The majority of these methods can yield quantitative information such as temperature and mixture fraction of the probed species, but as will be shown, only Rayleigh scattering proves suitable for the needs of this study.

Tracer PLIF can mark the combustion front in SI engines [56-58,62], as well as provide quantitative results of the mixing field; temperature can also be obtained from quantitative PLIF.

While PLIF measurements are able to provide the two pieces of required information, several issues exist. Results have shown the lack of tracer does not always equate to the location of the flame front [56]. For quantification, fluorescence from typical tracer species such as acetone, 3-pentanone, and toluene are dependent on temperature, pressure, and gas composition in a complicated manner [62], making the calibration intensive; in the case of toluene, oxygen quenching of the fluorescence adds another complication [63]. These dependencies typically result in a decrease in fluorescence yield during the compression stroke [62] and can be incorrectly interpreted as tracer consumption. Additionally, the tracer is consumed in the reaction front, thus measurements of the product gas are not possible, resulting in an incomplete temperature profile.

OH PLIF has been used for flame front tracking [56,57,59,64] because it is an abundant species in high-temperature reactions, but for HCCI combustion the low-temperature reactions result in low concentrations of OH, making measurements difficult and prone to low signal-to-noise ratios (SNR). The intermediate species formaldehyde (HCHO) is capable of showing the onset of ignition for single- and dual-stage ignition hydrocarbon fuels [65], and the product of HCHO-OH PLIF measurements [66] has been used in a diffusion flame to better indicate the location of peak HRR. HCHO has been shown to persist long after the completion of combustion [67] in low equivalence ratio regions, leading to incorrect conclusions about the reaction zone thickness. CH, another intermediate species, is used to indicate a flame front, but combined OH results show the lack of CH does not correspond to a lack of a flame front [64]. Numerical results of premixed flames show that the location of the fast-dissociating species HCO correlates very well to the locations of fuel consumption and heat release, but HCO PLIF has low signal levels and consequently low SNRs of ~2 [68], which is unacceptable for high-quality

measurements. Furthermore, the local temperature cannot be extracted without intense calibrations (when possible) and additional assumptions regarding the fluorescence yield's dependence on temperature, pressure, gas composition, and collisional quenching [68]. Similar to tracer PLIF, none of the intermediate species will exist across the whole combustion front from reactants to species yielding an incomplete temperature profile.

Mie scattering visualization has been performed with homogenously seeded tracer particles (e.g. TiO_2 in the intake charge [60,61]) and fuel doped with high-boiling-point liquids (e.g. lubricating oil [69]) under engine conditions. Changes in the Mie scattering intensity effectively marked the deflagration front with the optical system limiting the flame thickness measurements [60]. Quantitative Mie scattering proves challenging, though, as calibrations are required where the Mie scattering intensity is measured for a known concentration of scattering particles in known conditions [69]. The dependence of Mie scattering intensity on the diameter of scattering particles [70] results in calibrations prone to high levels of uncertainty because the particles are typically generated *in situ* during the injection [69], so the size distribution is unknown. Even when the particle size is initially known by seeding the fuel, the Mie scattering intensity changes with temperature [61]. Additionally, high-boiling-point liquids breakdown around 1100 K, and therefore information about the temperature gradient across the reacting front cannot be achieved.

Due to a lack of species that will exist across the combustion front, it is recognized that the best choice of reaction progress variable would be the temperature itself, as it is required as well. As previously mentioned, tracer-based PLIF methods [56,71-73] fail due to thermal decomposition of the tracer species. High temperature PLIF measurements can be made with two-line ratiometric methods using OH [74], but low signal levels due to low OH concentrations

in the HCCI regime limit the diagnostic. Spontaneous Raman scattering spectroscopy yields low signal levels that are easily masked by stray LIF or laser-induced incandescence (LII) [75,76]. Additionally, it is limited to 1D measurements, thus not fulfilling spatial requirements. Improvements in signal level is achieved with coherent anti-stokes Raman scattering (CARS), but only single-point measurements are made [77-79], and therefore, temperature gradient measurements are not possible. Phosphor-based methods [80,81] can provide accurate temperature measurements, but the technique is not currently capable of measuring combustion temperatures as the phosphor particles are consumed during combustion.

Due to the limitations of the other temperature measurement techniques, the most likely method to succeed is Rayleigh scattering which was used by Smith [8] to investigate the nature of the premixed flame in a SI engine in 1982. That pioneering work demonstrated for the first time that the engine flame was, in fact, a wrinkled laminar flame by measuring the temperature gradient in the flame and the flame thickness. Rayleigh scattering has also been applied in engines to study mixing phenomena, i.e. to study the fuel concentration field [82-84] because Rayleigh scattering offers several advantages for making quantitative measurements.

First, Rayleigh scattering is an elastic scattering method that works via every molecule in the laser path, thus no additives are required; additionally, because molecules exist before, during and after the combustion front, Rayleigh scattering radiation can be produced through the whole combustion event giving the full temperature profile necessary for the temperature gradient. Complex calibrations for temperature, pressure, and species concentration are not needed to make the measurements quantitative since the scattering is elastic and proportional to the molecules' cross section which scales with the molecular number density [85]. The elastic scattering process is also the downfall to Rayleigh scattering and the reason why the technique is

not more widely implemented. Scattered laser light from unwanted sources (e.g. fuel droplets, oil droplets, metal and optical surfaces) must be minimized to achieve acceptable SNR. Further discussion of the Rayleigh scattering theory is addressed in Sections 2.7-2.10. Despite the possible issues which can be overcome through the experimental design, Rayleigh scattering is believed to be the best solution to measure the temperature field across the combustion front to classify the combustion propagation mechanism per Eqn. (2-2).

2.7 Rayleigh Scattering Background and Theory

The flourishing scientific community in the 19th century led to discussion about the sky and the reason for its blue color. Several scientists attempted to explain the phenomenon, but John William Strutt, better known as Lord Rayleigh, provided the breakthrough when he published his initial derivations of light scattering by small particles [86]. Lord Rayleigh concluded, based on correspondence with James Maxwell, that electromagnetic radiation scattered from air molecules gave the sky its blue appearance. As such, Rayleigh developed his scattering theory with the following results: (1) Rayleigh scattering occurs for particles much smaller than the wavelength of the incident light ($d \ll \lambda$), (2) the amount of scattered light is inversely proportional to the wavelength of light to the fourth power and linearly proportional to the intensity of incident light, (3) the scattered light is not coherent and is dependent upon the observation angle, and (4) the scattering is symmetrical such that diametrically opposite points of the particle scatter equal amounts of light [85]. For a more in-depth discussion of the working theory of Rayleigh scattering, interested readers are referred to Refs. [87-89].

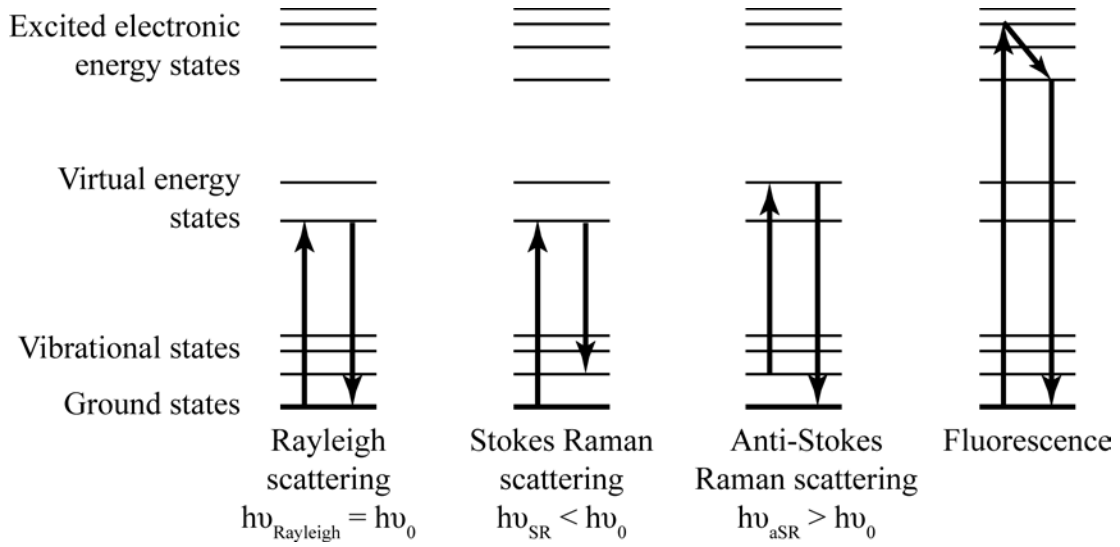

Figure 2-6: Energy state changes of common optical laser-based measurements. Adapted from Ref. [91].

Since the initial work, Rayleigh scattering was determined to be an elastic scattering process; that is, the scattered light's wavelength is the same as the excitation wavelength, with the exception being the case of moving particles in which a Doppler shift of the scattered radiation occurs [90]. Rayleigh scattering occurs when the electric fields of radiation interact with a polarizable molecule's electric field resulting in elastic scattering of electromagnetic radiation [87]. Figure 2-6 shows the photon scattering mechanisms of several common optical laser-based measurements. In the case of Rayleigh scattering, the interaction of a photon with a molecule raises the molecule's energy state to a virtual state. The virtual state is unstable, and the molecule relaxes to its original energy level emitting a photon at the same wavelength as the incident photon. In comparison, Raman scattering works on a similar principal except the relaxed energy state is different than the original one, which results in the emitted photon having a different wavelength than the incident radiation, and it is therefore inelastic scattering [75]. Fluorescence measurements (e.g. PLIF, as previously discussed) work by exciting a molecule to

a physical energy state, which requires knowledge of the correct excitation wavelength to achieve the transition [56,57]; fluorescence scattering is also inelastic.

The choice of the excitation source is critical to the experiment as it influences several factors. In many environments, such as combustion, there can be interfering signals emitted near the same wavelength that can exceed the Rayleigh scattering signal levels. Since Rayleigh scattering is the result of the induced dipole moment by the incident radiation, the scattering ceases when the excitation source is removed [92]. High power lasers operate in a burst mode, giving light pulses on the order of 10 ns in duration. With proper optical collection methods, the signal can be recorded for the just duration of the laser pulse, preventing excess contamination of the signal from errant sources. Due to the proliferation of high power lasers, laser Rayleigh scattering is the most prevalent implementation to date as it allows quick collection of the Rayleigh signal and consequential blocking of unwanted signals. Solid surface scatter and Mie-scattering are bigger issues, but they occur independent of the excitation wavelength and have to be eliminated through other means (see Section 2.10).

Rayleigh's first requirement that the scattering particle must be much smaller than the wavelength of incident light also impacts the light source choice. A typical criterion is given as $d < \lambda/10$ [89], where d is the particle diameter and λ is the light source wavelength. In the case of measuring the combustion propagation front, the gas-phase molecules (d=*O*(1 nm) [93]) in the system are the scattering source. This requires the excitation wavelength to be greater than ~100 nm. Commercial lasers (e.g. Nd:YAG, XeCl) and their harmonics are in the range of 250-1100 nm, satisfying this requirement.

Following Miles et al. [92], when dealing with spherical molecules (e.g. noble gases) the Rayleigh scattering equation is derived from expressions for the radiation from an infinitesimally small oscillating dipole [94]. The light intensity scattered from a single particle is:

$$I_s = \frac{\pi^2 \alpha^2}{\varepsilon_0^2 \lambda^4 r^2} I_I \sin^2 \phi \tag{2-3}$$

where I_s is the scattered light intensity [W/cm^2], α is the polarizability of the molecule [F-cm^2], ε_0 is the vacuum permittivity [F/cm], r is the molecular radius [cm], I_I is the incident light intensity [W/cm^2] of wavelength λ [cm], and ϕ is the observation angle relative to the dipole vector. The dipole moment is induced by the incident radiation with the dipole vector being parallel to the incident radiation's polarization. Referring to Fig. 2-7, the light propagating to the right along the y-axis has a vertical polarization as shown by its electric field E. This induces a dipole moment in the particle along the z-axis, thus ϕ is the angle relative to the z-axis.

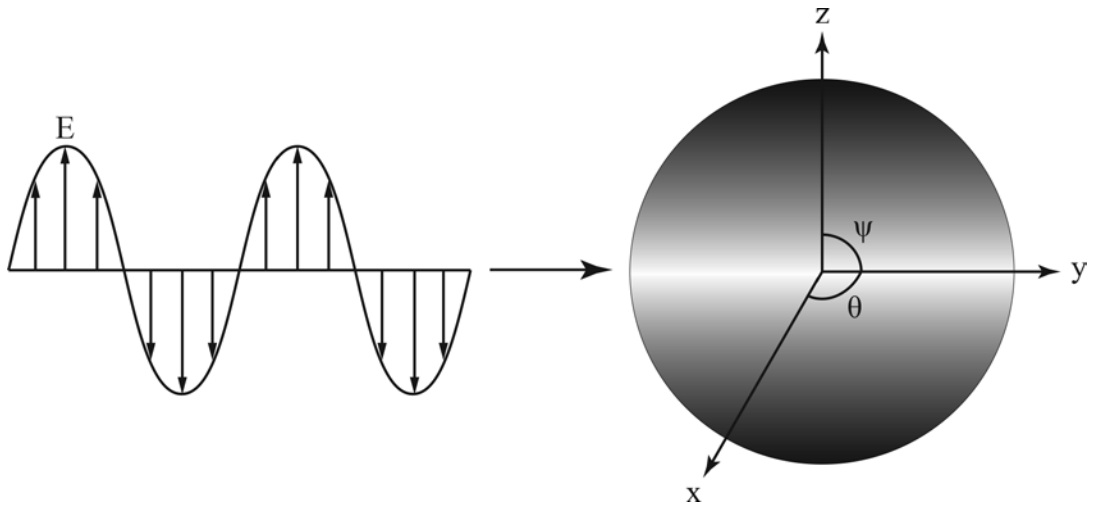

Figure 2-7: Diagram of a propagating light wave with a particle emitting Rayleigh scattering. The lighter area corresponds to greater Rayleigh scattering intensity. The wavelength and molecule size are not to scale.

Eqn. (2-3) demonstrates several important characteristics of Rayleigh scattering. The scattered intensity is inversely proportional to the wavelength of incident light to the fourth

power, thus a shorter wavelength significantly improves the signal yield. The scattered intensity is also linearly proportional to the incident intensity. While this influence is much weaker than the wavelength, it can be used to increase the scattered intensity once the wavelength is fixed. Finally, optimizing the observation angle is essential to visualizing Rayleigh scattering. Viewing the system parallel ($\phi = 0^o$, along the z-axis) to the dipole moment (and incident light polarization) will yield zero Rayleigh scattering per Eqn. (2-3), whereas viewing it perpendicular ($\phi = 90^o$, along the x-axis) will give the maximum intensity. This is visualized in Fig. 2-7 by the grayscale; lighter regions signify greater Rayleigh scattering intensity. Hence, to maximize the efficiency of the system, one would observe the Rayleigh scattering orthogonal to the polarization of the incident field.

For laser-based optical measurements, a species-dependent scattering cross section is typically defined. The cross section is dependent on several variables such as the molecular polarizability, index of refraction, and excitation wavelength. (Rigorous discussion of the cross section is found in Section 2.9.) Cross section dependent parameters and ancillary constants are placed in the scattering cross section term. The scattering cross section is dependent on the observation angle, and since one does not view from a single angle but rather through a solid angle Ω [sr] subtended by the collection optics. Rewriting Eqn. (2-3) for a differential Rayleigh scattering cross section $\partial\sigma_R/\partial\Omega$ [cm^2/sr]:

$$I_s = \frac{\partial\sigma_R}{\partial\Omega}\frac{1}{r^2}I_I, \qquad \frac{\partial\sigma_R}{\partial\Omega} = \frac{\pi^2\alpha^2}{\varepsilon_0^2\lambda^4}\sin^2\phi \tag{2-4}$$

The polarizability of the molecule α is related to the index of refraction n of the molecule by the Lorentz-Lorenz equation [94].

$$\alpha = \frac{3\varepsilon_0}{N}\frac{n^2-1}{n^2+2} \tag{2-5}$$

where N is the number density of the gas [molecules/cm^3]. Nominal Rayleigh scattering cross sections are computed at standard temperature and pressure (STP), so N is given by the Loschmidt number $N_0 = 2.687 * 10^{19}\, cm^{-3}$. The refractive index is easily measured experimentally and is, hence, used in calculations instead of the polarizability. Substituting Eqn. (2-5) into the differential cross section gives:

$$\frac{\partial \sigma_R}{\partial \Omega} = \frac{9\pi^2}{\lambda^4 N_0^2}\left(\frac{n^2-1}{n^2+2}\right)^2 \sin^2\phi \tag{2-6}$$

For a complete analysis of the Rayleigh scattering measurements, it is advantageous to know the scattered intensity and power. Eqn. (2-4) can be integrated over the surface area of a sphere with radius r to obtain the total power [W] scattered by a single particle.

$$P_{tot} = \frac{9\pi^2}{\lambda^4 N_0^2}\left(\frac{n^2-1}{n^2+2}\right)^2 I_I \int_0^{2\pi}\int_0^{\pi}\frac{\sin^2\phi}{r^2} r^2 \sin\phi \, d\phi d\theta \tag{2-7}$$

where θ and ϕ are the azimuthal and polar angles, respectively, per mathematical notation and depicted in Fig. 2-7. The total power after integration is:

$$P_{tot} = \frac{24\pi^3}{\lambda^4 N_0^2}\left(\frac{n^2-1}{n^2+2}\right)^2 I_I \tag{2-8}$$

When using pulsed lasers, the total scattered energy [J] can be more meaningful and is obtained by integrating Eqn. (2-8) over the laser pulse duration. Due to the linear dependence of the scattered power on the incident intensity, the energy-based intensity [J/cm^2] can be used instead of the temporal integration of the power-based intensity [W/cm^2]. The total scattering cross section is determined from the total scattered power:

$$P_{tot} = \sigma_R I_I, \qquad \sigma_R = \frac{24\pi^3}{\lambda^4 N_0^2}\left(\frac{n^2-1}{n^2+2}\right)^2 \tag{2-9}$$

The total scattering cross section was derived from integrating over the total surface area of a spherical particle. It is commonly used in literature but is incorrect because, in practice, all of the scattered light from a molecule is not collected as the light scatters in all directions. Another mislabeling of the cross section occurs due to a simplification. In many texts the Rayleigh cross section is reported as a function of $(n-1)^2$. By assuming the index of refraction is close to 1, the limit of Eqns. (2-6) and (2-9) as $n \to 1$ simplifies σ to [92]:

$$\frac{\partial \sigma_R}{\partial \Omega} \approx \frac{4\pi^2}{\lambda^4 N_0^2}(n-1)^2 \sin^2 \phi \qquad \sigma_R \approx \frac{32\pi^3}{3\lambda^4 N_0^2}(n-1)^2 \tag{2-10}$$

In the subsequent calculations, the non-approximated differential Rayleigh scattering cross section, Eqn. (2-6), is used; Eqn. (2-10) is presented for clarification as some texts erroneously list the simplified cross section as the full one.

The differential scattering cross section is necessary for accurate calculations. In principle, the differential Rayleigh scattering cross section is integrated over the solid angle Ω because the observation angle ϕ varies across the subtended angle, but it is typically taken as constant since the subtended angle is small for most optical systems.

$$P_{\Delta\Omega} = I_I \int_{\Omega} \frac{\partial \sigma_R}{\partial \Omega} d\Omega \approx \frac{9\pi^2}{\lambda^4 N_0^2}\left(\frac{n^2-1}{n^2+2}\right)^2 \sin^2 \phi \, I_I \Delta\Omega \tag{2-11}$$

The power expression in Eqn. (2-11) is for a single molecule. When a group of molecules are excited by an electric field, the total scattered power is equal to the sum of the power emitted by the individual molecules [92]. It is also of interest to know how the scattered light and

measured light compare. For a given observation volume V [cm^3] the total power measured optically becomes:

$$P_{\Delta\Omega} = \eta I_I NV \int_{\Omega} \frac{\partial \sigma_R}{\partial \Omega} d\Omega \tag{2-12}$$

where η is the optical system's collection efficiency and NV is the total number of scatterers in the volume. Again, because the individual effects are additive, the total power contribution from a mixture can be calculated with a mole-fraction-based effective cross section [85]. Equation (2-13) gives the total optically measured power for a mixture of j different molecules of mole fraction x.

$$P_{\Delta\Omega} = \eta I_I NV \sum_{i=1}^{j} x_i \int_{\Omega} \frac{\partial \sigma_{R,i}}{\partial \Omega} d\Omega \tag{2-13}$$

In the case of planar laser measurements, a camera captures the Rayleigh scattering in a finite region, and as previously mentioned, the energy form of the equations is more tangible for pulsed laser systems because the energy per pulse can be measured. Each pixel of the captured image will be a measure of the intensity [J/cm^2] in the area projected by the pixel in the laser plane. Equation (2-14) gives the Rayleigh scattering intensity for a measurement length ℓ [cm]. This form of the Rayleigh scattering equation will be the foundation for the forthcoming analyses.

$$I_R = \eta I_I N \ell \sum_{i=1}^{j} x_i \int_{\Omega} \frac{\partial \sigma_{R,i}}{\partial \Omega} d\Omega \tag{2-14}$$

2.8 Rayleigh Scattering Thermometry and Reaction Front Thickness Measurements

The basic Rayleigh scattering theory in Section 2.7 can be applied for thermometry. The nature of Rayleigh scattering only allows for three parameters to be determined; for binary mixtures (e.g. fuel and air), the mole fraction of the two gases and temperature can be determined, whereas three mole fractions can be solved in an isothermal flow field [85]. Given the restrictions, the experiment must be designed to accommodate determination of the desired information.

In the case of combustion, the mixture has much more than two components, and, for obvious reasons, is not an isothermal flow. These uncontrollable variables make the experimental design more difficult, but the temperature can still be measured. Assuming an ideal gas, the number density [molecules/cm^3] can be written as:

$$N = \frac{PN_A}{RT} \tag{2-15}$$

where P is the pressure [Pa], $N_A = 6.022 * 10^{23}\, mol^{-1}$ is Avogadro's number, $R = 8.314\ J/mol - K$ is the gas constant, and T is the temperature [K]. Because the local pressure is assumed to be equilibrated in an engine with successive autoignition or flame propagation (see Section 2.5), the number density is inversely proportional to temperature. Since the temperature increases from the reactants to products, the density will decrease, and per Eqn. (2-14), the density decrease will result in a decrease in the Rayleigh scattering intensity, thus marking the location of the combustion front. Figure 2-8 shows an example of the raw Rayleigh scattering signal across a flame front. The flame is propagating right to left, so the higher intensity dots

correspond to areas of unburned mixture whereas the lower intensity data are combustion products.

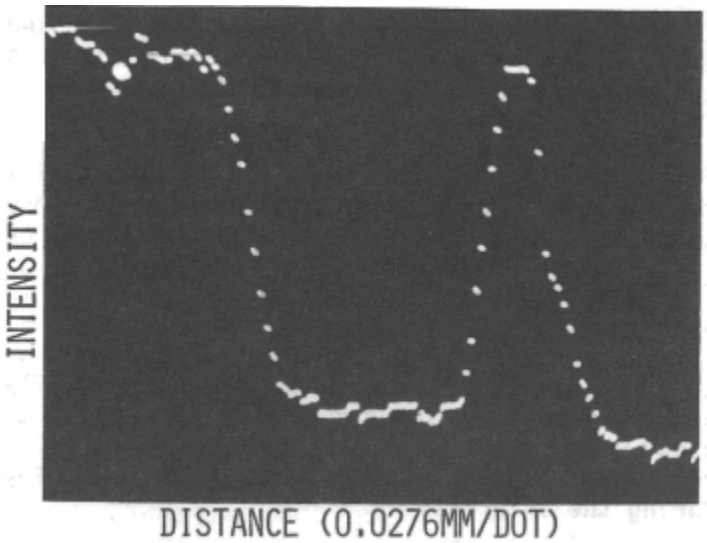

Figure 2-8: Rayleigh scattering intensity vs. distance across a flame front propagating from right to left. An island of unburned mixture exists behind the flame front. Adapted from Smith [8].

For a mathematical perspective, Eqn. (2-15) is substituted into Eqn. (2-14):

$$I_R = \eta I_I \frac{PN_A}{RT} \ell \sum_{i=1}^{j} x_i \int_{\Omega} \frac{\partial \sigma_{R,i}}{\partial \Omega} d\Omega \tag{2-16}$$

To obtain the temperature from Eqn. (2-17), the other variables must be accounted for, which is trivial except the scattering intensity I_R and optical efficiency η. Light scattering calculations [95] based in physics can be performed but must calibrated by means of the unknown optical efficiency. The paradox makes finding another solution appealing. A reference condition, denoted by subscript 0, can be defined in the same manner as Eqn. (2-16). The temperature is calculated by dividing the reference condition intensity $I_{R,0}$ by the desired condition intensity I_R. Assuming setup-specific constants such as the test section length ℓ, laser intensity I_I, solid angle Ω, and optical collection efficiency η are the same, the result is:

$$\frac{T}{T_0} = \frac{I_{R,0}}{I_R}\frac{P}{P_0}\frac{\partial \bar{\sigma}_R}{\partial \bar{\sigma}_{R,0}} \tag{2-17}$$

The mixture cross section given by the summation term in the previous equations is now represented by $\bar{\sigma}_R$. Equation (2-17) forms the basis for Rayleigh scattering thermometry measurements. The desired temperature is a simple function of the scattering intensity, pressure, and scattering cross section for the measured and reference conditions and the temperature of the reference condition. The scattering intensity variables are still present but in a ratio form. To circumvent the issue of calculating the amount of scattered light, the intensity as measured by cameras can be used. The amount of scattered light and the light measured by a camera are related by a constant, which is divided out by the ratio, thereby allowing the quantitative temperature measurements.

The error of the temperature measurement is minimized by careful design of the experiment. As previously mentioned, cameras can accurately capture the emitted Rayleigh scattering. The reference condition has well-known thermodynamic conditions to minimize the uncertainty of T_0 and P_0. In the case of engine experiments, in-cylinder pressure transducers accurately measure the pressure. During combustion the species concentration varies widely causing the cross section to be variable. If the reactant, intermediate, and product cross sections are significantly different from each other, too many uncertainties arise, and an accurate measurement cannot be achieved. Therefore, having a constant cross section from the reactants to products is a principle requirement of Rayleigh scattering thermometry, i.e. the cross section ratio is typically assumed to be equal to one. The error associated with the temperature measurement is then strongly dependent on the divergence of $\partial \bar{\sigma}_R / \partial \bar{\sigma}_{R,0}$ from unity and if the deviation can be accounted for.

It is difficult to maintain a constant mixture cross section when using hydrocarbon fuels as they have larger scattering cross sections than the main constituents of combustion: N_2, O_2, CO, CO_2, and H_2O. Because the products of hydrocarbon combustion have a smaller cross section than the reactants, the cross section ratio is less than one ($\partial\bar{\sigma}_R/\partial\bar{\sigma}_{R,0} < 1$), and the assumption of unity will over predict the products' temperature. The cross section error can be reduced in several manners such as employing low equivalence ratios/high dilution to reduce the molar impact of the hydrocarbons, or by choosing fuels that match the cross section of the products. Dibble et al. [96] used a mixture of methane and hydrogen that matched the reactant and product cross sections to within a 2% difference. With this fuel, turbulent diffusion flame Rayleigh scattering measurements were performed for the first time. Namer and Schefer [97] tested fuels ranging from hydrogen to propane and found that smaller hydrocarbon fuel molecules such as C_2H_4 could still be used up to equivalence ratios of 0.65 with a small amount of error; the error is too great for larger molecules without making corrections. To increase the accuracy of results, researchers [97-102] have been able to model the combustion event and account for the changing cross section across the reaction zone. This method is limited to simple flames, so the reaction zone cannot be perfectly cross section corrected, but the products can as their location is evident, as seen in Fig. 2-8.

As discussed in Section 2.1, there is a contrast in the combustion front thickness between the two combustion modes in that flame propagation has a thin reaction front. Thus further classification by the reaction front thickness can be calculated to provide more insight into the combustion mechanism, and it can be done with the same set of data. Figure 2-9 depicts a model that was used by Smith [8] to calculate the flame thickness. The thickness is defined as the distance between intercepts of the reactant and product densities with a line determined by the

maximum average density gradient. Smith used subscript *0* as the reactants and subscript *F* as the products, as illustrated by flame front. As a comparison, a similar definition of thickness can be calculated using temperature [10].

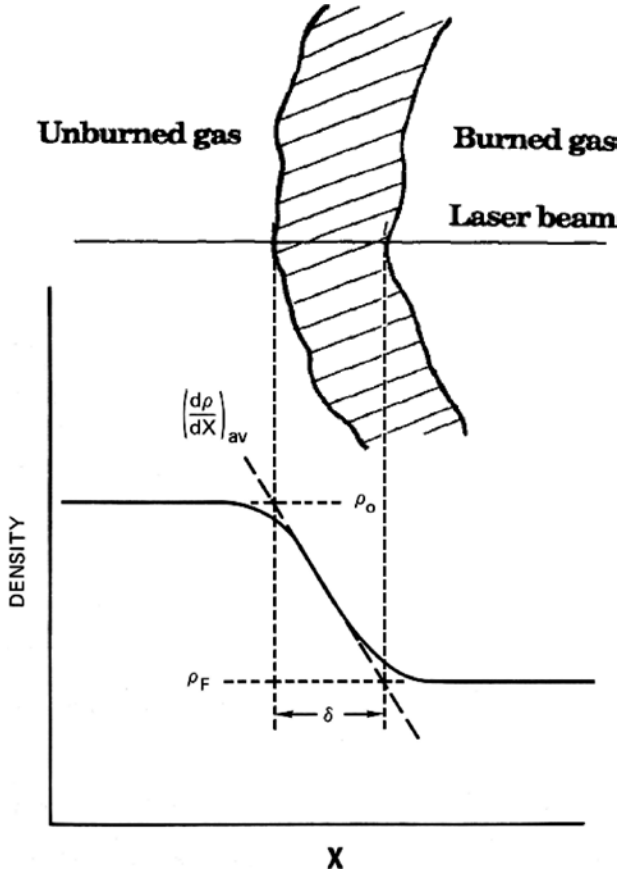

Figure 2-9: Smith's definition of flame front thickness based on the mixture density. Adapted from Smith and Zhao [8,85].

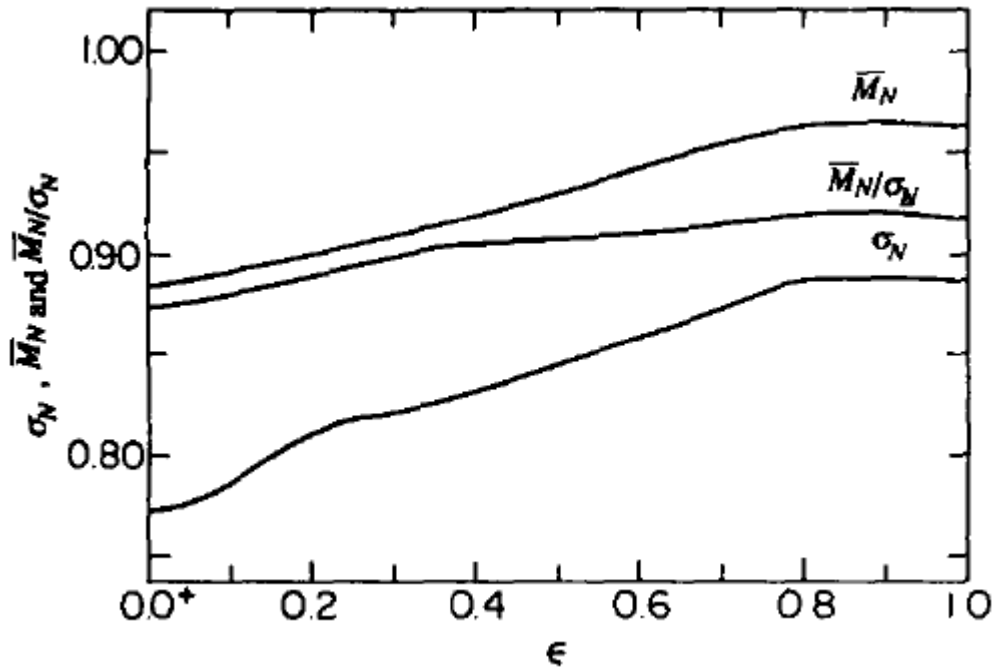

Figure 2-10: Variation of the Rayleigh cross section and mixture mean molecular weight as a function of the reaction progress variable through a stoichiometric ethylene-air flame. Adapted from Namer and Schefer [97].

To calculate the density ρ [kg/m^3], the ideal gas law is written as:

$$\rho = P\bar{M}/RT \tag{2-18}$$

such that

$$N = \rho N_A/\bar{M} \tag{2-19}$$

where $\bar{M}$ is the mean molecular weight of the mixture [kg/mol]. Substituting this definition of the number density into Eqn. (2-14) and defining a reference condition gives the Eqn. (2-20) to calculate density.

$$\frac{\rho}{\rho_0} = \frac{I_R}{I_{R,0}}\frac{\bar{M}}{\bar{M}_0}\frac{\partial\bar{\sigma}_{R,0}}{\partial\bar{\sigma}_R} \tag{2-20}$$

It was discussed with the temperature measurements that the error will be a function of scattering cross section. For the density measurements, the error will be a function of not only the cross section but also the mixture molecular weight. To determine which method is more accurate,

Namer and Schefer [97] calculated the change in the cross section and molecular weight through a stoichiometric ethylene-air flame as shown in Fig. 2-10. The results show there is less error associated with interpreting the Rayleigh scattering as density compared to temperature because $\bar{M}/\sigma$ (Eqn. (2-20)) changes less than σ (Eqn. (2-17)). First calculating the density and then the temperature via Eqn. (2-18) will not result in more accurate temperature measurements because combining the individual errors of $\bar{M}$ and $\bar{M}/\sigma$ will result in the same error as σ.

2.9 Rayleigh Scattering Cross Section

The Rayleigh scattering cross section of Eqn. (2-14) is the only non-self-explanatory component, and also turns out to be quite complex. Since each molecule scatters light in the Rayleigh scheme, it is important to understand how the cross section functions. It is known that the amount of elastically scattered light is proportional to the diameter of the scatterer to the sixth power [92], therefore the cross section is dependent on the physical size of the molecule and by extension, the molecular weight. In Eqn. (2-6) this is hidden in the index of refraction, but is also seen in Fig. 2-10 where the cross section increases with the molecular weight. This knowledge has been applied to mixing measurements in which large, heavy molecules (e.g. Freon-12 [83]) are used to scatter significantly more light than the mixing medium to achieve high SNRs, increasing the accuracy of the mixing field measurements. Due to its importance on the accuracy of the temperature measurements, it is necessary to completely understand the Rayleigh scattering cross section and the factors that affect it: index of refraction, temperature, and molecular depolarization. The basic cross section Eqn. (2-6) is given again for reference.

$$\frac{\partial \sigma_R}{\partial \Omega} = \frac{9\pi^2}{\lambda^4 N_0^2}\left(\frac{n^2-1}{n^2+2}\right)^2 \sin^2 \phi$$

2.9.1 Index of Refraction

The refractive index of a material is a measure of how the speed and wavelength of a wave, light or sound, change relative to a reference condition when propagating in a given material. This is a result of the interference between the wave's electric field and the field induced in the material; it is also wavelength dependent. The refractive index has been measured for many of the common combustion species and can be found in literature [97,98,103-107]. In the cases of larger and less-common molecules, measurements of the refractive index may not exist, but calculations can be performed based on the additive properties of atoms. Jenkins and White [108] stated molecular refractive indices are almost independent of molecular bonds, thus each atom's refractive index may be summed to obtain the molecule's refractive index.

Because refractive index is a function of the wavelength, relationships between refractive index and wavelength have been developed. The most robust equation was proposed by Sellmeier [109] and can be used to obtain refractive indices at the working wavelength. Equation (2-21) is the expanded form, where λ is the vacuum wavelength and the six coefficients are determined experimentally. Several databases contain Sellmeier coefficients for a wide range of mediums.

$$n^2(\lambda) = 1 + \frac{B_1\lambda^2}{\lambda^2 - C_1} + \frac{B_2\lambda^2}{\lambda^2 - C_2} + \frac{B_3\lambda^2}{\lambda^2 - C_3} \tag{2-21}$$

2.9.2 Temperature Dependence

Graham et al. [110] analyzed the temperature effects on the Rayleigh scattering cross section. The analysis was based on the increasing population of the more energetic rotational

states which cause the molecular bonds to stretch from the centrifugal forces. The stretched molecular bonds result in a larger diameter molecule, and thus a greater Rayleigh scattering cross section. Methane was used as an example to show a relative cross section change of 2e-5 K^{-1}; that is approximately a 4% increase as the temperature is changed from 300 to 2000 K. It was stated that the cross section increase due to temperature for simple molecules such as the predominant combustion products is not expected to be significantly more than methane, especially for strongly bonded molecules such as O_2, N_2, CO, and CO_2. Sutton and Driscoll [99] found a wavelength dependent response to temperature increases. Cross section increases were found to be 5-11% at 266 nm, but 2-8% for 355 nm over a temperature range of about 1200 K. The trend suggests longer wavelengths are less affected by temperature changes. Methane and homonuclear molecules (e.g. O_2, N_2) were the most affected, and CO and CO_2 showed less sensitivity to temperature changes.

2.9.3 Depolarization

When developing the Rayleigh scattering intensity equations in Section 2.7, the analysis assumed spherical particles. In reality, few spherical particles (i.e. individual atoms) exist in combustion systems making the sphericity assumption inappropriate. When non-spherical molecules are subjected to an electric field, their induced dipole moment does not necessarily align with the incident field polarization. The nonparallel dipole vector yields scattering with parallel and perpendicular polarizations relative to the field polarization. The perpendicularly polarized scattering is the product of depolarization. The depolarization ratio ρ characterizes the amount of incomplete polarization of scattered light and can be derived from the principal axes of the polarizability tensor; it can also be viewed as a measure of the sphericity of a molecule.

For example, methane (CH_4) is referred to as a spherical-top molecule due to it likeness of a sphere [111] and as such has a depolarization ratio of 2e-4 (see Table 4-1). Conversely, CO_2 is asymmetrical and has a depolarization ratio of 3.5e-2, two orders of magnitude greater than methane. This ratio is the foundation of the King correction factor F_k that accounts for the depolarization of molecules [98].

$$F_k = \frac{6 + 3\rho_n(\lambda)}{6 - 7\rho_n(\lambda)} = \frac{3 + 6\rho_p(\lambda)}{3 - 4\rho_p(\lambda)}, \quad \rho_n = \frac{2\rho_p}{1 + \rho_p} \tag{2-22}$$

ρ_n and ρ_p are the depolarization ratios for natural (unpolarized) and polarized light, respectively. Either equation works because the cross section is independent of the incident polarization. ρ is index-of-refraction dependent through the Lorentz-Lorentz equation (Eqn. (2-5) [94]), and is therefore a function of the incident wavelength. $F_k \geq 1$ which means non-spherical molecules have a larger effective cross section than their spherical counterparts of the same index of refraction. Several sources have reported King correction factors [92,98] and depolarization ratios [99,104] for species of interest. The depolarization ratio increases with decreasing wavelength, which will lead to greater error in the cross section if accurate depolarization data is not available.

Because random molecular orientation at the time of excitation adds to the effect of depolarization, Forkey [112] analyzed the depolarization while taking into account molecular orientation averaging to derive equations for the differential Rayleigh scattering cross section. In the analysis, the King correction factor was recovered demonstrating consistency, but the analysis also yielded terms that determine the amount of scattered light with parallel and perpendicular polarizations that arise from depolarization. The proportion of light with parallel and perpendicular polarizations is, respectively:

$$f_{\parallel} = \frac{1}{2 + \rho_n(\lambda)}[\rho_n + (2 - 2\rho_n)(1 - \cos^2 \phi)] \quad (2\text{-}23)$$

$$f_{\perp} = \frac{\rho_n(\lambda)}{2 + \rho_n(\lambda)} \quad (2\text{-}24)$$

where ϕ is the angle relative to the field polarization, which has a maximum at 90^o as previously discussed. For an example of the depolarization effect, Sneep and Ubachs [98] state ρ_n of N_2 for an excitation wavelength of 500 nm is 0.0213. This equates to a King correction factor of 1.036, the proportion of scattered light with parallel polarization to 0.979 and 0.021 for perpendicular polarization. The King correction factor shows that non-spherical molecules will scatter more light than their spherical counterparts of the same refractive index, and the polarization term demonstrates the slight depolarization of scattered light.

2.10 Experimental Difficulties

The elastic scattering process of Rayleigh scattering has presented significant difficulties when experiments have been performed in engines and engine-like environments [82,113-115]. With elastic scattering it is imperative to reduce the background scatter from the excitation light to a minimum in order to achieve the highest SNR possible. In an engine there are several sources of spurious scattering: metal and optical surfaces, oil and fuel droplets, and particles in the air and fuel. Fortunately steps can be taken to combat each issue.

Metal surfaces can be painted with a low-emissivity, high-temperature paint and be pre-coated with soot. Previous Rayleigh scattering and PLIF in-house experiments have shown soot-coated components result in the lowest background signal; however, the soot can release from the surfaces and then be problematic particles in the air. High-quality optics must be used in

which the scratch-dig (a measure of scratch width [μm] and dig diameter [hundredths of mm]) must be of laser quality, 20-10 or better. The surface flatness should be $\lambda/8$ or better to prevent wavefront distortions caused by lensing effects. In addition, the optical surfaces have to be periodically cleaned, otherwise dirty surfaces lead to diffuse light scatter.

In-cylinder oil droplets can be avoided in the experimental setup (Section 3.1) by using a Bowditch optical engine [116], in which polytetrafluoroethylene (PTFE, e.g. Teflon®) piston rings can operate without lubrication. Furthermore, an oil-less engine head reduces the risk of oil contamination from the head gasket and valve train. Internal combustion engines are traditionally operated with liquid fuels, e.g. gasoline and diesel, due to their high energy density, but liquid droplets from incomplete vaporization during injection pose an issue. Droplets are several orders of magnitude larger than molecules (d=*O*(1 μm) for diesel [117], d=*O*(10 μm) for isooctane [118]), which places them in the Mie scattering regime. The scattering cross section is proportional to the diameter to the sixth power [92], so droplets will scatter significantly more light than molecules. Droplets can be minimized by injecting into highly evaporating environments such as typical diesel conditions, premixing a volatile fuel like iso-octane upstream of the engine, or using gaseous fuels. Direct-injection of isooctane in a constant-volume vessel with SIDI engine conditions found fuel droplets contaminating Rayleigh scattering imaging 30 mm downstream of the injector despite the fuel's high volatility and favorable conditions for evaporation [114]. Therefore gaseous fuels present themselves as the best option providing a suitable surrogate for the traditional fuels exists.

Particles in the fuel, which were determined to originate from mechanical wear of the high-pressure diesel pump, have also led to bright spots in the Rayleigh scattering images [115]. Static fuel pressurization systems and fuel filtering have successfully managed fuel

contamination [113-115]. High-purity gases (99.99%+ purity) can be obtained, and in conjunction with gas filters that can efficiently filter particles to an order of magnitude larger than molecules, gaseous fuels are even more attractive. Particles in the air are typically introduced in the intake system especially when using general-use building air. Many commercial filters exist for filtering sizes down to 10 nm at the flow rates necessary for engine operation. Laboratory experiments with a 93% efficient, 10 nm filter have shown suitable particle removal when performing Rayleigh scattering experiments. Particle contamination can also occur via soot which will scatter and absorb the laser light [85] presenting unwanted scatter and attenuation issues. The spark-ignition and LTC combustion regimes to be investigated all provide sufficient mixing when properly implemented to prevent the formation of soot, thereby avoiding the problem.

Additional background scattering occurs when the laser's path deviates from the intended path via beam steering. In the case of an engine, the laser beam's direction be altered enough that it does not leave the cylinder and continually reflects off surfaces, tainting the results. As it pertains to the experiment, index of refraction gradients exist at the window-cylinder interfaces, in stratified mixtures, and across the combustion front. Unfortunately engine conditions are unpredictable, resulting in unpredictable beam steering, but the effects can be reduced by increasing the size of the laser-exit window to allow a divergent beam to exit the combustion chamber.

Besides elastic light scatter that interferes with Rayleigh scattering measurements, the combustion process can have emission spectra at the Rayleigh scattering wavelength. Kim et al. [119] made spectroscopic measurements of SI, and HCCI combustion modes. Each mode had broad band emission from CO oxidation extending from the ultraviolet (UV, <400 nm) into the

red wavelengths. SI experiments showed the spectra shifted towards red wavelengths due to soot oxidation, while HCCI spectra were centered around 400 nm. Individual species emissions were measurable for OH at 306 nm, CH at 431 nm, and C2 at 473 and 516 nm. Augusta et al. [120] performed detailed spectra analysis of HCCI combustion and found many species in the UV and near-UV range superimposed on the CO-O continuum: HCO at 295, 301, 312, 319, 330, 338, 350, and 359 nm, OH at 306-309 nm and HCHO at 341, 368, 412, and 422-424 nm. Additional CH bands exist at 387-389 nm, and fuel-rich combustion can lead to atomic carbon (C*) emission at 248 nm [121].

It is clear that many interfering signals can easily coincide with the Rayleigh scattering signal. The choice of Rayleigh scattering wavelength must then consider natural radiation emission of combustion species to avoid excessive interference. The choice of wavelength is not just dependent on the possible interference, though. It was shown that shorter wavelengths will yield greater Rayleigh scattering intensity, but depolarization and temperature effects are greater at lower wavelengths leading to increased error. Additional optical collection parameters have to be accounted for as well such as the camera quantum efficiency which is typically lower in the UV range than the visible. The choice of laser excitation wavelength and all measures taken to minimize scatter and increase the signal-to-ratio are discussed in Section 3.3.

Chapter 3 - Experimental Setup

This section details the optical engine setup and its various components and control points. The critical choice of fuels is discussed and well as the fuels' implications on the experiments and on a global scale. Finally, all of the engine and external optics required for the Rayleigh scattering measurements, as well as the steps taken to yield data with the least amount of uncertainty are presented in detail.

3.1 Engine Setup

The experiments were performed in a single-cylinder optical engine with an extended Bowditch piston [116] as shown in Fig. 3-1. The basic engine details are listed in Table 3-1. The small bore engine was based on the GM Fiat 1.9L high-speed diesel engine, and therefore has similar valve timings. Although the engine was also used for diesel research, the experiment's setup has a low compression ratio of 9.0-11.9 (depending on the setup), which is not optimal for HCCI; this is an artifact of the required optical setup. The engine was operated at 1200 RPM for all experiments to match the laser system that operates at 10 Hz, thus the laser will emit once per an engine cycle.

Table 3-1: Engine geometry. Crank angle timings are relative to TDC of compression.

Displacement [L]	0.4
Geometric compression ratio	9.0 (spark-ignition)
	9.6 (HCCI)
Engine speed [RPM]	1200
Squish height [mm]	8.1 (spark-ignition)
	7.5 (HCCI)
Bowl volume [mL]	0
Connecting rod length [mm]	144.8
Bore x Stroke [mm]	82.4 x 76.2
Valve timing	EVO = 164 ^{o}aTDC
	IVO = 346 ^{o}aTDC
	EVC = -346 ^{o}aTDC
	IVC = -164 ^{o}aTDC
Swirl ratio	0.1

The two combustion regimes tested used different piston and piston spacer combination to vary the squish height and compression ratio to optimize the combustion performance and Rayleigh scattering measurements. The greatest amount of clearance between the laser and the metal and optical surfaces were designed to reduce the amount of surface scatter. The pistons had a flat top so that they had no bowl volume as listed in Table 3-1. The combustion chamber shape is not expected to affect the combustion propagation mechanism as HCCI has no mixing requirements to function properly, just a uniform mixture. In fact, computational LTC results show the thermal efficiency increases when the piston surface area decreases due to less heat transfer [122]. With no bowl, the volume-to-surface-area ratio is maximized. A shrouded intake valve can be oriented to create a range of swirl ratios from 0.1 to 5.6, but for these tests was set to its minimum value to minimize the in-cylinder flow and subsequent turbulence. Less turbulence allows for easier tracking of the combustion front in the sequential imaging. The choice of swirl ratio is not expected to greatly impact the results because swirl ratios are tuned for each engine to yield the highest efficiency and lowest emissions, and thus on a global scale

are arbitrary. Because HCCI has a premixed fuel-air mixture the swirl ratio only affects the thermal stratification.

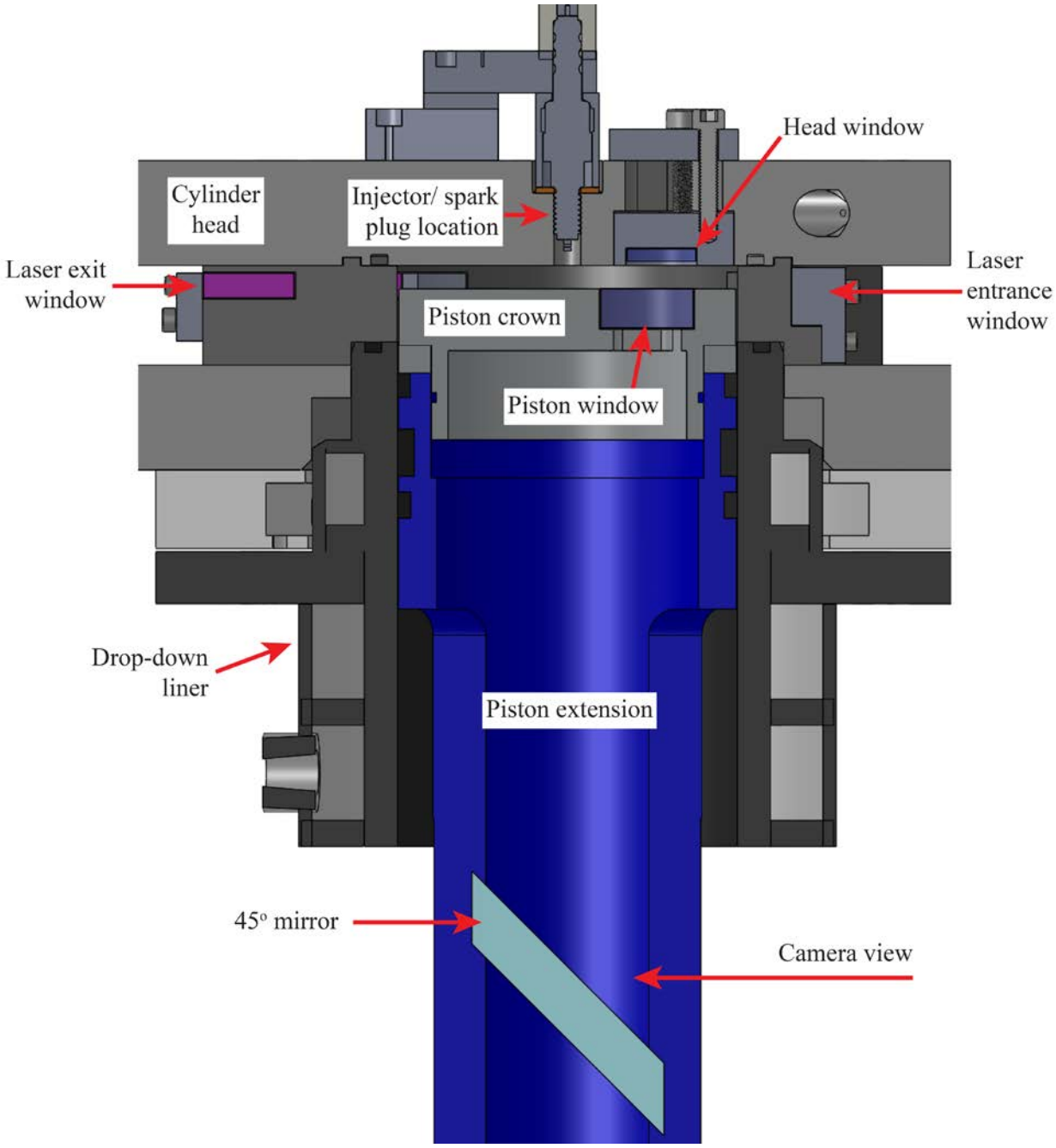

Figure 3-1: Optical engine assembly.

A centrally located hole was used for the spark plug and an injector blank for the HCCI experiments. Premixed fuel was introduced into the intake system far upstream of the engine (45 cylinder volumes) to ensure a homogeneous mixture. Sonic flow orifices were used to control the gaseous fuel concentration in the intake system. The intake air originated from dried, compressed building air. The air was heated with a 1 kW in-line coil heater, and the downstream intake system was heated with surface tape heaters to maintain the intake temperature. Three thermocouples placed throughout the intake system provided feedback for the heater's PID controller. The coolant system was used to maintain the cylinder head and liner at a constant 50 ^{o}C.

A Kistler non-cooled, cylinder pressure transducer, type 6053BB, is located in the laser-access plate to measure the in-cylinder pressure. All data were recorded with a NI USB-6356 DAQ system synced to an optical encoder with 0.25 crank angle resolution. Recorded data included the in-cylinder pressure, intake pressure, spark timing, laser timing and camera timing. Individual cycles of pressure data were linked to the images to give quarter-crank angle resolved pressure for the thermometry calculations.

Because the engine was maintained at 50^{o}C it has greater heat transfer than its metal counterpart. The compression ring also sits well below the top of the piston, resulting in increased crevice flow. The net effect is an engine that is further from an ideal engine than a similar metal engine. The non-ideality is visualized in a logP-logV plot where the compression stroke is not linear, particularly near TDC. As such, the heat release calculator was developed to include a crevice flow term, which tracks the total mass -at the bulk gas temperature- in the cylindrical combustion chamber and the total mass -at the wall temperature- in the crevice

volume. The crevice term was “tuned” by adjusting the crevice volume until the motored heat release was zero. The tuned volume worked well across all operating conditions.

Due to the particle contamination concerns outlined in Section 2.10, many of the proposed engine solutions were implemented. A PTFE piston ring was used to allow oil-less operation in the drop-down liner. A felt oiling ring below the piston ring was added for slight lubrication to reduce piston ring wear. This configuration had been used for several years without oil droplets mixing with the in-cylinder charge. An in-house designed oil-less cylinder head (camshafts are not exposed to oil flow) was used to eliminate the risk of oil entering the combustion chamber through the head gasket, valves, or injector port. To combat particles in the air, an initial 5 μm air filter (Wilkerson FRP-96-639) preceded a 10 nm air filter (Parker-Balston 2104N-1B1-DX). It was later discovered the intake system itself generated particles downstream of the filters negating most of the filtering efforts. To reduce stray scatter, all metal surfaces inside the combustion chamber were painted with Pyromark 2500, a flat black paint of 0.95 absorptivity (0.05 reflectivity) that is capable of withstanding continuous temperatures of 1100^{o}C. The paint did not chip nor crack during experimentation and was easily reapplied when the absorptivity decreases. Soot coating, another suggested method to reduce background scatter, was found to be highly dependent on the soot source (wax candle, oxyacetylene torch, etc.) and where in the flame the soot was formed. Regardless of the sooting method, the soot easily came of the surface and contaminated the optical surfaces, making it an unacceptable method for reducing laser scatter.

3.2 Fuels

3.2.1 Preliminary Considerations

The possibility of incomplete fuel vaporization necessitates choosing gaseous fuels for the experiments. Selection of a suitable surrogate has to take into account octane/cetane number, the Rayleigh scattering cross section and the effect on combustion. Due to the low compression ratio a higher reactivity fuel was necessary for HCCI operation. To maintain similarity, a traditional gasoline-like fuel was used for the spark ignition experiments. For these reasons ethylene (ethene, C_2H_4) was chosen as the low-reactivity fuel and dimethyl ether (DME, CH_3OCH_3) as the high-reactivity fuel. Research grade fuels with >99.99% purity were used.

Various other gaseous fuels were considered as possible substitutes for gasoline but were ultimately eliminated: acetylene (C_2H_2), ethane (C_2H_6) and methane (CH_4). The low autoignition pressure of acetylene (~103 kPa) makes the fuel unusable for port injection during boosted intake pressure operation. Methane has an octane number of 122 [123]; previous HCCI experiments in the optical engine failed to ignite methane even with a geometric compression ratio of 17:1 and intake temperature of 140 ^{o}C. Ethane has an octane number of 101 [123]. Ethylene is expected to have a lower octane number as it autoignites easier than its saturated hydrocarbon counterpart ethane [3], although no experimental data exists for confirmation. Either ethylene or ethane was acceptable based on the octane number, but ethane was ultimately eliminated because of its larger scattering cross section as shown in Section 3.2.2. Dimethyl ether is an attractive gaseous high-reactivity fuel as it has a cetane number of >55 [124] and has already been used in numerous engine studies [125,126]. DME has a vapor pressure of 5.3 bar at 20 ^{o}C, which was sufficient for choked flow at the tested intake conditions. Because the DME was stored in liquid form it had to evaporate before injection which decreases it’s temperature and changes the mass

flow rate. To ensure the choked flow calibrations were accurate, the DME liquid was allowed to evaporate in a large tank upstream of the orifice to reach the calibrated temperature. The tank volume was sufficiently large to allow continuous operation for 12 minutes at the highest DME mass flow rate. (The engine was only operated for approximately 5 minutes at a time.)

Despite the fact that dimethyl ether was chosen for this study solely based on the experiment's requirements, it is a fuel of great interest. DME has been researched as an alternative for diesel because of its high cetane number and flexibility in production source (e.g. natural gas, coal, bio-mass) [124]. It also produces the same thermal efficiency and UHC as diesel but has near-zero soot, significantly lower NOx and the same or less CO emissions [125,126]. The soot-free operation is a result the low boiling point (248 K) allowing for faster mixing, the simple chemical structure (CH_3-O-CH_3) lacking carbon-carbon bonds resulting in quicker fuel breakdown, and a fuel-bound oxygen atom causing quicker fuel oxidation. In terms of the Rayleigh scattering measurements, the lack of soot reduced possible scatterers that contaminate the data (see Section 2.10).

3.2.2 Rayleigh Scattering Cross Section

Consideration of the Rayleigh scattering cross section is important as discussed in Section 2.8. To calculate the cross sectional change across a combustion front, ignition delay calculations were performed for an air-fuel mixture to obtain the species' mole fraction and the mixture's cross section with the summation term in Eqn. (2-13). See Section 4.1.2 for details on the ignition delay calculations. The initial conditions were set to 11 bar and 800 K, which are representative of the tested SI and HCCI's pressure and temperature at the time of imaging. Figure 3-2 shows the percent difference in the reactant and product cross sections normalized by

the reactant cross section as a function of equivalence ratio. The difference is negative because the products' cross section is smaller than that of the reactants which is a result of the fuel having a larger scattering cross section than the major combustion product species (i.e. H_2O, CO_2, etc.). Accordingly, a higher equivalence ratio yields a greater difference because a greater portion of the reactants is fuel. As mentioned earlier, ethylene-air mixtures maintain a more uniform cross section across the combustion front compared to ethane-air, demonstrating the choice of ethylene over ethane.

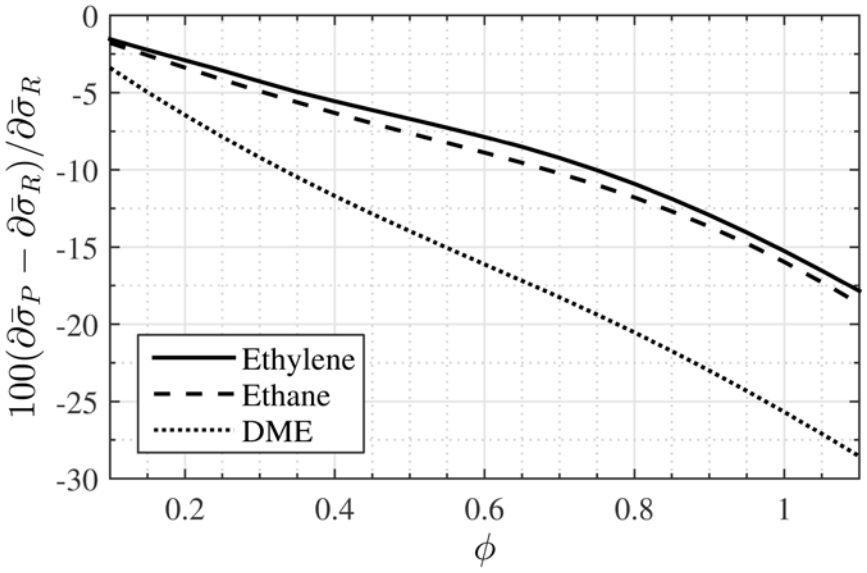

Figure 3-2: Percent difference between reactant and product differential cross section as a function of equivalence ratio. Mixture species are obtained from ignition delay simulations at 800 K and 11 bar.

For the baseline case of spark-ignition, stoichiometric operation of ethylene yields a 15.3% decrease in the mixture's Rayleigh scattering cross section. The HCCI was operated with DME at Φ=0.6, giving a cross section decrease of 16.1%. These are nominal values and each experimental run has its own cross sectional change based on air and fuel flow rates and the temperature and pressure at time of imaging. As discussed in Section 2.8, a variable mixture cross section is not detrimental if it can be accounted for. With homogenous mixtures it is easy to

correct the product cross section since the reactants and products are easily distinguished in the images.

3.2.3 Combustion Effects

Combustion is a physicochemical process in that it is dependent on temperature, pressure, and composition. Therefore the fuel choice could impact the propagation mechanism. It is thereby necessary to understand how ethylene and DME are expected to impact the combustion compared to the most common LTC fuels, gasoline and diesel. As discussed in Section 2.5, the combustion is categorized by the combustion speed and temperature gradient. (See Eqn. (2-2) repeated here.) For a fixed temperature gradient, whether it is the pre-ignition gradient that's inherent to the engine or the gradient across the combustion front, to obtain the same combustion speed amongst fuels the ignition delay's temperature sensitivity must be equal. The easiest way to classify a fuel's ignition delay temperature sensitivity is through ignition delay measurements as a function of temperature.

$$s_{ig} = \left|\frac{d\tau}{dT}\right|^{-1} \left|\frac{1}{\nabla \mathrm{T}}\right|$$

3.2.3.1 Ethylene

Few studies of ethylene's ignition delay exist which adds to the uncertainty surrounding its octane number. Of the few studies that exist, Kumar et al. [127] is the only one to address the ignition delay under engine-like conditions. For fundamental studies such as ignition delay, it is common to use surrogate fuels because their component makeup and kinetic pathways are well characterized. In the case of gasoline, surrogate fuel blends of iso-alkanes, n-alkanes, aromatics,

olefins and napthenes are made to simulate gasoline [128] or, simply, pure isooctane (C_8H_{18}) is used [129,130]. Table 3-2 shows the four studies (1 ethylene and 3 gasoline surrogate) used to compare the ignition delay. In each study pressure measurements were used to calculate the onset of high-temperature oxidation. The experimental device used was either a rapid compression machine (RCM) or a shock tube. The tabulated experimental conditions correspond to the comparison and are not necessarily the full set from the respective study. Due to the ethylene mixture being highly dilute, which increases the ignition delay, the ignition delay is scaled by the oxygen concentration to the first power [mol/cm^3]; a recent literature review reported oxygen concentration scaling to the power of -1.1, -1.2, -0.95 and -0.92 [131]. This allows for a more one-to-one comparison as it also eliminates the pressure dependency. All data compared are for an oxygen-based equivalence ratio of one.

Table 3-2: Ignition delay studies of ethylene and gasoline surrogates.

Study	Device	Fuel	Temperature [K]	Pressure [bar]	Φ	O_2 [%]
Kumar et al. [127]	RCM	ethylene	850-1050	15, 30, 45	1	7.9
Kukkadapu et al. [128]	RCM	surrogate blend	800-900	20, 40	1	20.7
He et al. [129]	RCM	isooctane	943-986	8-18	1	9-17
Fieweger et al. [130]	Shock tube	isooctane	800-1100	13, 40	1	20.7

Figure 3-3 shows the scaled ignition delay of the four studies. The gasoline surrogate and isooctane studies agree well, especially for the overlapping data of Kukkadapu et al. and Fieweger et al. in the 800-900 K range. For engine ignition temperatures of 750-950 K, ethylene has a longer ignition delay, which is unexpected based on ethylene's predicted lower octane number [3]. The difference in the ignition delays decrease until about 1000 K, above which

ethylene has a shorter ignition delay than isooctane. The slope of the curves shows ethylene's ignition delay is more sensitive to temperature such that $|(d\tau/dT)_{C2H4}| > |(d\tau/dT)_{C8H18}|$ with the implication that ethylene's combustion speed is lower than isooctane per Eqn. (2-2).

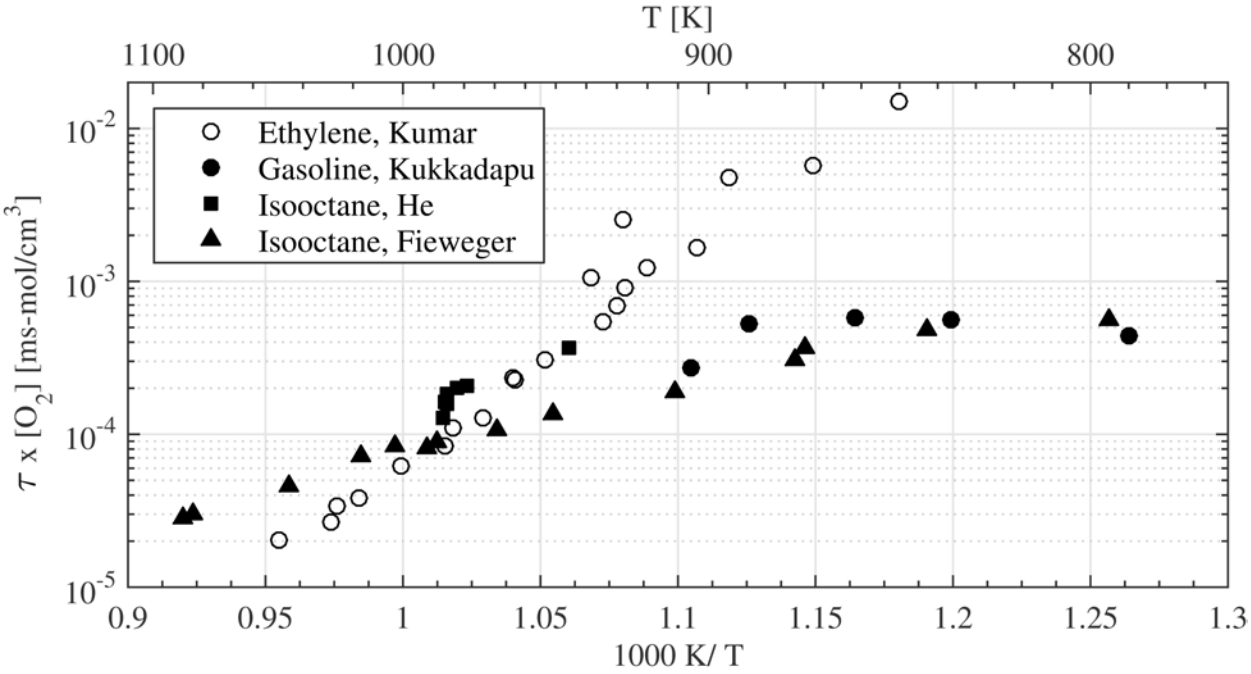

Figure 3-3: Ignition delay measurements of ethylene, gasoline surrogate and isooctane fuels scaled by oxygen concentration. The data were adapted from Refs. [127-130].

3.2.3.2 DME

In the case of DME, ignition delay measurements have been performed in the same shock tube albeit for separate studies [132,133]. Again, owing to the variation in diesel fuel production, ignition delay measurements are typically performed with n-heptane (C_7H_{16}), a single component, primary reference fuel. Figure 3-4 shows the ignition delay for stoichiometric DME/air and n-heptane/air mixtures at pressures of approximately 13 and 40 bar; the pressure difference between the data is considered to be small enough to not pressure adjust the data. DME and n-heptane both have low-temperature heat release (cool flames), so pressure data were

used to determine the onset of the high-temperature combustion to mark the ignition delay. The cetane number of n-heptane is around 56 [132], which is quite similar to DME's 55, and as such the ignition delays are similar with DME's being shorter. DME's short ignition delay has been attributed to its simple structure and multiple pathways for initiating the chain reaction for high-temperature oxidation [124]. The similar ignition delay temperature sensitivities of DME and n-heptane, and by extension diesel, suggest the combustion speeds are similar for a given temperature gradient via Eqn. (2-2).

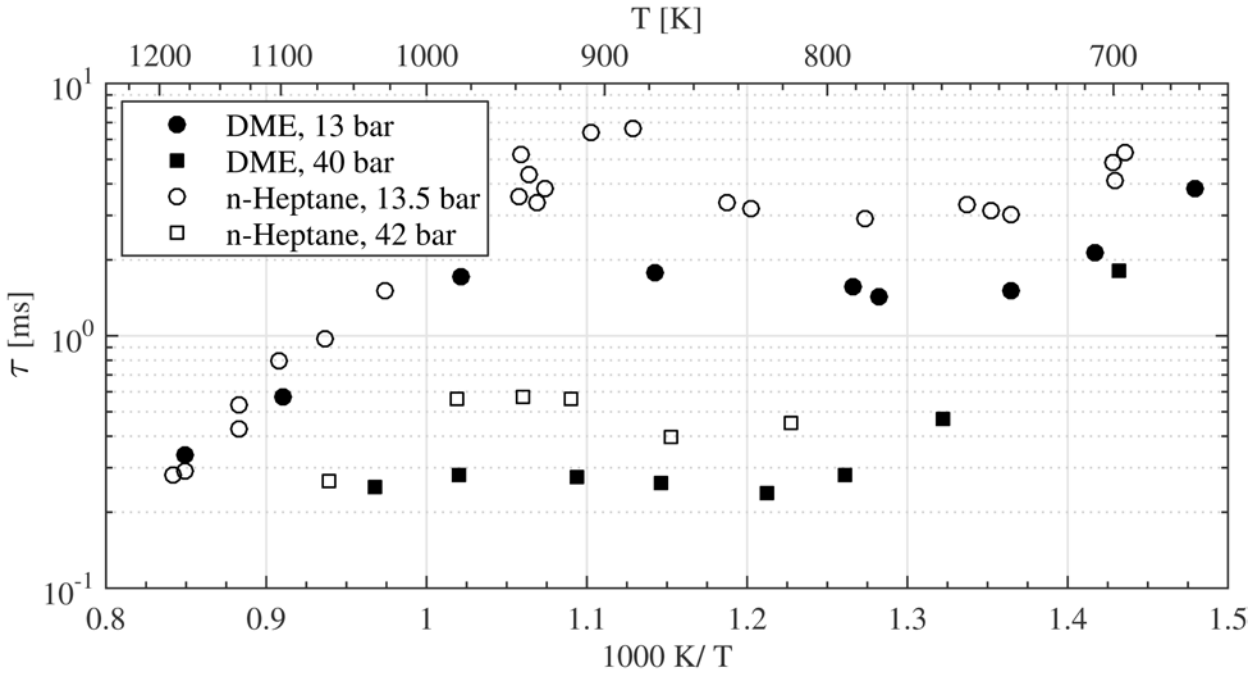

Figure 3-4: Shock tube ignition delay measurements of stoichiometric DME/air and n-heptane/air mixtures. DME data were adapted from Pfahl et al. [132]. n-heptane data were adapted from Ciezki and Adomeit [133].

Shock tube ignition delays are the most fundamental measurements of ignition delay as they are performed with well-mixed (homogeneous) mixtures, and the mixture's temperature increase is nearly instantaneous. Fluid dynamic and heat transfer effects are added when the ignition delay of sprays is measured in a constant volume chamber. Wakai et al. [134] and Yao et

al. [135] measured ignition delays of DME and diesel at 41 and 45 bar, respectively, determined by combustion luminosity. Figure 3-5 compares the data from the two studies. The 41 bar data shows the ignition delays are within experimental uncertainty. For the 45 bar data, DME has a noticeably shorter delay, but the difference decreases with increasing temperature. Again, it is seen that DME combustion occurs on the same timescale as diesel, but more importantly the ignition delay temperature sensitivities are similar with the diesel's being slightly greater at 45 bar pressure. Regardless of DME's feasibility of representing diesel, it is important to know its propagation mechanism given the fuel's future in research.

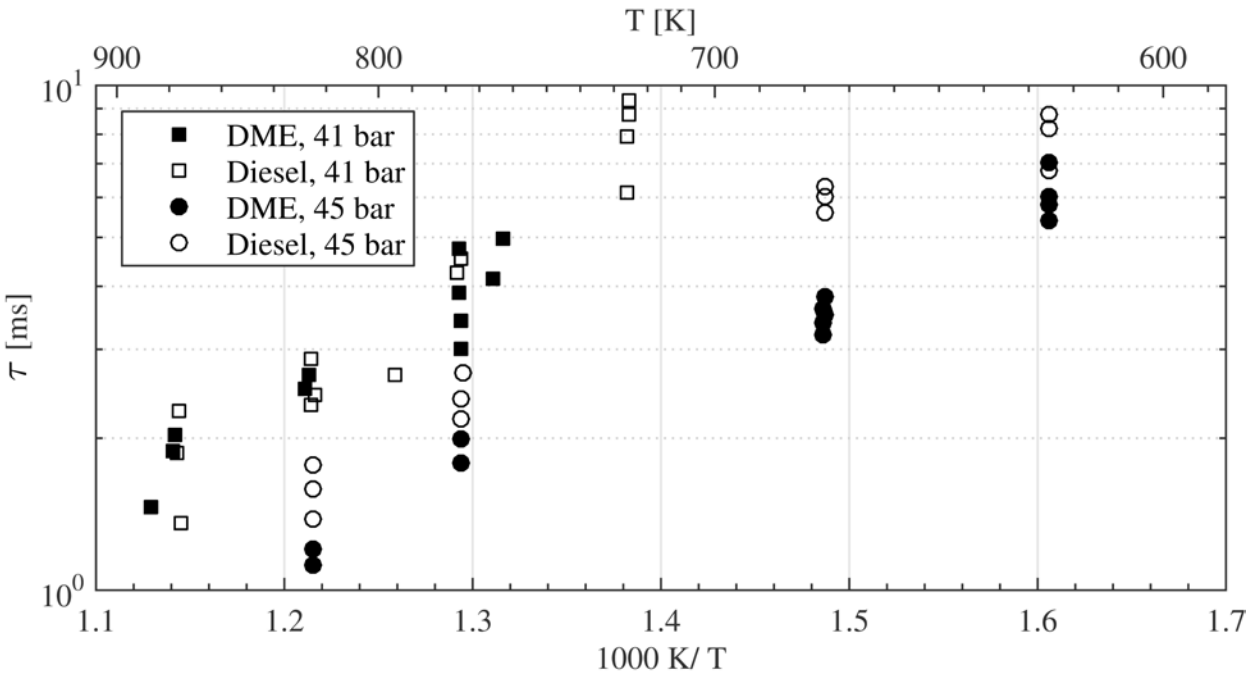

Figure 3-5: Ignition delay of direct-injection DME and Diesel fuel in constant-volume vessels. 41 bar data were adapted from Wakai et al. [134]. 45 bar were data adapted from Yao et al. [135].

3.3 Optical Setup

3.3.1 Laser

Figure 3-6 shows a schematic of the optical arrangement. An Ekspla NL303D dual-headed Nd:YAG laser was used to produce two 532 nm wavelength laser pulses per cycle at 50 mJ/pulse. The laser's optics separate the harmonic outputs, but two extra external harmonic separators remove more than 99% of any remaining fundamental light (1064 nm) for a cleaner signal. The second harmonic separator redirected the laser upwards and a 532 nm reflector set the laser to the engine height. 532 nm light exited the laser with the required horizontal polarization, but the polarization became vertical after the height change; a half-wave plate was used to set the polarization back to horizontal before entering the engine. A photodiode was used to sync the camera exposure timing to the laser pulse. The sheet-forming optics consisted of a single 300 mm focal length cylindrical lens that formed the beam into a horizontal sheet with a waist of 320 μm determined from Gaussian equations using a measured M^2 value of 13.4 [136]. The thickness was not measured as beam steering encountered in the engine results in the measurements only providing a lower limit to the laser sheet thickness. The sheet thickness does not affect the Rayleigh scattering process, but maintaining a thin sheet in the measurement region is desirable to reduce the effect of oblique combustion fronts crossing the laser plane; oblique combustion fronts will skew the results to be interpreted with a larger front thickness and faster combustion speed. The Rayleigh range, the distance from the waist where the intensity halves, is 11 mm, and the unclipped sheet width was optically measured as 8.5 mm. A shorter focal length lens can be used to achieve a thinner waist, but the Rayleigh range also decreases, resulting in the majority of the measurement region having a nonuniform thickness; a longer

focal length lens has the opposite issue. The 300 mm lens balanced sheet thickness and uniformity (i.e. Rayleigh range) well.

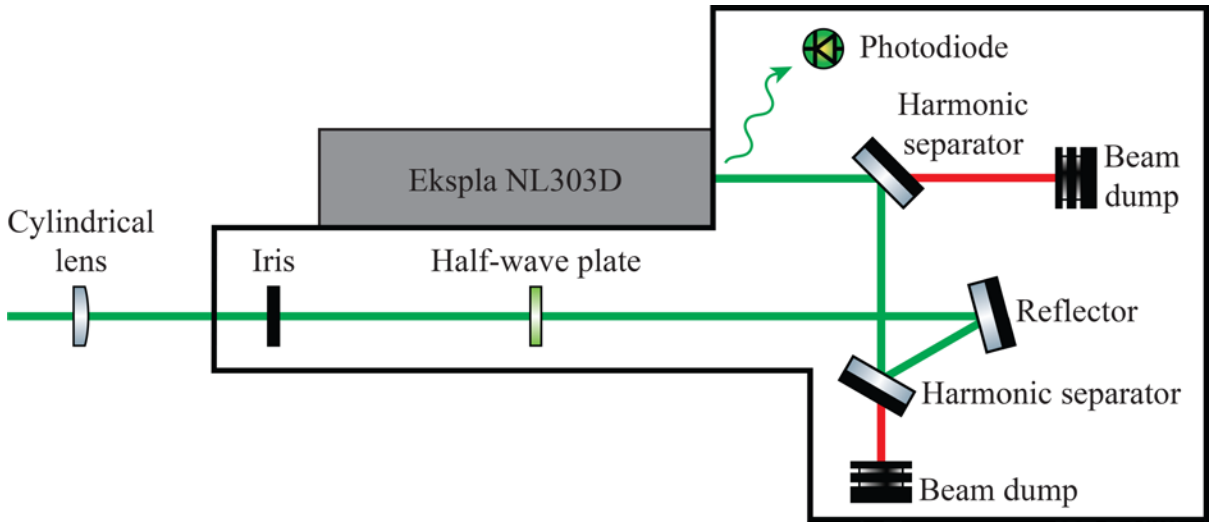

Figure 3-6: 532 nm laser optical setup. The black lines indicate a shield that enclosed the optics.

The laser was operated at the 2nd harmonic at 532 nm despite the λ^{-4} scattering intensity dependence for a number of reasons. Previous discussion highlighted a significant number of combustion species that fluoresce in the UV and near-UV range. The closest emission line is a strong C_2 line at 516 nm that terminates at 519 nm [121], so the major emission lines are avoided at 532 nm. At longer excitation wavelengths the cross section temperature dependence and depolarization decreases resulting in a better characterized Rayleigh scattering cross section, i.e. less uncertainty. Longer wavelengths also mean lower refractive indices in materials [109], which reduces surface reflections (see Section 3.3.3.1). Researchers [113] have also seen higher harmonic generation of Nd:YAG lasers results in less uniform laser sheets, and the cameras used have a greater quantum efficiency at 532 nm than at the higher harmonics of 266 and 355 nm (see Section 3.3.5).

Several steps were taken to minimize the amount of scatter in the laser arrangement. A single cylindrical lens was used for the sheet forming optics to limit the number of surface reflections from optics. Furthermore, the lens has an anti-reflectivity coating for 532 nm. From Fig. 3-6, all of the optics except the cylindrical lens were contained within a box made of low-reflectivity panels to shield the engine and camera from the laser optics; the panel joints were sealed with black optical-grade tape. The surface of the stainless steel optical table were covered with black felt to prevent reflections inside the shielding, and an iris at the exit of the box ensured only collimated light exiting the box entered the engine. An electronically actuated solenoid at the exit of the box only allowed the laser to exit on imaging cycles. This reduced the amount of laser pulses that passed through the laser-access windows, which in turn reduced the laser burn that resulted in diffuse scatter.

3.3.2 Imaging Optical Access

Optical access was obtained through a window mounted in the piston crown at the top of the extension (see Fig. 3-1). A 45^{o} mirror located in the piston extension's slot allowed viewing through the piston window into the combustion chamber; the UV-enhanced aluminum mirror has 87% reflectance at 532 nm. A window mounted in the head provided a low-scattering background for the Rayleigh scattering measurements. Metal surfaces, regardless of the anti-reflectivity coating, scattered too much light that overpowered the Rayleigh scattering signal.

As mentioned earlier, the SI and HCCI experiments had their own piston and piston spacer setup; the piston spacer was used to increase the height of the piston thus varying the compression ratio and squish height. The SI piston had a full window that had the maximum clear aperture diameter of 57.9 mm. Due to thermal stress issues resulting in engine failure while

running HCCI experiments, a full-windowed piston could not be used for the HCCI experiments. Instead the HCCI piston used a smaller window mounted in an aluminum piston crown to mitigate thermal stress in the window during operation; the smaller window was placed to maintain a clear aperture to 57.9 mm. Figures 3-7 and 3-8 show the two piston crowns without the windows mounted. The SI piston has fixture points for bowl windows, but they were left off in favor of a flat piston design to prevent lensing of the laser sheet and increased scattering from extra optical surfaces.

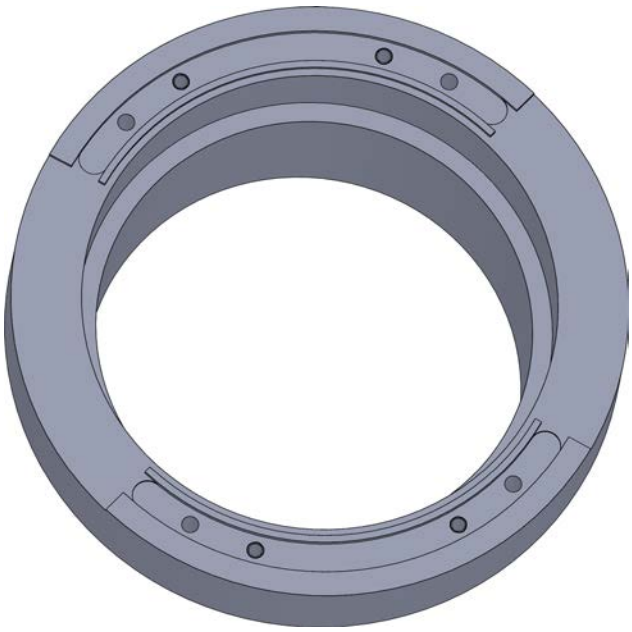

Figure 3-7: SI full window piston crown.

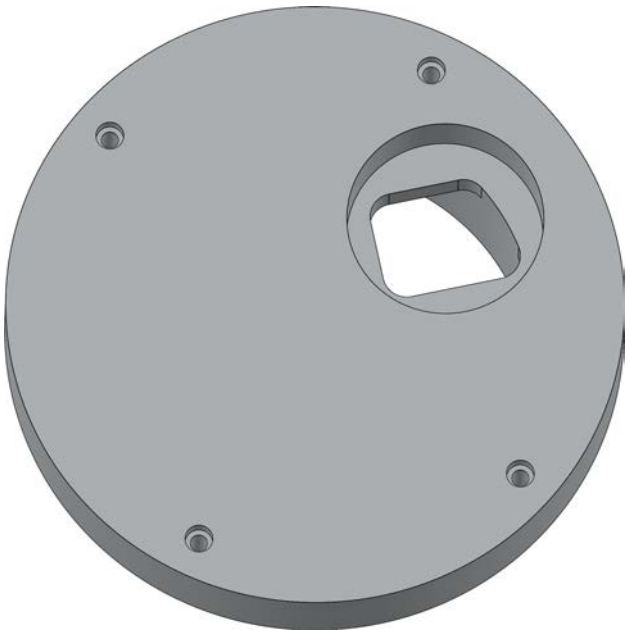

Figure 3-8: HCCI small window piston crown.

The anomalous viewing area in the HCCI piston crown is a result of the overlapping region of the maximum piston and head window sizes. Figure 3-9 illustrates the optical access in the confines of the engine. The bore is given by the 82.4 mm circle, and the maximum piston and head window sizes are the dashed lines. The maximum piston window diameter allows visible access from the center of the cylinder to 70% of the total bore radius, and the maximum head

window size allows visible access from 34-91% of the total cylinder radius. Because the head window provided the necessary background to obtain images with the minimal amount of laser scatter, the field of view (FOV) was confined to the overlapping region of the piston and head windows. Additionally, because an injector blank used for the HCCI experiments protruded into the cylinder, the laser sheet was positioned off center to avoid any interference. (The spark plug was recessed into the head.) The FOV is given by the crosshatched area in Fig. 3-9. It was discovered through experimentation that the full window piston gave slightly better background signal levels, but, again, current piston designs did not tolerate the thermal stresses from HCCI experiments. The full head window area was also not used due to window sizing and mechanical component stress.

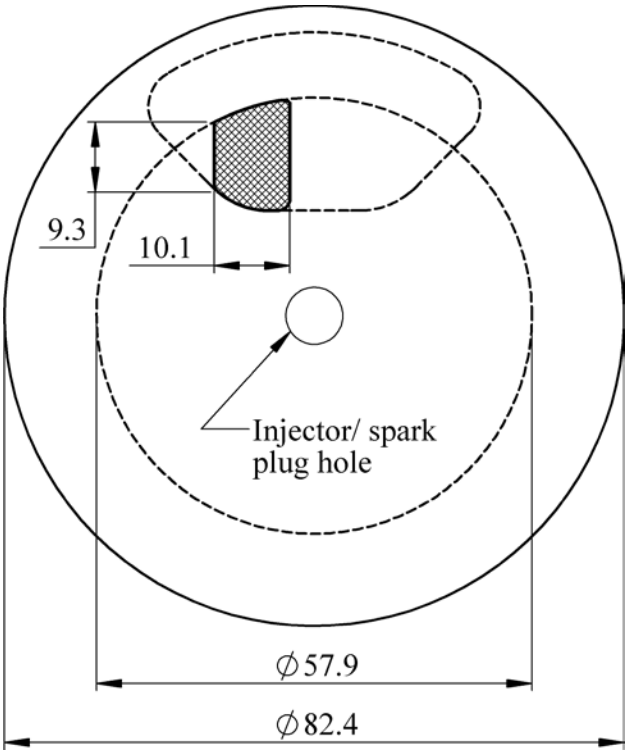

Figure 3-9: Overhead view of the optical access layout. The imaging region, marked by the cross hatched area, is the overlapping region of the piston and head windows. The dashed lines indicate the largest piston and head window sizes. Dimensions are in millimeters.

For the 8.5 mm wide laser sheet, 0.8 mm of clearance on either side of the sheet was added to the viewable area of the head window to ensure a sufficiently large background. The HCCI piston window had 2.8 mm of clearance to prevent mechanical vignetting for various imaging crank angles. Clearance did exist on all sides of the piston and head windows due to physical constraints. The resulting rectangular FOV (width x length) was 10.1 x 9.3 mm as indicated in Fig. 3-9. The center of the FOV was 23 mm from the center of the cylinder.

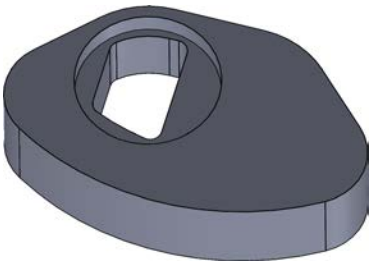

Figure 3-10: Head window holder.

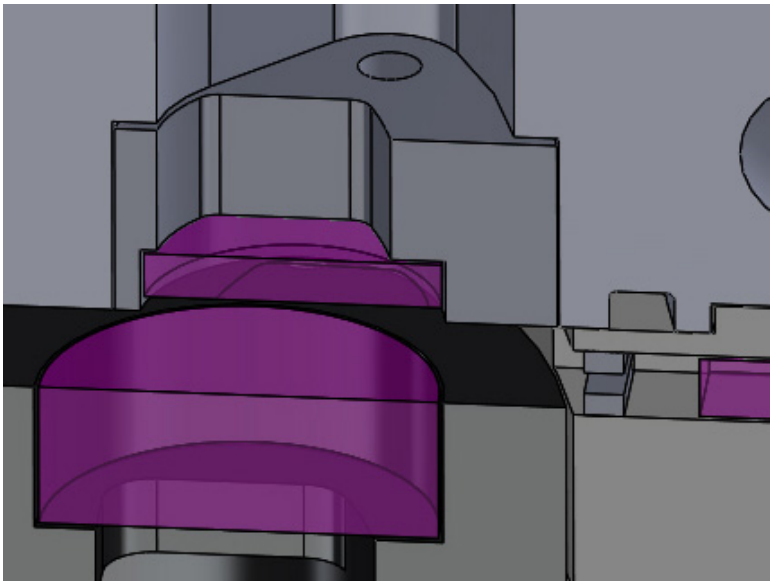

Figure 3-11: Cross sectional view of the HCCI piston crown and recessed head window.

Figure 3-10 shows the head window holder with window geometry similar to the HCCI piston. Figure 3-11 is a cross section of the HCCI piston and head window as designed in the engine solid model. The head window is seen recessed 1 mm to increase the distance between the laser sheet and the optical surface. The HCCI piston window was made of fused silica and the SI piston and head window were sapphire. Because none of the windows had any laser-transmission requirements their material choice was based on readily available sizes and required strength.

3.3.3 Laser-Access Plate

Laser access was achieved with a metal plate below the head in which a pair of opposing windows allowed the laser to enter and exit the engine (see Figs. 3-1 and 3-12). The windows were epoxied into holders and then sealed in the plate with high-strength Room Temperature Vulcanization silicone. The windows were painted black before epoxying to reduce internal reflections. The entrance window holder has a small aperture on the external side to limit divergent scatter from the sheet-forming optics from entering the engine. The aperture has 1 mm clearance on all sides for the laser beam. At TDC the laser plane was 4.8 and 3.6 mm from the piston for the SI and HCCI, respectively; the laser was 3.9 mm from the head (4.9 mm from the head window). The laser was not centered between the head and piston at the worst case scenario because laser-access plate material thickness limitations prevented the windows from being located closer to the head.

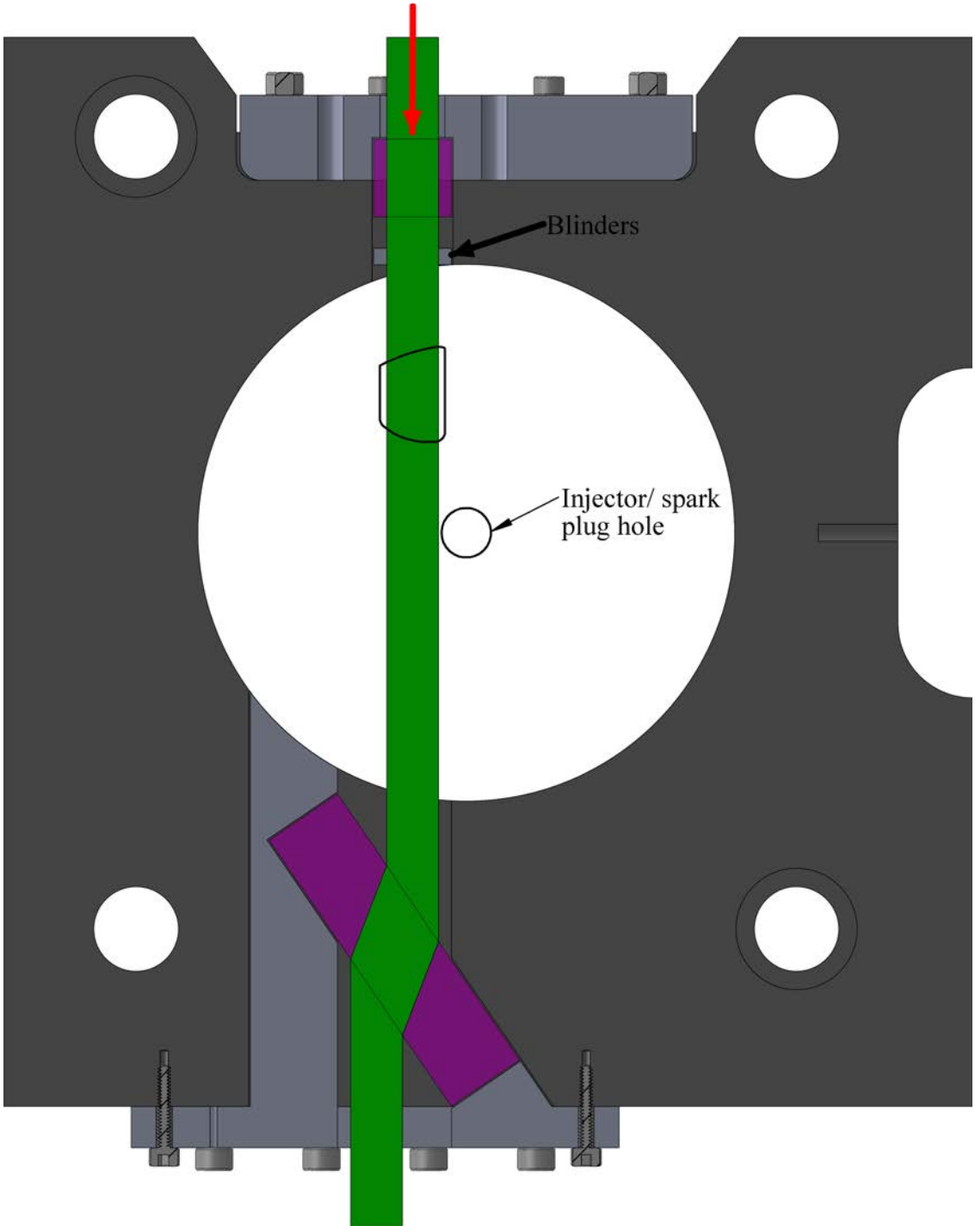

Figure 3-12: Overhead cutaway view of the laser-access plate. Windows are shown in purple, and the green laser path's direction is indicated by the red arrow. The laser sheet avoids the injector/ spark plug hole.

Several measures were taken to minimize the background signal level. Figure 3-12 shows the engine entrance and exit windows are recessed from the bore. Transmitted light can diffusely scatter off surfaces due to particles or surface imperfections, so the recessed windows reduce the amount of light that scatters into the FOV by reducing the view factor. The windows could not be anti-reflective coated due to the combustion temperatures. Experiments showed diffuse transmission off the cylinder-side of the entrance window, despite the laser-quality surface finish, was a limiting factor as discussed later. Accordingly, blinders were added to the cylinder-side of the entrance window channel to limit the amount of scattered light entering the combustion chamber (see Figs. 3-11 and 3-12). Preliminary tests found light reflected off the cylinder-side exit window resulted in very high background levels. The Fresnel equations [137] dictate that a change in refractive index (i.e. air-window interface) will result in the partial reflection of the incident light. The light will be purely refracted (no reflection) if the angle of incidence is equal to Brewster's angle for the window [138]. Experiments with the exit window at Brewster's angle reduced background scatter to a satisfactory level. See Section 3.3.3.1 for reflectance calculations and Brewster's angle. The recessed windows and exit window oriented at Brewster's angle result in large dead volumes in the combustion chamber, and are therefore the biggest contributing factor of the low compression ratio in the HCCI experiments.

The laser entrance and exit windows have a 20-10 scratch-dig to minimize diffuse scatter. The entrance window's flatness was $\lambda/10$ at 532 nm, whereas it was $\lambda/4$ for the exit window due to manufacturing limitations related to the window size. Both windows are made of UV-grade fused silica, although the UV specification was not necessary because the incident wavelength, 532 nm, is in the visible range. Compared to the other common material, sapphire, the choice of fused silica required thicker windows due to a lower tensile strength, but the optical advantages

greatly outweighed the simple design constraint. Fused silica has an index of refraction of 1.46 at 532 nm compared to sapphire's 1.77 [139]. Per the Fresnel equations for a normal incident beam, the reflectance is 3.5% and 7.7% for fused silica and sapphire, respectively, thereby fused silica has less reflectance resulting in a background levels. The exit window ideally has zero reflectance from the Brewster angle orientation, but the slightest misalignment and depolarization (reflectance is polarization sensitive) results in reflections, thus a lower index of refraction is still desirable. Fused silica transmits 93% of incident light compared to 84% for sapphire [139], which allows for lower laser energy operation to avoid window laser burn.

Fused silica also has an advantage when considering stress-induced birefringence, the phenomenon of transmitted light depolarizing due to the material's birefringent axes rotating under mechanical or thermal stress [140]. Owing to Rayleigh scattering's dependence on the incident light polarization, the scattering intensity is reduced as a smaller portion of the incident light has the correct polarization for Rayleigh scattering. Fused silica has been shown to be less birefringent than sapphire [141], which allows for more efficient Rayleigh scattering. Beam steering effects at the window-cylinder surface are also reduced because the smaller index of refraction change from the window to the cylinder contents. Beam steering still occurs because the refractive index change is large, and additional effects from thermal boundary layers and fuel stratification exist as discussed in Section 2.10.

3.3.3.1 Brewster's Angle

When light travels through media of different refractive indices a portion of the incident light is reflected. The Fresnel equations [137] predict the amount of reflection based on the polarization of the incident light. Two types of light polarization exist: s-polarization that is perpendicular to

the plane containing the incident, reflected, and transmitted light, and p-polarization that is parallel to the aforementioned plane. In this study, the incident, reflected, and transmitted light was in the horizontal plane parallel to the piston crown. The laser polarization is also horizontal to produce Rayleigh scattering in the vertical direction; accordingly the light is p-polarized. The reflectance for p-polarization is given by:

$$R_p = \left| \frac{n_1 \sqrt{1 - \left(\frac{n_1}{n_2} \sin\theta_i\right)^2} - n_2 \cos\theta_i}{n_1 \sqrt{1 - \left(\frac{n_1}{n_2} \sin\theta_i\right)^2} + n_2 \cos\theta_i} \right|^2 \qquad (3\text{-}1)$$

where n_1 is the first medium, n_2 is the second medium and θ_i is the angle of incidence relative to the normal of the interface.

For analyzing the reflectance of the exit window, n_1 corresponds to refractive index of the gas mixture in the cylinder and n_2 is the refractive index of the window. Assuming the cylinder contents at the exit window is air, $n_1 = 1.000293$. Linear interpolation of the window refractive index for 1.46669 at 435.84 nm and 1.46008 at 546.07 nm gives 1.46092 at 532 nm [139]. The reflectance for the range of incident angles of fused silica is shown in Fig. 3-13. From the inset figure a minimum is seen around 55^o. Per Brewster's law [138], light with p-polarization will not be reflected if the angle of incidence is:

$$\theta_i = \theta_B = \tan^{-1}\frac{n_2}{n_1} \qquad (3\text{-}2)$$

which equals 55.6^o for this setup. Therefore to achieve zero reflectance off the exit window's cylinder-side surface, the window must be rotated 55.6^o. If the window is not oriented perfectly at Brewster's angle, the reflectance is still less than 1.6% with $\theta_i = \theta_B \pm 10^o$, which is less than half the 3.5% reflectance if the incident light is normal to the window.

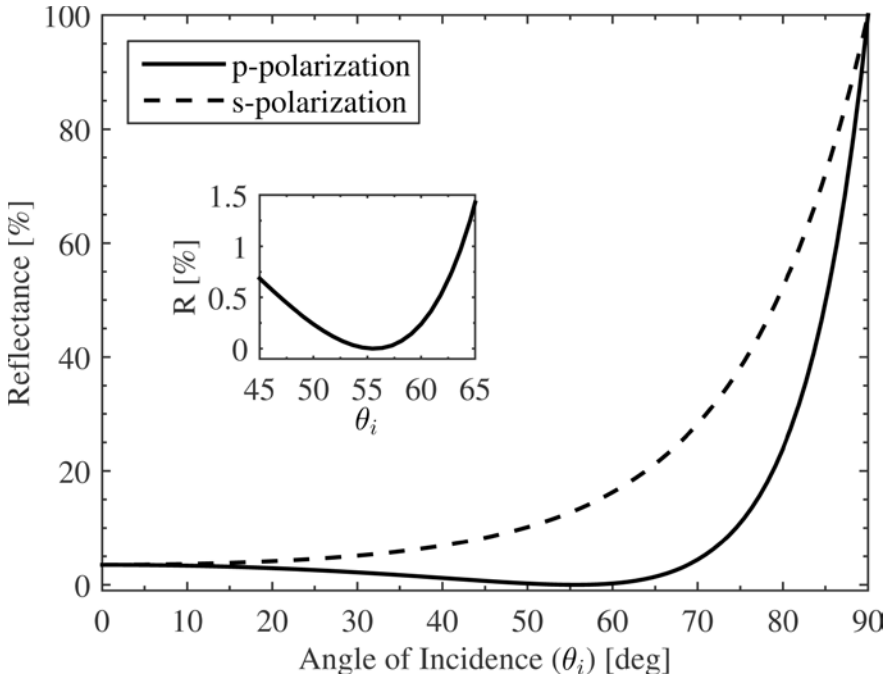

Figure 3-13: Incident light reflectance vs. angle of incidence in fused silica. The inset plot shows the reflectance is zero at Brewster's angle.

When evaluating the reflectance of s-polarized light (also plotted in Fig. 3-13), fused silica's advantage becomes twofold. Not only does sapphire's light depolarization from stress-induced birefringence result in less light contributing to Rayleigh scattering, the depolarized light (s-polarization) reflects more causing greater background signal levels. Keep in mind the higher refractive index yields more reflectance regardless of polarization.

3.3.4 Filters

Although the cameras are gated for a short time period, any combustion light during the exposure will increase the measured signal level tainting the Rayleigh scattering measurements. To achieve the most efficient combustion light blocking, a three-filter stack preceding the camera lens was used: a 532 nm laser-line, a colored glass bandpass (Schott BG39) and a long pass filter

(Schott GG475). Figure 3-14 shows the transmission curves of the three filters, and Table 3-3 lists the filter specifications. A measure of the filter's narrowness is the full width at half maximum (FWHW), defined as the difference in wavelength between the two points where the transmission is half of the maximum transmission. The blocking range is determined by transmission less than 0.1% and is given for wavelengths only tested by the manufacturers.

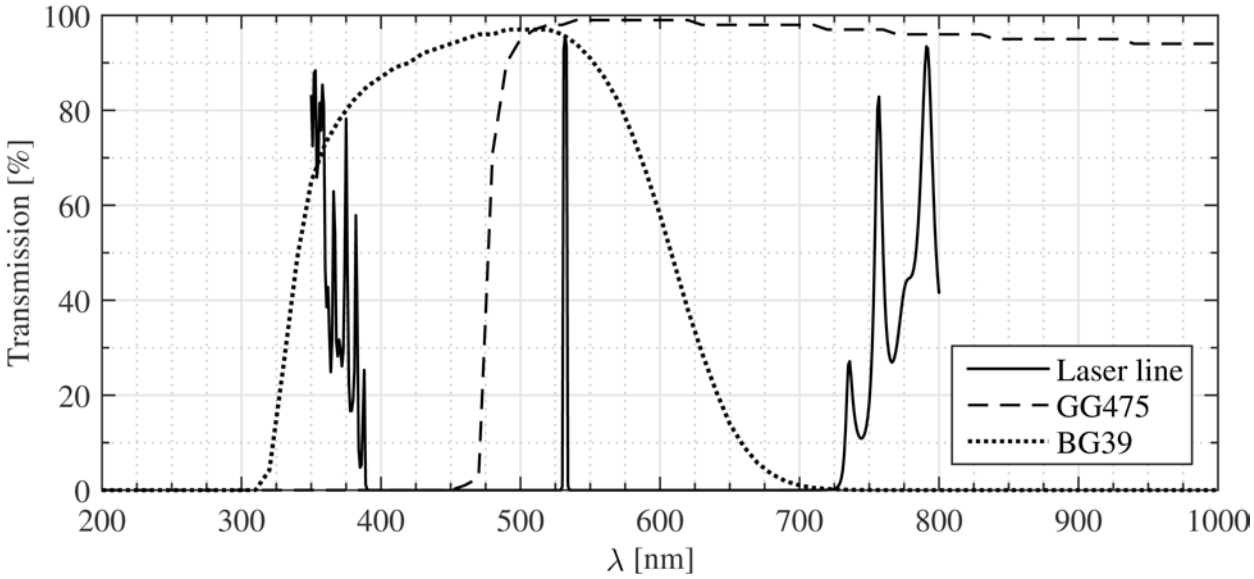

Figure 3-14: Filter transmission as a function of incident light wavelength for the three filters used.

Table 3-3: Individual and combined camera filter specifications.

Filter	Center wavelength [nm]	FWHW [nm]	Transmission at 532 nm [%]	Blocking range [nm]
Laser line	532	3	96	391-529, 535-722
BG39	507	210	96	200-311, 734-1147
GG475	-	-	98	200-452
Combined	532	3	90	200-529, 535-1148

The 3 nm FWHM of the filter stack will not reject any laser light since standard Nd:YAG lasers have a laser linewidth of 120 GHz [142], which gives second harmonic generation of 532.05 ± 0.11 nm. With respect to the cameras' sensitivity, all of the light, less 529-535 nm, will

be filtered out as the combined sensitivity of the cameras (see Section 3.3.5) ranges from 280-1050 nm. Although the FWHM is 3 nm, the full width at 0.001 of maximum is only 5 nm.

It was discussed in Section 3.3.3 that a portion of the depolarized light from birefringence can become background signal. It is recognized that the depolarized light can be filtered with a polarizing filter. Tests were performed with a high efficiency polarizing filter to evaluate the feasibility. It was found that a minimal portion of the background signal was removed as only a small portion of the depolarized light, which is also expectedly small with fused silica windows, scatters. The adverse effect of the polarizing filter was to reduce the absolute signal level by 33%, therefore it was not deemed beneficial. Light does not depolarize when diffusely scattered, so the filter cannot be used to remove background scatter that has the correct initial polarization; to do so, filtered Rayleigh scattering must be used.

3.3.5 Cameras

Two cameras, a Princeton Instruments MicroMAX and Princeton Instruments PI-MAX4, were used to image the Rayleigh scattering. Table 3-4 lists the key specifications of the each camera. The MicroMAX is a non-intensified CCD with a mechanical shutter, whereas the PI-MAX4 has an intensified CCD with electrical gating via the intensifier. Both cameras' CCDs have an interline transfer design such that each pixel has a light-sensitive area that transfers its charge to a masked area. The masked area has 4000:1 light attenuation to prevent extra exposure during data readout. The interlined feature allows two images to be taken successively with a short delay time. The time it takes to shift the exposed area's charge to the masked area, the inter-frame delay, is 200 ns for the MicroMAX and 3 ns for the PI-MAX4. The fast decaying P46 phosphor in the PI-MAX4 intensifier has a photon emission that decays to 1% after 2 μs, so

despite the ability of a 3 ns inter-frame delay, to prevent light from the first exposure in the second image, the delay must be greater than 2 μs. This was not a problem for the experiments as the inter-frame delay was a minimum of 30 μs.

Table 3-4: MicroMAX and PI-MAX4 camera specifications [143,144].

	MicroMAX	PI-MAX4
Full resolution	1300 x 1030	1024 x 1024
Pixel size [μm]	6.7 x 6.7	12.8 x 12.8
Read noise [e^-/p]	8	12.9
Dark current [e^-/p/s]	0.01	0.82
CCD quantum efficiency	0.44	0.41
Photocathode quantum efficiency at 532 nm	-	0.49
Digitization [bits]	12	16
Minimum exposure [ns]	1000	3
Readout [MHz]	5	2
Pixel well depth [ke^-]	18	130
Pixel bin size	-	2x2
Combustion mode	dual HCCI, single HCCI, single SI	dual SI

The MicroMAX has a mechanical shutter with a closing time of 8 ms which will expose the second image during the completion of the combustion. The first image has a short exposure duration and was shifted under the mask such that combustion light did not have any adverse effects on those data. For the HCCI experiments, the combination of the low combustion luminosity and the filters rejected the combustion light such that the Rayleigh scattering signal was not tainted in the second image. Conversely, it was found that in spark-ignition experiments combustion light overpowered the Rayleigh scattering during the shutter closing of the second image despite the narrow bandwidth filter stack. This resulted in the MicroMAX not being able to provide flame speed measurements for the SI data, and is the reason for using two cameras.

3.3.5.1 Imaging Resolution

Because the MicroMAX camera has small pixels and is un-intensified, the expected signal level was small. To combat the issue, an f/1.4, 85 mm focal length lens was used to maximize light collection. With this setup, the magnification and in-plane resolution was maximized by placing the lens as close to the engine as possible; the physical confines of the engine, and in particular the piston extension, limited the magnification of the setup. Sufficient signal levels were achieved to operate the MicroMAX without pixel binning, resulting in a pixel pitch (Δ) of 24.9 μm/pixel. The PI-MAX4's resolution is almost equivalent to a 2x2 binning of the pixels due to the "wire mesh" configuration of the microchannel plate (MCP) in the intensifier. With a 90% bigger pixel length than the MicroMAX, 2x2 binning and the same magnification, the in-plane resolution of the PI-MAX4 would be 3.8x larger, or Δ = 95.1 μm/ pixel. This pixel pitch, and the subsequent measures of resolution, is too big to resolve combustion fronts, so a f/4, 200 mm focal length lens was used with the PI-MAX4. The decrease in aperture was compensated by the increase in pixel area and the ability to intensify such that sufficient light levels were collected. A similar pixel pitch of 25.6 μm/pixel was achieved with the PI-MAX4 setup. The corresponding camera FOVs in the laser plane are 14.9 x 18 mm and 13.0 x 13.0 mm for the MicroMAX and PI-MAX4. The MicroMAX FOV is smaller than allowed by the full pixel resolution due to using a sub region in order to decrease image readout time and engine run time.

Owing to the requirement of a high spatial resolution, the imaging system's resolution was rigorously analyzed. While the simple method of imaging a linear scale or an alternating black and white pattern (e.g. USAF-1951 target) was used to determine the pixel pitch and obtain the physical size to the image, it is not an accurate measure of the resolution of the image because it does not properly calculate the contrast. The contrast allows the edges of structures to

be resolved allowing more definitive conclusions. According to Wang and Clemens [145], the modulation transfer function (MTF) is the best metric for quantifying imaging resolution as it represents the response of the optical system to sine wave objects of varying spatial frequencies. The MTF is measured using the scanning knife edge technique, in which a single pixel is monitored as a knife edge is translated across a uniformly-lit field of view; this is the preferred method because it avoids aliasing and accounts for optical system blur.

To calculate the MTF, scanning knife edge measurements were performed *in situ* with a translational stage with 1 μm resolution. 50 images were taken at 10 μm intervals over a total range of 700 μm. The 50 images were averaged at each interval and the intensity of a fixed pixel in a row was monitored over total knife edge translation; one fixed pixel per a row was analyzed to create a statistical average of the resolution calculations. A step response function (SRF) was made by normalizing the data from 0 to 1 and shifting the array such that $y = 0.5$ was at $x = 0$. With this form, Eqn. (3-3) was used to fit the SRF [136]:

$$P(x) = \frac{1}{2}\left[1 + erf\left(\frac{x}{\Lambda}\right)\right] \tag{3-3}$$

where $P(x)$ is the intensity profile as a function of x, the knife edge position, and Λ is the characteristic width. A smaller width corresponds to a sharper step function, and therefore an increase in resolvable contrast and resolution. Figure 3-15 shows an example SRF fitted with Eqn. (3-3).

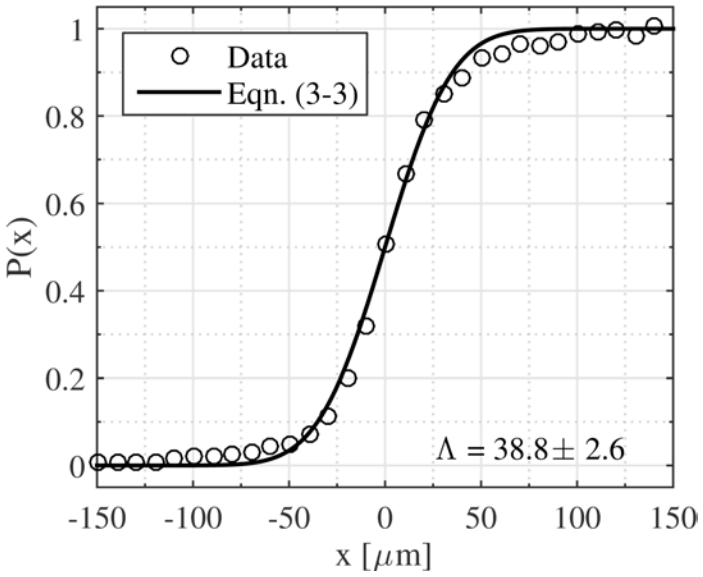

Figure 3-15: Example step response function from the PI-MAX4 scanning knife edge test. The fit parameter Λ is shown with its 95% regression confidence interval.

The derivative of the SRF is the line spread function (LSF), which is a Gaussian with standard deviation $\sigma_{LSF} = \Lambda/\sqrt{2}$:

$$LSF(x) = \frac{1}{\sigma_{LSF}\sqrt{2\pi}} e^{-x^2/2\sigma_{LSF}^2} \tag{3-4}$$

The resolution measure of the LSF is the full width at $1/e^2$ (0.135) of the maximum. The MTF is the Fourier transform of the LSF [145]:

$$MTF(s) = e^{-4\pi^2\sigma_{LSF}^2 s^2/2} \tag{3-5}$$

where s is the spatial frequency in cycles per unit length. Because both the LSF and MTF depend on σ_{LSF} and the MTF is derived from the LSF, either resolution method is acceptable. Per standard, the LSF resolution is reported as the FWHM, and the MTF resolution is given at 4%; both are reported for reference. Table 4-1 lists the calculated resolution parameters with one standard deviation.

Table 3-5: Camera image resolution specifications with mean ± 1σ.

Camera	Magnification	Δ [μm/pixel]	σ_{LSF} [μm]	FWHM [μm]	4% MTF [cycles/mm]
MicroMAX	0.27	24.9	32.1 ± 3.2	75 ± 7.6	12.8 ± 1.7
PI-MAX4	1.00	25.6	28.1 ± 2.2	66 ± 5.2	14.4 ± 1.1

Despite the two cameras having the same pixel pitch, the MicroMAX has a lower spatial resolution. This was likely a result of minute out-of-plane focusing during the scanning knife edge measurements. The error associated with the spatial resolution in regards to the temperature gradient is quantified in Section 4.6.

Chapter 4 - Calculations

In this chapter, chemical mechanisms for ethylene and dimethyl ether are validated for use in ignition delay and flame propagation simulations, and Rayleigh scattering cross section corrections re performed. The image acquisition procedure is discussed followed by the image analysis. Finally, all necessary calculations for the Rayleigh scattering measurements and quantification of their respective uncertainties are derived.

4.1 Simulations

To aide in the analysis of the results, ignition delay and flame speed simulations were performed. The chemical mechanisms used were validated and presented. Ignition delay calculations were performed to calculate the intermediate and product species of the combustion event to calculate the instantaneous Rayleigh scattering cross section as well as obtain the ignition delay temperature sensitivity. It is shown in Section 4.2.2 that the simulation types (homogeneous reactor or freely propagation flame) have a minimal difference in the calculated cross section for SI and HCCI conditions. The choice of ignition delay calculations was made for optimal implementation with the heat release and image post processors. The flame propagation simulations were performed to obtain the adiabatic laminar flame speed under engine conditions. The flame speed was later used in the temperature gradient-flame speed correlation (see Eqn. (2-2)) and compared to the measured combustion speed of the SI and HCCI experiments.

4.1.1 Mechanism Validation

4.1.1.1 Ethylene

Several chemical mechanisms have been developed for ethylene oxidation. Two notable ones are the University of California – San Diego (UCSD) complete mechanism (50 species, 247 reactions) [146] and the University of Southern California (USC) H_2/CO/C1-C4 mechanism (111 species, 784 reactions) [147]. As stated in Section 3.2.3.1, Kumar et al. [127] is the only known publication about ethylene oxidation at engine conditions, and it was therefore used to compare with simulations. The reactant molar composition was 1/3/6/27.84 for ethylene/oxygen/nitrogen/argon. Kumar et al. performed a comparison of the UCSD and USC mechanisms in their paper and found the UCSD mechanism showed good agreement; the USC mechanism was found to under-predict the ignition delay by an order of magnitude. Despite those results, the UCSD mechanism has had several revisions since the Kumar et al. publication, and the ignition delay calculator needed to be evaluated.

Figures 4-1 and 4-2 compare the experimental and predicted ignition delay for the aforementioned mechanisms at 15 and 50 bar pressures, respectively. The mechanisms agree with each other, but at realistic engine conditions of 850-950 K, both mechanisms predict the ignition delay to be shorter than observed in the experiment. In the worst case, the ignition delay was calculated to be an order of magnitude smaller for both mechanisms. This discrepancy is not expected to affect the scattering cross section calculation because the major combustion species (in terms of number of moles) O_2, N_2, H_2O, CO_2, CO, OH, and C_2H_4, which have typically well characterized chemistry due to their prominence, account for 98.7% of total moles during a stoichiometric ethylene ignition delay simulation at 11 bar, 750 K. The UCSD mechanism was

chosen as the ethylene ignition delay mechanism as it converged quicker and was more stable than the USC mechanism across the thermodynamic conditions of the experiments.

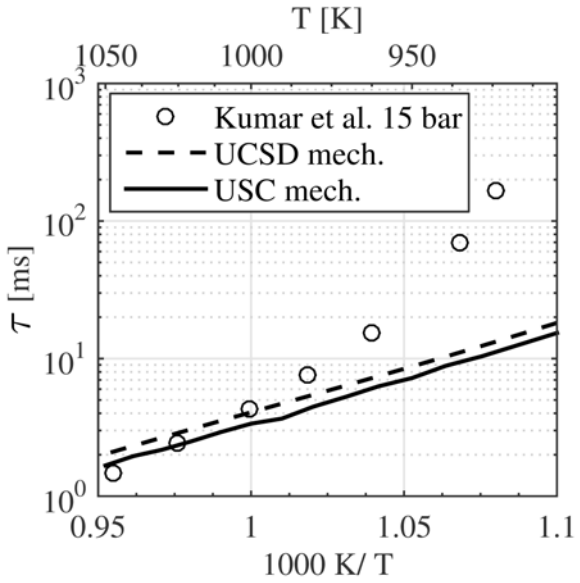

Figure 4-1: Comparison of stoichiometric 15 bar experimental ethylene ignition delay adapted from Kumar et al. [127] compared to simulations.

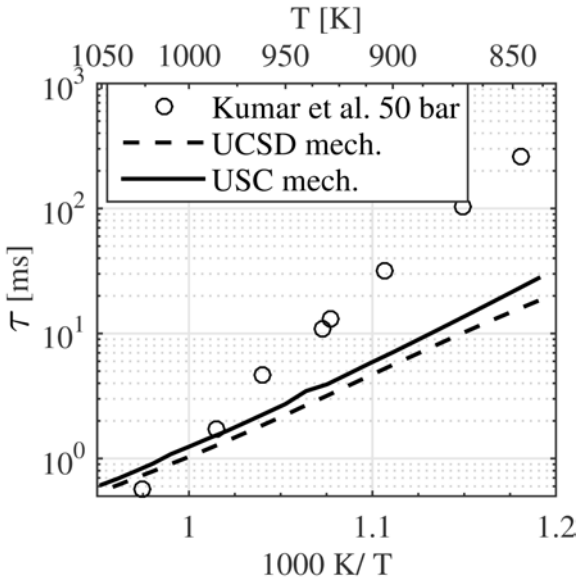

Figure 4-2: Comparison of stoichiometric 50 bar experimental ethylene ignition delay adapted from Kumar et al. [127] compared to simulations.

Validation of the same mechanisms was performed for flame speeds. Additionally a skeletal ethylene mechanism based upon the USC mechanism was tested [148]; the skeletal mechanism has 32 species and 206 reactions. The USC mechanism provides a comparison to experimental results, which shows good agreement for pressures of 1, 2 and 5 atm at 300 K. One representative data set was used for comparison in the validation. The skeletal mechanism was not tested for the ignition delay as it does not contain argon, which was required for the comparison to the Kumar et al. data. From Fig. 4-3 it is observed that the USC mechanism replicates the laminar flame speed well, whereas the UCSD and reduced mechanisms over-predict the flame speed in the near-stoichiometric region. As the pressure is increased to 5 atm

(see Fig. 4-4) the skeletal mechanism performs well over the whole range of equivalence ratio whereas the USC and UCSD mechanisms over-predict the lean region.

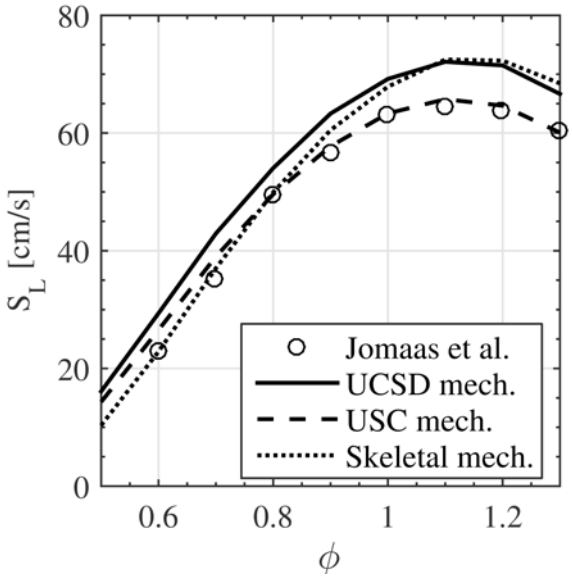

Figure 4-3: Ethylene flame speed comparison at 1 atm and 300 K. Experimental data were adapted from Jomaas et al. [149].

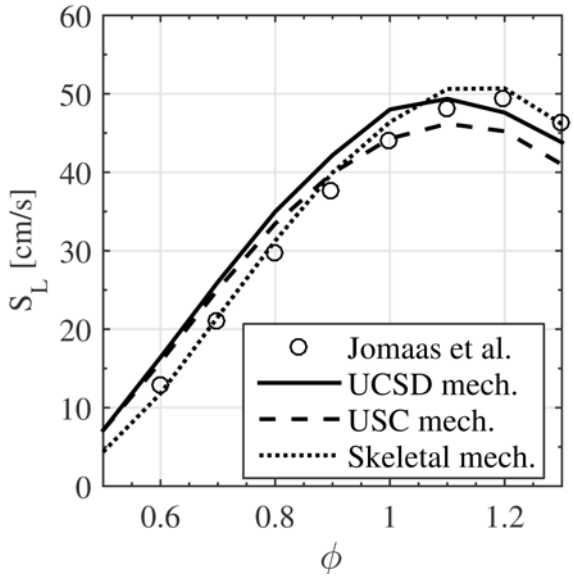

Figure 4-4: Ethylene flame speed comparison at 5 atm and 300 K. Experimental data were adapted from Jomaas et al. [149].

Temperature sensitivity was tested by comparing to data reported by Kumar et al. [127]. Ethylene laminar flame speeds measured in a counterflow experiment with the temperature varying from 298 to 470 K at 1 atm of pressure; the highest temperature case is compared to the simulation results in Fig. 4-5. The UCSD mechanism responded best to the temperature change across the range of equivalence ratios while the USC and skeletal mechanisms, in general, under-predict the flame speed. Owing to the lack of ethylene research, flame speed measurements at elevated temperature and pressure do not exist for a combined effect comparison. Instead, the error between the simulations and experimental values for the presented elevated pressure and temperature cases were combined in quadrature to assess the overall performance of the three mechanisms. Doing so yielded an average error of 19.0%, 18.8% and 15.0% for the USC, UCSD

and skeletal mechanisms, respectively. Thus the skeletal mechanism was used for the flame speed simulations. Referring to Fig. 4-6, the laminar flame speed is plotted as a function of temperature for a stoichiometric mixture with 11 bar pressure. These conditions are typical of the nominal SI case. It is seen that the predicted flame speeds for the UCSD and skeletal mechanisms are quite comparable, whereas the USC mechanism calculates a 3-5% lower flame speed. The skeletal mechanism could calculate a flame speed up to a temperature of 925 K for the stoichiometric, 11 bar condition, whereas the UCSD and USC could only simulate flame speeds to 850 and 875 K, respectively.

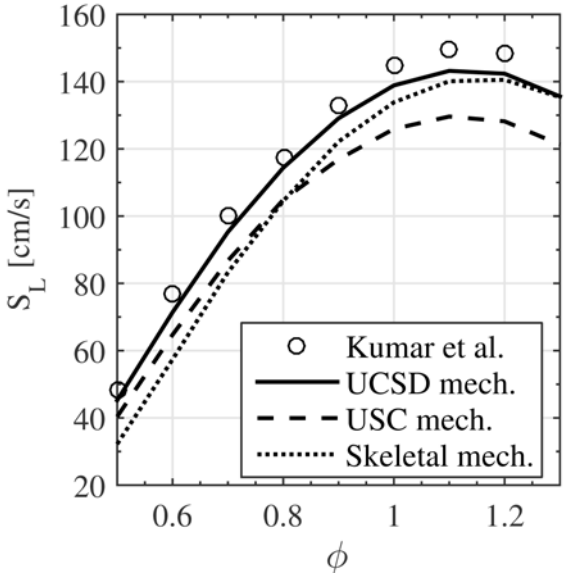

Figure 4-5: Ethylene flame speed comparison for 1 atm and 470 K. Experimental data were adapted from Kumar et al. [127].

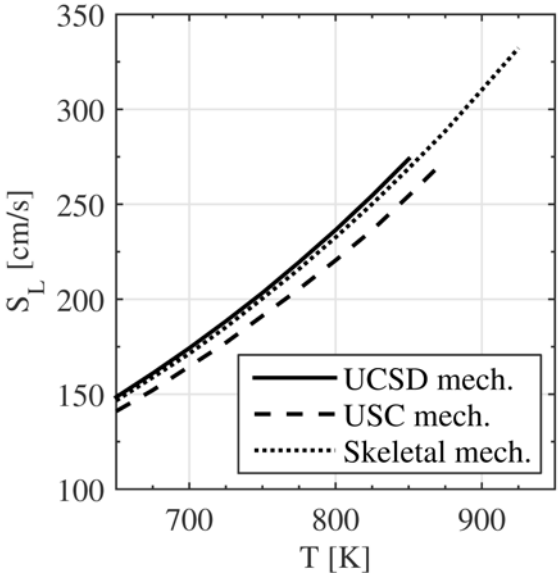

Figure 4-6: Ethylene flame speed simulation comparison for 11 bar and Φ=1 reactant conditions.

4.1.1.2 Dimethyl Ether

In-house analysis already determined that the CH_4/DME chemical mechanism from the National University of Ireland – Galway (NUI) [150] performs the best in terms of ignition delay at engine-relevant conditions. The mechanism has 113 species and 708 reactions. Figure 4-7

compares the mechanism with stoichiometric shock tube ignition delay data from two experimental studies. The most relevant conditions for the current study are temperature of 700-900K and 10-20 bar pressures, which are predicted well enough to capture the kinetics and thus obtain pertinent species mole fractions through the combustion event. The largest deviations occur in the negative temperature coefficient (NTC) region, but the ignition delay gradients appear to be matched to that of the data. Figure 4-8 adds a lean condition with $\Phi = 0.5$. Again, the largest deviation happens in the NTC region, but the shallow gradient is matched.

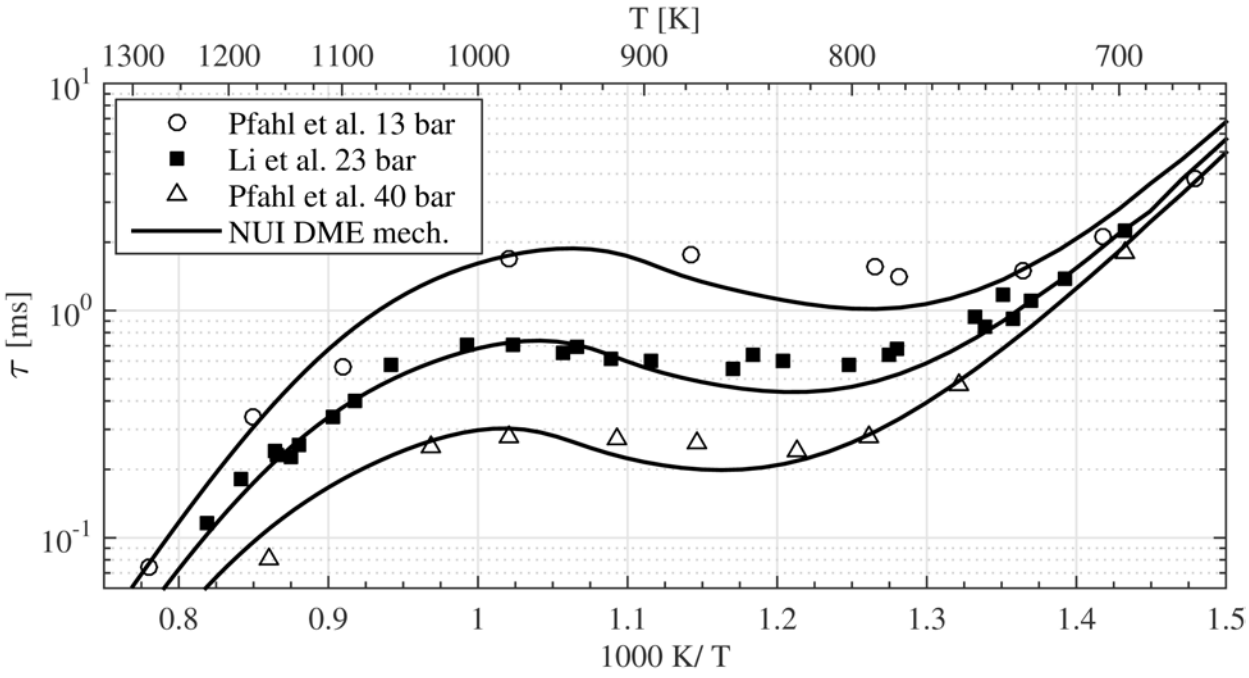

Figure 4-7: Comparison of stoichiometric DME ignition delay adapted from Pfahl et al. [132] and Li et al. [151] compared to simulations using the NUI DME mechanism.

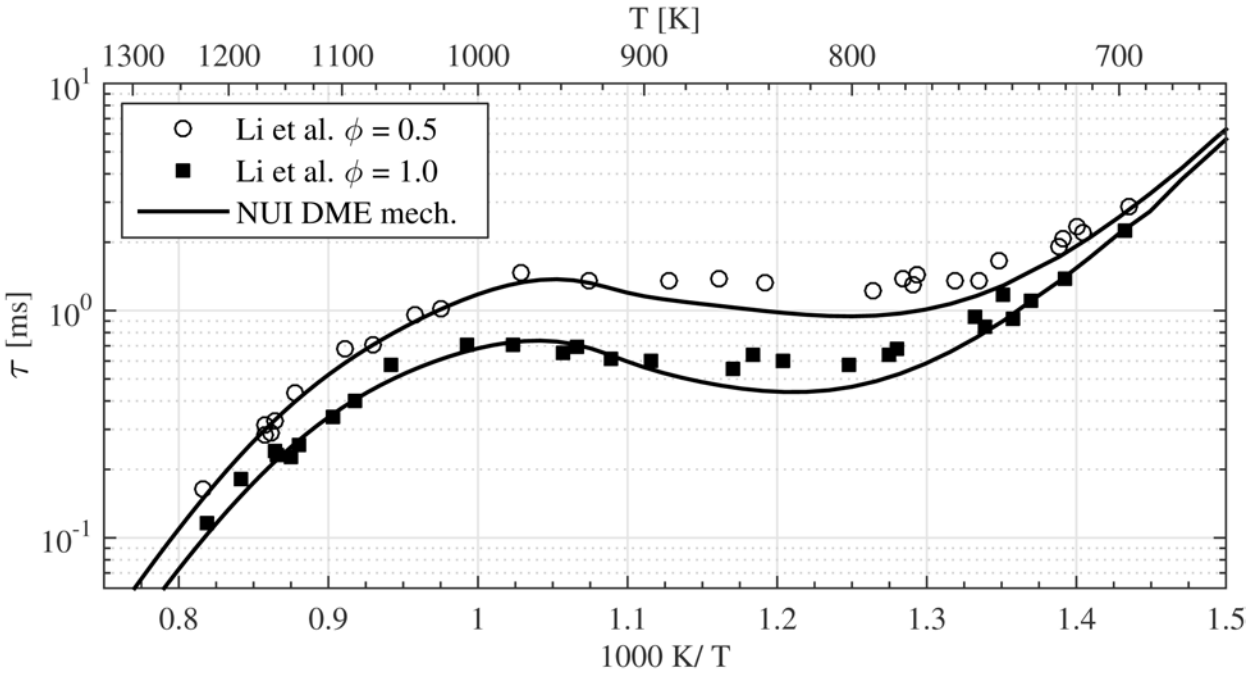

Figure 4-8: Comparison of DME ignition delay at 23 bar adapted from Li et al. [151] compared to simulations using the NUI DME mechanism.

To complete the characterization of the HCCI combustion propagation mechanism, the laminar flame speed under engine conditions must be known to compare to the measured combustion speed and the calculated combustion in Eqn. (2-2). As with ethylene, only a handful of studies have addressed the laminar flame speed of DME, likely due to DME's high reactivity being used for diesel-like combustion. Of the studies that exist, only pressure (1-10 atm) and equivalence ratio (0.6-1.7) effects have only been tested, and a large amount of variability exists in the laminar flame speed due to different experimental vessels, optical methods and data processing [152]. The tested mechanisms included the Lawrence Livermore National Laboratory (LLNL) DME 2000 mechanism [153-155], and the Zhao et al. mechanism [156], which is based upon the LLNL mechanism. The NUI DME mechanism was not compared because the flame speed simulations would not converge regardless of the solver settings.

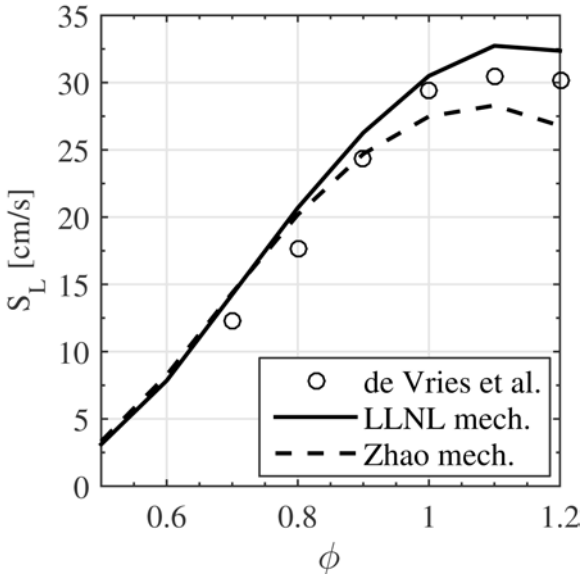

Figure 4-9: DME flame speed comparison at 5 atm and 298 K. Experimental data were adapted from de Vries et al. [152].

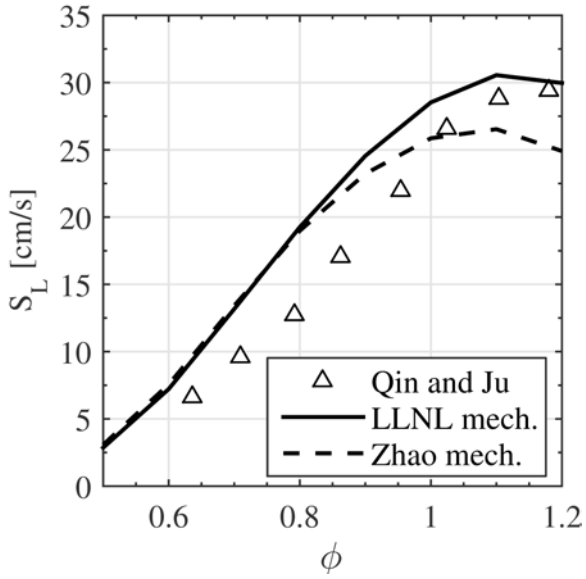

Figure 4-10: DME flame speed comparison at 6 atm and 298 K. Experimental data were adapted from Qin and Ju [157].

Figure 4-9 compares the two mechanisms to experimental data taken in a constant-volume bomb at 298 K, 5 atm [152]. For lean conditions the two mechanisms gave flame speeds similar to the experimental results, and they agree well with each other; the mechanisms start to diverge from each other at an equivalence ratio of 0.8. Figure 4-10 shows a comparison at a pressure of 6 atm performed in a pressure-release spherical chamber [157]. The simulations significantly over-predict the flame speed at lean conditions. This comparison highlights the high variability seen in the few DME flame speeds measurements. Two experimental setups performed experiments at a pressure of 10 atm, see Fig. 4-11. The mechanisms again compare well to the de Vries et al. data at lean conditions but over-predict the Qin and Ju data. The Zhao mechanism was not able to converge for equivalence ratios greater than 0.8 at the 10 atm condition. Due to the variability in measurements it is difficult to discern how well the

mechanisms truly capture the physics. There are not any experimental flame speed measurements at elevated temperature much less at elevated temperatures and pressures; therefore, the selection of the mechanism is almost arbitrary. For the lean region of interest they perform similarly, but it was found that the LLNL mechanism was more stable, was able to work across the desired thermodynamic conditions, and was, therefore, used for the DME flame speed calculations.

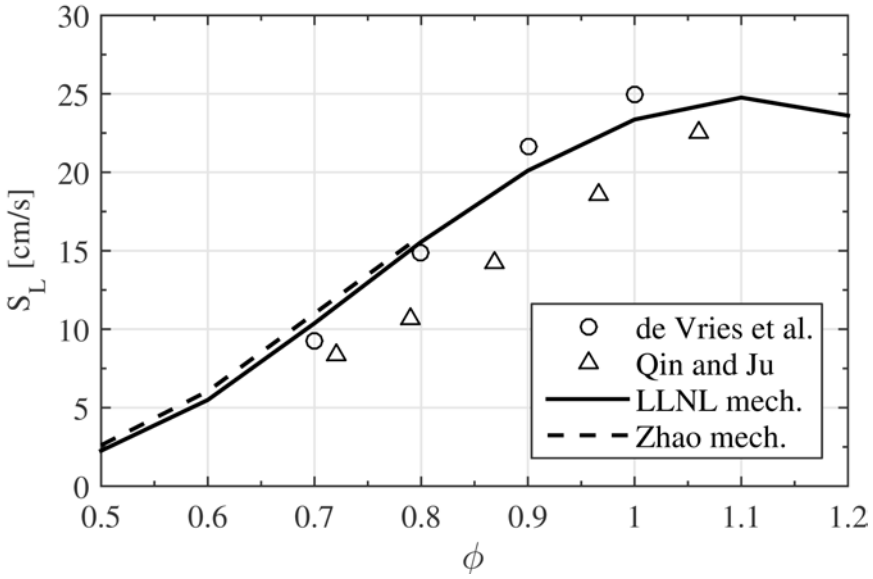

Figure 4-11: DME flame speed comparison at 10 atm and 298 K. Experimental data were adapted from de Vries et al. [152] and Qin and Ju [157].

4.1.2 Ignition Delay

The ignition delay simulations were performed in Cantera version 2.1.2 [158]. The software is capable of solving numerous chemical kinetic, thermodynamic and transport process simulations, but was solely used in this work for ignition delay simulations. Cantera was run on a base Python 3.4 library and interfaced through Matlab version 8.4.0 (R2014b). A 0-D reactor model with the appropriate mechanisms analyzed in Section 4.1.1 was used for the ignition delay calculation. The ignition delay was defined as the time of peak pressure rise rate, similar to that of shock tube

experiments. For all simulations, the time step was decreased until the ignition delay changed by less than 0.1%, and the simulation time was set long enough such that chemical equilibrium was reached and the gradient in the temperature and species mole fractions was less than 0.1%. This was interpreted as the point of convergence, and the species mole fractions were extracted for the differential Rayleigh scattering cross section calculations. The final time step was taken as the product mixture.

The ignition delay measurements were used for two purposes: 1) to calculate the differential Rayleigh scattering cross section for the thermometry equation (Eqn. (2-17)) and 2) to calculate DME's ignition delay temperature sensitivity for the combustion speed-ignition delay relationship in Eqn. (2-2). The initial mixture was set to the cycle-specific in-cylinder mixture. For SI experiments, a ten cycle skip-fire operation was used where nine motored cycles preceded each combustion cycle, thereby the residuals were the fresh air-fuel mixture. For HCCI, combustion residuals existed and were accounted for by using ideal combustion stoichiometry. The initial thermodynamic conditions for purpose 1) were set to the temperature and pressure at the time of imaging. Examples of the scattering cross section are presented in Section 4.2. For purpose 2), the imaging pressure was held constant while the temperature was varied by ± 20 K to obtain a range of ignition delays. A cubic spline was fit to the data, and its derivative was evaluated at the imaging temperature.

The HCCI experiments had mild variability in the experiments that arose from the stochastic nature of HCCI combustion. The temperature at image timing was 760-820 K, while the pressure was 10-14 bar. The ignition delays with varying pressure and equivalence ratio in Figs. 4-7 and 4-8 demonstrate negative temperature coefficient behavior around the imaged temperatures, which results in a shallow, sometimes horizontal, ignition delay gradient. The

temperature sensitivity for the HCCI experiments was found to be on average +8.5e-6 μs/K (1.7 μs/K standard deviation).

4.1.3 Laminar Flame Speed

CHEMKIN release 10113 x64 [159] was used for the premixed laminar flame speed calculations. All simulations used mixture-average transport calculations and included Soret effects, which accounts for thermal diffusion; the tested mechanisms would not converge with full multicomponent transport calculations. Convergence was determined by running multiple continuations until the *GRAD* and *CURV* parameters were satisfied at 0.05. These settings were used to calculate the laminar flame speed for ethylene and DME across their range of operating conditions.

The spark-ignition measurements had image timing temperatures of 680-730 K and pressures of 6-13 bar for which flame speed simulations were performed. The resulting 2-D map of flame speed for equivalence ratios of 1.03 and 0.82 are shown in Figs. 4-12 and 4-13. Their temperature and pressure limits were adjusted according to the thermodynamic conditions for the given equivalence ratio experiments; the false color scale is the same. As expected the laminar flame speed is a strong function of temperature; the flame speed increases by 35% across the temperature range for $\Phi = 1.03$ and 65% for $\Phi = 0.82$. The increase in equivalence ratio increases the flame speed by approximately 30% for a given temperature-pressure condition. The laminar flame speed typically has a relatively weak pressure dependence [10]; the flame speed decreased by approximately 14% across the pressure range. To link the calculated flame speed to the data, the 2-D maps were linearly interpolated using each image's temperature and pressure at

the image timing. The simulated conditions used a sufficiently fine 2-D grid to allow linear interpolation with trivial error.

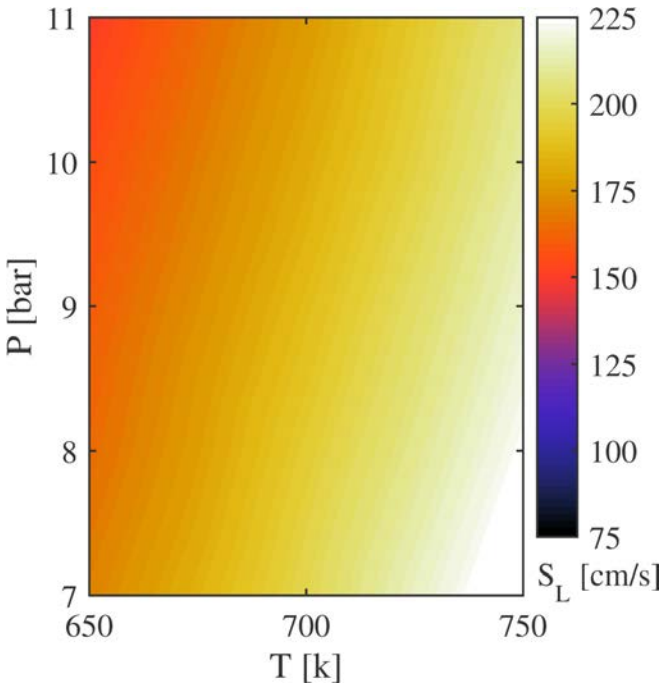

Figure 4-12: Ethylene laminar flame speed calculations over tested thermodynamic conditions. Φ = 1.03.

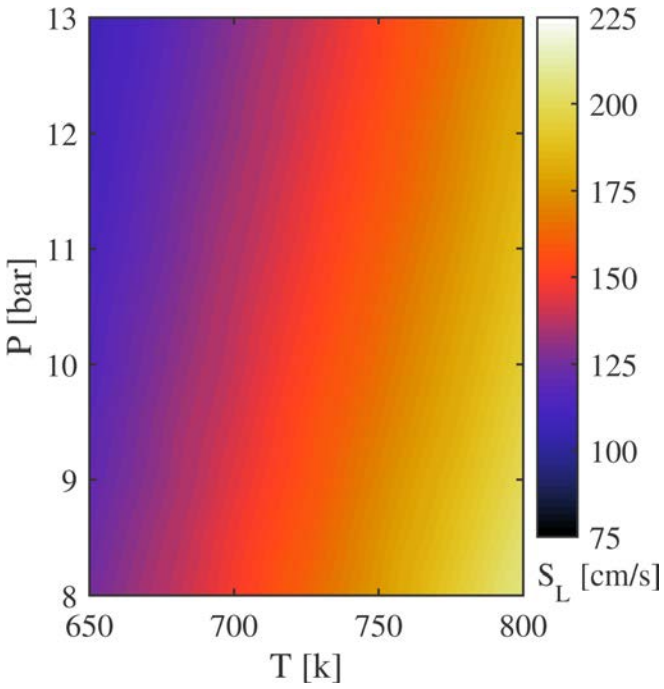

Figure 4-13: Ethylene laminar flame speed calculations over tested thermodynamic conditions. Φ = 0.82.

The same flame speed calculation methodology was used for the HCCI conditions; the corresponding laminar flame speed map is shown in Fig. 4-14. DME's flame speed is significantly slower than ethylene's for a given condition, but it has a much greater sensitivity to temperature. At a pressure of 8 bar, the flame speed increases by 150% across the temperature range; at 20 bar it is 375%. The 20% decrease in flame speed as the pressure is increased across the range is comparable to ethylene's pressure response of -14%. Because of the complete absence of experimental data for these conditions, it is acknowledged that these flame speed calculations in the region of autoignition are prone to error or do not even exist. The calculations

provide a point of comparison to collected data, and consequently are not a crucial underpinning to the presented work.

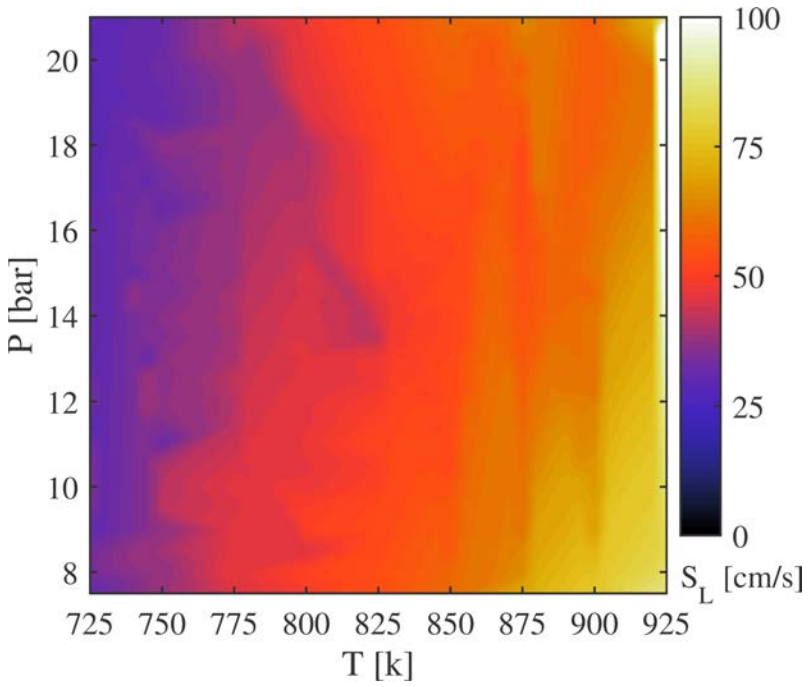

Figure 4-14: DME laminar flame speed calculations over tested HCCI thermodynamic conditions. Φ = 0.6.

4.2 Rayleigh Scattering Cross Section

4.2.1 Example Cross Sections

For reasons explained in Section 3.3.4, a polarizing filter was not used, thus the terms separating Rayleigh scattered light with parallel and perpendicular polarization in Eqns. (2-23) and (2-24) were not considered. The full form of the differential Rayleigh scattering cross sections used in the study is the combination of Eqns. (2-6) and (2-22) assuming a 90^{o} observation angle:

$$\frac{\partial \sigma_R}{\partial \Omega} = \frac{9\pi^2}{\lambda^4 N_0^2}\left(\frac{n^2-1}{n^2+2}\right)^2\left(\frac{3+6\rho_p(\lambda)}{3-4\rho_p(\lambda)}\right) \qquad (4\text{-}1)$$

Again, the Loschmidt number is $N_0 = 2.687 * 10^{19}\, cm^{-3}$. The polarized form of the King correction factor was chosen as Rayleigh scattering measurements are typically performed with polarized laser light, thus the depolarization measurements are for polarized light. Also, temperature corrections were not made as discussed in Section 2.9.2.

Due to variability amongst Rayleigh scattering cross section measurements [98,99], the cross sections were calculated for all combustion species using Eqn. (4-1) with indices of refraction and depolarization constants found in literature. In the case that experimental data did not exist for the refractive index of a given species it was computed using the summation of the individual atoms per Jenkins and White [108]. Gardiner et al. [103] curve fitted experimental refractive index measurements for many common combustion species as well as calculated indices based on atomic and bond refractivities. Between the two sets of curve fits, refractive indices were calculated for the species in the combustion mechanisms that did not have experimental data. Table 4-1 details the differential Rayleigh scattering cross section for notable combustion species at 532 nm excitation wavelength.

Table 4-1: Differential Rayleigh scattering cross section [cm^2/sr] of common combustion species at 532 nm.

Species	Formula	$\frac{\partial \sigma_R}{\partial \Omega} * 10^{28}$	$(n-1) * 10^6$	$\rho_p * 10^2$	F_k
Hydrogen	H	0.93	117[a]	0	1
Oxygen	O	1.08	126[a]	0	1
Molecular hydrogen	H_2	1.38	140[a]	0.98[d]	1.0331
Methylidyne radical	CH^*	4.04	243[b]		
Water	H_2O	4.38	253[a]	0.03[e]	1.0010
Dioxygen	O_2	5.65	272[a]	3.40[d]	1.1187
Hydroperoxyl radical	HO_2	5.70	289[c]		
Nitrogen	N_2	6.38	300[a]	1.12[d]	1.0379
Carbon monoxide	CO	7.88	337[a]	0.51[d]	1.0171
Formyl radical	$^*CHO$	8.51	353[c]		
Hydrogen peroxide	H_2O_2	8.75	358[c]		
Hydroxyl radical	$^*HO$	9.36	370[a]		
Methyl radical	CH_3^*	9.94	381[b]		
Formaldehyde	HCHO	12.55	422[c]	0.95[f]	1.0321
Methane	CH_4	13.45	444[a]	0.02[g]	1.0007
Carbon dioxide	CO_2	15.36	448[a]	3.49[d]	1.1220
Acetylene	C_2H_2	25.73	595[a]	1.88[h]	1.0644
Ethylene	C_2H_4	37.01	721[a]	1.24[h]	1.0421
Ethane	C_2H_6	39.76	761[a]	0.18[h]	1.0062
Dimethyl ether	CH_3OCH_3	52.54	872[c]	0.38[h]	1.0123

[a] From Gardiner et al. [103] – experimental refractive indices of stable gases.
[b] From Gardiner et al. [103] – refractive index based on atomic and bond refractivities.
[c] Calculated from summation of atomics contributions provided by Gardiner et al. [103].
[d] From Sutton and Driscoll [99].
[e] From experimental at 515.5 nm from Murphy [105].
[f] From Bacskay et al. [107].
[g] From Sneep and Ubachs [98].
[h] Adapted from Fuest et al. [104] – Linear interpolation to 532 nm from experimental using 514.5 nm and 632.8 nm from Bogaard et al. [106].

The elemental species refractive indices used for summation are $(n-1) * 10^6 = 69, 110, 161$ and 174 for H, O, N and C respectively, which are different than the measured values for H and O given in Table 4-1. The summation method is capable of recovering the measured refractive index for compounds such as H_2 (140 measured, 138 calculated) and CH_4 (448 measured, 450 calculated), but it is recognized that it does not work for every species. OH,

for example, has an $(n-1)*10^6$ experimental value of 370 but is 179 for the summation technique, which under-calculates the differential scattering cross section by 77%. For this reason, the experimental values take precedence over the summed values. From ignition delay simulations of a stoichiometric ethylene mixture at 11 bar and 750 K, the combustion species with experimentally known indices of refraction account for a minimum of 98.8% of total moles during the combustion event, ultimately yielding a minimal amount of error in the Rayleigh scattering cross section from calculated refractive indices. In the case of HCCI with a DME mixture of 11 bar, 800 K and Φ = 0.6, the minimum combined mole fraction percent of species with known indices of refraction is 95.3%.

4.2.2 Combustion Correction

One of the criteria for fuel selection was the consistency of the combustion gas mixture's scattering cross section through a combustion front as represented by the ratio $\partial\bar{\sigma}_R/\partial\bar{\sigma}_{R,0}$ in Eqn. (2-17). A lower-than-anticipated cross section overestimates the temperature of the products, which in turn increases the temperature gradient and can lead to misclassification of the propagation mechanism. The following subsections quantify the variable cross section for the combustion propagation modes of interest at typical conditions from the experiments. The cross section ratio was used in Eqn. (2-17) to account for the change in cross section across the combustion front, which greatly reduced the experimental error. The actual values used in the data analysis are specific to each image and engine cycle, so the values presented here provide the magnitude of the correction as well as the quantification process and justification for its use.

4.2.2.1 Flame Propagation

To visualize flame propagation's effect on the instantaneous combustion mixture and consequently the mixture cross section, flame simulations were performed using typical ethylene SI conditions. As discussed in Section 4.4, the reference condition was taken as the reactants side of the combustion front. With this definition, the cross section ratio is simply the change in cross section across the combustion front, which was used in Fig. 3-2. Figure 4-15 shows the thermometry cross section ratio $\partial\bar{\sigma}_R/\partial\bar{\sigma}_{R,0}$ for flame propagation at different unburned thermodynamic conditions. As expected the ratio is less than unity in the products, with the equilibrium cross section ratio being close for both conditions. The equilibrium ratio is 0.847 and 0.848 for the 650 and 800 K cases, respectively, yielding only a 0.1% difference. The results indicate that the cross section ratio is insensitive to the thermodynamic conditions as the products of flame propagation are essentially the same. This result reduces the amount of error introduced into the analysis as the temperature at the time of combustion can only be discerned through isentropic relations. The factor that does matter is the fuel-air mixture and equivalence ratio as seen in Fig. 3-2, but the fuel and air delivery are well characterized by choked flow orifices. The minute difference in the equilibrium composition is from the intermediate species H, H_2 and O not forming H_2O as the temperature and pressure increased; additionally, incomplete oxidation of CO yielded less CO_2. The smaller species give a smaller product mixture cross section and consequentially a cross section ratio farther from one (see Table 4-1). It also appears that the cross section change during combustion is the same when taking into account the higher pressure-temperature condition has a smaller length scale from a thinner flame.

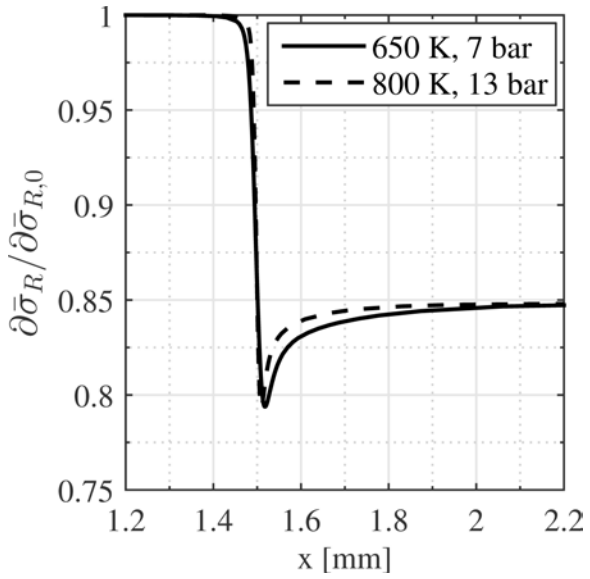

Figure 4-15: Differential Rayleigh scattering cross section ratio for ethylene flame propagation simulations. Φ=1.03.

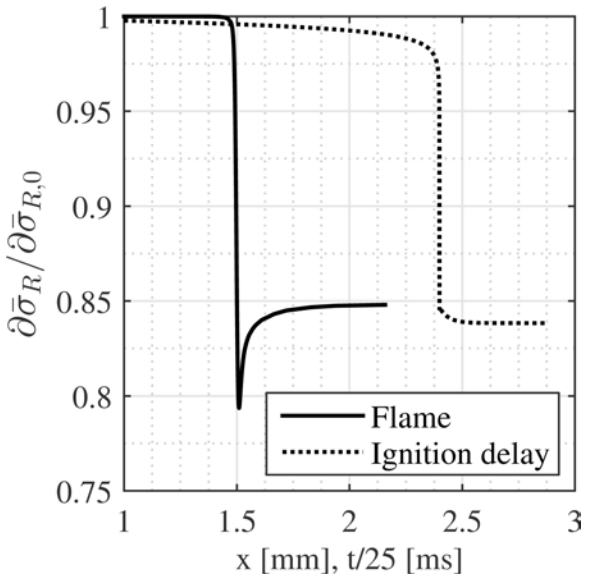

Figure 4-16: Cross section ratio of ethylene flame propagation and ignition delay simulations. 800 K, 13 bar, Φ=1.03.

To justify the use of ignition delay simulations to calculate the cross section change for ethylene flame propagation, a comparison is made between the two calculations in Fig. 4-16. The time scale for the ignition delay simulation was scaled to fit for a better comparison. By inspection, the final cross section ratio is the same for both propagation mechanisms. The flame simulation yields a final ratio of 0.848, and the ignition delay gives 0.838 resulting in a difference of 1.1%. This was deemed close enough to use ignition delay simulations for scattering cross section calculations of ethylene flame propagation. The intermediate combustion cross sections are different, and this effect is addressed in Section 4.6.1.

4.2.2.2 Homogenous-Charge Autoignition

Homogenous-charge autoignition occurs with HCCI, so as an example the Rayleigh scattering cross section was analyzed for autoignition under HCCI conditions from the experiments. To

simulate the combustion front, ignition delay calculations were used as HCCI combustion is kinetically controlled. Combustion residuals were added to the reactant mixture based on the cycle's residual mass fraction and ideal combustion products, i.e. CO_2, H_2O, N_2, O_2. Figure 4-17 shows the differential Rayleigh scattering cross section for two temperature-pressure combinations. The thermodynamic conditions are presented to demonstrate the range of cross section ratios that occurred in the HCCI experiments. Both cases have a final cross section of $6.795*10^{-28}$ cm^2/sr, giving a decrease of 13.3% from the reactants (delivered air-fuel mixture plus residuals) to products. Compared to Fig. 3-2 where DME combustion at $\Phi = 0.6$ yielded a decrease of 16.1%, the inclusion of the residual combustion mixture in the current simulations decreased the overall cross sectional change by decreasing the reference cross section. As with the flame propagation simulations, the results show that the thermodynamic conditions did not affect the product mixture's Rayleigh scattering cross section.

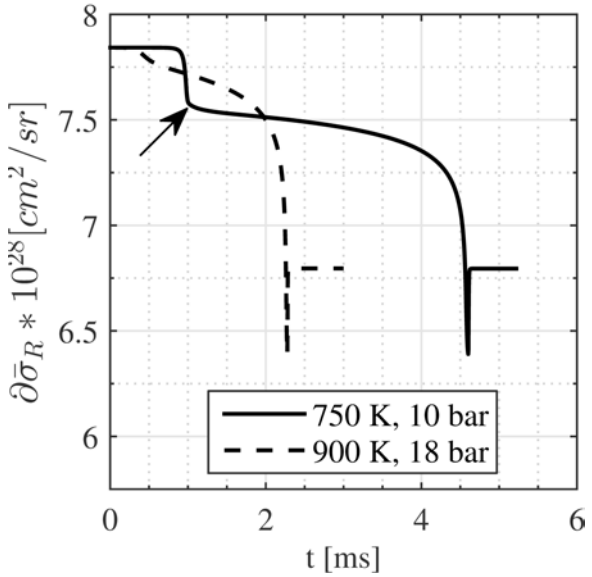

Figure 4-17: Differential Rayleigh scattering cross section using ignition delay simulations. The arrow indicates the modified reference condition.

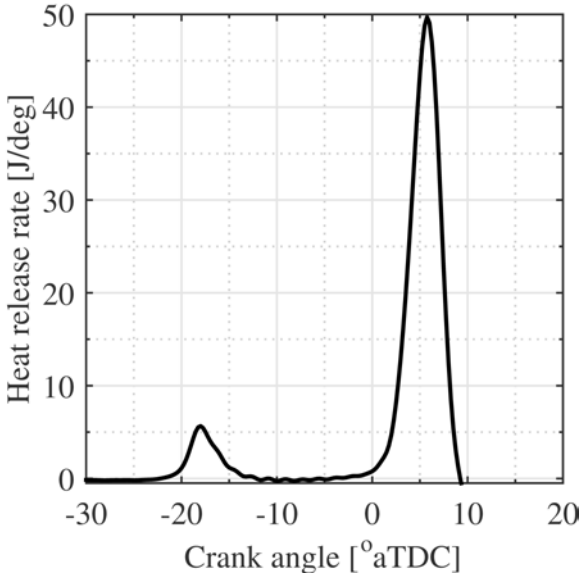

Figure 4-18: Apparent heat release rate for the HCCI experiments. The low-temperature oxidation coincides with the initial cross section decrease.

In the 750 K case, and to a smaller extent in the 900 K case, the cross section has an initial decrease before the large decrease from the combustion event. This initial decrease is the result of low-temperature oxidation (LTO, also called low-temperature heat release), which is seen in the corresponding HCCI heat release rate in Fig. 4-18. The peak LTO rate from the experiments occurred at approximately 20 crank angle degrees (2.8 ms) before the main heat release event, which corresponds well to the 3.4 ms time delay from the initial cross section decrease to the large decrease. (There are further discrepancies with the temperature and pressure of the simulation since it was not performed at the temperature and pressure of the in-cylinder contents at LTO timing but rather at the image timing). Yamada et al. [160] found through engine experiments and simulations, the LTO of DME HCCI ceases around 850 K due to the consumption of OH overtaking the production. These results are consistent with the simulations of Fig. 4-17 where LTO was greatly reduced in the 900 K case due to it being above the 850 K threshold.

From this analysis, it is apparent that the nominal reactants of the imaged combustion event were different than the delivered air-fuel mixture plus residuals, which required a new definition of the reference condition. To account for the change in cross section from the LTO event, the reference cross section was taken as the cross section just after the LTO event. The ignition delay simulation was performed at the average temperature and pressure of the LTO to calculate the *in situ* mixture. The reference cross section location is marked by the arrow pointing to the “knee” in the curve in Fig. 4-17. Figure 4-19 shows the cross section ratio using the new reference condition definition, where the 690 K, 6.9 bar simulation is the LTO thermodynamic condition from the 750 K, 10 bar case in Fig. 4-17. For clarification, the reactants in the combustion images were taken as the post-LTO mixture, which is shown by the

cross section ratio of one. By accounting for the combustion residuals and low-temperature oxidation, the product cross section ratio is 9.1% lower than the reference compared to 16.1% in Fig. 3-2. This averted over-correction of the data that would have resulted in an under calculated temperature.

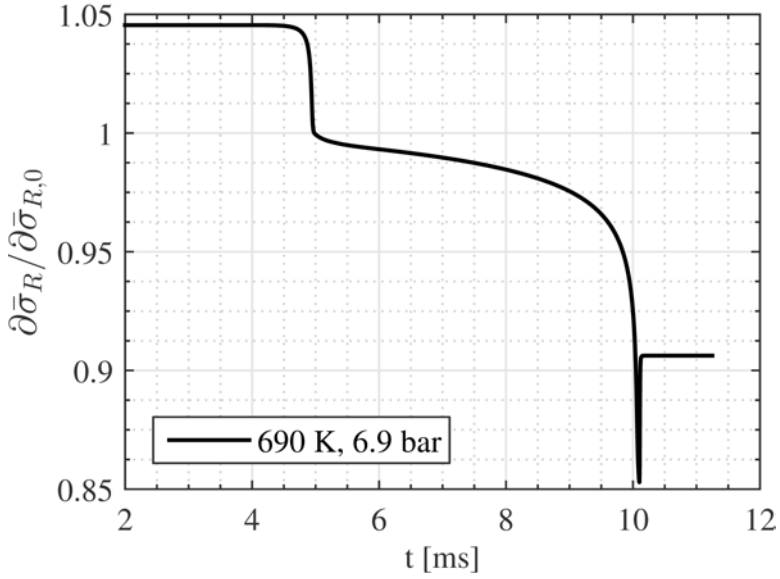

Figure 4-19: Differential Rayleigh scattering cross section ratio using the post-LTO mixture cross section as the reference condition. The ignition delay simulation was performed at the LTO thermodynamic conditions.

4.2.2.3 Autoignition/ Flame Propagation Comparison

In the grand scheme of the measurements, classification of the HCCI propagation mechanism occurs via the combustion speed and temperature gradient. However, to determine the temperature gradient the temperature was calculated with Eqn. (2-17) which involves the cross section ratio. In Section 4.2.2.1, it was shown the final cross section ratio can be determined with 1% error by using ignition delay simulations instead of flame propagation, but it is not known if this works for dimethyl ether combustion. Thus, as it stands, to ultimately determine the HCCI propagation mechanism one has to know the propagation mechanism to calculate the cross

section ratio resulting in a paradox, especially if the choice of cross section calculation changes the calculated propagation mechanism.

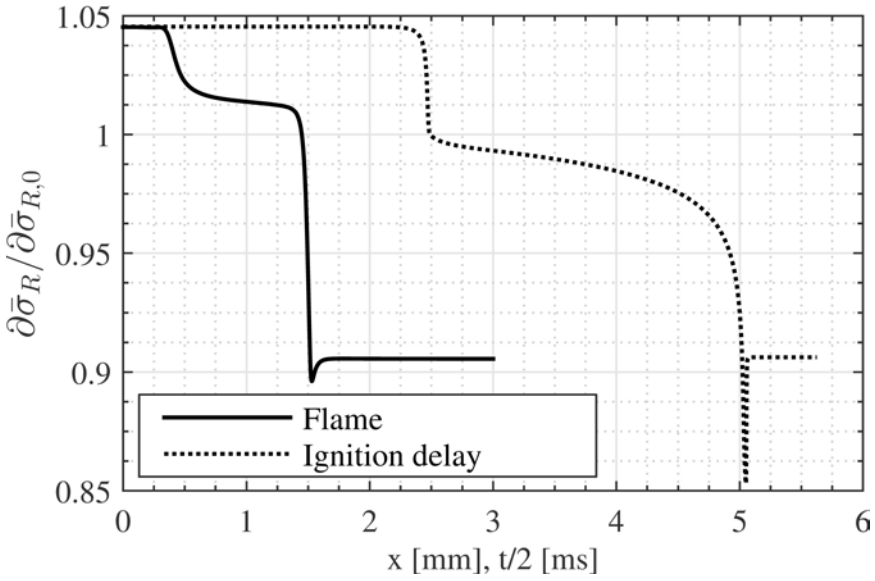

Figure 4-20: Differential Rayleigh scattering cross section ratio using flame propagation and ignition delay simulations for the HCCI condition 750 K, 10 bar.

Figure 4-20 compares the cross section ratio for the flame propagation and ignition delay simulations using the 750 K, 10 bar HCCI condition. With the revised reference condition definition for HCCI, the ignition delay curve was calculated from the LTO conditions, also shown in Fig. 4-19. The flame propagation simulation used the 750 K, 10 bar condition since the flame would occur during image timing. Both curves use the same reference condition taken from the ignition delay simulation. It is observed that both curves start and end at the same cross section ratio; the difference for the products is less than 0.1%, which shows sufficient consistency between the simulations. Additionally, since the two simulations are at different thermodynamic conditions, this further suggests that either simulation can be used to calculate the Rayleigh scattering cross sections. The difference arises when determining the reference cross section. Based on the definition of using the “knee” after the low-temperature oxidation,

the flame propagation reference cross section is 1.9% larger than the ignition delay's, but this arises from the temperature used in the simulation. As discussed earlier, a greater temperature results in less low-temperature oxidation [160]. This signifies that one must use the LTO temperature and pressure for the flame propagation simulations as well to obtain the correct cross section change. The final result is that the ignition delay simulations give the same cross sectional change across the combustion front as the flame propagation simulations, solving the parody, but the simulation must be performed at the thermodynamic conditions of the low-temperature heat release to calculate the correct reactants mixture at image timing.

4.3 Image Acquisition

For the most accurate measurements all non-Rayleigh scattering signals have to be accounted for, such as stray laser scatter and combustion luminosity. This section details the images taken for correction purposes.

4.3.1 Dark Current and Read Noise Image

The dark current refers to the thermally generated charge on the CCD array that builds up while the camera is waiting to be exposed or during readout. The read noise is amount of noise introduced to the signal during the charge-to-digital signal conversion process. The thermal charge generation can be reduced by operating the camera at as low of a temperature as possible. Accordingly, the cameras were operated at -20 ^{o}C using their built-in Peltier coolers. Dark current is time dependent (see Table 3-4), so any changes in the image acquisition settings such as exposure duration (if very long), inter-frame delay or readout speed require new dark current corrections. The dark current has shot noise associated with it that is characterized by Poisson

statistics [161], and since the dark current image served as the baseline subtraction for all images (see Section 4.4.1), it was necessary to obtain the statistical average of the dark current and read noise. 100 dark current images were taken each operational day at least 30 minutes after the camera reached thermal stability. The images were recorded with the lens cap on to ensure only the thermally generated charge and read noise were measured.

4.3.2 Room Light Image

To check if the room lights were contributing to the measured signal, room light correction images were taken each day of operation. Because of the anomalously shaped HCCI piston window that can cause mechanical vignetting, the engine was set to the imaging crank angle to ensure same viewing area. Again, 100 images were taken (now with the lens cap off) with the same acquisition settings as the Rayleigh scattering images.

4.3.3 Combustion Luminosity Image

Similar to the room light imaging, it was necessary to know if the combustion luminosity was contributing to the measured signal, because although the chosen laser wavelength of 532 nm is outside major emission lines, broadband CO-O chemiluminescence does occur at 532 nm. For each operation mode images were taken at the nominal engine timing without laser operation so that the only contributors to the measured signal were combustion, room light and the dark current and read noise. Using the two previous images, the combustion component was separated for assessment.

4.3.4 Motored Image

For every set of combustion images, a set of motored Rayleigh scattering images were taken before the combustion images during a single continuous engine run. For spark-ignition experiments, all the fuel was present, but for HCCI the DME was not included as combustion would have occurred. The motored images were taken at the same crank angle as the fired images, which gave the initial insight into the expected signal quality of the combustion images as any optical issues (i.e. dirty windows, particles in the air, etc.) would be obvious. Although the motored images were a good candidate for the reference condition, without cycle-resolved laser energy it was better to do in-image referencing with the combustion images. Instead, they served as an indicator of non-uniform background scattering signal originating from surfaces or possible mechanical vignetting due to the imaging area's close proximity to the piston extension internal bore diameter.

Figure 4-21 shows any example of a processed motored image from a spark-ignition data set. Figure 4-22 shows the location of the imaging area relative to the cylinder. The head window template was used to mask the scattering area such that only the head window region is shown. The laser propagation direction is shown by arrow in the imaging region in Fig. 4-22. Mechanical vignetting was assessed by monitoring the measured intensity collinear with the beam propagation. Because the beam propagates from top to bottom, a signal with vignetting would have a signal level that increases as the beam propagates, such that it would be brighter at the bottom farther away from the inner bore of the piston extension. This was not observed in any of the acquired images. In the case of surface scatter, bright areas would be visible at the bottom of the image. In Fig. 4-21 two distinct bright areas exist, each with their own origin. The very bottom edge of the image was affected by the high levels of background scatter caused the

metal-metal interface of the head window holder. Although the metal interface is outside the shown head window area, it affected the viewing area pixels through charge bleeding as the metal background area easily saturated. (Charge bleeding is the process of electrons "overflowing" from one pixel to its neighbor pixel.) The second bright area is just above the previously discussed region. The extra scattering continues from the main bright spot along an arc. This caused by reflections in the imaging optics. If the bright areas were limited to a small region (e.g. at the bottom of the image), the image was still analyzed because rest of the image was not affected.

Particle scatterers are highlighted with the colored circles. The red circles indicate particles in the laser sheet. These are easily identified as being smaller and not persisting between engine cycles. Particles on window surfaces, however, would persist from cycle to cycle. Particles on the in-cylinder window surfaces (head and piston) were characterized by rings which sometimes had a bright spot in the middle due to the out-of-plane defocusing. This is seen clearly in the green circle. It could not be determined which surface the particles lied on since both surfaces were relatively the same distance from the laser plane. Particles on the bottom surface of the piston window could be differentiated as they were much farther away from the laser plane and were therefore even larger as seen in the blue circle. Data were not processed in the regions of surface particles or reflections to prevent skewed data. If the motored images showed significant issues, the combustion images would as well, so the engine was stopped to clean the window surfaces and reattempt data collection.

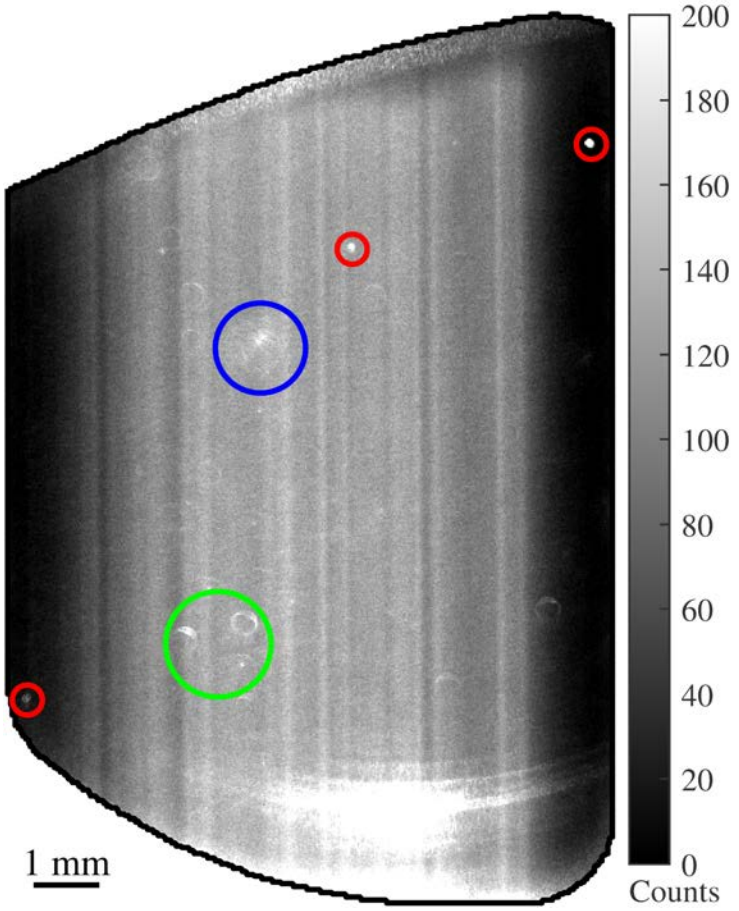

Figure 4-21: SI Rayleigh scattering motored image. The laser beam propagates from top to bottom. Different types of particle scatterers are indicated by the colored circles.

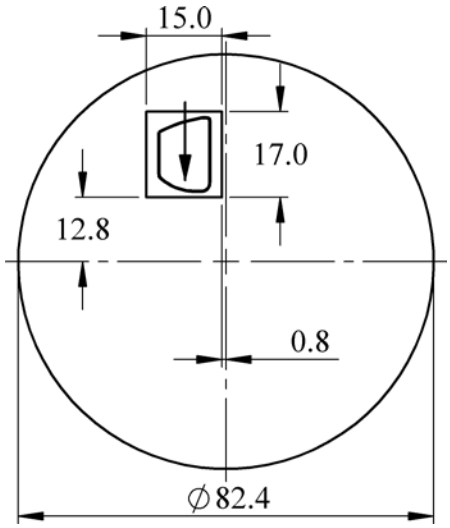

Figure 4-22: Overhead view of the imaging area relative to the center of the cylinder. The recorded image is given by the rectangle around the imaging area. Dimensions are in millimeters.

Another noteworthy feature are the striations aligned collinear to the beam propagation. The sharp changes in intensity are thought to be beam steering as a result of either an index of refraction change due to thermal boundary layers at the entrance window or from stresses induced in the laser entrance window. Similar effects were seen in Rayleigh scattering mixing measurements [113,114]. The striations added another layer of complexity to the data analysis, but with the proper corrections, the image intensity in a small region was uniform, suggesting the temperature was uniform as expected. The striations worsened as the pressure increased. Data at a higher load HCCI case (~50 bar in-cylinder pressure compared to ~10 bar) were taken, but the

striations made the data analysis unmanageable. Figure 4-23 is an example of a high-pressure motored Rayleigh scattering image with intense beam steering. Besides the striations leading to non-uniform intensity in the horizontal direction, the sheet forming optics contributed to the issue by focusing the laser beam into a sheet without expanding it for uniformity. The result was a laser sheet with the greatest intensity the center of the sheet than at the edges.

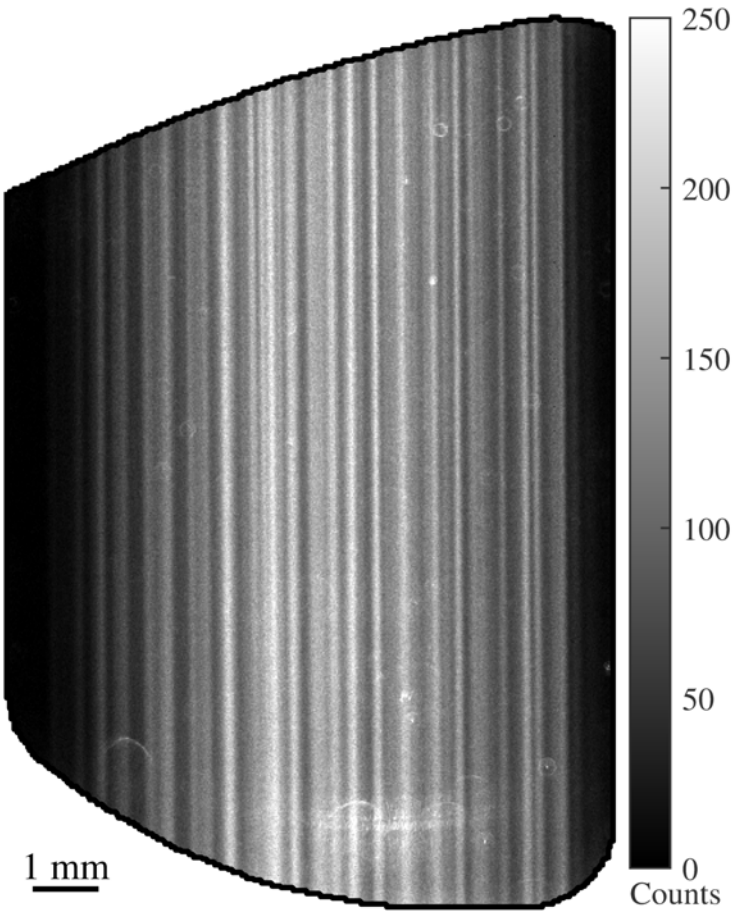

Figure 4-23: Rayleigh scattering high-pressure motored image. The striations were caused by beam steering.

4.3.5 Combustion Image

The combustion images were taken after the motored images during the same engine run. For spark-ignition experiments, all of the fuel was already introduced into the intake system, so the

engine was at a quasi-steady state and the combustion images could be taken right away. For SI experiments, the engine was operated on a ten cycle skip-fire count in which the spark plug was triggered every 10^{th} cycle. This prevented the optical engine components from heating up too much, which could cause failure due to thermal stress, and was experienced with the HCCI experiments. For HCCI, DME was introduced into the intake system after the completion of the motored images. Once combustion initiated, the engine was allowed to reach a more thermally stable condition. It is noted that the engine never reached a quasi-steady state condition as the combustion continuously advanced as the engine components increased in temperature. The increase in in-cylinder pressure and pressure rise rate from the combustion, as well as the hotter optical components, put the engine in danger of failure, so the engine was operated for a only short period of time. The MicroMAX camera was operated as fast as it could at the 5 MHz readout rate (see Table 3-4), which was typically every 5^{th} cycle. Camera gating signals were recorded to know when imaging occurred, so individual engine cycle pressures were matched to the images.

A typical SI Rayleigh scattering combustion image is shown in Fig. 4-24. See Fig. 4-22 for orientation. The flame front is clearly defined by the intensity change where the low intensity regions within the laser sheet are higher temperature and thus the products of combustion. As expected the combustion is propagating outwards from the spark plug (center of the cylinder) towards the periphery. The intensity changes by approximately a factor of 3.5 across the combustion front. It is observed that in some regions along the flame front the change is sharp, but in others it is more gradual. Because the combustion propagation mechanism is known to be flame propagation, shallow intensity gradients signify the flame was not perpendicular to the laser sheet, i.e., it was oblique to the laser plane. The effect of oblique combustion fronts are

addressed in Section 5.5. Other notable features consist of the wrinkled flame front as well as the finger-like structures that were also visualized in previous spark-ignition experiments in the same facility [136].

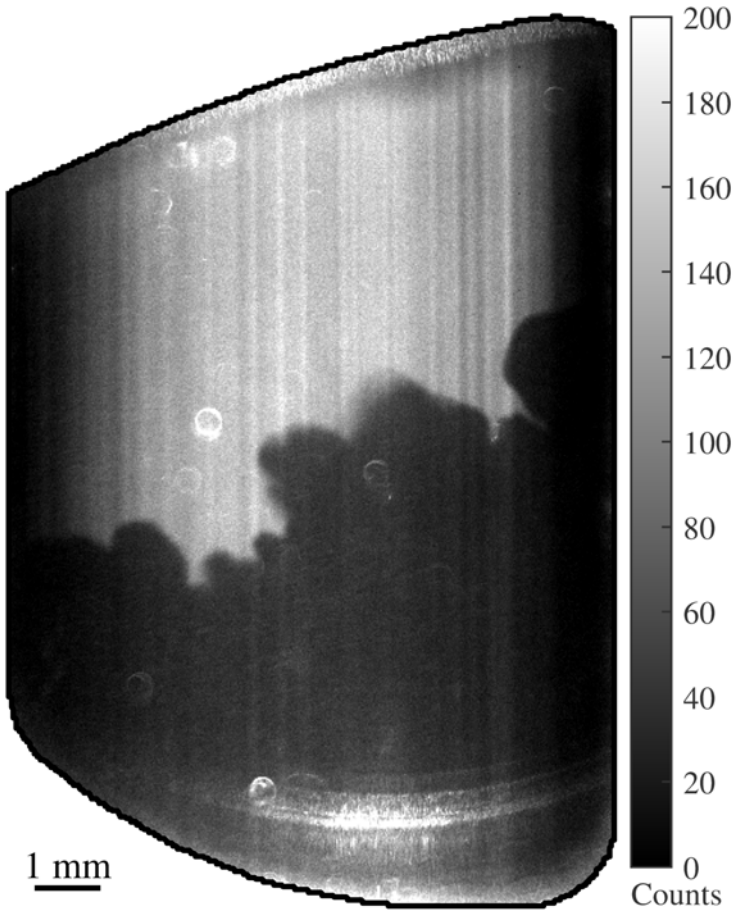

Figure 4-24: SI Rayleigh scattering combustion image. The flame front has several characteristics: smooth and rough curvature, sharp and shallow intensity (temperature) gradients, and inclusions.

Figure 4-25 is an HCCI Rayleigh scattering combustion image. In contrast to the SI image, the combustion is more randomly oriented with no common propagation direction. Every HCCI combustion image was starkly different with regards to the combustion location and structure; at the best image timing the majority of images did not even contain combustion. The combustion fronts are seen to be generally smooth without wrinkling, but the intensity gradients

vary widely. Because the combustion propagation mechanism is unknown for HCCI, it is not known whether the shallow intensity, and by extension, temperature gradient was due to an oblique combustion front like SI or if the combustion front width was large. Additionally combustion is seen to occur in the middle of the reactants, as indicated by the black ellipse. It is unknown whether this is an autoignition site or out-of-plane combustion propagation. Although there is significant charge bleeding at the bottom of the image, the combustion contours in rest of the image are suitable for analysis given the lack the particles and extraneous scatter contaminating the fronts.

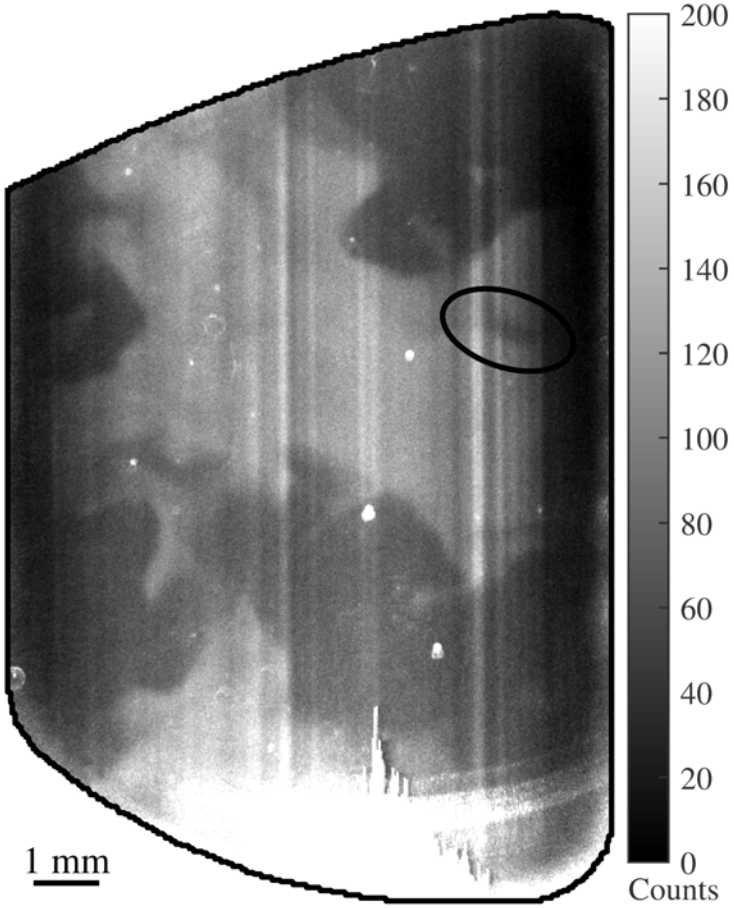

Figure 4-25: HCCI Rayleigh scattering combustion image. The combustion front locations are random with a variety of intensity gradients. Charge bleeding at the bottom of the image caused the saturated structure.

4.3.6 Background Image

In addition to the Rayleigh scattering and particles, the recorded intensity is also comprised of general background scatter from metal and optical surfaces within the cylinder. The final image captured in the data collection procedure was used to assess this background scatter. The background images were taken after the fired images with the engine positioned statically at the same imaging crank angle. The half-wave plate was removed from the optical setup so that the laser had vertical polarization and would not produce Rayleigh scattering in the imaging direction. Because the Rayleigh scattering intensity is several times greater than the background intensity, adverse scattering structures can add intensity to the Rayleigh scattering image without one knowing. Taking the background images allows one to assess whether or not any hidden structures exist that need be corrected or avoided altogether. The background images were used to decide whether or not to use the combustion images based on the uniformity of the background scatter as well as their absolute levels in relation to the Rayleigh scattering intensity.

Figure 4-26 is a background image from a spark-ignition experiment. In general the intensity field is uniform except for a few particles on the window surfaces. These particles have a large enough intensity that they would stand out in the Rayleigh scattering field and are then avoided. More important, though, is understanding what the underlying background scatter is. The uniform field observed in Fig. 4-26 shows the background signal levels are predictable and make for an easy but nontrivial correction. While the average intensity is low at approximately seven counts, when considering the Rayleigh scattering combustion in Fig. 4-24, the seven counts of additional non-Rayleigh scattering intensity accounts for 5% and 15% of the reactants' and products' intensity, respectively, for the fired SI image in Fig. 4-24. Raising the intensity

floor decreases the intensity ratio which serves to decrease the temperature. Continuing the example, the temperature would be reduced by 10% if the background intensity was ignored.

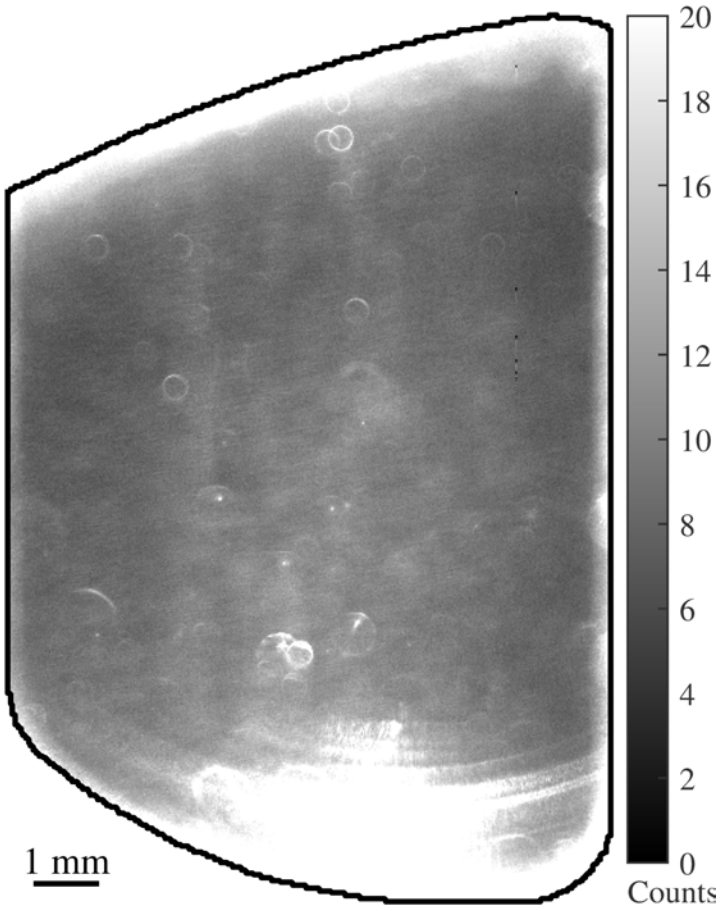

Figure 4-26: SI background image. The uniform, low-intensity field with few particles indicates the Rayleigh scattering images are free of hidden errant sources of intensity.

It was found during image analysis that the background image intensity was always less than the intensity outside the laser sheet of the motored and combustion images. The region outside the laser sheet would ideally have the same intensity given no Rayleigh scattering occurred there. The inconsistency was likely due to beam steering that caused extra light scattering while the engine was operating. It was attempted to scale the background image intensity level using the area outside the laser sheet as a reference point, but the subtraction

resulted in structures in the Rayleigh scattering images. Further investigation revealed the intensity of the particles in the background image was different than those of the Rayleigh scattering image despite the scaling correction. This was, again, a result of beam steering. Therefore, to have the most accurate correction, the intensity from the uniform regions outside the laser sheet was taken from each individual processed image. This correction is henceforth called the flare to prevent confusion with the static background images, which were still used to determine if the background was free of underlying structures.

4.4 Image and Data Analysis

This section details step-by-step all of the calculations that were used in the image processing and data analysis to correct the images, identify the combustion fronts, track the combustion front, and calculate the temperature, temperature gradient, combustion front thickness and combustion speed.

4.4.1 Image Correction

To decide the appropriate corrections to apply to the raw images, calculations were performed to determine if the image correction was worthwhile given its respective uncertainty. That is, was the correction statistically more significant than its uncertainty? Data points from typical images from the different conditions were used in the development of the image correction process. Single data points from the reactant and product side of nominal SI combustion are presented as an example.

The first correction considered was the dark current image because it gives a measure of the dark current and read noise, but it also accounts for the camera bias. The bias is a constant

added to the measured signal level to set a minimum intensity level, thereby giving a baseline to make quantitative measurements. The bias does not add uncertainty to the measurement, thus when taking the dark current images, the dark current and read noise is quantified as the root mean square signal less the bias. This was determined by calculating the standard deviation of a single pixel for the repeated dark current images and averaging over the array. To demonstrate the image correction process, the processing information used to make the final image in Fig. 4-24 is presented. The image was taken with the MicroMAX camera. The dark current image had a signal level of 82 counts with a standard deviation of 2 counts. Because the dark current (DC) image was subtracted from all images, the camera bias was not separated from the DC image. For assessment of the other correction images, their dark current corrected signals levels and uncertainty were calculated. The dark current corrected intensity was determined by:

$$I_{corrected} = I_{raw} - I_{DC} \tag{4-2}$$

where I_{raw} is the interested image's intensity straight from the camera and I_{DC} is the dark current image intensity, which is 82 counts in this case. Eqn. (4-2) was applied to sample data set and their values are given in Table 4-2. The uncertainty was calculated with the equations discussed in Section 4.6.1.3.

Table 4-2: Sample dark current-corrected intensities and their uncertainties.

Image	Intensity uncorrected [counts]	Uncertainty [counts]
Room light	0.0	2.8
Combustion luminosity	-1.9	2.8
Flare	29.2	3.8
Rayleigh scattering reactants	165.2	6.4
Rayleigh scattering products	71.1	4.4

The room light, combustion luminosity and flare images were all considered as possible correction images. The room light average image intensity was found to be zero, which means the camera filter stack effectively blocked out all the room light with 532 nm wavelength. The combustion luminosity corrected intensity is actually negative meaning all the combustion light at 532 nm was also blocked. The negative value is not alarming, though, as its magnitude is less than the uncertainty. Based on the correction value being less than the uncertainty, room light and combustion luminosity corrections were not performed. If they were subtracted from the Rayleigh scattering images, they would only increase the uncertainty more than they would affect the intensity. The flare correction, however, has a correction level significantly greater than its uncertainty. It was also mentioned in Section 4.3.6 that omission of the flare correction will under calculate the temperature, quite significantly in some cases. Therefore the flare correction was the only other image correction used to obtain the final Rayleigh scattering images. Mathematically the corrected Rayleigh scattering intensity, reference or desired, used in the thermometry is:

$$I_R = (I_{raw} - I_{DC}) - \left(I_{raw,flare} - I_{DC}\right) \tag{4-3}$$

where I_{raw} is the uncorrected Rayleigh scattering intensity and $I_{raw,flare}$ is the uncorrected flare intensity.

4.4.2 Combustion Front Identification

With the corrected Rayleigh scattering intensity from Eqn. (4-3), the combustion front was identified. Several steps were taken to correct the intensity striations induced by the beam steering seen in Figs. 4-24 and 4-25, as well as the non-uniform intensity from the circular beam being focused into a sheet. The ideal correction would be to divide each column of pixels by an

average intensity that would account for the laser variation from the sheet forming optics and beam steering. On the scale of the full image, the striations were not guaranteed to be perfectly aligned with the beam propagation. In fact, in most images the striations deviated by approximately five pixels in the horizontal direction from the top to bottom of the image. This was enough deviation to cause further striations from the aforementioned correction. Beam steering is also a 3-D event further complicating the correction. Instead, because the deviation of five horizontal pixels occurred over the range of 600 vertical pixels, a sub region, nominally with a height of 50-100 pixels, was used to perform the striation correction and subsequent combustion front detection.

Figure 4-27a) shows a flare-corrected sub region of an SI combustion image. The beam steering correction was performed by dividing each column of pixels by the average of 15 reactant pixels in that column. The reactants were used as they were the higher intensity pixels, thus their relative uncertainty was less via the signal-to-noise ratio (see Section 4.5) allowing for a more accurate average; theoretically, using the reactants or products would yield the same intensity ratio for the thermometry calculation. For the SI experiments where the combustion generally progressed from the bottom to top of the image, the averaging pixels were at the top of the sub image. The result of the beam steering correction is seen in Fig. 4-27b). The given intensity was then normalized by the reactants, yielding the ratio $I_R/I_{R,0}$ which is the inverse of Eqn. (2-17). Because of the small sub region that was being analyzed, all of the reactants were assumed to be at the same thermodynamic conditions; the same assumption was applied to the products. When processing HCCI images, extra care was taken to ensure this condition was satisfied as combustion locations were in close proximity to each other such that the reactants of one front were at the beginning stages of becoming the products of another combustion front.

These locations were determined by monitoring the intensity and ensuring the reactants' intensity was not decreasing, i.e. initiating combustion. The predictable spark-ignition flame progression did not result in these dubious situations. Sharp intensity gradient across the combustion front were also required as they would give the greatest temperature gradient and be the most probable to support flame propagation. This does skew the HCCI distribution as a large range of gradients was seen, but it was the purpose of the study to investigate the role of deflagrations in HCCI.

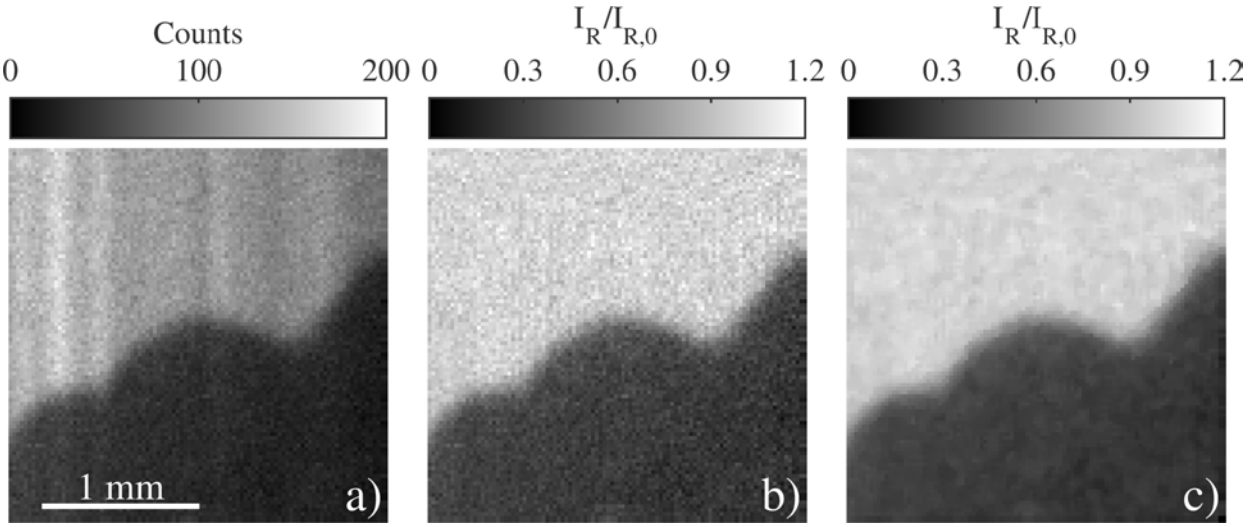

Figure 4-27: Image processing methodology of a flare corrected Rayleigh scattering sub image. a) Rayleigh scattering image, b) beam steering corrected, c) median filtered.

After the striation correction, the intensities on either side of the combustion front should only have noise variations around the mean. Depending on the severity of the beam steering, column-to-column variation still existed after the correction which would add noise to intensity profiles that cross several columns. To remove any remnants of beam steering and to reduce the noise seen in Fig. 4-27b), median filtering with a 3x3 stencil was applied to the striation-corrected image. Median filtering was chosen as it has been shown to preserve length scales in turbulent measurements [162], thus it will not significantly decrease the spatial resolution and

alter the temperature gradient or combustion front thickness. A 3x3 stencil size was selected to keep the filtering block smaller than half the combustion front thickness. For an estimated 200 μm flame front thickness and a pixel pitch of 25 μm/pixel (see Table 3-5), a 3x3 filter is the only size to meet the requirement. (The filter size must be an odd whole number greater than one.) The median filter yielded more uniform reactant and product intensity fields as seen in Fig. 4-27c).

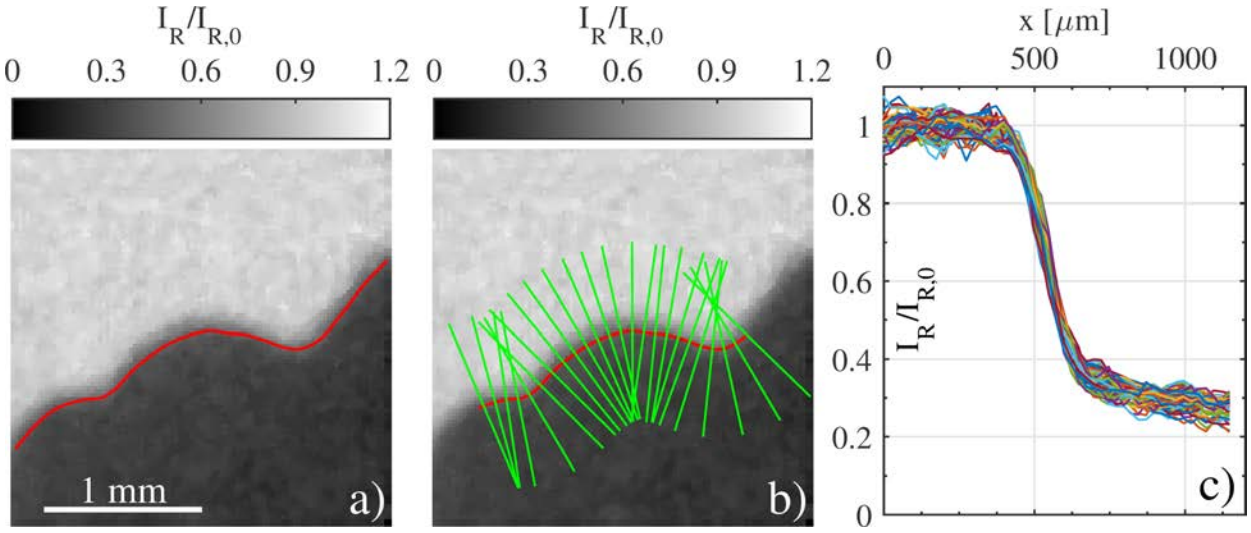

Figure 4-28: Contour identification methodology. a) threshold-identified contour, b) orthogonal lines fit to the identified contour, c) intensity ratio along the orthogonal lines

The next step identified the combustion front contour by applying a black and white threshold to the filtered image. The threshold was adjusted until satisfactory results were achieved, such as the red contour identified in Fig. 4-28a). One contour point was allowed per pixel. It is seen that the contour is not always at the same intensity level in the combustion front, but the location in the combustion front does not matter as long as the contour is tangent to the front. Cubic polynomial fits were performed to each point in the contour, and analytical derivatives were used to calculate lines normal to the contour as shown by the green lines in Fig.

4-28b). (Every third normal line is shown for clarity.) As mentioned earlier, tangency of the contour line was the only requirement since the normal lines were extended as far as necessary to obtain intensity profiles (along the normal lines) that reached quasi-steady signal levels for both the reactants and products as seen in Fig. 4-28c). The individual contours were shifted later to account for the contour location. Individual contour points were removed if the normal line exceeded the bounds of the sub image, hence the contour in Fig. 4-28b) has a reduced length.

4.4.3 Temperature

The intensity ratio profiles identified in Fig. 4-28c) were used as the foundation to the thermometry equation repeated here. The pressure term has been removed from the equation as in-image referencing was used, and the pressure was assumed to be constant across the combustion front.

$$T = T_0 \frac{I_{R,0}}{I_R} \frac{\partial \bar{\sigma}_R}{\partial \bar{\sigma}_{R,0}} \tag{4-4}$$

Similar to the camera resolution measurements in Section 3.3.5.1, an error function with form

$$I(x) = \frac{1}{2}\left[1 + erf\left(\frac{x}{\Lambda}\right)\right] \tag{4-5}$$

was used to fit the intensity profiles to remove the noise effects on the system. The fit parameter Λ is related to slope of the curve such that a thicker combustion front yields a larger lambda. The combustion front temperature profile for flame propagation and successive autoignition is not necessarily, and in all likelihood is not, described by an error function. Any sigmoid function would work as they all describe the “S” shape of a combustion front, but the error function in the presented form was chosen as it has been used to calculate the uncertainty in the spatial resolution of flow scalar length scales given its fit parameter Λ and the spatial resolution of the

imaging system [145]. Figure 4-29a) shows an intensity profile from Fig. 4-28c) fitted with the error function. The x-axis origin has been shifted to approximately the beginning of the flame front. Indeed the function fits well in that it captures the reactants' and products' quasi-steady intensity as well as the gradient through the combustion front. Figure 4-29b) is an enlarged view of the combustion front. The raw data profile is seen to be quite noisy, and the fitted equation passes between the various peaks in the raw data. In its raw form, a temperature gradient could not be calculated without significant error. Additionally, the combustion front thickness is based upon the temperature gradient (see Section 2.8), so useful data could not be extracted from the raw intensity profile. This necessitated the use of the fitted profile.

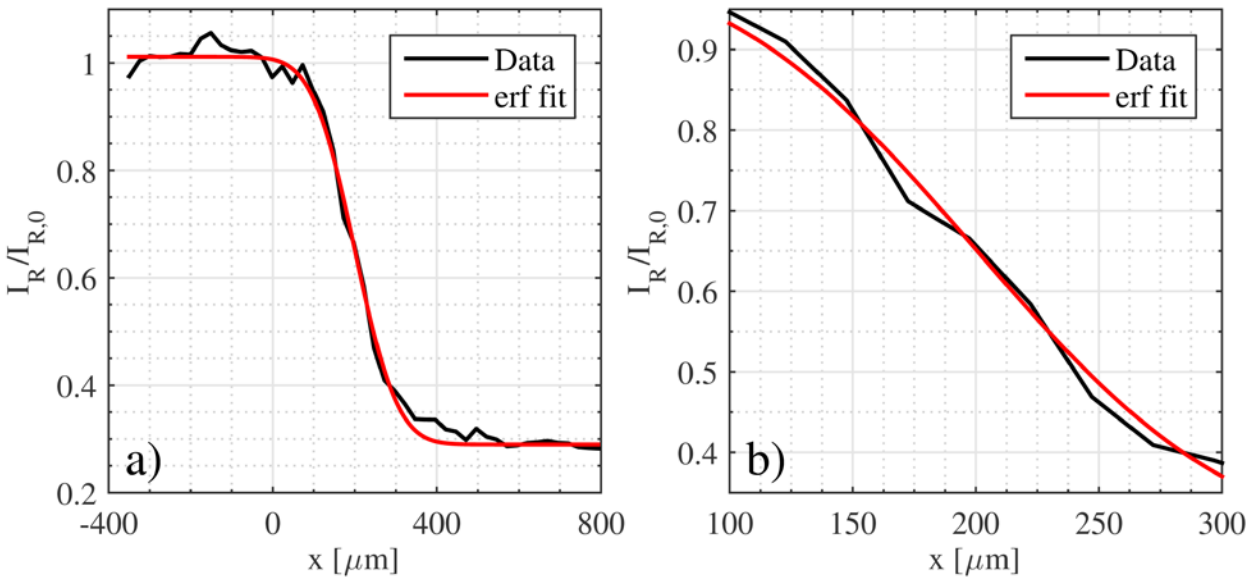

Figure 4-29: Error function fit to a single intensity ratio profile from Fig. 4-28c). a) The fit captures the gradient and end points well. b) Zoomed in section of the combustion front shows the noise in the raw data.

Because the rest of the analysis relies on the temperature gradient measurement, it was crucial for the error function fit to reproduce the gradient of the intensity profile. To validate the nonlinear fitting process, flame propagation simulations were used to fit an error function, and comparisons between the simulation's temperature gradient and that of the fit were made. A

range of initial temperatures and pressures were used to vary the gradient and test the robustness of the curve fit. The results showed the fit under-calculated the temperature gradient by 17% on average, which was deemed unacceptable for the study. Because the number of pixels in the gradient region was small in comparison to the reactants and products, a least-squares regression could neglect the fit through the gradient and still achieve a high coefficient of determination. To improve the nonlinear fit, a weighting function, based on the initial fit, was applied that strongly favored minimizing the residuals in the combustion front over the residuals of the reactants and products. Due to the nature of the sigmoid shape, it would naturally fit the reactants and products without having to intentionally minimize the error. The weighting function had an inverse parabolic shape centered on the peak intensity gradient and with a height proportional to the number of points in the curve; a greater number of points gave a higher peak as it had more residuals to outweigh. The width of the parabola was nominally set to the fit parameter of the initial fit and was further controlled by dividing by a width parameter. A second validation of this methodology was performed with the same flame propagation simulations while sweeping the width parameter. Figure 4-30 shows the peak temperature gradient error as a function of the width parameter for the initial, unweighted fit and the weighted fit. The shaded regions indicate the 95% confidence interval. Clearly the weighting function improves the fit in the combustion front region, so all intensity profiles were fitted via the two-step process with a width parameter of 1.8, such as the one in Fig. 4-29.

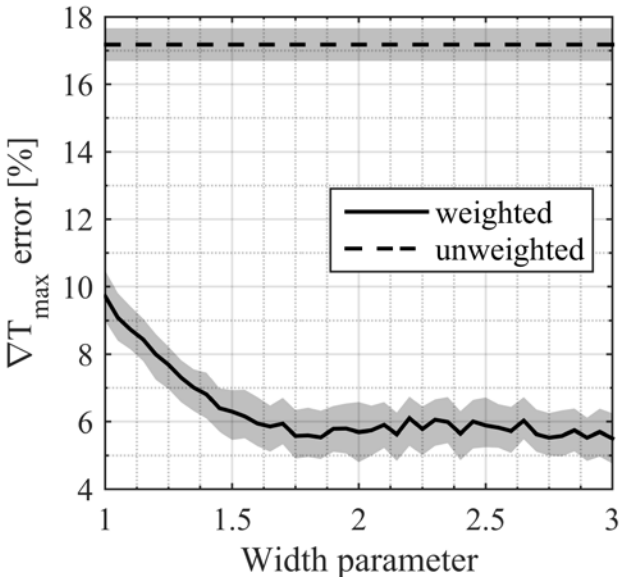

Figure 4-30: Temperature gradient error as a function of the weighting function width. The shaded regions indicate the 95% confidence interval.

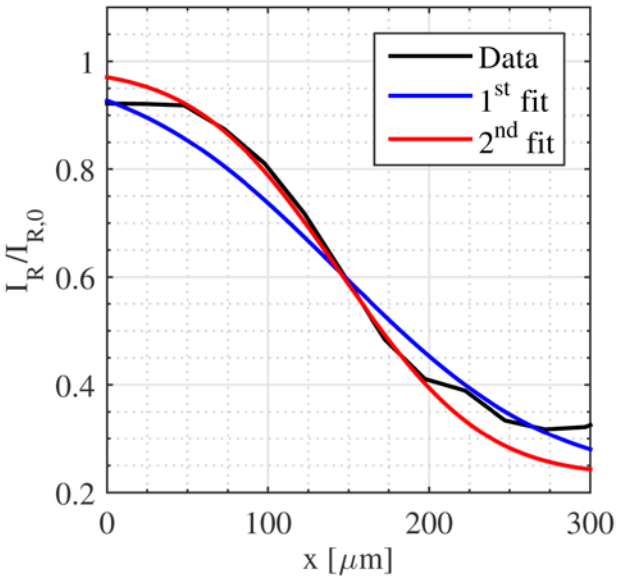

Figure 4-31: Unweighted (blue) and weighted (red) error function fits of an intensity ratio profile. The weighted fit captures the gradient.

Figure 4-31 shows a raw intensity profile with its unweighted (1st) and weighted (2nd) error function fits. The unweighted fit visibly does not match the gradient through the combustion front while the weighted fit can. This example is more egregious than the average, but it demonstrates the need of the two-step process to preserve the gradient. With the noise-less fitted intensity profile, the Rayleigh scattering cross section could be calculated. As was seen in Section 4.2, the scattering cross section was variable through the combustion front. This presented a dilemma in how it would be handled. In the majority of the flame propagation and ignition delay simulations there was a sharp decrease in the cross section (see Figs. 4-15 - 4-20), but it was not found to be predictable in the magnitude or width. Several of the mechanisms were also questionable in their predictive abilities at the tested thermodynamic conditions given no experimental data existed for comparison. It was deemed detrimental to add physics to a situation that was not verified. The end points of the temperature profile are well known, though;

this led to using linear interpolation between the reactants' and products' cross sections through the combustion front. Because this was applied to all profiles there was not a bias, and the uncertainty, although hard to quantify, was equally applied as well. Figure 4-32 is the resulting temperature profile from the intensity ratio profiles in Fig. 4-29. Again, the fitted function captures the characteristics of the data well. The biggest difference is in the post-peak temperature gradient region in which the data approaches the peak temperature slower than the fitted profile. Flame propagation simulations displayed a similar behavior, but it is shown in the following section that this is a nonissue. The temperature gradient was calculated with an numerical derivative of the temperature fit; the raw data could not be used because of the noise in the signal. The spatial resolution of the fit data was decreased until the change in the temperature gradient was sufficiently small; a resolution of 1 μm was used as the gradient changed less than 1% with further refinement. The temperature profile in Fig. 4-32 has a temperature gradient of 7.2 K/μm.

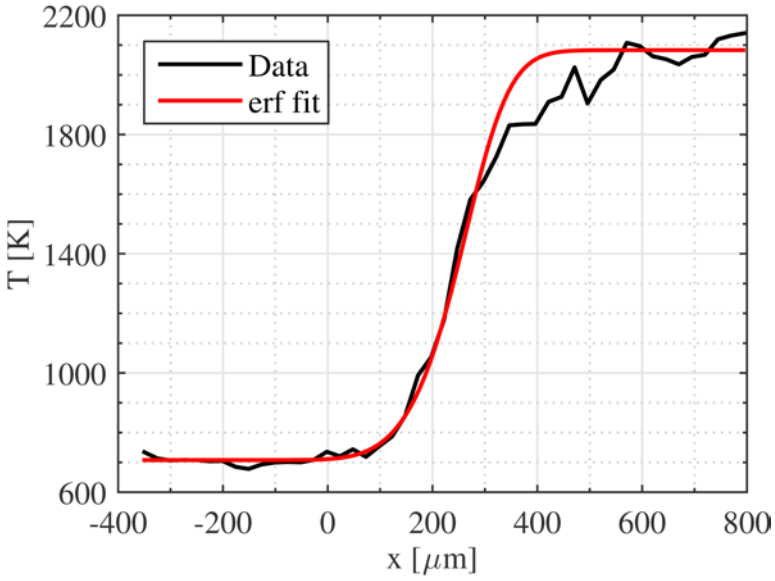

Figure 4-32: Temperature profile calculated from the intensity ratio profiles in Fig. 4-29.

4.4.4 Combustion Front Thickness

The definition of the combustion front thickness applied in this study was adopted from Smith [8]. The width was defined as the distance between intercepts of the reactant and product densities with a line determined by the maximum density gradient. This is shown schematically in Fig. 4-33 and mathematically in Eqn. (4-6) where subscript R signifies the reactants and P are the products. The density was calculated using Eqn. (4-7) which used the same reference case as the temperature calculations. The reference case density was determined using the ideal gas law via Eqn. (4-8), which was substituted into Eqn. (4-7) to get the utilized form in Eqn. (4-9). Same as the temperature data, the error function fit intensities were used because the peak gradient for the raw data could not be accurately defined due to the noise. The fit data does have a sharper transition from the combustion front to the reactants, but three components required for the thickness calculation are the quasi-steady reactants and products temperature and the peak gradient, all of which the curve fit maintains. It can be seen in Fig. 4-33 how the over-predicted temperature region is not involved in the calculation.

Because the molecular weight $\overline{M}$ is for the mixture (indicated by the overbar) it had the same characteristics as the scattering cross section. Ignition delay simulations provided the mixture molecular weight for the cases presented in Section 4.2 are shown in Fig. 4-34. The initial mixture molecular weight for HCCI was taken at the same point after the low-temperature oxidation as the scattering cross section. Linear interpolation between the initial and final molecular weights was used through the combustion front. For comparison of the thickness calculation methodology, the thickness was also calculated using temperature per Eqn. (4-10); this formulation has been used in simplified flame calculations [10]. The combustion front

thickness for the profile in Fig. 4-32 is 205 µm using density and 190 µm for temperature, and the density profile in Fig. 4-33 is the profile from Fig. 4-32.

$$\delta_\rho = \frac{\rho_R - \rho_P}{\nabla \rho_{max}} \tag{4-6}$$

$$\frac{\rho}{\rho_0} = \frac{I_R}{I_{R,0}} \frac{\bar{M}}{\bar{M}_0} \frac{\partial \bar{\sigma}_{R,0}}{\partial \bar{\sigma}_R} \tag{4-7}$$

$$\rho_0 = \frac{P_0 \bar{M}_0}{R T_0} \tag{4-8}$$

$$\rho = \frac{P_0 \bar{M}}{R T_0} \frac{I_R}{I_{R,0}} \frac{\partial \bar{\sigma}_{R,0}}{\partial \bar{\sigma}_R} \tag{4-9}$$

$$\delta_T = \frac{T_P - T_R}{\nabla T_{max}} \tag{4-10}$$

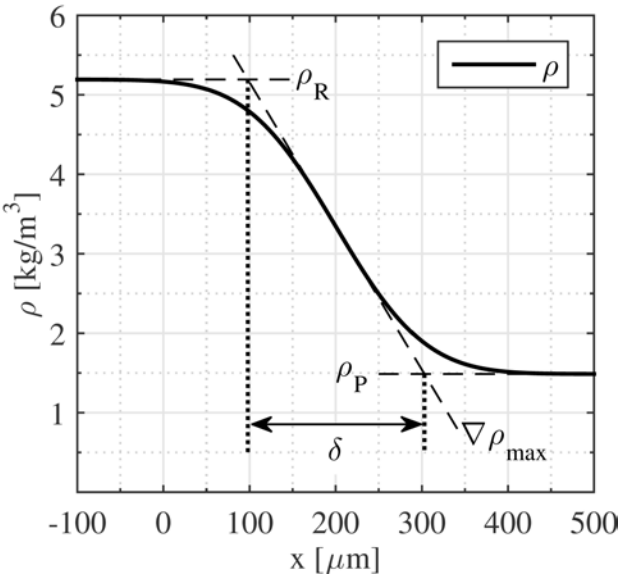

Figure 4-33: Definition of the density-based combustion front thickness.

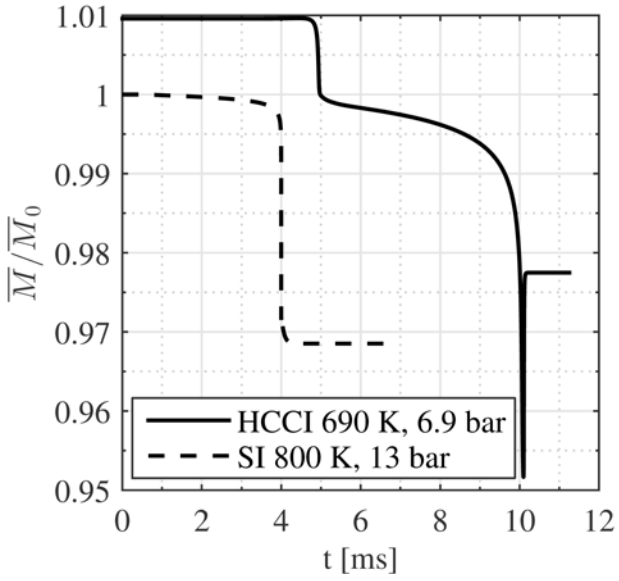

Figure 4-34: Mixture molecular mass ratio through combustion. The SI time scale was adjusted to fit.

4.4.5 Combustion Speed

To calculate the combustion speed, dual imaging data were used to track the identified combustion front between successive images. The inter-laser separation time was set to control how far the combustion front moved between images. Choosing the separation time was a tradeoff between having the front move sufficiently beyond the spatial resolution uncertainty but small enough such that the combustion front shape did not appreciably change. Several iterations were required to achieve an appropriate separation time for each operating condition. Typically, the combustion moved 10-20 pixels for separation times that ranged from 30-75 μs. In the analysis the combustion front shape was assumed to be constant between images, and it was only allowed to translate to the displaced position. With the set swirl ratio of 0.1, the tangential velocity was approximately 29 cm/s, which is small compared to front-displacement speeds measured, thus rotational flow was not considered. Any combustion front that appeared to change structure or underwent rotation was discarded. Several tracking analyses were attempted to auto fit the displaced combustion front, but all required manual intervention, therefore the front movement was tracked manually.

To assist in the tracking, combustion fronts with unique features such as corners or arcs were used to ensure the fronts were consistent and could be easily aligned between images. This procedure placed the tracked front within a pixel of the actual front in the second image. It was stated in Section 4.4.2 that the contour's position in the combustion front was not important, but for tracking the combustion front it was. To get the most accurate movement, the contour was tracked to the same spot in the combustion front, such that refinement of the tracked front was done through comparison of the intensities along the contour. The same beam steering corrections and median filtering was applied to the second image to obtain the intensity ratio

through the combustion front (see Section 4.4.2). This method assumed the temperature profiles were constant between successive images. For first and second image reactant conditions of 696 K, 11.2 bar and 699 K, 11.4 bar, respectively, flame propagation simulations predicted the peak temperature gradient to increase by 1.2%, which was sufficiently small enough for placement of the combustion front within a pixel resolution.

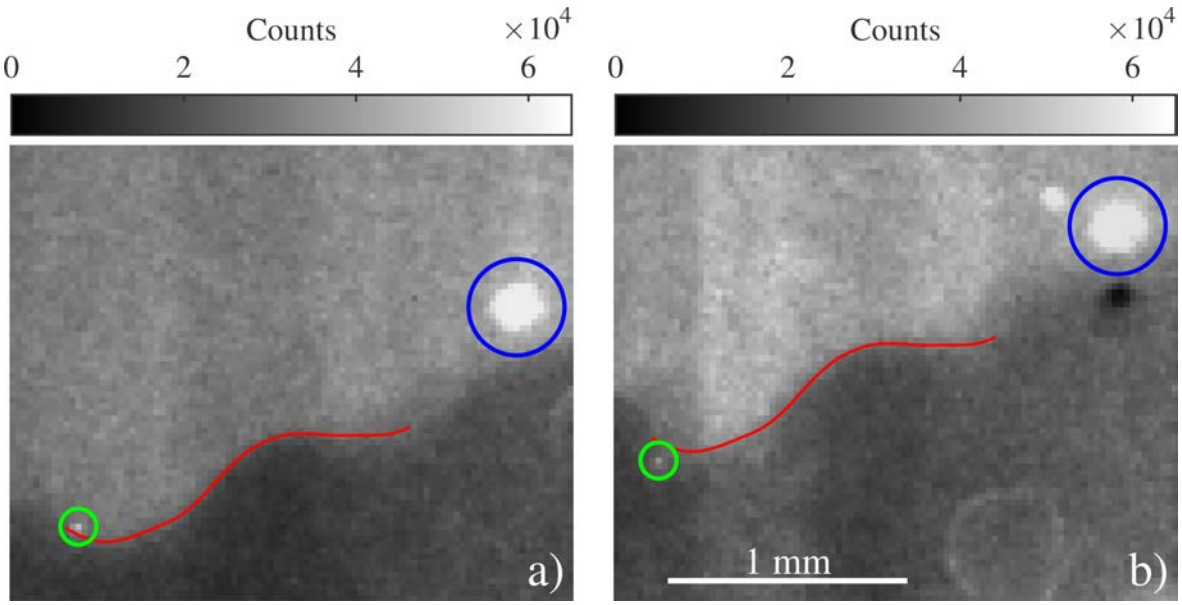

Figure 4-35: First (a) and second (b) image of a tracked SI flame front identified by the red contour. The particles circled in green and blue were used to monitor in-cylinder motion.

Figure 4-35 illustrates a spark-ignition flame front tracked from image a) to b). The tracked contour (red) is a model contour since it has distinguishing characteristics that allows it to be easily tracked from one image to the next. Additionally the combustion front in the second image does not change form or rotate, it only translates. In this case, the combustion front moved 15 pixels up and 3 to the left.

But not all of the movement was from flame propagation. It was determined that a significant amount of in-cylinder motion occurred during the experiments, which most likely is

from the combustion-induced expansion due to the low swirl ratio and the tumble flow being normal to the measurement plane. The total combustion front movement was defined as a combination of the combustion propagation and in-cylinder motion:

$$\vec{r}_{CF} = \vec{r}_{CP} + \vec{r}_{FF} \tag{4-11}$$

where $\vec{r}_{CF}$ is the combustion front movement, $\vec{r}_{CP}$ is the movement due to combustion propagation and $\vec{r}_{FF}$ is the movement from the in-cylinder flow field. All of the movements are given as vectors to track the individual x and y components for the speed. Therefore, the in-cylinder flow at the combustion front had to be known to accurately calculate the combustion speed. This was achieved by tracking particles in the vicinity of the front. From Fig. 4-35, the two particles circled in blue and green were tracked between the successive images. The middle of the particle was used as the tracking point, so a smaller particle was preferred as it gave less uncertainty to its positional change. Thus, only the particle in the green circle was used. Further requirements were imposed on the usable tracked fronts by requiring the particles to be close to the combustion front such that they represented the local in-cylinder motion at the combustion front. Continuity also required the particle's movement to be less than the tracked contour's movement, otherwise the combustion speed would be negative, which for obvious reasons is wrong.

The particle circled in green moved 12 pixels up and 2 pixels to the left, resulting in a net combustion propagation movement of 3 pixels up and 1 to the left. The vector components were combined in quadrature to yield the magnitude of the displacement, which was divided by the separation time to calculate the combustion propagation speed.

$$u_{CP} = \frac{|\vec{r}_{CP}|}{dt} \tag{4-12}$$

This formulation of the combustion speed represents the average speed during the inter-image time. Using the simulations that addressed the changing temperature gradient, the flame speed was predicted to increase by 0.8% from the first to second image; thus a negligible over-calculation of the flame speed is expected. This gives a distance of 81 μm, and with an inter-laser separation time of 30 μs, the flame speed was 269 cm/s for contour in Fig. 4-35.

In summary, to successfully track a combustion front four requirements had to be satisfied. 1) The shape of the combustion front could not change between the two images. 2) The front had to have unique features to ensure the tracked front was aligned properly. Monitoring the intensity ratio along the contour further aided the tracking procedure. 3) The front was only allowed to translate. Tracked fronts that fit better when rotated were not allowed. 4) There had to be a trackable particle in close vicinity to the combustion front, and the particle could not move more than the tracked combustion front. Violation of any of the four requirements resulted in the tracked contour not being used. In the end, to acquire successful dual-image measurements, the images could not be saturated with particles, yet they could not be completely devoid of them. So ironically, despite all the effort to eliminate particles in the images, they proved vital to the experiment.

4.5 Signal-to-Noise Ratio

The signal-to-noise ratio (SNR) is a measure of the desired signal level to the background signal level and is useful in understanding the variability of the measurement. While it is not an absolute measurement of uncertainty, it is simple to calculate compared to the full uncertainty and can give an indication of the signal quality. In optical systems, noise arises from shot noise and the measurement equipment. Optical shot noise originates from the discrete nature of photon

emission in which photons arrive in non-uniform packets. The measured signal follows the Poisson distribution for discrete probabilities, and the magnitude of shot noise is equal to the square root of the measured signal, $\sqrt{N}$. For statistical measures, the Poisson distribution requires the use of chi-squared or gamma distributions for confidence interval calculations, although this is typically ignored because the root-sum-square uncertainty calculation is for Gaussian distributions [163]. When considering only shot noise, the *SNR* is given as $S/N = N/\sqrt{N} = \sqrt{N}$ such that the SNR increases with the number of photons. The full signal-to-noise ratio that applies when not in the shot-noise-limited regime is given for a non-intensified camera as:

$$S/N = \frac{S}{C_{AD}\sqrt{\frac{S}{C_{AD}} + N_{bin}(N_{dark}^2 + N_{read}^2)}} \tag{4-13}$$

where S is the camera signal intensity [counts], C_{AD} is the analog to digital conversion constant [counts/e$^-$], N_{bin} is the number of binned pixels, N_{dark} is the detector dark current noise [e$^-$] and N_{read} is the detector read noise [e$^-$]. This formulation gives the SNR in terms of the measured camera signal. Other formulations can be derived knowing the relationship between the number of incident photons N_{pp} and the measured signal level:

$$S = \eta_{CCD} C_{AD} N_{pp} \tag{4-14}$$

where η_{CCD} is the CCD's quantum efficiency at the incident light wavelength. Eqn. (4-13) was used to calculate the SNR for the MicroMAX data once the Rayleigh scattering signal level was obtained after the appropriate corrections.

For an intensified camera such as the PI-MAX 4, the SNR is defined by [161,164]:

$$S/N = \frac{\mathrm{S}}{C_{AD}\sqrt{\frac{\kappa\eta_{CCD}GS}{C_{AD}} + N_{bin}(N_{dark}^2 + N_{read}^2)}} \tag{4-15}$$

where, G is the photonic gain and κ is the intensifier gain-dependent noise factor typically taken as 2 [165]. Again, this is formulated for calculating the SNR in terms of the measured camera signal. The relationship between N_{pp} and S is different for an intensified camera due to the intensifier that has a photocathode quantum efficiency η_{pc}, as shown in Eqn. (4-16).

$$S = \eta_{pc}\eta_{CCD}GC_{AD}N_{pp} \tag{4-16}$$

From Eqns. (4-13) and (4-15) it is trivial to calculate the *SNR* when the variables are known, but in the case of the intensified camera, knowing the actual photonic gain and gain-dependent noise factor is difficult. Instead, to calculate the *SNR*, a series of camera calibration tests were performed in which images were taken of a uniform intensity field. The variation of the measured camera signal was found over a small uniform region, and through repeated experiments was quantified as the noise. This methodology takes into account the read, dark current, shot and intensifier noise but is specific to the gain setting. 2x2 pixel binning was also included in the tests, as was done in the engine experiments. All of the PI-MAX4 experiments used the same gain for consistent results. With the signal-to-noise ratio now known for a given intensity, the product κG can be solved for using Eqn. (4-15).

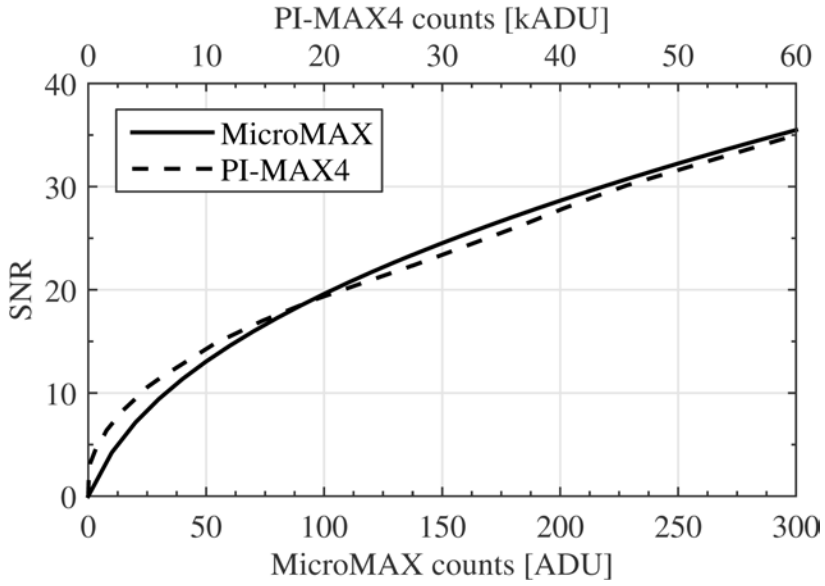

Figure 4-36: Signal-to-noise ratio of the MicroMAX and PI-MAX4 for collected signal levels.

Figure 4-36 shows the signal-to-noise ratio of the two cameras used during experimentation. The MicroMAX signal level range, which is 0-4095 (12 bit, see Table 3-4) was limited to 300 counts as that was the maximum corrected Rayleigh scattering signal achieved. The low signal levels were a result of the low in-cylinder pressure and the laser energy. The laser energy could have been increased, but window damaged was already an issue at the tested energy level of 50 mJ/pulse. The PI-MAX4 has a full range of 0-65535 counts and is shown up to 60000 in the top x-scale. For the fixed gain, the collected signal level was controlled by adjusting the f-stop until the full range was utilized without saturation. Rayleigh scattering signal levels for the PI-MAX4 testing were on the order of 10-40 kcounts. If the x scale was extended, it would be observed that the MicroMAX has superior signal-to-noise ratios, but at the collected low signal levels, the two cameras are comparable. This begs the question: why wasn't the PI-MAX4 used for all tests to avoid optical setup changes? It was originally assumed the PI-MAX4's resolution would be inferior to the MicroMAX since it required 2x2 pixel binning

which made the effective pixel area 15 times larger. In the end this was overcome by the use of the f/200 mm lens and 88 mm of tube extensions. The more potent reason, though, was that intensified cameras are sensitive to saturated signals in that it will damage the MCP in the intensifier. It was seen in the example images in Section 4.3 that particles and solid surface scattering resulted in saturated pixels and even charge bleeding. Extended use of the camera under those conditions would have caused damage; therefore the PI-MAX4 use was limited to the dual SI imaging.

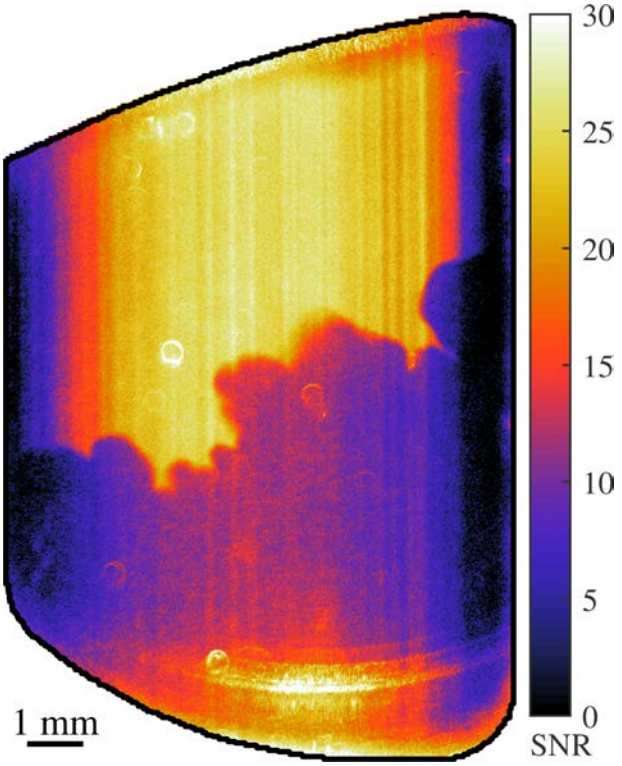

Figure 4-37: Signal-to-noise ratio of an SI image (Fig. 4-24).

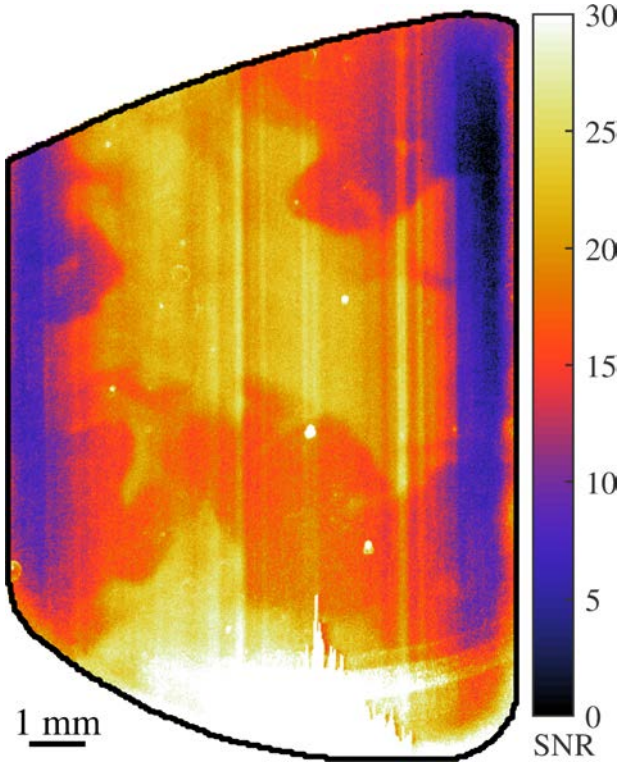

Figure 4-38: Signal-to-noise ratio of an HCCI image (Fig. 4-25).

Figures 4-37 and 4-38 are the signal-to-noise ratio for the Figs. 4-24 and 4-25. The corrected Rayleigh scattering signal was used because it is the desired signal. The reactants are seen to have a higher SNR because the Rayleigh scattering intensity is greater. The difference in

SNR between the SI and HCCI cases arises from the combination of the Rayleigh scattering intensity (temperature, pressure, etc.) and the image corrections applied. It is easy to see the non-uniform laser induced by the sheet forming optics in the SI image where the products in the middle have a greater SNR than the products on the edges.

4.6 Uncertainty Analysis

As with any experimental measurement, quantification of the uncertainty is required to objectively assess the statistical relevance of the results, and to definitively make conclusions. The equations used in the analyses that were presented in Section 4.4 are simple enough that the uncertainty was calculated analytically, as opposed to numerically through sensitivity analysis. The uncertainty of a result R due to measurement X_i is given by [163]:

$$\Delta R_{X_i} = \frac{\partial R}{\partial X_i} \Delta X_i \tag{4-17}$$

For results determined by several measurements (e.g. temperature via Rayleigh scattering), the total uncertainty of the result can be calculated from the individual measurement contributions using a root-sum-square method [166]. This equation assumes repeated measurements would fall into a Gaussian distribution, which is not true for optical measurements. Nevertheless Eqns. (4-17) and (4-18) were applied to the calculation equations.

$$\Delta R = \left[\sum_{i=1}^{N} \left(\frac{\partial R}{\partial X_i} \Delta X_i \right)^2 \right]^{1/2} \tag{4-18}$$

4.6.1 Temperature

The Rayleigh scattering thermometry equation was:

$$T = T_0 \frac{I_{R,0}}{I_R} \frac{\bar{\sigma}_R}{\bar{\sigma}_{R,0}}$$

The differential part of the scattering cross section term was removed to prevent confusion with the partial derivatives. Eqn. (4-18) was applied to the thermometry equation:

$$\Delta T = \left[\left(\frac{\partial T}{\partial T_0} \Delta T_0 \right)^2 + \left(\frac{\partial T}{\partial I_{R0}} \Delta I_{R0} \right)^2 + \left(\frac{\partial T}{\partial \bar{\sigma}_R} \Delta \bar{\sigma}_R \right)^2 + \left(\frac{\partial T}{\partial I_R} \Delta I_R \right)^2 + \left(\frac{\partial T}{\partial \bar{\sigma}_{\mathrm{R},0}} \Delta \bar{\sigma}_{\mathrm{R},0} \right)^2 \right]^{1/2} \tag{4-19}$$

$$\Delta T = \left[\left(\frac{I_{R,0}\bar{\sigma}_R}{I_R \bar{\sigma}_{\mathrm{R},0}} \Delta T_0 \right)^2 + \left(\frac{T_0 \bar{\sigma}_R}{I_R \bar{\sigma}_{\mathrm{R},0}} \Delta I_{R,0} \right)^2 + \left(\frac{T_0 I_{R,0}}{I_R \bar{\sigma}_{\mathrm{R},0}} \Delta \bar{\sigma}_R \right)^2 + \left(\frac{T_0 I_{R,0} \bar{\sigma}_R}{I_R \bar{\sigma}_{\mathrm{R},0}} \frac{\Delta I_R}{I_R} \right)^2 + \left(\frac{T_0 I_{R,0} \bar{\sigma}_R}{I_R \bar{\sigma}_{\mathrm{R},0}} \frac{\Delta \bar{\sigma}_{\mathrm{R},0}}{\bar{\sigma}_{\mathrm{R},0}} \right)^2 \right]^{1/2} \tag{4-20}$$

$$\Delta T = \mathrm{T} \left[\left(\frac{\Delta T_0}{T_0} \right)^2 + \left(\frac{\Delta I_{R,0}}{I_{R,0}} \right)^2 + \left(\frac{\Delta \bar{\sigma}_R}{\bar{\sigma}_R} \right)^2 + \left(\frac{\Delta I_R}{I_R} \right)^2 + \left(\frac{\Delta \bar{\sigma}_{\mathrm{R},0}}{\bar{\sigma}_{\mathrm{R},0}} \right)^2 \right]^{1/2} \tag{4-21}$$

Evaluating the partial derivatives yielded Eqn. (4-20) to calculate the temperature uncertainty. By factoring out the temperature, the uncertainty terms have a form of the inverse signal-to-noise ratio seen in Eqn. (4-21). The necessary quantities for the temperature uncertainty calculation are discussed in the following subsections. Figure 4-39 shows the temperature profiles from Fig. 4-32 plotted with their calculated uncertainties. The absolute uncertainty increases with temperature, which was foreshadowed by the signal-to-noise ratios in Figs. 4-37 and 4-38. The increasing temperature decreases the Rayleigh scattering signal, which in turn decreases the signal-to-noise ratio and increases the uncertainty. The uncertainty for the images is approximately 60 and 320 K in the reactants and products, respectively. This equates to relative uncertainties of 8 and 15%. The uncertainty from the scattering intensity (desired and

reference) account for 80% of the total uncertainty in the reactants and 90% in the products. Increasing the signal-to-noise ratio of the measurements would decrease the Rayleigh scattering contribution to the uncertainty, but this would require increased scattering intensity via increased laser energy or increased in-cylinder pressure. Increasing the laser energy would require redesigning the optical components to handle more laser energy, and increasing the pressure resulted in intense beam steering that made image processing unmanageable (see Fig. 4-23).

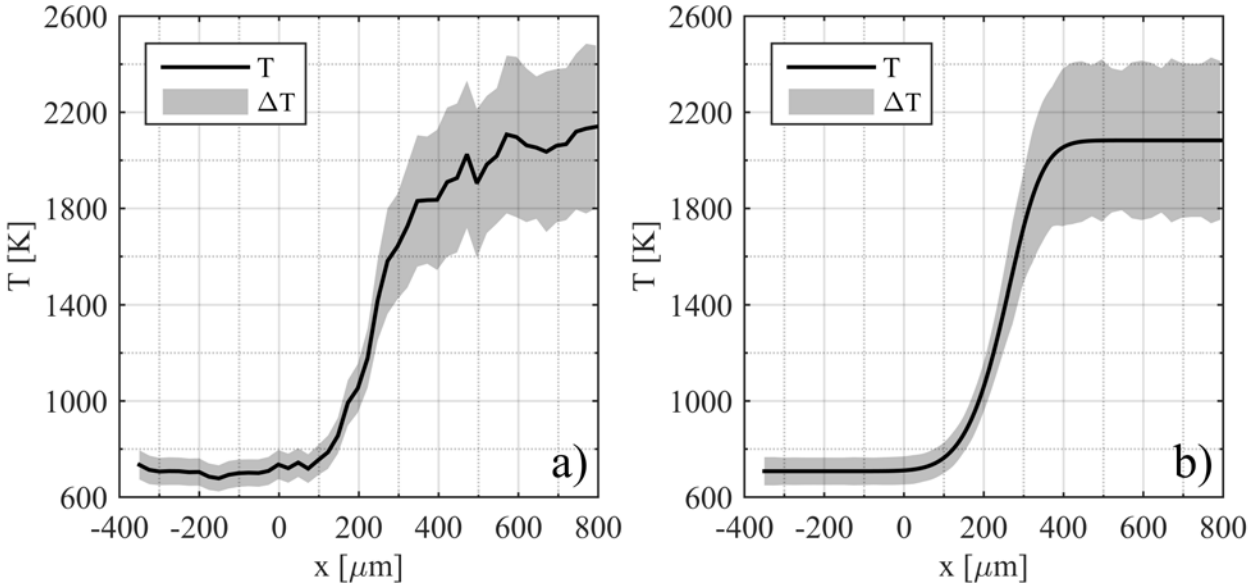

Figure 4-39: Raw (a) and fit (b) temperature plotted with its uncertainty for the profiles from Fig. 4-32. The measurement uncertainty is indicated by the shaded region.

4.6.1.1 Reference Temperature

The reference temperature was calculated from the isentropic relation given by Eqn. (4-22). The base state for the isentropic relation was taken as the bottom dead center crank angle where it is assumed the trapped mass, temperature and pressure are well characterized by the intake conditions. The mean specific heat (between the BDC and reference condition) was calculated iteratively with an error tolerance of 1e-5. Performing the system error calculation for the

reference temperature by applying Eqn. (4-18) to Eqn. (4-22) gives Eqn. (4-23) after simplification. Each term was assumed to have error.

$$T_0 = T_{BDC}\left(\frac{P_0}{P_{BDC}}\right)^{(\gamma-1)/\gamma} \tag{4-22}$$

$$\Delta T_0 = T_0\left[\left(\frac{\Delta T_{BDC}}{T_{BDC}}\right)^2 + \left(\frac{\gamma-1}{\gamma P_0}\Delta P_0\right)^2 + \left(\frac{1-\gamma}{\gamma P_{\mathrm{BDC}}}\Delta P_{BDC}\right)^2 + \left(\left[\frac{1}{\gamma} - \frac{\gamma-1}{\gamma^2}\right]\ln\frac{P_0}{P_{BDC}}\Delta\gamma\right)^2\right]^{1/2} \tag{4-23}$$

The intake temperature sensor is a high-accuracy thermistor with a specified 1 K tolerance. It has a narrow operating range such that its measurement resolution is 0.07 K, so its total uncertainty is 1 K. The intake pressure sensor calibration has a 3 kPa uncertainty. The Kistler 6053BB piezoelectric in-cylinder pressure transducer that measured the reference pressure has uncertainty that was modeled as a combination of the transducer itself, the Kistler 5010 charge amplifier and its deadweight calibration system. The transducer has a sensitivity shift of 0.5%, and the charge amplifier has an accuracy of 0.5%. The calibration system has an uncertainty of 0.1% of the measurement. Combining all three uncertainties gives a total reference pressure uncertainty of 0.7% of the measurement. The specific heat uncertainty was modeled through sensitivity analysis in which Eqn. (4-22) was evaluated with the aforementioned uncertainties added to T_{BDC}, P_0 and P_{BDC} to calculate the change in the γ [163]. Doing so for the range of tested conditions showed γ changed by 0.001 on average, which is approximately 0.07%. As an example of reference temperature, a specific spark-ignition cycle had an intake temperature of 313 K, intake pressure of 52 kPa and reference pressure of 1046 kPa. The average specific heat ratio is 1.382, and the resulting reference temperature and uncertainty is 718 ± 12 K. While the value is likely underestimated, the intake conditions were similar between the SI

and HCCI conditions such that the calculated isentropic temperatures were not vastly different. Therefore the calculated temperatures and gradients all scale similarly.

4.6.1.2 Differential Rayleigh Scattering Cross Section

Assigning an uncertainty to the cross section requires knowledge of the mixture distribution from cycle to cycle or even within cylinder. Because the air and fuel were mixed upstream, cycle-to-cycle variations in the delivered mixture are not expected to exist. In-cylinder mixture gradients also did not occur due to the premixing. Instead, the uncertainty in the delivered mixture scattering cross section was charged to the accuracy of the pressure gauges used to regulate the air and fuel through their respective choked flow orifices. The air delivery system used a pressure gauge with 0.2 psia accuracy which is a relative error of 1.4-3.5% depending on the operating condition. The fuel pressure gauge had an accuracy of 0.5 psia; the relative error for SI operation was 1.0-1.6% and 1.5% for HCCI. These values were used in a sensitivity study to assess the impact of the uncertainty of the delivered air and fuel on the reference and reactants' mixture scattering cross section. The reference mixture cross section uncertainty was 0.3-0.6% for SI and 0.2% for HCCI; the HCCI value is reported using the reference condition definition of the post-LTO mixture. These errors propagated to a product uncertainty of 0.06-0.1% for SI and 0.1% for DME. It is observed the combustion mitigated the effects of the reactants' uncertainty.

A couple additional uncertainties were added to these values. For SI experiments, it was shown in Section 4.2.2.1 the ignition delay simulations have an error of 1.1% when predicting the product cross section ratio compared to the flame propagation simulations. This equates to an additional error of 0.7% for the products' cross section, which was added in quadrature to the previously reported value. Additional error was included in the HCCI reactants to account for the

difference in the ignition delay and flame propagation simulations. Referring to Fig. 4-20, the post-LTO cross section ratio is different for the two simulations. Because the propagation mechanism was unknown, the reactants cross section could have been either mixture. The difference is 2.5% of the reference cross section. Furthermore, it is seen that there is a slow decomposition of the fuel before the main combustion event. The cross section ratio decreases by approximately 2%, so the 2.5% uncertainty covers this uncertainty as well and was added in square with the previous 0.2% uncertainty. The final cross section uncertainties used are presented in Table 4-3. The cross section uncertainties were linearly interpolated between the reactants and products through the combustion front just like the cross section themselves.

Table 4-3: Relative uncertainties of the reactant (reference condition) and product cross sections.

Mode	$\Delta\bar{\sigma}_0$ [%]	$\Delta\bar{\sigma}_P$ [%]
SI	0.3-0.6	0.7
HCCI	2.5	0.1

4.6.1.3 Rayleigh Scattering Intensity

The equation used to determine the Rayleigh scattering intensity was (Eqn. (4-3)):

$$I_R = (I_{raw} - I_{DC}) - \left(I_{raw,flare} - I_{DC}\right)$$

where I_{raw} is the combustion image intensity, either from the reactants or products, I_{DC} is the dark current and read noise signal and $I_{raw,flare}$ is the flare correction intensity taken from outside the laser sheet in the image. The dark current term contains the camera bias level such that the flare and raw image were also bias corrected when dark-current corrected. The uncertainty of the corrected intensity is determined by the root-sum-square method:

$$\delta I_R = \sqrt{(\delta I_{raw}^2 + \delta I_{DC}^2) + \left(\delta I_{raw,flare}^2 + \delta I_{DC}^2\right)} \quad (4\text{-}24)$$

The uncertainty of the image and its corresponding flare were determined by the shot, read and dark current noise, as given by the denominator of Eqn. (4-13):

$$\Delta I_{Raw} = C_{AD}\sqrt{\frac{S}{C_{AD}} + N_{bin}(N_{dark}^2 + N_{read}^2)} \tag{4-25}$$

Again, all units are in the camera signal counts. Eqn. (4-25) is for the non-intensified MicroMAX camera, and Eqn. (4-26) is for the intensified PI-MAX4.

$$\Delta I_{Raw} = C_{AD}\sqrt{\frac{\kappa\eta_{CCD}GS}{C_{AD}} + N_{bin}(N_{dark}^2 + N_{read}^2)} \tag{4-26}$$

When evaluating the uncertainty of the Rayleigh scattering signal (or flare), the total measured signal minus the camera bias was used: $S = I_{raw} - bias$. This is because the shot noise is linked to the measured signal, not the corrected signal level. This means that for a constant Rayleigh scattering intensity, as the magnitude of the flare correction increases so does the uncertainty in the Rayleigh intensity because the measured signal level increases which results in greater shot of the image (ΔI_{raw}) but also of the flare correction $\Delta I_{raw,flare}$. Therefore even if the background scatter can be completely accounted for, it is necessary to minimize the background scatter to minimize the two-fold effect. Since the error function fit data were derived from the intensity ratio in Section 4.4.3, there was not a measured camera signal associated with it. To calculate the uncertainty of the Rayleigh scattering signal, the raw intensities were linearly interpolated. Consequently the temperature uncertainty for the raw and fit temperatures is nearly identical except for small differences that arise from the scattering cross section interpolation because of the noise in the raw profiles.

4.6.2 Temperature Gradient

Because the error function in Eqn. (4-5) was used to fit the intensity profile, the calculated fit parameter Λ also describes the temperature distribution. Per Wang and Clemens [145], when the error function fit is used the relative uncertainty in the peak derivative is:

$$\frac{\Delta(\nabla T_{max})}{\nabla T_{max}} = 1 - 1/\sqrt{1 + \frac{2\sigma^2}{\Lambda^2 - \sigma^2}} \tag{4-27}$$

where σ is the standard deviation of derivative of the line spread function, which was previously determined in Section 3.3.5.1 and given in Table 3-5. As lambda is decreased towards the system resolution limit, the relative resolution error increases because the structures cannot be resolved. Λ typically ranged from 100-250 μm for the spark ignition experiments, so with the MicroMAX setup where σ = 32.1 μm, the relative temperature gradient error was 1.6-9.8%, with the smaller Λ having the greater error. For temperature gradient of Fig. 4-32 was calculated to be 7.2 ± 0.5 K/μm.

4.6.3 Combustion Front Thickness

The equations used to calculate the combustion front thickness via the density are repeated here.

$$\delta_\rho = \frac{\rho_R - \rho_P}{\nabla \rho_{max}}$$

$$\rho = \frac{P_0 \bar{M}}{R T_0} \frac{I_R}{I_{R,0}} \frac{\partial \bar{\sigma}_{R,0}}{\partial \bar{\sigma}_R}$$

The equation for the uncertainty of the density-based front thickness was derived to be:

$$\Delta\delta_\rho = \sqrt{\left(\frac{\Delta\rho_R}{\nabla\rho_{max}}\right)^2 + \left(\frac{\Delta\rho_P}{\nabla\rho_{max}}\right)^2 + \left(\frac{\rho_P - \rho_R}{\nabla\rho_{max}^2}\Delta[\nabla\rho_{max}]\right)^2} \tag{4-28}$$

where the uncertainty of the density is given in Eqn. (4-29). The universal gas constant is certain to the 7th decimal place, so its uncertainty was omitted. The peak density gradient uncertainty was calculated via Eqn. (4-27). The only new term compared to the temperature uncertainty is the mixture molecular weight. The same simulations that were used for the scattering cross section sensitivity analysis were used to analyze the molecular weight uncertainty (see Section 4.6.1.2). Because the molecular weight changes considerably less than the scattering cross section (see Fig. 4-34), the analyses yielded minimal uncertainties. From the uncertainty in the air and fuel delivery systems, both the SI and HCCI gave uncertainties less than 0.1%, so baseline uncertainty of 0.1% was used. The additional uncertainty in the products' molecular weight for SI due to using ignition delay simulations as opposed to flame propagation simulations was 0.8%. For HCCI a post-LTO mixture uncertainty of 0.5% covered the slow decomposition before the main combustion event and the difference in the flame propagation simulation post-LTO mixture. The final values are tabulated in Table 4-4. Again, the uncertainty was interpolated between the reactants and products. The temperature-based combustion front thickness uncertainty was calculated by substituting density for temperature in Eqn. (4-28).

$$\Delta\rho = \rho\left[\begin{array}{c}\left(\frac{\Delta P_0}{P_0}\right)^2 + \left(\frac{\Delta\bar{M}}{\bar{M}}\right)^2 + \left(\frac{\Delta I_R}{I_R}\right)^2 + \left(\frac{\Delta\bar{\sigma}_{\mathrm{R},0}}{\bar{\sigma}_{\mathrm{R},0}}\right)^2 \\ + \left(\frac{\Delta T_0}{T_0}\right)^2 + \left(\frac{\Delta I_{R,0}}{I_{R,0}}\right)^2 + \left(\frac{\Delta\bar{\sigma}_R}{\bar{\sigma}_R}\right)^2\end{array}\right]^{1/2} \tag{4-29}$$

Table 4-4: Relative uncertainties of the reactant (reference condition) and product molecular weights.

Mode	$\Delta\bar{M}_0$ [%]	$\Delta\bar{M}_P$ [%]
SI	0.1	0.8
HCCI	0.6	0.1

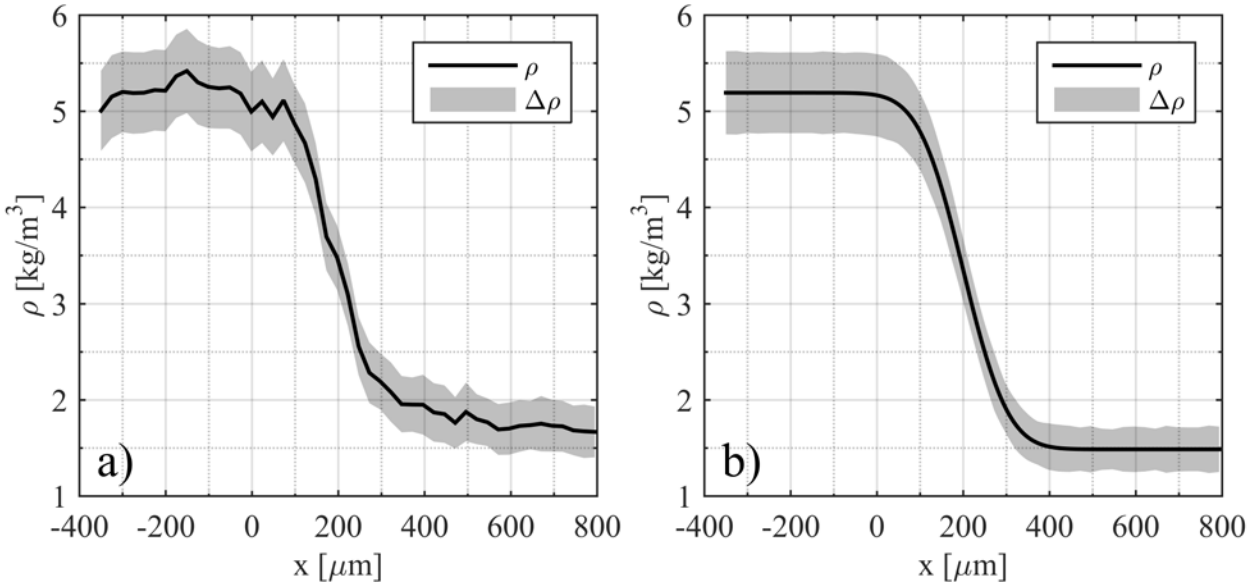

Figure 4-40: Raw (a) and fit (b) density plotted with its uncertainty for the data in Fig. 4-32. The measurement uncertainty is indicated by the shaded region.

Density profiles through the combustion front were calculated for the example SI temperature profiles and are shown in Fig. 4-40. The reactants' uncertainty has a greater absolute value of approximately 0.4 kg/m^3 compared to 0.25 kg/m^3 for the products, but the relative uncertainty is 8 and 15% for the reactants and products, respectively. Comparing the temperature and density equations, the Rayleigh scattering intensity, reference temperature, and scattering cross sections are common to both meaning the temperature and density interpretations have nearly identical uncertainties. The combustion front thickness calculation of the example profile yields a density-based calculation of 205 ± 31 μm (15% uncertainty), whereas it is 190 ± 48 μm (26% uncertainty) for the temperature-based calculation. These trends were typical where the

temperature-based calculation was smaller and had greater relative and absolute uncertainties than the density-based thickness.

4.6.4 Combustion Speed

The uncertainty in the combustion speed calculation is a function of the relative movement, the optical resolution and the time separation. Eqn. (4-30) is the expanded form of the calculated combustion speed. The position vectors are represented by their change in each component given by the subscripts i and j. The initial position of the combustion front contour and tracked particles were treated as exact numbers. Therefore the uncertainty lies in the chosen position of the displaced contour and particles. From visual inspection during the tracking process and by matching the intensity along the contour, the uncertainty was set to ±1 pixel, which was applied to each of the terms. The laser separation time was controlled with a pulse generator that has one nanosecond resolution. The laser duration was approximately seven nanoseconds. When adding the two uncertainties, the uncertainty relative to the shortest separation time of 30 μs was 0.02%, thus the separation time was taken without error. Performing the analysis for the tracked contour presented in Fig. 4-35, the combustion speed was 269 ± 5 cm/s, which is 1.8% uncertainty. Given the assumption that the flow field velocity was represented by the particle tracking and the amount of flow-field velocity correction required to calculate the combustion speed, the calculated uncertainty values were dwarfed in comparison and are considered unreliable.

$$u_{CP} = \frac{\sqrt{\left[dr_{CF,i} - dr_{FF,i}\right]^2 + \left[dr_{CF,j} - dr_{FF,j}\right]^2}}{dt} \tag{4-30}$$

$$\Delta u_{CP} = \frac{1}{u_{CP} dt^2}\Big[\left(dr_{CF,i} - dr_{FF,i}\right)^2 \Delta dr_{CF,i}^2 + \left(dr_{FF,i} - dr_{CF,i}\right)^2 \Delta dr_{FF,i}^2 + \left(dr_{CF,j} - dr_{FF,j}\right)^2 \Delta dr_{CF,j}^2 + \left(dr_{FF,j} - dr_{CF,j}\right)^2 \Delta dr_{FF,j}^2\Big]^{1/2} \quad (4\text{-}31)$$

Chapter 5 - Results

In this chapter, the engine operating conditions and heat release parameters are presented. Comparisons between the single and dual imaging set are performed. The spark-ignition tests are analyzed to assess the abilities of the measurement system to in terms of capturing known physical trends. Finally, the temperature, temperature gradient, combustion front thickness and combustion speed are presented and used in the determination of the combustion propagation mechanism.

5.1 Operating Conditions

Three spark-ignition operating conditions were tested to measure the effect on the flame propagation properties. Table 5-1 lists the operating conditions and combustion parameters for each condition. For the given fuels, the controllable variables known to affect flame propagation are temperature, pressure, and the equivalence ratio. The nominal case was a low load condition based on previous experiments. Because the combustion duration ($CA_{10\text{-}90}$) occurred within 10 crank angle degrees for the nominal SI case, the temperature aspect was not tested as it would have further decreased the combustion duration. (The rapid combustion proved to be an issue with the combustion speed measurements.) Therefore, the first variable tested was pressure. The second case used the same operating conditions as the nominal, but the indicated mean effective pressure (IMEP) was decreased to decrease the pressure at the image timing. The last SI case tested equivalence ratio effects via lean operation while maintaining the pressure at image timing. Comparison of these cases tested the measurement technique’s ability to discern the effects of variable inputs on flame propagation.

In terms of combustion matching for engine conditions, the IMEP and crank angle of 50% cumulative heat release (CA_{50}) are typically used to align conditions. In this study, matching the thermodynamic conditions at image timing was the most important factor resulting in the IMEP and CA_{50} not being perfectly matched. This is apparent when comparing the HCCI operating condition where the load was less than half of the nominal SI case. Owing to the low compression ratio and high heat transfer rate of the engine, HCCI was a difficult combustion mode to operate. Only a few operating points worked in the engine, and the presented case was the only one with an image timing pressure matching the nominal SI case. The differing loads and CA_{50} timings are not a detriment, though, because the study is concerned with the propagation mechanism, which is a local event dependent on the thermodynamics and fuel fraction not a global one based on the total fueling or engine crank angle.

Table 5-1: SI and HCCI engine operating conditions and nominal combustion parameters.

	Nominal SI	Low-pressure SI	Lean SI	HCCI
IMEP [bar]	5.3	3.8	4.6	2.2
CA_{50} [^{o}aTDC]	6.9	5.2	5.6	6.0
$CA_{10\text{-}90}$ [deg]	9.4	9.5	12.5	4.9
Φ	1.03	1.03	0.82	0.60
Intake pressure [kPa]	62	46	61	48
Intake temperature [^{o}C]	40	40	40	68
Spark timing [^{o}aTDC]	-10.4	-12.9	-15.4	-
Fuel/ mass [mg]	Ethylene/ 11.8	Ethylene/ 7.7	Ethylene/ 9.4	DME/ 10.5
Image timing [^{o}aTDC]	-0.5	-1.5	-1.75	4.0
Image pressure [bar]	10.7	8.3	11.3	11.5
Image temperature [K]	710	715	720	785
Image cumulative heat released [%]	4.5	7.2	8.5	22.0

A quick analysis of the data summary shown in Table 5-1 gives some initial insights to the results. Comparing the nominal and low pressure case, it is seen the combustion duration was the same, suggesting the flame speed was the same. This means the decreased pressure, albeit 22%, had a weak effect if any on the flame propagation. For the lean condition, though, the combustion duration increased by 33% suggesting the flame speed was considerably slower. This agrees with the flame propagation simulations in Section 4.1.3 as well as flame speed correlations [3]. This is reinforced by the spark timings, where the leaner case required an earlier timing to achieve a similar CA_{50}. Applying this reasoning to the HCCI experiments leads to the traditional thought that flame propagation does not exist as the combustion occurs twice as fast as the nominal SI case ($CA_{10\text{-}90}$ was one half), or historically four times as fast as SI $CA_{10\text{-}90}$ is typically on the order of 20 crank angle degrees [3]. It is unclear, though, whether or not flame propagation could be originating from multiple sites versus the single source like SI, which was the purpose of the study.

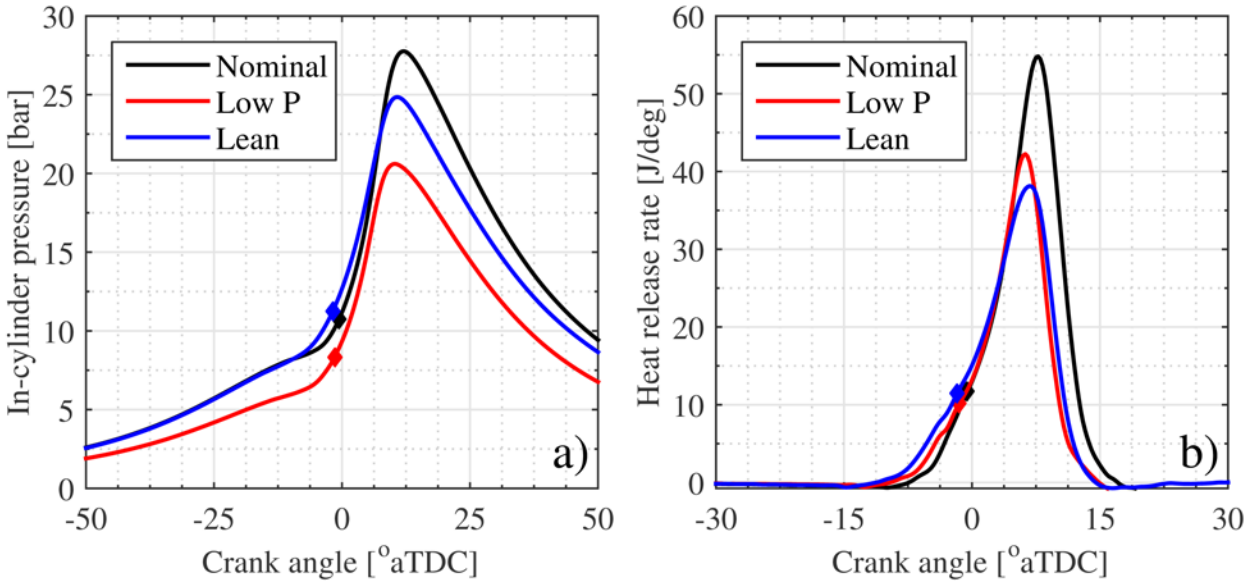

Figure 5-1: Pressure (a) and rate of heat release (b) plots of the three spark-ignition cases. The markers indicate the image timing.

Figure 5-1 shows the in-cylinder pressure and rate of heat release for the three SI cases. In accordance with the spark timings in Table 5-1, the lean case had the earliest heat release followed by the low pressure case. At the image timing, indicated by the diamond markers, the three conditions had similar rates of heat release. This was not by chance because the flame propagation heat release rate is proportional to the flame's surface area:

$$\dot{q} = \rho_R A S_L \Delta H \tag{5-1}$$

where $\dot{q}$ is the heat release rate [J/s], ρ_R is the density of the reactants [kg/m^3], A is the flame surface area [m^2], S_L is the laminar flame speed [m/s] and ΔH is the (lower) heating value [J/kg]. There were moderate differences in the unburned gas density and flame speed between the cases, but because a small, fixed imaging area was used, the total flame surface area was approximately equal for all cases.

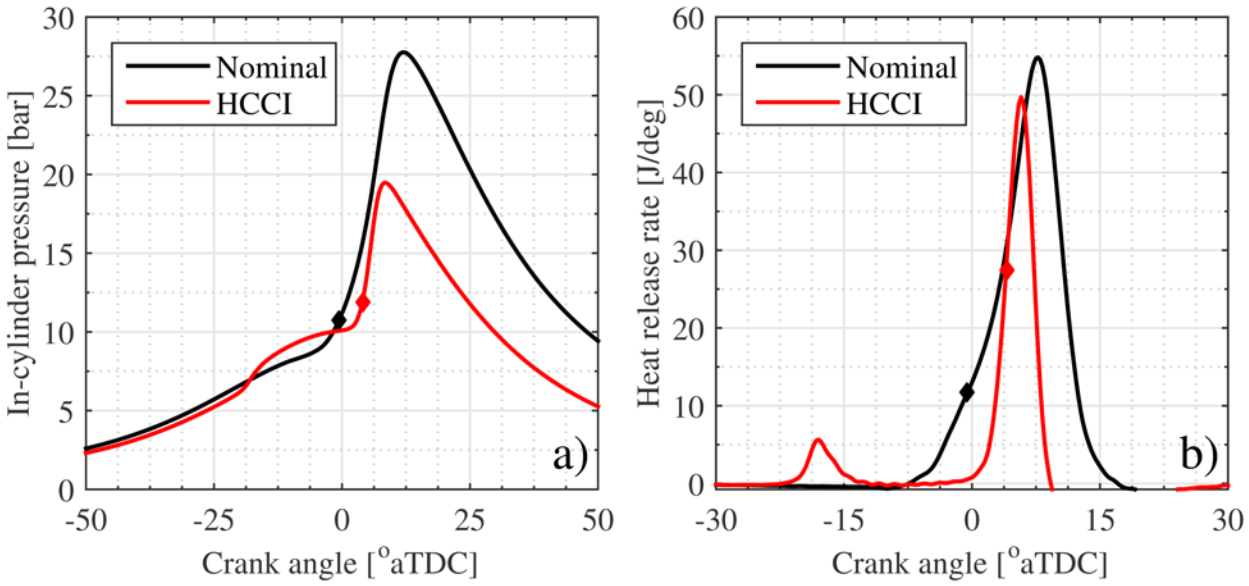

Figure 5-2: Comparison of the nominal SI and HCCI pressure (a) and rate of heat release (b). The markers indicate the image timing.

Figure 5-2 compares the pressure and heat release rate of the nominal SI case to the HCCI. The low-temperature oxidation is clearly seen in both the pressure and heat release traces

for HCCI. Although the nominal SI and HCCI fueling rates were comparable, the total amount of heat release (given by the area under the rate of heat release curve) was much smaller for HCCI. This resulted from the fuel-bound oxygen in DME giving a lower heating value of 28.9 MJ/kg compared to 47.2 MJ/kg for ethylene. The rate of heat release at the HCCI image timing was twice that of the SI, but the presented value is averaged across all images. Because of the rapid increase in heat release for HCCI combustion, the cumulative heat release at image timing on a cycle-by-cycle basis was quite variable compared to SI.

Figure 5-3 compares the probability density functions of the cumulative heat release percent at image timing for all cases. It is seen the SI cases had less variability and earlier cumulative heat release fractions than the HCCI experiments. The small range of SI image timings was a result of the flame progressing linearly converse to the stochastic autoignition sites of HCCI. Image timings were determined by timing sweeps to know when, on average, the combustion front was in the field of view. The low-pressure and lean SI experiments had greater cumulative heat release due to earlier spark timing (see Fig. 5-1b). The variability of the SI thermodynamic conditions at image timing was reduced by the earlier cumulative heat release timings, giving more results at consistent conditions. The wider range of cumulative heat release for the HCCI experiments meant the conditions were more varied at image timing. The standard deviation of the distribution of the in-cylinder pressure at image timing was 90 kPa for all HCCI images, where as it was 40 kPa for the nominal SI images. The greater variability also meant the combustion was easily missed in the imaging area resulting in less efficient data collection.

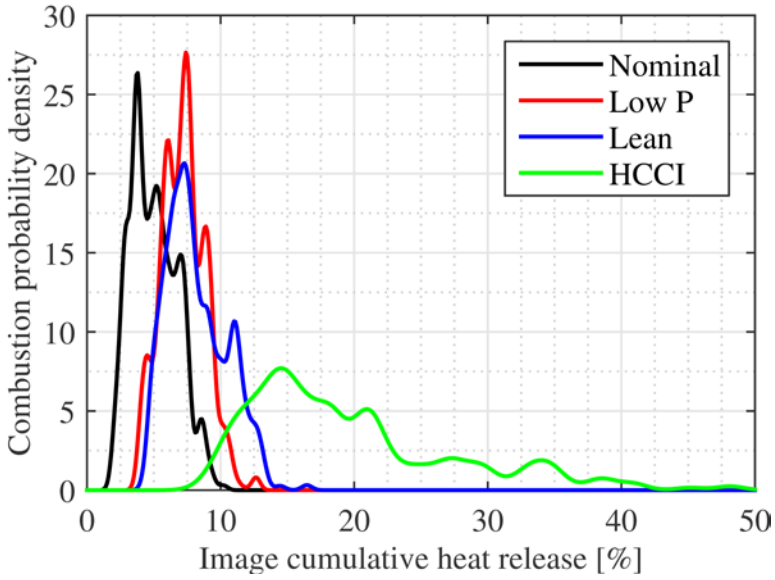

Figure 5-3: Probability density of the cumulative heat release percent at image timing for the processed images.

5.2 Imaging Summary

For each of the four combustion cases presented in Table 5-1 two sets of images were taken: a higher signal-to-noise ratio single images, and dual images. The single images were performed by operating the dual-headed laser with a 500 ns inter-laser separation time. Based on the measured combustion speeds, the combustion fronts moved approximately 0.1 pixels during this time which was sufficiently small to ignore any movement. A smaller separation time could have been used but with increased risk of damaging the laser-access windows more quickly. By combining both laser pulses for a single image the Rayleigh scattering intensity was increased which in turn increased the SNR. Since combustion speed measurements were not simultaneously performed, the single HCCI images were used with Eqn. (2-2) to calculate the combustion speed to compare to the SI data and test the robustness of the classification metric. The dual images were used to link specific temperature profiles and gradients with measured combustion speeds.

5.2.1 Image Collection Statistics

Table 5-2 summarizes the number of images, detected contours and temperature profiles collected for the four operating modes. Each image taken was first checked for combustion, and if combustion existed, it was analyzed for detectable contours. The *Images with contours* row represents the number of images in which contours were extracted. For the dual imaging, the identified contours were tracked in the successive image. Contours that failed the tracking guidelines presented in Section 4.4.5 were discarded, hence *Images with trackable contours* is less than *Images with contours*. The same applies to *Contours* and *Trackable contours*. The dual image contours that were initially identified were ones that the contour was trackable and did not change shape, so the ones that failed the tracking were due to a lack of particles or inconsistency in the particle movement relative to the combustion front. The *Profiles* row is the total count of the temperature profiles from all usable contours. The overall image success rate, i.e. the number of images that yielded usable temperature profiles divided by the total number of taken images is given in the last row. The stochastic nature of HCCI resulted in a lot of images not having a combustion front, hence the low success rate. With a large number of calculated temperature profiles from different engine cycles, a good representation of the combustion distribution was obtained. The density distributions of the measurements are presented in Section 5.2.3.

Table 5-2: Image statistics summary listing the number of collected images, identified combustion front contours and calculated temperature profiles.

	SI - nominal		SI - low pressure		SI - lean		HCCI	
	Single	Dual	Single	Dual	Single	Dual	Single	Dual
Total images	450	250	250	150	200	150	560	1280
Images with contours	139	107	131	50	101	59	70	107
Images with trackable contours	-	87	-	48	-	45	-	90
Contours	208	210	162	69	123	93	194	185
Trackable contours	-	148	-	60	-	57	-	156
Profiles	9416	5160	6312	1820	4794	1725	6181	4952
Success rate [%]	31	35	52	32	51	30	13	7

5.2.2 Single vs. Dual Imaging Uncertainty

Since the dual image data could also fulfill the role of the single image data, the uncertainties of each measurement are examined. Because the single images used two laser pulses to increase the Rayleigh scattering intensity, higher signal-to-noise ratios and less uncertainty were achieved. Figure 5-4a) shows well-matched HCCI error function temperature profiles from single and dual imaging data sets with their relative uncertainties in Fig. 5-4b). The dual image uncertainty is approximately 55% higher for the presented profiles. Owing to the nonlinearity of the temperature uncertainty Eqn. (4-21) and the shot noise, the uncertainty did not halve by doubling the laser energy for the single images. With greater uncertainty in the dual images, more care had to be taken with the data analysis.

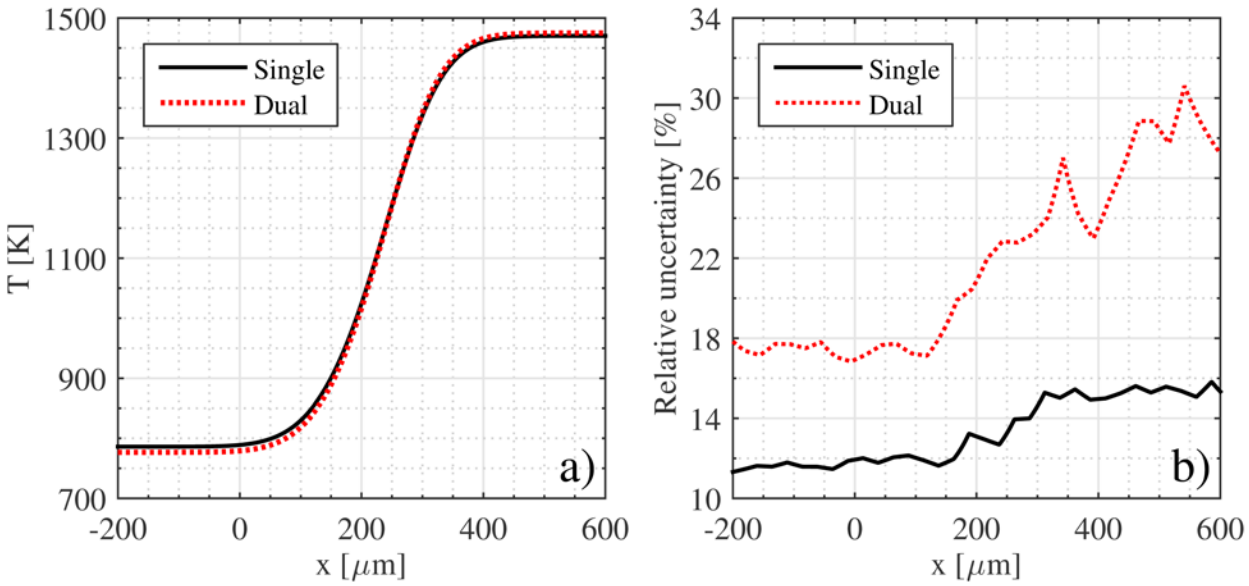

Figure 5-4: Comparison of single and dual image HCCI temperature profiles (a) and their relative uncertainties (b).

Figure 5-5a) compares two nearly identical temperature profiles from single and dual image SI data sets; Fig. 5-5b) shows their respective relative uncertainties. It is seen there is not much difference in the uncertainties of the single and dual image temperatures even though half the laser energy was used in the dual image. This was because the dual image SI data was taken with the PI-MAX4 camera for which the gain and aperture was set to maximize the measured signal. This yielded a higher SNR than the dual MicroMAX images, allowing for less uncertainty. Because the dual imaging HCCI data were taken with the MicroMAX it did not have the benefit of increasing the SNR that was achieved by binning the PI-MAX4 camera.

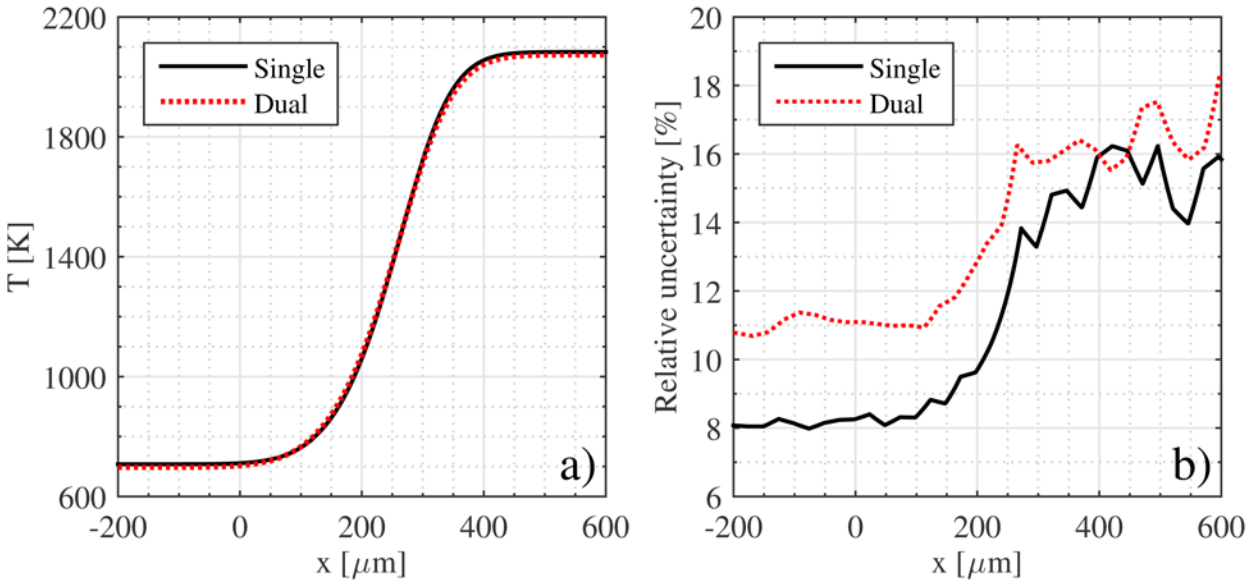

Figure 5-5: Comparison of single and dual image SI temperature profiles (a) and their relative uncertainties (b).

5.2.3 Combustion Distributions

Table 5-2 showed that a large amount of data was collected; in order to effectively display the data, distributions were made of the relevant parameters such as the temperature gradient and the combustion front thickness. Kernel density estimations were used to make probability density functions because the non-parametric model avoids making assumptions about the data that parametric distributions require. Figure 5-6 shows the kernel density estimations of the density-based combustion front thickness, temperature gradient and product temperature for the single-image nominal SI case; Figure 5-7 gives the respective distributions for the single-image HCCI data. By quick comparison, it is seen the SI temperature gradients and temperatures are greater than for HCCI, but the combustion front thicknesses show similar values. This is confirmed by the mean values presented in Table 5-3; one standard deviation of the mean is provided if one were to assume Gaussian distributions, which does not appear to be the case for the temperature gradient and combustion front thickness.

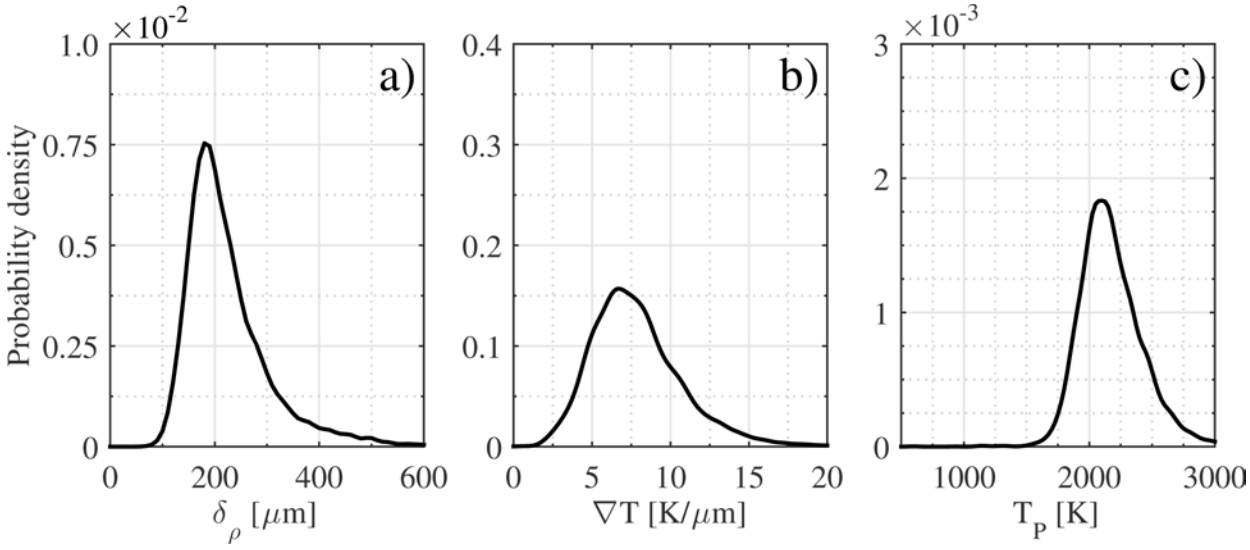

Figure 5-6: Single-image nominal SI density-based combustion front thickness (a), temperature gradient (b) and product temperature (c) kernel density distributions.

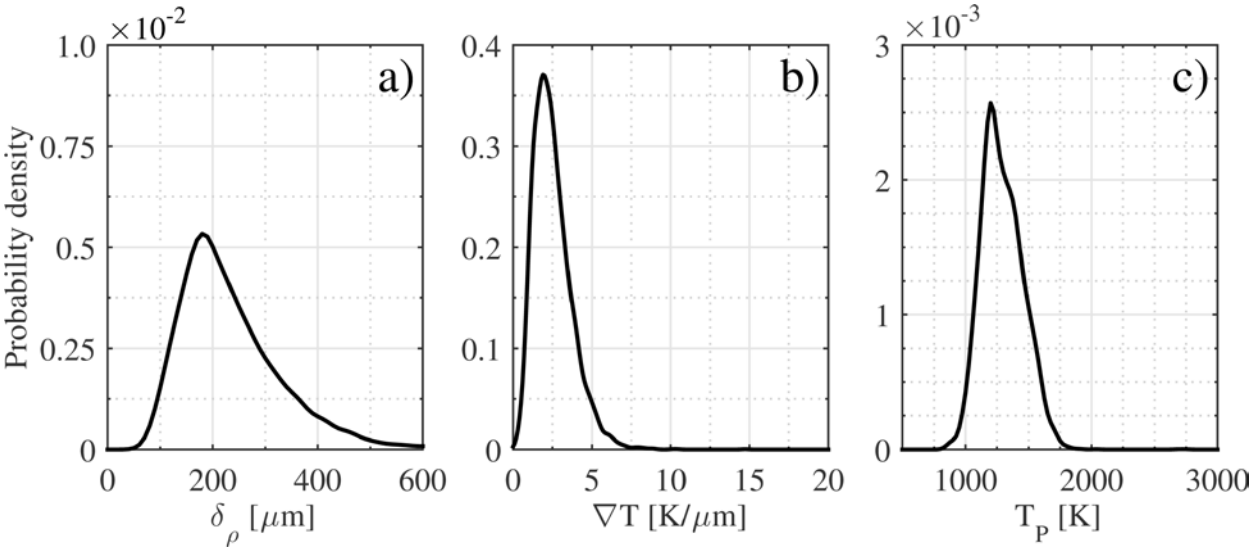

Figure 5-7: Single-image HCCI density-based combustion front thickness (a), temperature gradient (b) and product temperature (c) kernel density distributions.

Table 5-3: Mean value ± 1σ for the temperature gradient, product temperature and density-based combustion front thickness for single-image nominal SI and HCCI data.

	∇T [K/μm]	T_P [K]	δρ [μm]
SI	7.9 ± 2.9	2180 ± 265	227 ± 88
HCCI	2.5 ± 1.3	1290 ± 165	236 ± 102

The general shapes of the distributions give insight to the phenomena occurring during combustion. It is reasonable to expect that there is a minimum combustion front thickness for a given set of fueling and reactant thermodynamic conditions; therefore, when the same condition is continually repeated, as in the study, a minimal thickness would be clearly established. This is visualized as a right-skewed distribution which can be achieved by a Poisson or lognormal distribution. This behavior was captured by the SI and HCCI thickness distributions, where they both have a sharp probability decrease towards a minimum but a right-hand tail. The tail is indicative of combustion fronts that are oblique to the laser plane. It is seen the temperature gradient distributions have similar characteristics, albeit contrary to expectations. Because the thickness reaches a minimum and the combustion products temperature should be consistent, the temperature gradient would reach a maximum and tail off to a minimum as the thickness is increased. This deviation from the expectation is a result of the combustion temperature T_P. It is seen there is a large amount of variability in the post-combustion temperature distributions, which should not be the case given the same fueling and reactant thermodynamic conditions. Because the temperature profiles across the combustion front span a small spatial range, the combustion temperature experienced negligible radiative and convective heat transfer losses such that it can be modeled as adiabatic. Figure 5-8a) shows the calculated constant-pressure adiabatic flame temperature for the thermodynamic conditions at the image timing, which is, indeed,

almost single valued. Figure 5-8b) shows the combustion temperature distributions from Figs. 5-6 and 5-7 normalized by their respective adiabatic flame temperatures. Although some of the SI combustion temperatures reach, and sometimes surpass, the adiabatic flame temperature, the clear majority do not; the HCCI temperatures rarely reached the adiabatic value. Before any more analyses or conclusions can be made, the temperature magnitude needs to be addressed to determine if it was acceptable, or if there were issues with the measurement technique.

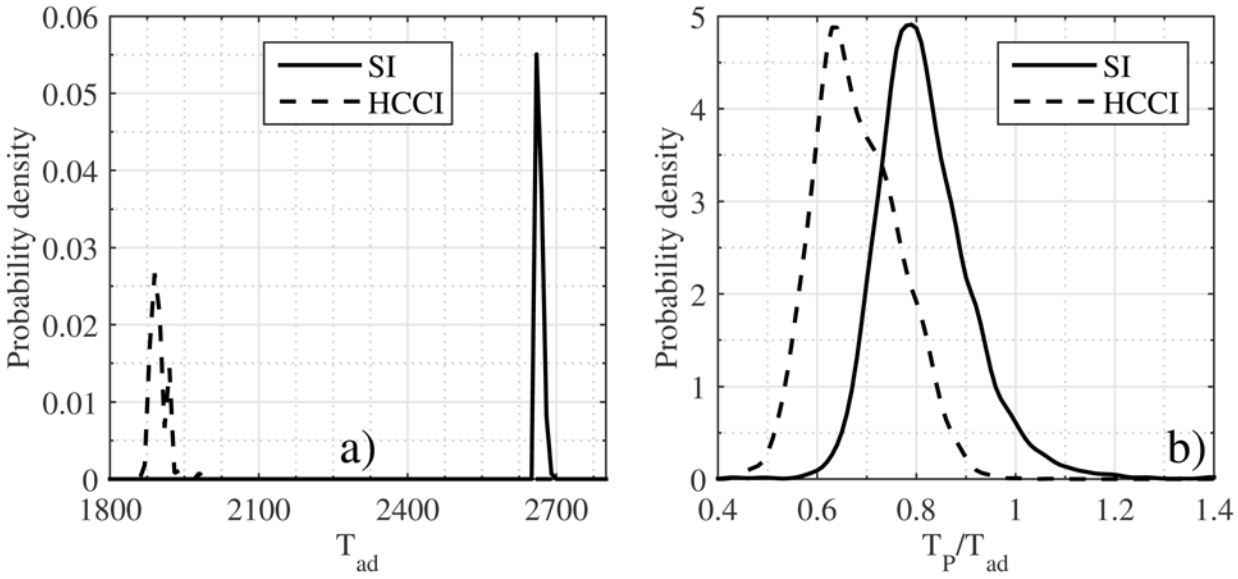

Figure 5-8: Constant pressure adiabatic flame temperature (a) and product to adiabatic flame temperature ratio (b) of the single-image nominal SI and HCCI cases.

5.2.4 Combustion Temperature Analysis

The thermometry equation is dependent on three variables: the reference temperature, the Rayleigh scattering cross section ratio and the Rayleigh scattering intensity ratio. If the reference temperature were wrong, the product temperature distribution would shift accordingly; however, the adiabatic flame temperature would also change. Therefore, the product temperature would still not reach the adiabatic flame temperature. The scattering cross section was believed to be reasonably well known since it was shown in Section 4.2.2 that the cross section ratio was highly

dependent on the reactant composition. The uncertainties associated with the reactant mixture due to the inlet air and fuel metering and consequential combustion were low (see Section 4.6.1.2). Therefore, intensity ratio is expected to be the largest contributor to the product temperature determination. As discussed in Section 4.3.6, not subtracting the flare signal under-calculates the temperature as the intensity ratio is decreased. The images were flare corrected using the intensity outside the laser sheet in the data images (see Section 4.3.6). The static background images and raw combustion images did not reveal any detrimental scattering structures. Nevertheless the effects of the flare correction were assessed.

Tests were performed by varying the amount of flare subtracted from the Rayleigh scattering image. By changing the amount of flare correction, the $I_R/I_{R,0}$ ratio shown in Fig. 4-29 changes in the products. That is, with less flare correction the products ratio increases thereby decreasing the product temperature, and vice versa. For the analysis the single-image nominal SI and HCCI profiles shown in Figs. 5-4a) and 5-5a) were used. Figure 5-9 shows the error function fit parameter, Λ, as a function of the additional flare fraction. Negative additional flare signifies less flare correction was used, such that at -1 no flare correction was performed. Zero additional flare is the value at which the data were analyzed, and an additional correction of 1 is doubling the flare correction. For all presented images in this analysis, image a) is the nominal SI case and image b) is HCCI, and the calculation's uncertainty is shown by the shaded area. From Fig. 5-9 it is seen that the fit parameter does not vary with the flare correction. This was not unexpected since the fit was performed with the intensity ratio normalized from zero to one (see Fig. 3-15), thus negating the intensity ratio shift. The important feature, though, is that the characteristic width established by the intensity change remained the same such that

widening or narrowing of the combustion front, indicated by the intensity, was not observed to be biased by the flare correction.

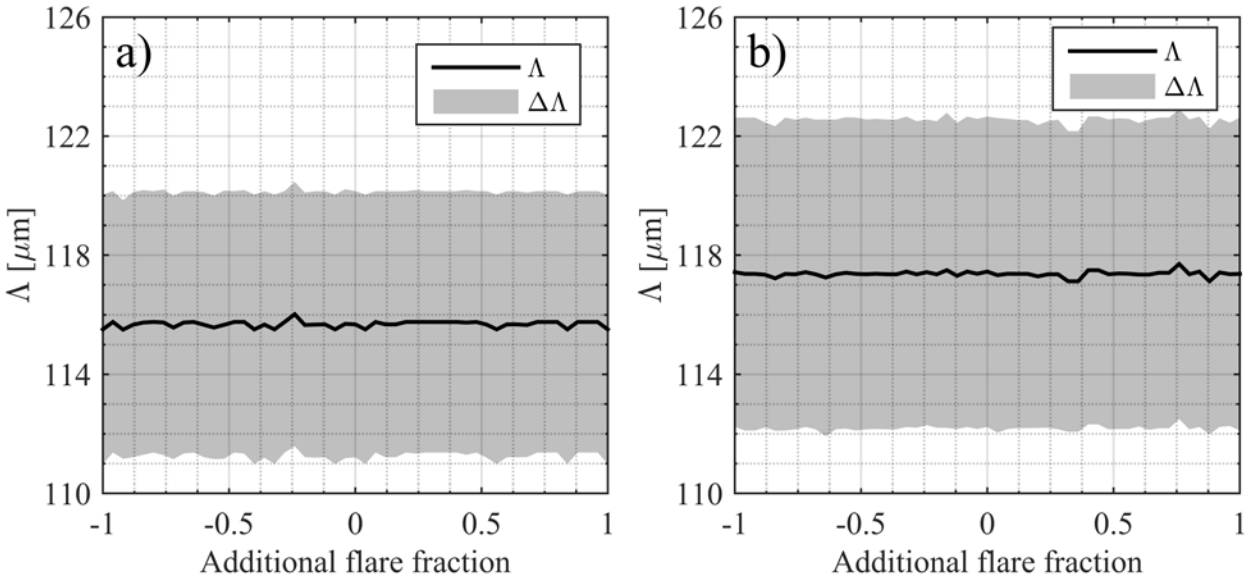

Figure 5-9: Error function fit parameter as a function of additional flare correction for the single SI (a) and HCCI (b) profiles in Figs. 5-4a) and 5-5a). The shaded region is the measurement uncertainty.

Using the fitted intensity profile, the temperature was calculated as previously discussed. Figure 5-10 shows the combustion temperature for the additional flare fraction sweep. As expected, the temperature decreases as the flare correction was reduced and increased when the flare increased. The product temperature is seen to be sensitive to the flare correction such that unrealistic temperatures, greater than 3000 K, could be calculated by simply increasing the flare correction by 50-75% over the nominal value. The greater sensitivity of the HCCI condition was driven by its lower raw Rayleigh scattering intensity, which was ~100 counts in the reactants compared to ~130 for SI, so for any additional flare correction the ratio increases more.

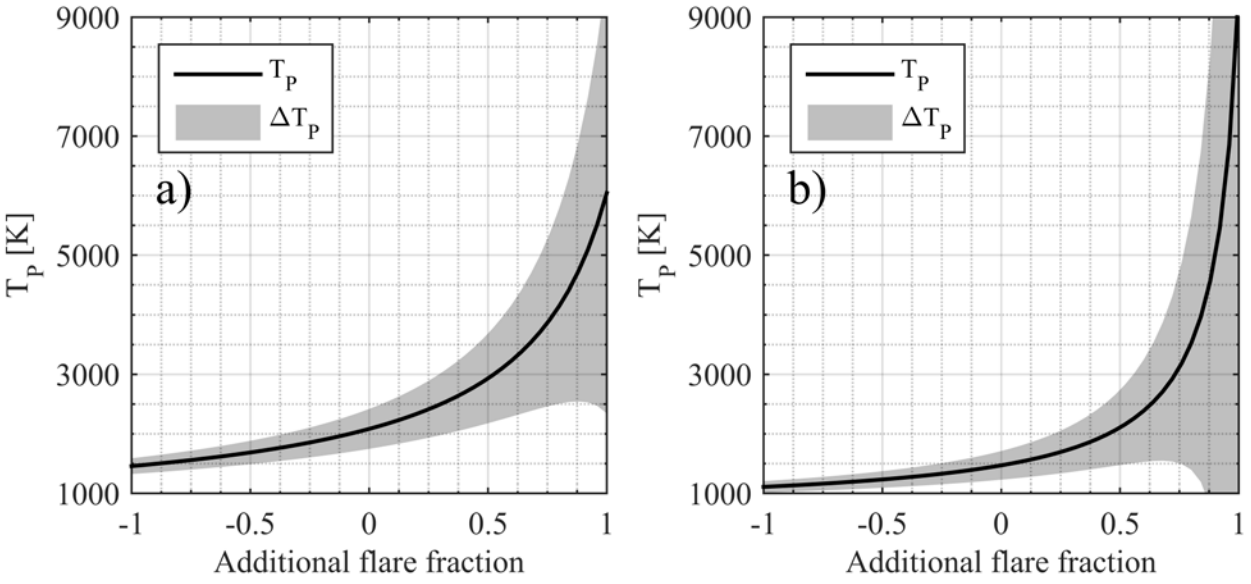

Figure 5-10: Product temperature as a function of additional flare correction for the single SI (a) and HCCI (b) profiles in Figs. 5-4a) and 5-5a). The shaded region is the measurement uncertainty.

This brings into question the amount of flare correction that should be used. One could adjust the flare until the combustion temperature matches the adiabatic flame temperature, but this could be perceived as adjusting the data to fit expectations which is contrary to the scientific method. Alternatively, the flare could be unchanged from the method described in Section 4.3.6. The choice affects the temperature gradient because the fitted function maintained the same width, thus temperature changes were mirrored by the temperature gradient as shown in Fig. 5-11. Ultimately, the temperature gradient appears in the combustion mode classification equation (2-2), consequently its handling was critical.

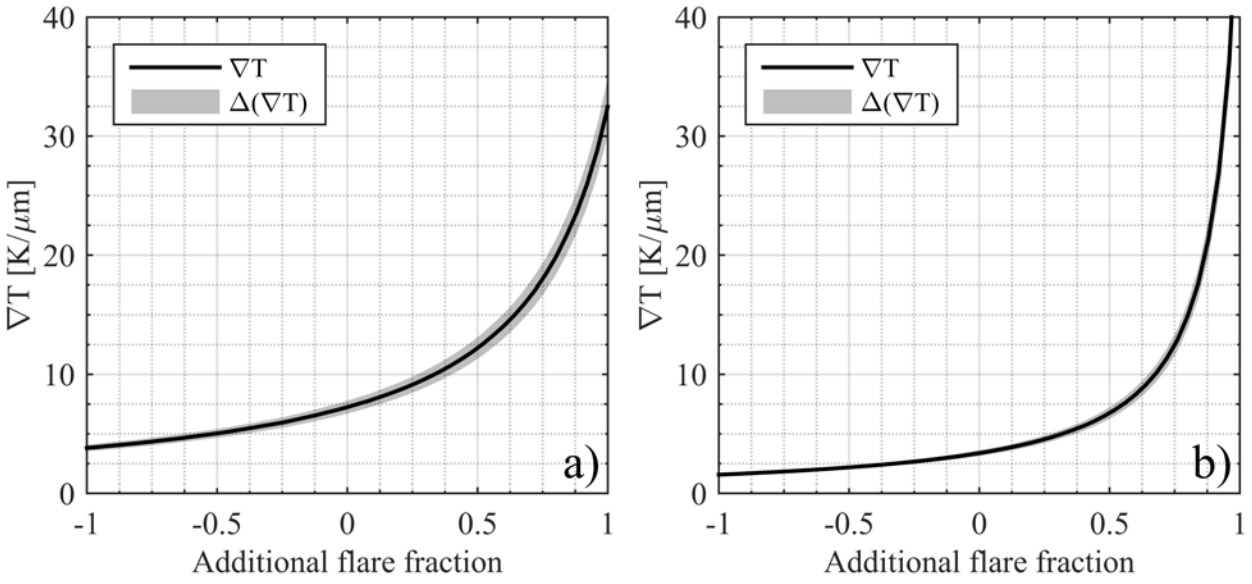

Figure 5-11: Temperature gradient as a function of additional flare correction for the single SI (a) and HCCI (b) profiles in Figs. 5-4a) and 5-5a). The shaded region is the measurement uncertainty.

For the sake of discussion, it is interesting to see how much the flare would need to be adjusted to reach the adiabatic flame temperature on the product side of the fitted $I_R/I_{R,0}$ profile. Figure 5-12 shows the distributions of the additional flare fraction required to reach the adiabatic flame temperature. The negative values were a result of calculated temperatures greater than the adiabatic flame temperature as seen in Fig. 5-8b). For the majority of the SI data, less than an additional 50% flare would be required. Considering the stochastic nature of beam steering, 50% more flare correction is not unreasonable. The HCCI data, however, would require significantly more correction.

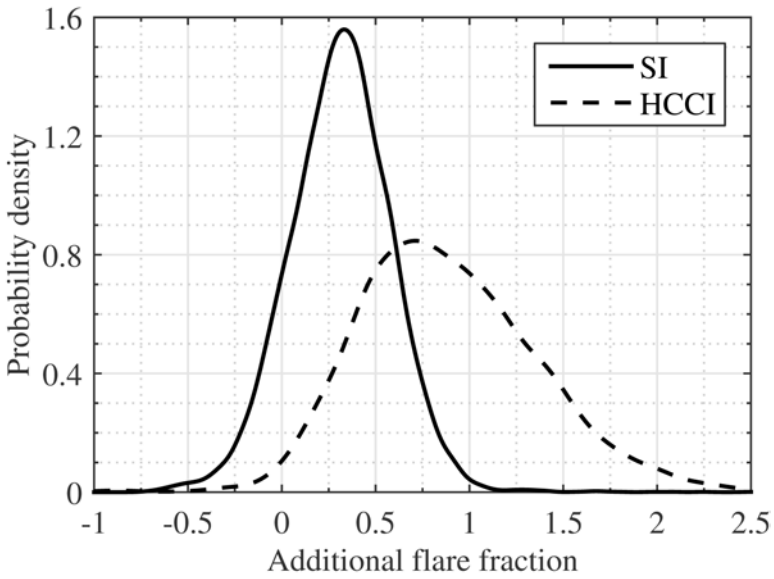

Figure 5-12: Required additional flare correction to achieve the adiabatic flame temperature for single SI and HCCI data sets.

Figure 5-13 shows the ratio of the flare correction to the Rayleigh scattering intensity in the reactants and products if the additional flare needed to reach the adiabatic flame temperature in the products was used. The SI data show the reactants ratio to be less than 50%, which could be an acceptable level, but when considering the products, the ratio becomes greater than one signifying the flare level was greater than the products' Rayleigh scattering intensity. From an experimental point of view, this demonstrates the difficulties of Rayleigh scattering, but from a data analysis point of view, corrections being larger than the signal level are clearly prone to high levels of uncertainty and should be avoided if unnecessary.

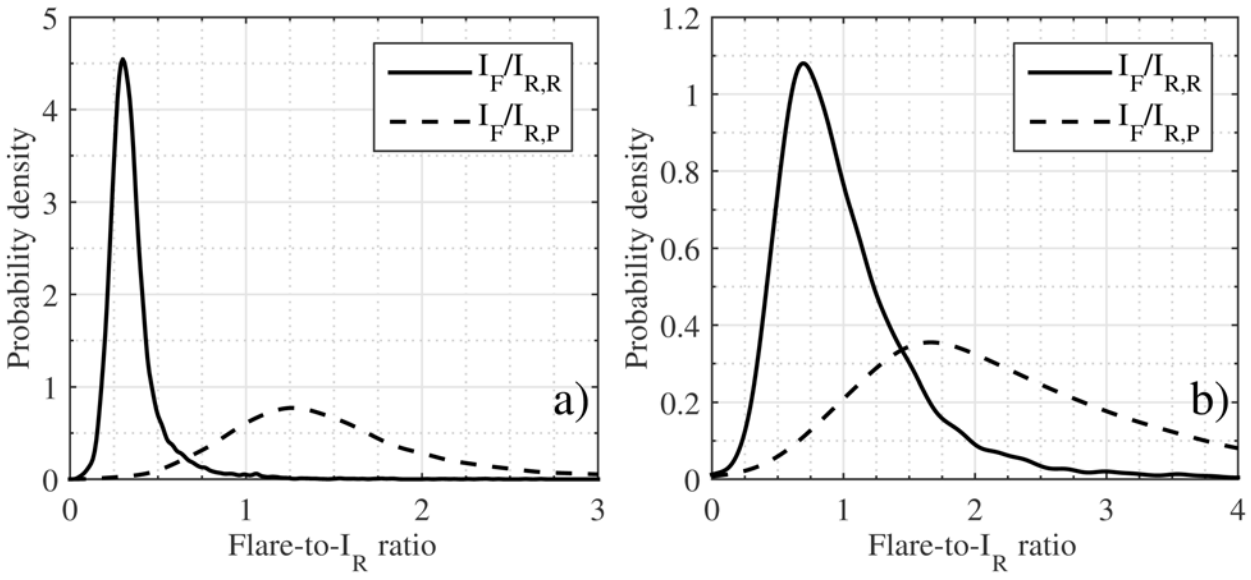

Figure 5-13: Ratio of the flare correction to the Rayleigh scattering intensity in the reactants (*R*) and products (*P*) if the flare was corrected for single SI (a) and HCCI (b) data sets.

Additional evidence suggests corrections may not even be necessary. It was explained in the Section 4.4.2 that the intensity profiles were extended until it appeared the signal leveled off, that is, reached a quasi-steady temperature. This was typically on the order of 400 μm after the combustion front. Upon closer inspection, some of the product intensity profiles continued to slowly decrease suggesting the temperature was slowly increasing. This was typically hard to discern during profile extraction, but an obvious case is shown in Fig. 4-28c). Flame simulations also showed an elongated temperature profile after the major combustion event. Unfortunately the intensity profiles could not be simply extended as the sub region used for the laser sheet intensity corrections (see Section 4.4.2) could not be increased in size without compromising its correction effectiveness. Therefore, to test if the decreasing intensities were affecting the results, intensities were selected far from the combustion front (~1200 μm) in both the reactants and products. Only images with uniform intensities in the reactants and products were used in this analysis. To calculate the temperature, the average of 15 pixels in the reactants and products

were used to calculate the intensity ratio for the thermometry equation. This was performed on a column-by-column basis for a simple non-uniform laser sheet intensity correction. Column selection was also limited to those that had calculated temperature profiles so that a one-to-one comparison could be made. A total of 1400 and 1600 “far-away” temperatures were calculated for the nominal SI and HCCI cases, respectively.

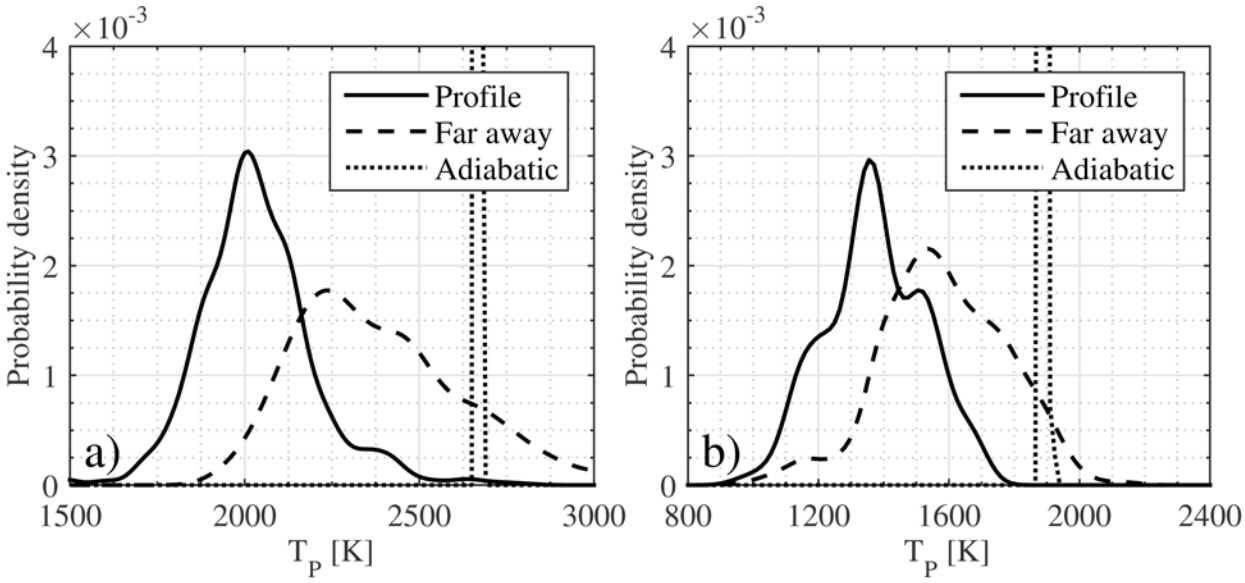

Figure 5-14: Single SI (a) and single HCCI (b) product temperature distributions for intensities measured far away from the combustion front and their respective profile and adiabatic flame temperature.

Figure 5-14 shows that the temperature calculated using the intensities far away from the combustion front yielded significantly higher combustion temperatures than the extracted profiles. While, on average, they still do not reach the adiabatic flame temperature, the increase shows the flare corrections were not responsible for all of the under-estimation of the product temperature. The observed increase resulted from an increase in the intensity ratio, which came from either an increase in the reactants’ intensity or a decrease in the products’ intensity. An increase in the reactants’ intensity suggests the intensity profiles were in a preheating zone, whereas the decrease in the products’ intensity indicates small exothermic reactions were still

continuing. Regardless, the additional flare correction would be smaller than presented in Fig. 5-12.

Continuing the discussion of the additional flare sweep, the impact on the combustion front thickness was also calculated. Figure 5-15 shows how the temperature-based thickness varied with additional flare. It is seen there was an minimal impact as any increase in temperature increased the temperature gradient, which had a negating effect per Eqn. (4-10). The greatest impact was the changing level of uncertainty which dwarfed the thickness value in many cases. The density-based thickness measurements are given in Fig. 5-16, where it is observed the changing flare had zero effect on the thickness value; the flare only affected the uncertainty which was significantly lower than the temperature-based calculations.

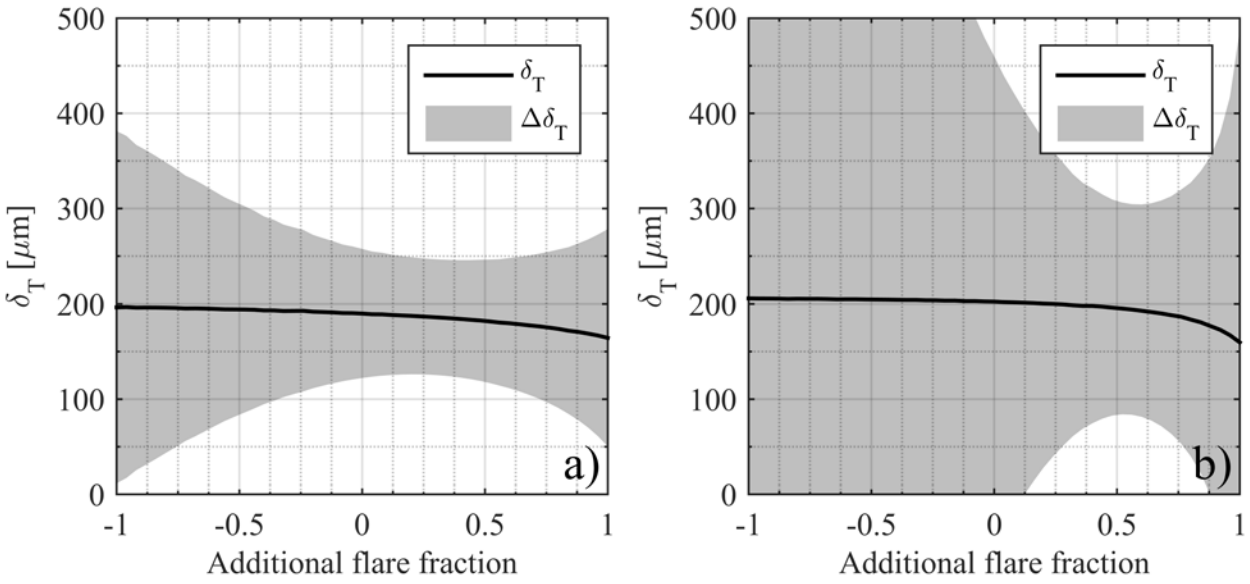

Figure 5-15: Temperature-based combustion front thickness as a function of additional flare correction for the single SI (a) and HCCI (b) profiles in Figs. 5-4a) and 5-5a). The shaded region is the measurement uncertainty.

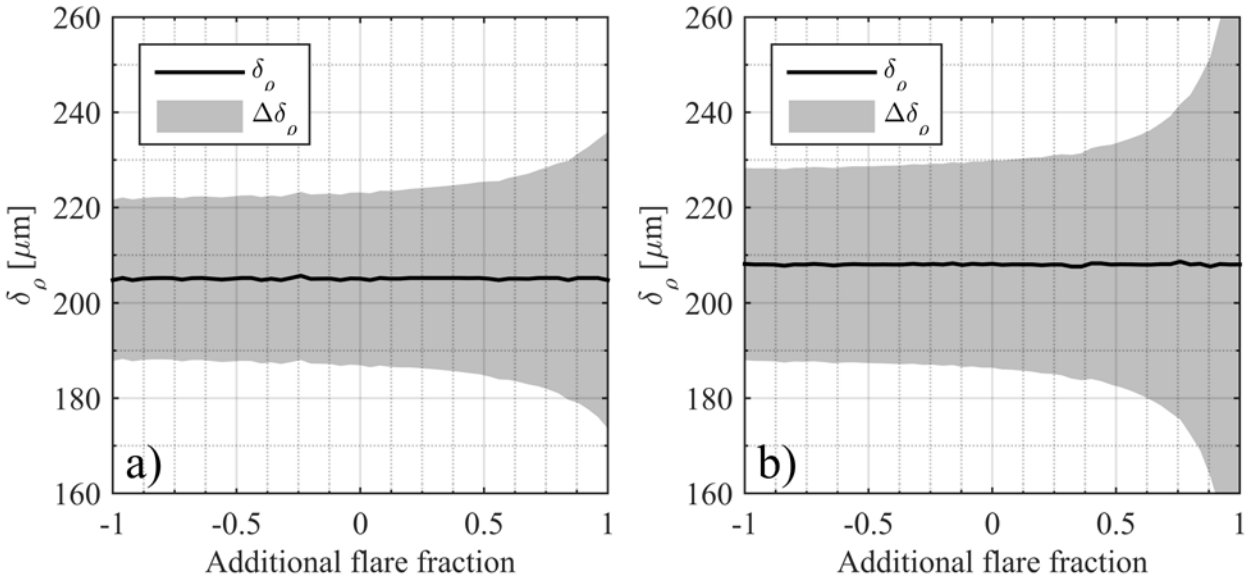

Figure 5-16: Density-based combustion front thickness as a function of additional flare correction for the single SI (a) and HCCI (b) profiles in Figs. 5-4a) and 5-5a). The shaded region is the measurement uncertainty.

As seen with the fit parameter, the thickness was not affected by the flare correction value, thus the thickness measurements were determined to be robust measurements. Based on the presented results, the temperature measurements used the flare correction method described in Section 4.3.6 with no changes implemented to force the combustion temperature to the adiabatic value. While the temperatures and subsequent gradient may be lower than the actual value, data show higher temperatures when using data points farther from combustion front than the extracted profiles. Additionally it is not known whether or not the temperature even reaches the adiabatic point, thus no assumptions about the physics were imposed on the data by applying additional corrections.

5.3 Spark-Ignition Baseline

Before analyzing the HCCI data further, the three SI conditions were compared to assess if the expected thermodynamic scaling laws of flames were captured in the data. The temperature and flame thickness for single-image data sets were used for comparison. The single and dual images were then compared for each condition to see if the data sets were agreeable given the temperature accuracy issues described above.

5.3.1 Combustion Temperature

The product temperature probability distributions for the three SI conditions are shown Fig. 5-17a). Based on the similar thermodynamic conditions at image timing and the equivalence ratios, one would expect the two stoichiometric conditions to have similar temperatures and the lean condition to have the lowest temperatures. This assumption was reinforced by their constant-pressure adiabatic flame temperature distributions shown in Fig. 5-17b). The adiabatic temperatures were calculated using the cycle-specific mixture and thermodynamic conditions at image timing. There is a 175 K difference between the mean nominal and lean adiabatic flame temperatures; the difference between the mean nominal and low pressure case is 6 K. Performing the same calculation on the collected data yielded a 300 K difference between the nominal and lean conditions and 350 K between the nominal and low pressure cases. From these results, it was concluded the expected impact of decreasing pressure and lean conditions on the flame temperature was not reliably captured. The temperature did decrease with the leaner condition, although too much, and the low pressure case did not match the nominal case as it should have per the adiabatic flame temperature calculations. As previously discussed, all of the temperatures are decidedly low compared to the adiabatic temperature due in part to the flare correction.

Additionally, even though a range of temperatures were expected, the broad ranges calculated are not realistic given how similar the reactant mixtures were.

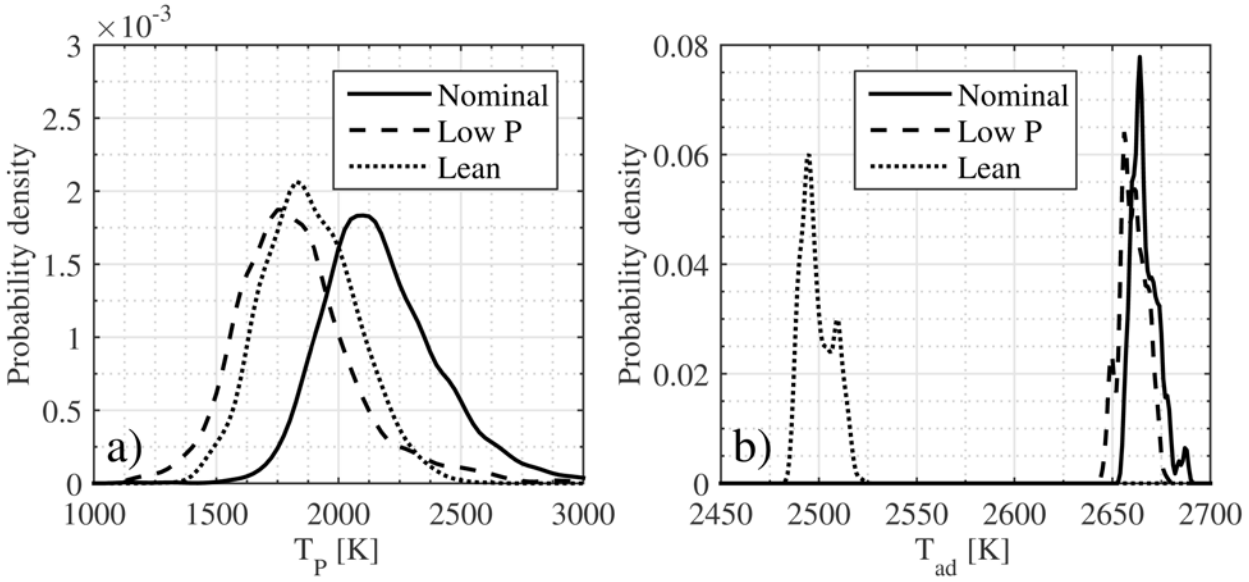

Figure 5-17: Product temperature (a) and constant-pressure adiabatic flame temperature (b) of the SI cases.

5.3.2 Flame Thickness

The flame thickness data were also compared. With a simplified analysis, the flame thickness can be shown to scale with the reactant and product temperature and system pressure as [10]:

$$\delta \propto \left(\frac{T_R + T_P}{2}\right)^{3/8} T_P^{-n/2} \exp\left(E_A/2R_u T_P\right) P^{-n/2} \tag{5-2}$$

where the subscripts R and P are the reactants and products, respectively, E_A is the activation energy, n is the overall reaction order (typically 1.7-2 for hydrocarbons) and R_u is the universal gas constant. When accounting for the decreased calculated combustion temperature and the lower pressure of the low pressure case compared to the nominal, the lower pressure flame thickness increases by 50%. If the combustion temperatures were the same per theory in Section 5.3.1, the flame thickness would still increase 30% due to the decreased pressure alone. This was

not captured by the density-based flame thickness measurements shown in Fig. 5-18a). Instead of an increase in combustion thickness, the mean value actually decreased.

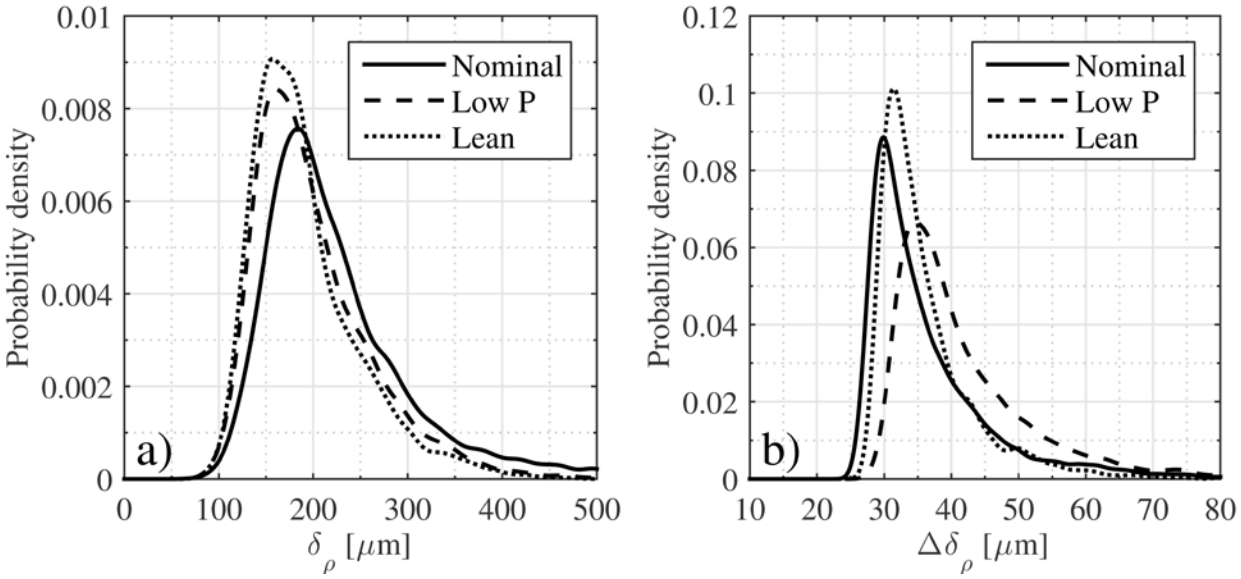

Figure 5-18: Density-based flame thickness distribution (a) and uncertainty (b) for the SI conditions.

With regards to the lean condition, its lower combustion temperature and slightly increased pressure predict a flame thickness increase of 4% per Eqn. (5-2). While thickness correlations do not directly account for equivalence ratio, the equivalence ratio affects the thickness inversely through the product temperature. In other words, the thinnest flame occurs at the highest adiabatic flame temperature equivalence ratio and increases in thickness as the equivalence ratio diverges [10]. Therefore the lean condition should have an increased flame front thickness which was also not captured by the measurements. Its distribution mirrors that of the low pressure case. An interesting point of the Fig. 5-18a) is that all three distributions reach roughly the same minimum thickness around 100 µm, the difference is just that the nominal distribution is more heavily weighted towards a thicker flame. It is known the flame front could have crossed the laser plane at a non-perpendicular angle thereby increasing the measured

thickness and decreasing the temperature gradient. This is likely the reason the nominal case is weighted towards a thicker flame, as compared to it actually having a thicker flame. Arguably the only data points that should be used are the ones with the thinnest flame as they most closely represent the actual flame thickness. If this were done, the SI cases would still not follow the expected trends as they all converged to a similar minimum thickness. Considering the simplicity of the scaling laws in Eqn. (5-2) and the measurement uncertainty, it is likely the flame thickness did not vary enough to be detected by the optical system. Flame simulations yield an 18% increase in thickness from the nominal to lean condition. For a 150 μm thick nominal SI flame, the lean flame would be 27 μm thicker, this increase was not quite resolvable by optical system; the uncertainty of a 177 μm thick combustion front is ~27 μm. Given this, the inconclusive SI baseline results were not alarming.

5.3.3 Single vs. Dual Imaging

Due to the multiple camera setup, the single and dual image sets were compared to check for consistency; that is, the single-image MicroMAX SI data and dual-image PI-MAX4 SI data should have similar distributions for a given measurement. Figure 5-19 shows the kernel density functions of the temperature gradient, product temperature and density-based combustion front thickness for the nominal SI case. The single images are given by the solid lines. The dual images (dashed lines) used the first image of each image pair as the ensuing combustion speed was related to the temperature gradient in the first image. From visual inspection the distributions do not align. The dual image data had, on average, smaller values for all three metrics shown. Since it has been shown that the temperature measurements can be easily changed, there is no reason to expound on their differences. Instead, the robust metric of the

combustion front thickness in Fig. 5-19a) is of interest. Both the single and dual image distributions converge to the same minimum value of ~65 μm, but the dual imaging has a much more abrupt minimum value. This suggests that more of the flame fronts were traveling perpendicular to the laser sheet in the dual imaging, resulting in a more defined measurement of the flame thickness at the nominal SI conditions.

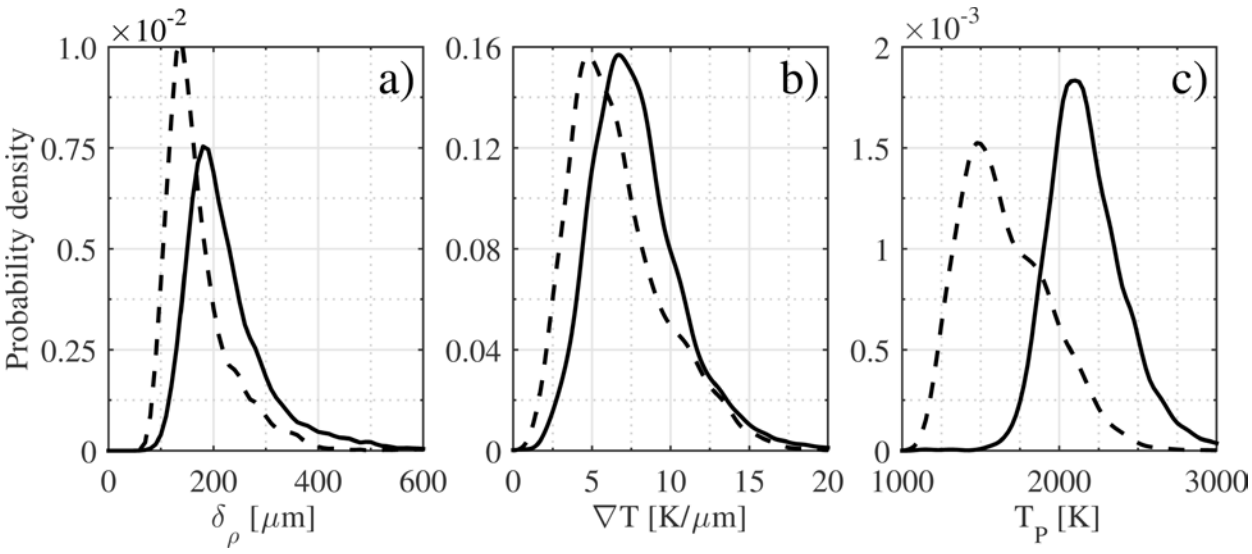

Figure 5-19: Nominal SI density-based combustion front thickness (a), temperature gradient (b) and product temperature (c) for single (solid line) and dual (dashed line) image data sets.

Although we are more concerned with the minimum thickness values (i.e. the actual flame thickness), the overall distributions were tested for agreement. Based on visual inspection they do not agree with each other, but statistically this was assessed with the Kolmogorov–Smirnov test (KS test). The KS test is a one-dimensional, non-parametric inferential statistical method with which a sample probability distribution is compared to a reference distribution to see if it was drawn from said reference (one-sample KS test), or two sample distributions are compared to determine if they were drawn from the same reference distribution (two-sample KS test). The null hypothesis is that the sample distribution was taken from the reference

distribution. The important feature of the KS test is that it is non-parametric such that no assumptions were applied to the probability distributions tested; furthermore it is sensitive to not only the shape of the distribution, but also its location. Two-sample KS tests were applied to the thickness measurements in Fig. 5-19. Because the number of data points for each distribution was large (5,000+), any statistical test would show each distribution to be an independent reference distribution, resulting in the null hypothesis always being rejected unless the distributions were nearly identical. Therefore a random sample of 300 points was taken from each distribution to use in the KS test. For 1000 iterations of the KS test (because the random sampling), the null hypothesis was rejected for every test combustion front thickness distributions at a 5% α level. When a -48 μm shift was applied to the single image front thickness distribution, the rejection rate reduced to 35%. The average uncertainty for the single image density-based front thickness measurements was 37 μm, which places the shift outside the uncertainty range.

Figures 5-20 and 5-21 contain the single-dual image comparisons of the low pressure and lean SI cases. Just like the nominal case, all the dual image distributions are shifted to lower values with the exception of the lean temperature gradient in Fig. 5-21a). There was less discrepancy between the single and dual image data for the low pressure and lean SI cases than for the nominal case. This does not necessarily mean the single image thicknesses are incorrect, just that the flame fronts of the dual imaging data propagated more normal to the combustion front thereby shifting the probability distribution to smaller values. This is again evidenced by the distributions having similar minimum values.

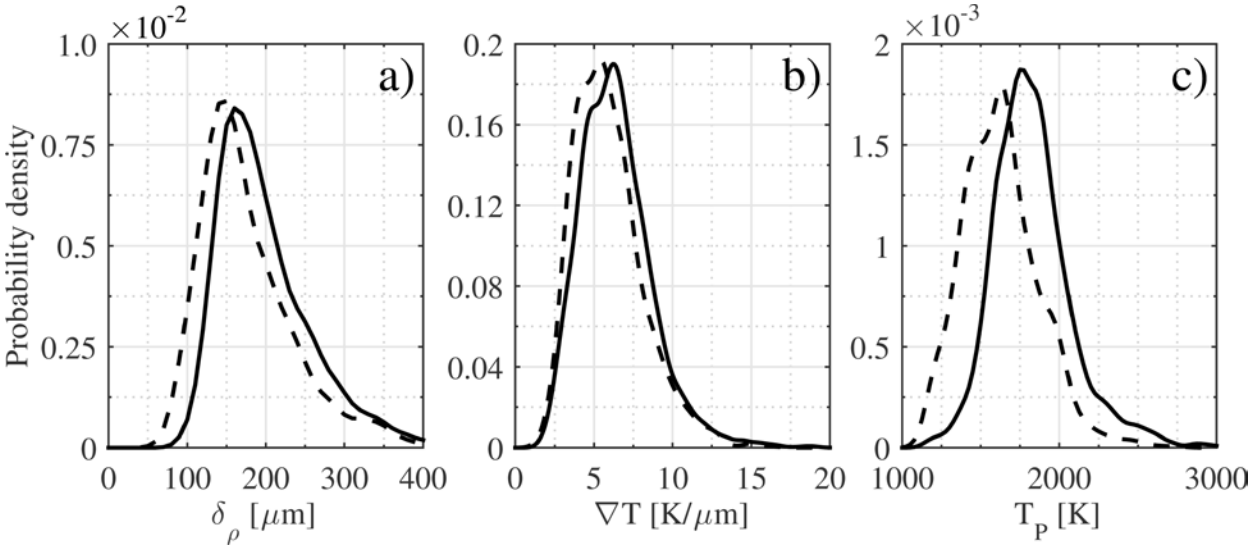

Figure 5-20: Low-pressure SI density-based combustion front thickness (a), temperature gradient (b) and product temperature (c) for single (solid line) and dual (dashed line) image data sets.

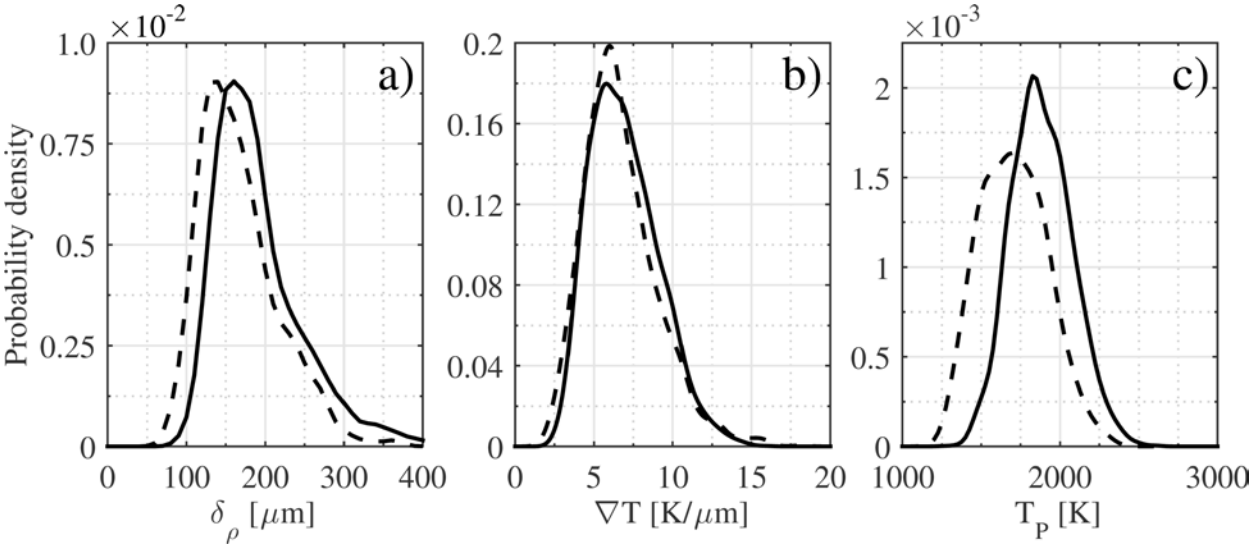

Figure 5-21: Lean SI density-based combustion front thickness (a), temperature gradient (b) and product temperature (c) for single (solid line) and dual (dashed line) image data sets.

For the sake of completing the single-to-dual image comparison, the HCCI distributions are given in Fig. 5-22. Clearly the single- and dual-image HCCI distributions agree better than the SI distributions. Slight differences exist in the temperature gradient and combustion front

thickness distributions, but overall, the shape and position was comparable for both data sets. Performing the KS tests on the HCCI data resulted in the null hypothesis being rejected in 15% of the combustion front thickness tests. Applying shifts of 0.25 K/µm and 75 K to the single image temperature gradient and product temperature distributions, respectively, yielded rejection rates of 8% and 7%; their respective average uncertainties were 0.34 K/µm and 350 K, which contain the shift values. It was therefore concluded that the single and dual image HCCI data sets are comparable to each other and are representative samples of the same reference distribution.

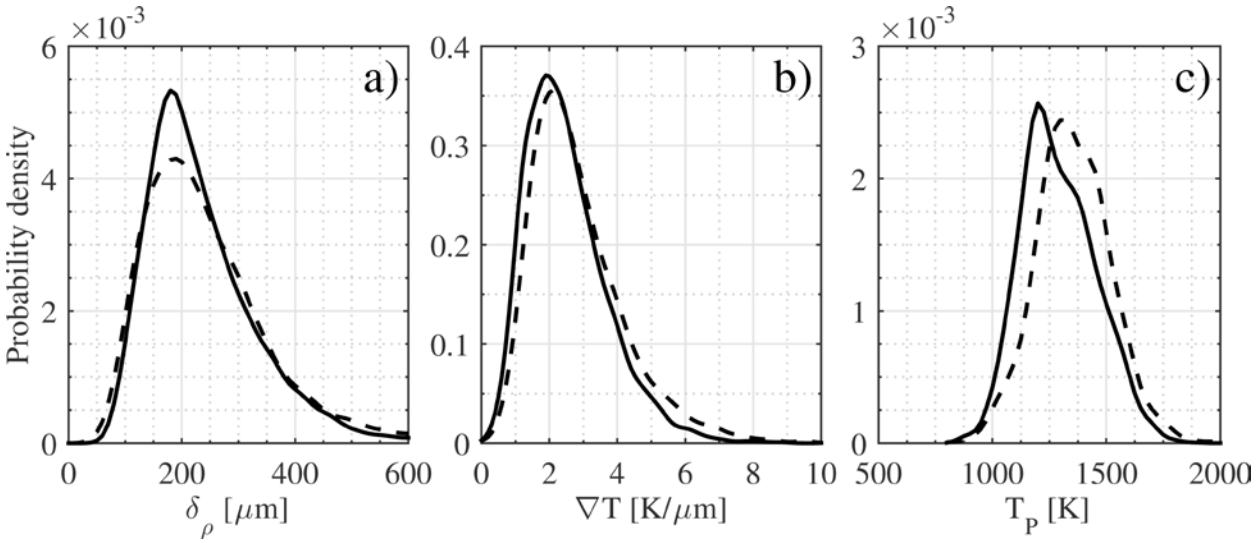

Figure 5-22: HCCI density-based combustion front thickness (a), temperature gradient (b) and product temperature (c) for single (solid line) and dual (dashed line) image data sets.

5.4 Temperature

Figure 5-23a) shows the product temperature distributions that have been seen in the preceding sections. The single-image nominal SI case is shown as it yielded the temperature distribution closest to the adiabatic flame temperature. Since the reactant thermodynamic conditions at image timing were comparable between the nominal SI and HCCI cases, the lean HCCI mixture (Φ = 0.6) gave an adiabatic flame temperature of ~1850 K (see Fig. 5-8a). Expectedly, HCCI had

lower combustion temperatures than SI, so that physical trend was reproduced by the results. The uncertainties presented in 5-23b) were a result of the laser energy and the combustion temperature as both directly affected the shot noise. The single HCCI images used twice the laser energy, so for similar product temperatures as the dual HCCI images, the single images had much lower uncertainty as shown in Fig. 5-4b). Comparison of the single SI and HCCI data sets shows that the greater SI combustion temperatures (lower Rayleigh scattering signal) resulted in higher uncertainty, higher than even the dual-image HCCI.

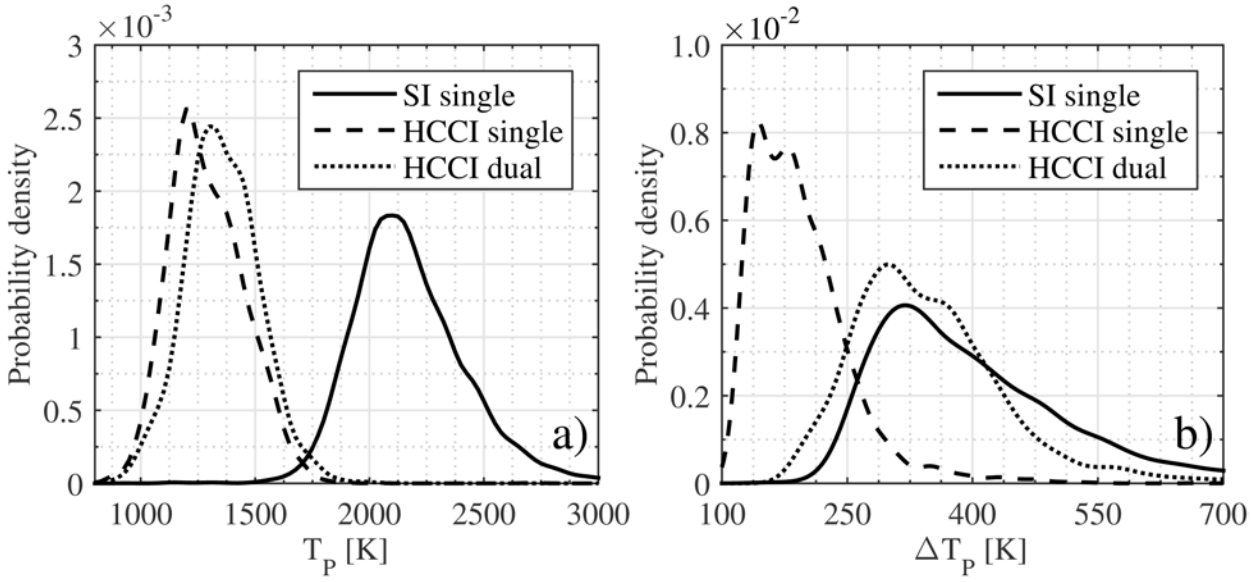

Figure 5-23: Single-image nominal SI and single- and dual-image HCCI product temperature (a) and uncertainty (b) distributions.

When considering the influences of the low product temperature measurements in Section 5.2.4, the flare correction and preheat or late, slow heat release zones were discussed. In the case of SI, these are considered the two influences that erroneously affected the calculated temperatures. For HCCI, partial combustion was a third possibility that was explored. Partial combustion was not considered for SI because the mixture had ideal conditions for flame propagation and it was assumed that the flame propagated with high combustion efficiency; a

partially combusting flame would not propagate as the post-combustion temperatures would not be high enough to drive thermal diffusion. In this context, partial combustion is defined such that the product mixture is at an intermediate state between the reactants and the final post-combustion state as determined by combustion simulations. If partial combustion was captured, it would resemble under-corrected flare images as the intensity ratio would not be as high as necessitated by the adiabatic flame temperature; therefore additional clues were necessary to identify partial combustion locations. It is recognized that a partially oxidized reactant mixture would also decrease the ratio, but given the uniformity of the reactant intensities this was not believed to be the case.

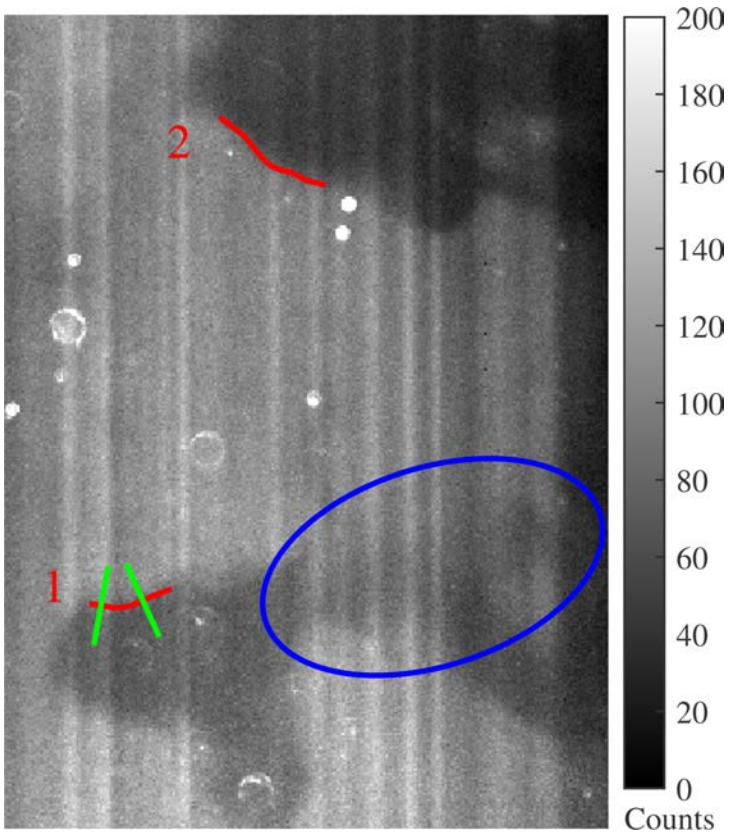

Figure 5-24: Single HCCI image demonstrating partial combustion. Combustion contour 1 identifies partial combustion. The blue ellipse identifies another partial combustion location.

Figure 5-24 shows a flare-corrected single HCCI image in which partial combustion has been identified through comparison of the two combustion front contours (red lines). Figure 5-25a) compares the Rayleigh scattering intensity across the combustion front as identified by the extracted normal profiles; the contours are identified per the red numbers next to each contour in Fig. 5-24. Both contours start at approximately the same Rayleigh scattering intensity, where some variation did occur due to the laser sheet intensity distribution and beam steering striations. This suggests, though, that no reactant oxidation occurred. Additionally, the static background images did not show any extra surface scattering. Therefore, for the same mixture and thermodynamic conditions, the combustion temperature would be the same and consequently the measured scattering intensity. Figure 5-25a) reveals this not to be the case. Contour 2's intensity decreased more than Contour 1 resulting in a higher temperature shown in Fig. 5-25b). Based on visual inspection alone, the products' intensity for Contour 1 is greater than that of Contour 2. Because the initial states were very close, the ~300 K difference in product temperature indicates that Contour 1 was at an intermediate combustion state.

Further evidence is given by slope of the profiles at the post-combustion end. The intensity gradual decreases for Contour 2, which slowly increases the temperature. This is the same behavior seen by some of the SI images (see Fig. 4-28c). This suggests Contour 2 was undergoing slow reactions as the main combustion already occurred and places it in the 2nd category of anomalous temperature measurements where the product temperature is greater when measured far from the combustion front. Contour 1 on the other hand actually reached a steady product intensity and temperature. For a more detailed view of the individual contours, Fig. 5-26 shows the temperature profile for the green lines plotted in Fig. 5-24; the left profile is image a) and the right is image b). There are clear differences in the shape of two profiles on opposite

sides of the contour, but, regardless, both have a low product temperature that leveled off. This eliminated the slow reaction influence, and the flare correction influence was the same as the Contour 2, which would almost reach the adiabatic flame temperature based on the far-away temperature measurements. Therefore there was still a 300 K difference that is only explainable by imaging the combustion at an intermediate combustion phase.

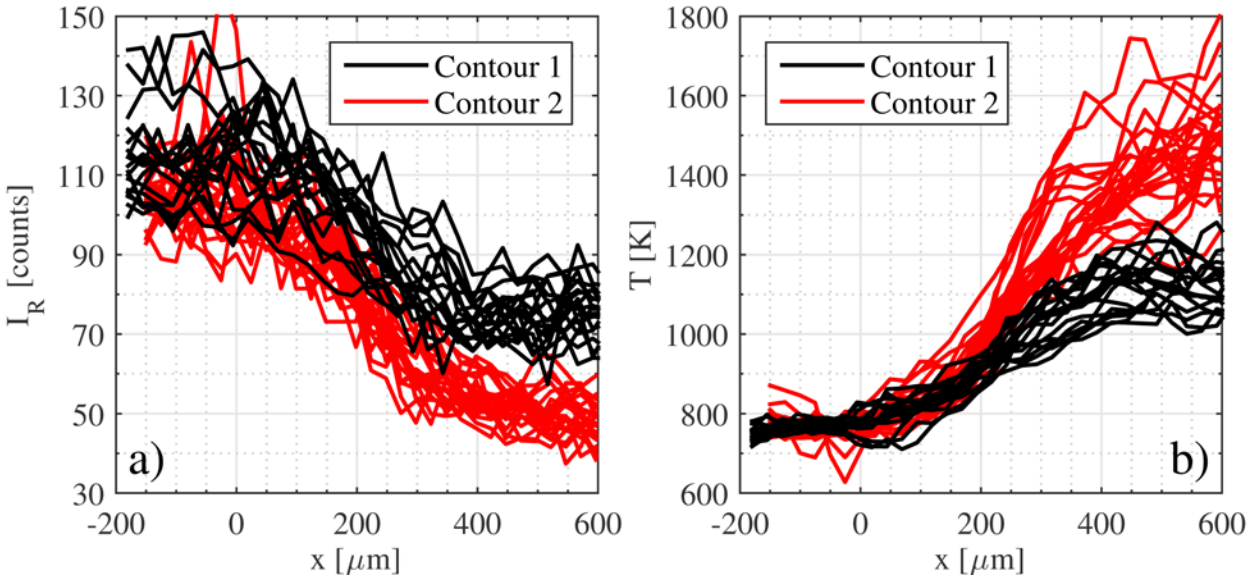

Figure 5-25: Rayleigh scattering intensity (a) and temperature profiles (b) of the combustion front contours identified in Fig. 5-24.

In fact, it was quite common to see partial combustion in the HCCI images. The blue ellipse in Fig. 5-24 encloses a region where partial combustion occurred as the temperature was calculated to only increase from 767 to 869 K. Several locations were also seen in the sample fired HCCI image (Fig. 4-25). Although imaging the partial combustion of HCCI is a finding in and of itself, the intention of the study was to find propagating combustion fronts; therefore, these obvious regions of partial combustion were avoided during image processing (see Section 4.4.2). Combustion front contours with sharp gradients were sought out as they would yield the greatest chance of flame propagation. It appears the contours presented in Fig. 5-25 did not meet

the aforementioned criterion but at the time of identification it was difficult to discern. Reinspection of the data found few contours where partial combustion was distinguished by the presence of other contours with higher temperatures. The clear majority of images with multiple contours all had comparable combustion temperatures, thus the distributions were not overly influenced by partial burn data.

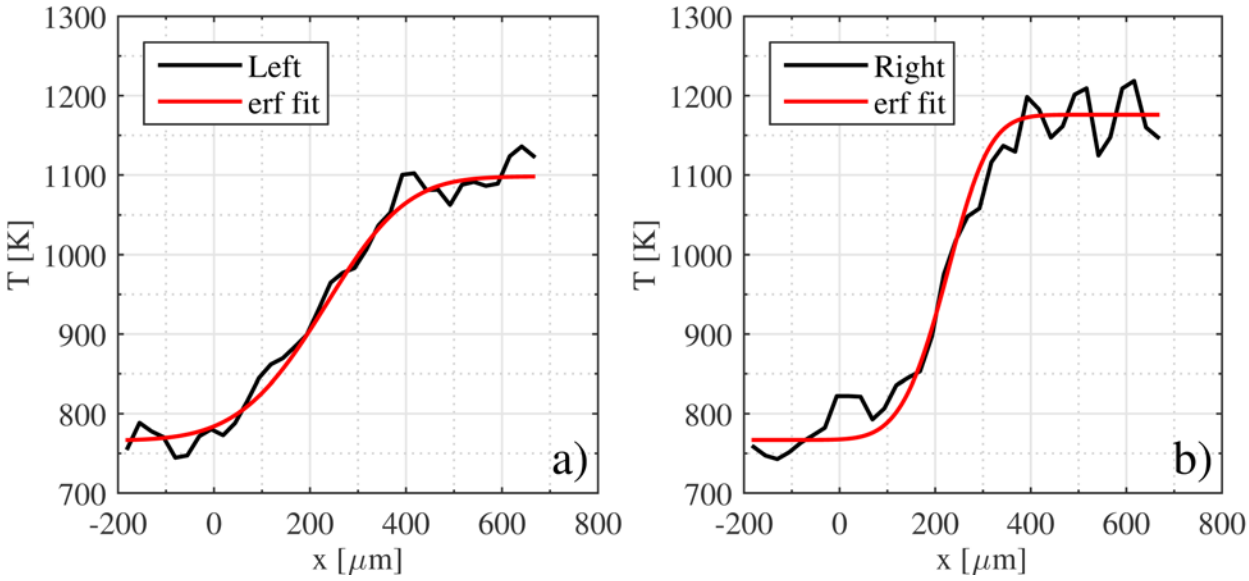

Figure 5-26: Contour 1 temperature profiles indicated by the green lines in Fig. 5-24.

The most direct and compelling evidence of partial burns was produced by tracking temperature profiles from the first to second image of a dual image pair. Since the combustion front contours were assumed to remain the same between the first and second image, the same profile lines were used to extract the intensities from the second image to calculate the temperature. This assumption was discussed in Section 4.4.5 where it was stated that only contours with distinguishing characteristics that did not change and could be confidently tracked were used for the dual image data. Figure 5-27 shows one such HCCI contour, where image a) is the raw temperature profiles and image b) is the fitted profiles given for clarity. The important

aspects are 1) the average product temperature increases by ~100 K between the images and 2) the product temperatures reach a quasi-steady value. The increase is more easily visualized in Fig. 5-27b) by removing the noise in the raw data with the error function fit. The steady product temperature indicates the combusted region was uniform but at an intermediate phase. If a slowly increasing temperature was seen like in Fig. 5-25b), the increased temperature could be perceived as completion of slow reactions in the products, which is not truly an intermediate phase. Similar to the partial combustion detected within a single image, partial burns detected by contour tracking was rare. In addition to initially avoiding contours with indistinct intensity changes from reactants to products, calculating the temperature of the second contour was difficult as combustion typically started influencing the reactants side such that the temperature calculation methodology was no longer valid. In the majority of cases, when the second temperature could be calculated, the temperature profiles lied on top of each other for the first and second image, indicating complete combustion. Again, it was rare to find partial combustion in the HCCI images, and nothing considered partial burns were seen in the SI dual imaging data.

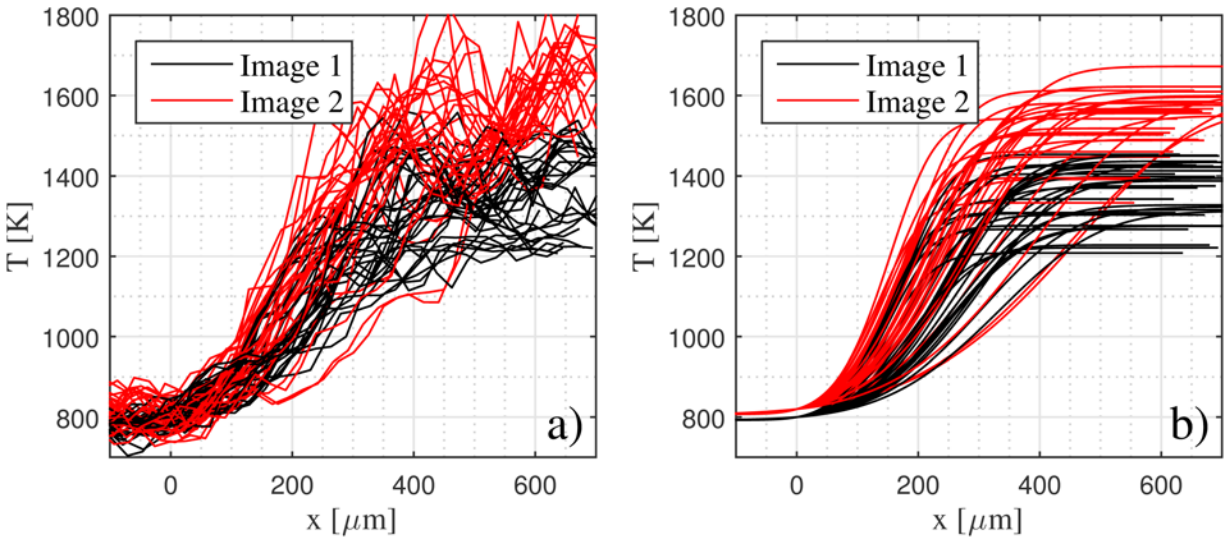

Figure 5-27: Raw and fitted tracked temperature profiles from the first to second image of a dual HCCI image pair. The raw profiles show the temperatures leveled off.

To summarize, three aspects in the measurements influenced the measured product temperatures: imprecise flare correction, not measuring the temperature far enough away from the combustion front and partial combustion. The SI experiments experienced the first two cases but did not include any partial burns, whereas all three conditions were seen in the HCCI data. The combination of the three influences and the uncertainty in the measurements easily accounts for the discrepancies seen with the theoretical adiabatic flame temperature. Several of the expected trends such as lower HCCI and lean SI combustion temperatures were captured with the data, but in the end, the accuracy of the temperature was limited and underscores the difficulty in applying Rayleigh scattering measurements to engine experiments.

5.5 Combustion Front Thickness

The HCCI and dual-image nominal SI density-based combustion front thicknesses are shown in Fig. 5-28a) with their uncertainties in image b). The dual-image SI data were used as they were shown to provide a more uniform minimum flame thickness, which is thought to represent the true flame thickness. The issue to consider was whether the HCCI combustion had combustion fronts with similar thicknesses to flame propagation. Therefore, the near minimum values are of interest. It is seen that all three traces have similar minimum values with the SI having the smallest mean value of 170 μm; the HCCI data had mean values of 236 and 245 μm for the single- and dual-imaging, respectively. Although the mean values are not a proper metric for comparing the average minimum value, it demonstrates that HCCI combustion had a significant amount of relatively thin combustion fronts. Again, it is noted that thinner combustion fronts were targeted during image analysis, therefore the distributions are skewed from the total HCCI combustion front thickness distribution; if combustion fronts such as the ones in the blue ellipse in Fig. 5-24 were included, the population would undoubtedly shift towards greater thicknesses. Even within a single identified contour the thickness changed; for example, going from the left to right temperature profiles (500 μm distance) in Fig. 5-26, the thickness decreased from 346 to 185 μm. This behavior was common for the HCCI data, but was rare for the SI experiments. For the flame propagation thickness to change so abruptly the flame would have significant curvature out of the laser plane.

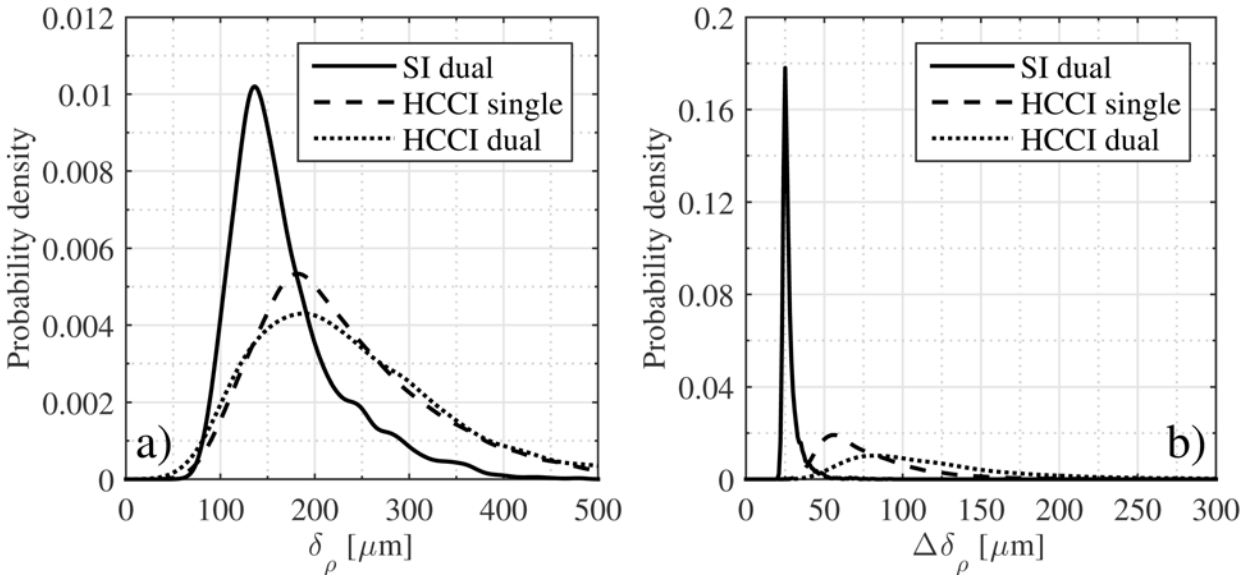

Figure 5-28: Dual-image nominal SI and single- and dual-image HCCI density-based combustion front thickness (a) and uncertainty (b) distributions.

It has been shown several times throughout the study that the density-based thickness measurements have less error than their temperature-based counterparts (see Sections 2.6, 4.6.3 and 5.2.4). As a final point of discussion on the topic, the temperature-based thickness distributions are given in Fig. 5-29. The mean thicknesses were 162, 232 and 239 μm for the dual-image SI, single- and dual-image HCCI cases, respectively. The temperature and density definitions have been used extensively in research [10, 97] as a standard definition has not been prescribed, so typically the most handily calculated value is used. The value of the calculations are close with the temperature-based thickness being ~8% less than the density-based calculation, but the thickness-based uncertainty is 36% greater than that of the density-based calculations for the dual-image SI case. Both HCCI cases yielded a 2% lower temperature-based thickness with 31% error. Thus it is recommended to use the density-based thickness calculations when possible to minimize the error.

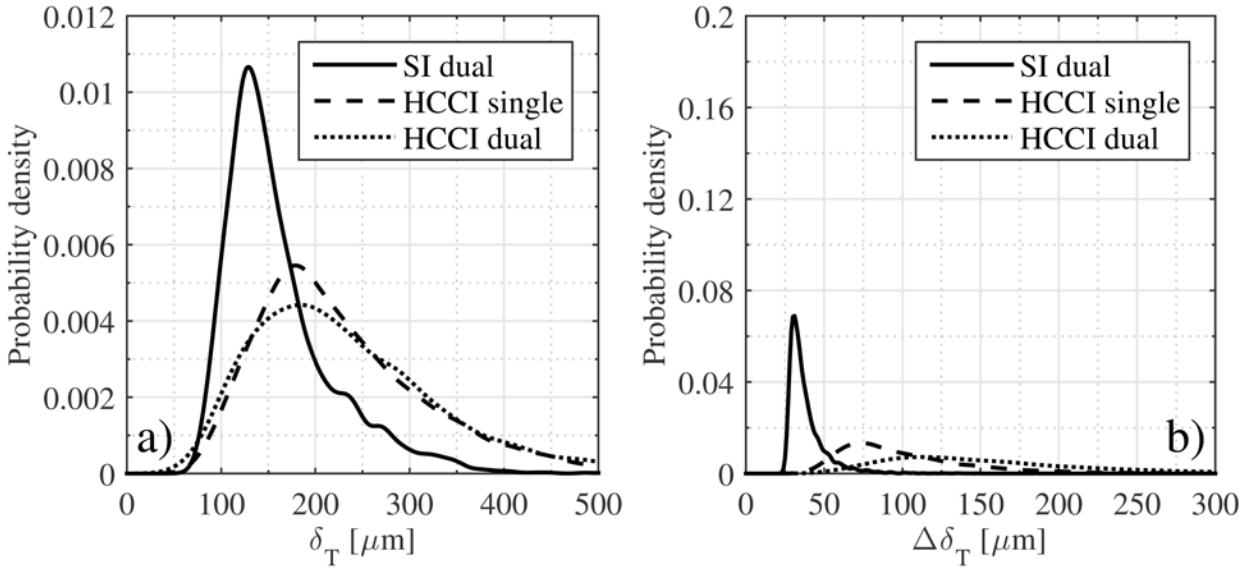

Figure 5-29: Dual-image nominal SI and single- and dual-image HCCI temperature-based combustion front thickness (a) and uncertainty (b) distributions.

Based on the presented results, there are locations with HCCI where the combustion front thickness was very similar to flame front thicknesses at similar thermodynamic conditions. Smith [203] measured stoichiometric methane, isooctane and propane SI combustion to have density-based flame thicknesses of approximately 200 µm for imaging thermodynamic conditions of 700 K and 10 atm, which were quite comparable to this study's conditions. The 2-D DNS results from Chen et al. [49] were performed for hydrogen/air mixtures 1070 K, 41 atm and $\Phi = 0.1$. The front thickness was not explicitly given, but the fronts considered to have flame propagation had temperature gradients greater than 2 K/µm and peak combustion temperatures of 1450 K. Per Eqn. (4-10) the temperature-based front thicknesses were a maximum of 190 µm. The density-based thickness is on par with the temperature-based measurements, so, again, there exists combustion front thicknesses very similar to flame propagation during HCCI, though not as frequent.

To be certain of the measured thicknesses, all influences must be accounted for as was done with the temperature measurements. It was already shown in Section 5.2.4 that the flare correction had no effect on the precision of the front thickness; the density-based uncertainty increased slightly with larger flare corrections, but no additional flare correction was performed therefore keeping the density-based uncertainty near its minimum (see Fig. 5-16). The second influence, an increasing product temperature, increases the thickness as the profile becomes more drawn out on the products side. Mathematically, the numerators in Eqns. (4-6) and (4-10) increase while the peak gradient stays the same, thereby increasing the thickness. The SI and HCCI cases with increasing temperatures then have under-calculated thicknesses. Analyzing which contours led to the increasing product temperature was problematic as increasing the sub region size to fit a longer normal profile (see Section 4.4.2) led to issues with the beam steering corrections. Instead the temperatures calculated using the far-away regions from Section 5.2.4 were used as models. The SI temperatures increased by an average 350 K which increased the temperature-based thickness by 24%. The HCCI temperatures increased 110 K, increasing the thickness by 22%. It was not known how many and where in the thickness distribution the increasing temperature profiles were, thus the fortuitously close increases were not used to adjust the thickness data. Arguably this decreased the accuracy of the measurements, but relative to each other, the SI and HCCI thickness distributions had no net change.

The third influence discussed in the temperature measurements was partial combustion which only affects the HCCI measurements. Considering the temperature profiles in Fig. 5-27, it is hard to perceive if the front thickness is increasing while the temperature increases due to combustion progression. Figure 5-30 shows the thickness distributions for the two images. The distributions align well, and a two-sample KS test did not reject the null hypothesis. This shows

the combustion front maintained thickness while increasing the temperature of the products, and therefore did not impact the thickness distributions in Fig. 5-28a).

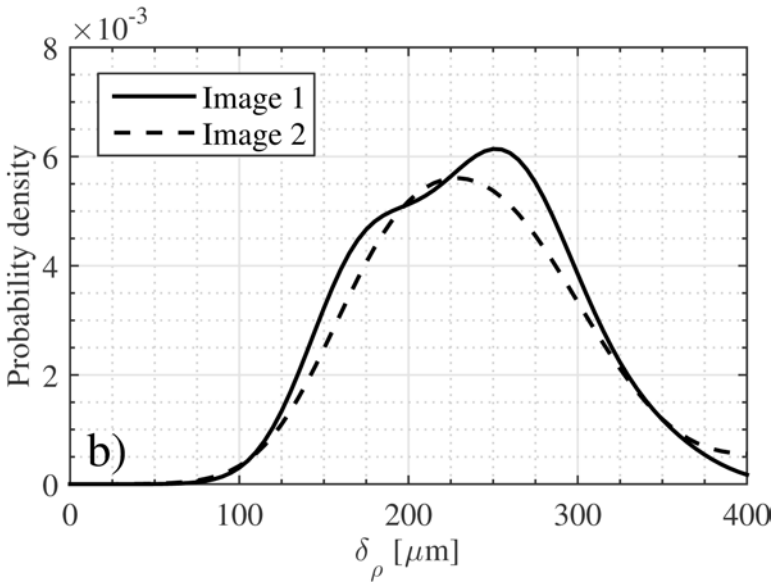

Figure 5-30: Density-based combustion front thickness distributions of the 1st and 2nd image of the tracked HCCI contour presented in Fig. 5-27.

An additional factor influencing the distributions was the effect of oblique combustion fronts, that is combustion fronts that are not oriented perfectly normal to the laser sheet. Owing to the finite thickness of the laser sheet, any non-normal angle of the reaction front relative to laser plane artificially increased the thickness, which decreased the temperature gradient. Smith [8] encountered this problem when measuring the flame front with Rayleigh scattering thermometry. To mitigate the effects, the author convoluted a distribution of angles with the measured flame thicknesses distribution to shift the probability towards a smaller thickness; the angular distribution favored the global flame propagation angle relative to the laser sheet. From previous studies, HCCI tends to progress from the center of the cylinder to the periphery. Although the global reaction direction could tentatively be established, the autoignition points are randomly located relative to the laser sheet confounding the instantaneous combustion

progression angle captured in the images. The angular distribution adjustment would require a lot of (likely poor) assumptions to be applied to the data, especially for HCCI. Additionally, the convolution does not change the measured thickness, but only serves to shift the thickness distribution; that is, a higher probability would be applied to the minimum values already in the distribution. For this reason the probability distributions were not altered. As mentioned in Section 5.3.2, comparison of the minimum thicknesses is all that is needed since the minimum values represent the thinnest combustion front that could only be achieved if the front propagated normal to the laser sheet.

It has been seen in the Rayleigh scattering images that laser beam steering occurred due to density gradients at the laser windows. This brings into question the effects of the combustion front density gradient on the measured signal. Smith [8] performed ray tracing calculations and found the front to be displaced by 60 μm but with minimal changes in the thickness. Smith confirmed this experimentally by using the Rayleigh scattering measurements to obtain the laminar flame thickness of hydrogen, which agreed with calculations, therefore, it was concluded the Rayleigh image was not distorted by the density change across the combustion front. Because similar engine conditions were used, the density and density gradients were similar, thus Smith's conclusions were applied to this study.

5.6 Temperature Gradient

Figure 5-31 shows the temperature gradient of the single-image nominal SI, and single- and dual-image HCCI data sets. The single-image nominal SI case is shown since it yielded the best temperature distribution with respect to the adiabatic flame temperature. Even with the wider flame thickness distribution, the temperature gradients are greater than the dual-image nominal

data (see Fig. 5-19). Their relative uncertainties, shown in Fig. 5-31b), were based on the fit parameter and system resolution (see Section 4.6.2). Because the fit parameters were all similar, hence the comparable combustion widths, the relative uncertainties were close which means smaller gradients yielded a smaller absolute uncertainty.

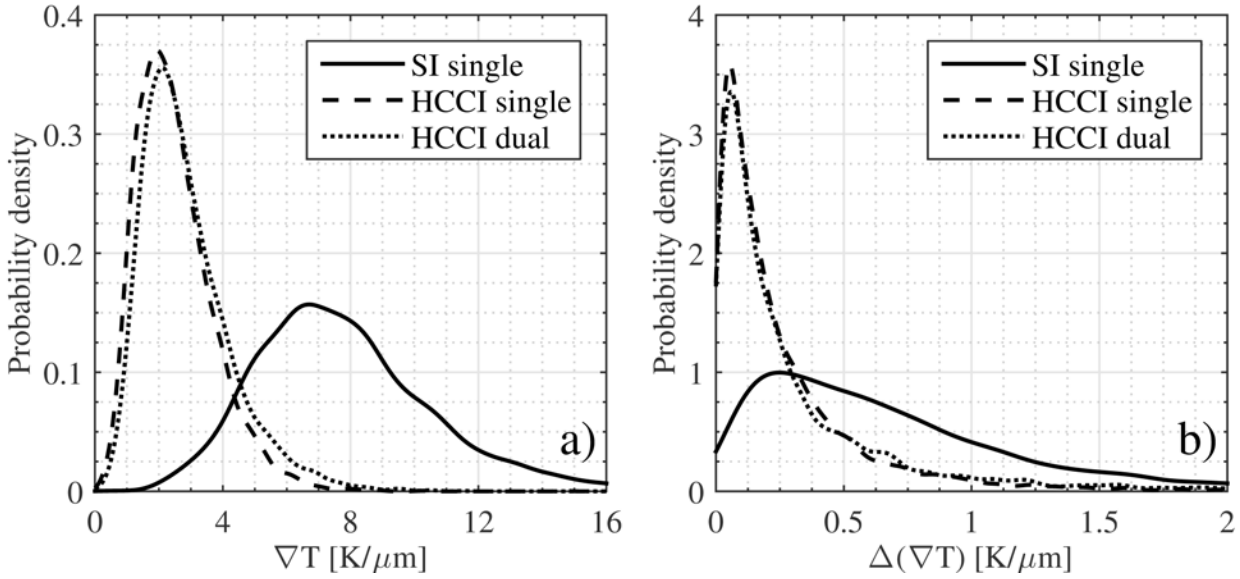

Figure 5-31: Single-image nominal SI and single- and dual-image HCCI temperature gradient (a) and uncertainty (b) distributions.

The previous two sections discussed the factors affecting the temperature and combustion front thickness. Together they combine to be the factors that affect the temperature gradient by the temperature controlling the "rise" and the thickness setting the "run." Since the smallest SI thicknesses were taken as being the true thickness, the greatest temperature gradient would represent the true value. When considering this, the SI distribution clearly had greater temperature gradients. The HCCI distributions have little area in common with the SI distribution. Their peak temperature gradients were ~8 K/μm, which is approximately the average value of the SI distribution, but this is only half of the maximum SI temperature gradient. From Fig. 5-28, if the true SI flame thickness is taken as 90 μm, the temperature

gradient using the adiabatic temperature is 21 K/μm. Clearly the HCCI cases did not have gradients that high, and neither did SI since their temperatures did not reach the adiabatic flame temperature. If an average calculated SI temperature of 2100 K is used, the temperature gradient is 15 K/μm which was achieved by the SI data. If the HCCI data also had a minimum thickness of 90 μm and reached the adiabatic temperature, the gradient would only be 12 K/μm. Clearly a direct comparison of the temperature gradients is futile, as the low-temperature nature of LTC precludes it from even being comparable to SI conditions.

The 2-D DNS results from Chen et al. [49] give a better comparison as they were from lean HCCI conditions; the combustion fronts they labeled as flame propagation had temperature gradients greater than 2 K/μm. Correcting for the reactant and product temperature differences, the minimum temperature gradient for deflagrations was 3 K/μm, which was achieved in this work. This is not confirmation that flame propagation was seen in the HCCI data because 1) the temperature gradients were from different conditions and 2) the classification methodology proposed by Chen et al. requires the propagation speed.

5.7 Combustion Speed

The final measurement to aid in the classification of the HCCI propagation was the combustion speed via the contour tracking in sequential images. As a reminder, particles in the laser sheet were tracked to calculate the in-cylinder flow field velocity to correct the tracked combustion front movement. The flow field correction was typically twice that of the resulting combustion speed which adds uncertainty to the measurements that was not fully reflected in the uncertainty calculations. Figure 5-32 compares the nominal SI flame speed to the HCCI combustion speed. The first notable feature is the significant spread in the nominal SI flame speed which was

common to the low-pressure and lean SI cases as well (see Fig. 5-33). Just like the adiabatic flame temperature calculations, each case had repeatable mixture and thermodynamic conditions, giving rise to little variation in the calculated flame speed, as seen in Fig. 5-34. The expected spread of the HCCI speed distribution was unknown since it could have had distinct values like the laminar flame speed calculations or a continuous spectrum determined by the temperature gradient distribution and Eqn. (2-2). The second feature to stand out is the distinctive bumps. These were caused by discrete combustion speeds stemming from the one pixel resolution used during combustion front tacking. The distributions could have been smoothed by increasing the bandwidth, but this compromised the overall distribution shape.

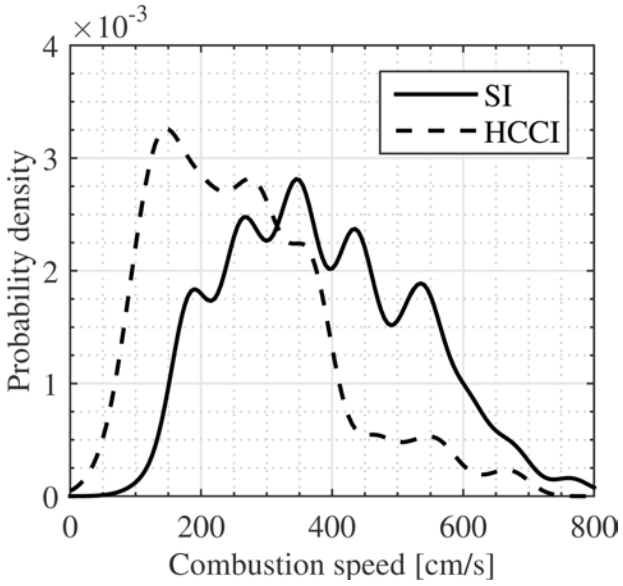

Figure 5-32: Nominal SI and HCCI combustion speed probability distributions.

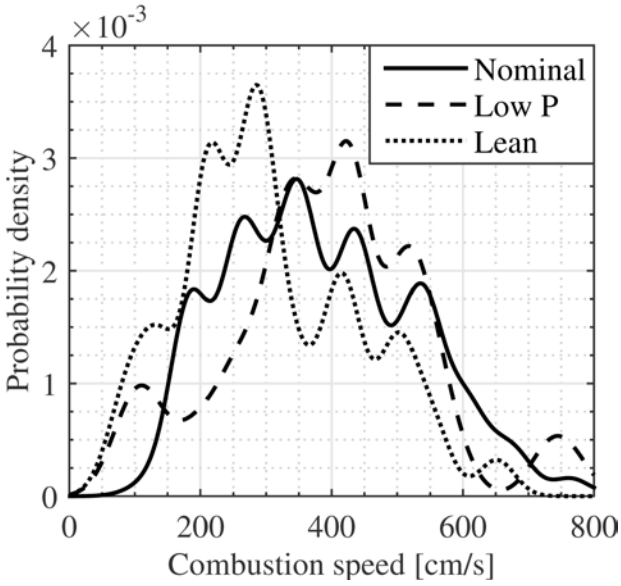

Figure 5-33: Nominal, low-pressure and lean SI combustion speed probability distributions.

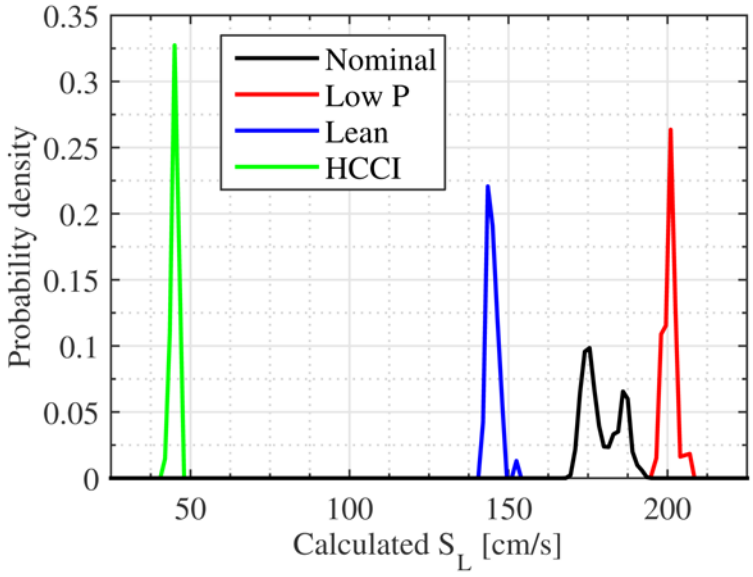

Figure 5-34: Calculated laminar flame speed probability distributions.

Two factors resulted in the combustion speed distributions. The first was due to the oblique combustion fronts. Any combustion front that propagated at any non-normal angle to the laser sheet had an increased measured speed. This is illustrated in Fig. 5-35 where two sets of contours move 10 units each to their second position. The contour oriented normal to the laser plane (black line) is measured to move 10 units. The oblique contour angled at 45^o to the laser plane also moves 10 units, but in the laser plane it is measured to move 14 units ($10/\cos 45^o$). Consequently the combustion front speed increases which adds to the variation seen in Fig. 5-32. As discussed in 5.5, angled combustion fronts also have an increased measured thickness. To understand if this was a dominant effect, scatter plots of the combustion speed as a function of the front thickness were analyzed. Because the SI cases were expected to have uniform speeds and thin flames, any angled flames would deviate with detectable patterns (i.e. increased thickness and speed). Figure 5-36 shows the nominal SI case's scatter plot. It is seen there was no correlation between thicker flames and faster speeds, which was true for the low pressure and

lean cases as well. The results suggest that another factor influenced the wide variance of flame speeds. The scatter plot analysis only works for the SI cases as the speed and thickness distributions had a presumed shape stemming from uniformity of the thickness and speed. For HCCI, the thickness and speed distributions were unknown, but for reference, the HCCI scatterplot has a similar shape to the Fig. 5-36.

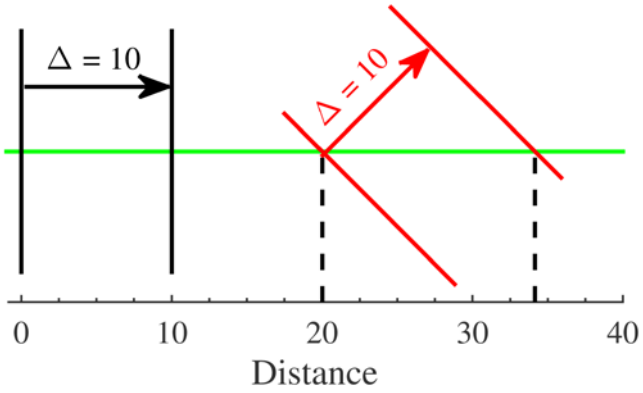

Figure 5-35: Diagram of an oblique combustion front (red lines) giving a greater measured displacement than a normal combustion front (black lines). The laser plane is marked by the green line.

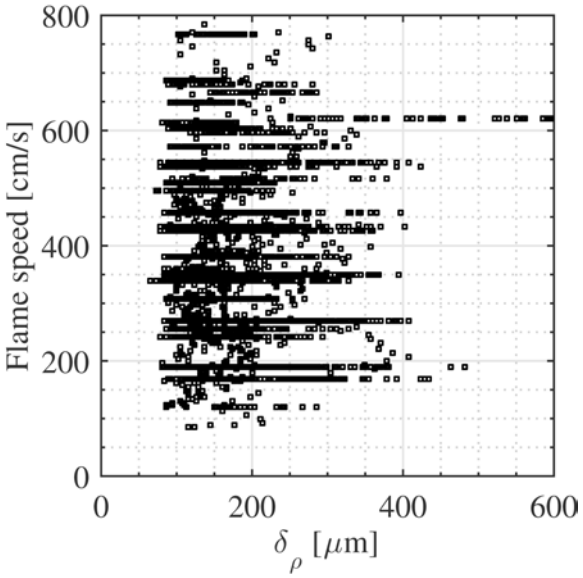

Figure 5-36: Nominal SI measured flame speed vs. combustion front thickness.

The second and likely more influential factor was the in-cylinder flow. Section 4.4.5 discussed that the swirl velocity was set to a minimum, yet large in-cylinder flow velocities were measured by tracking particles in the flow. The tracked particle velocities used to correct the combustion front velocities were assumed to be representative of the in-cylinder flow at the combustion front location, but the wide SI speed distributions of Fig. 5-33 say otherwise. Figure 5-37a) and b) are 2-D histograms of the flow field velocity vector components of the nominal SI and HCCI data sets, respectively. One data point was used for each tracked contour, which was 148 and 156 for the nominal SI and HCCI (see Table 5-2). For reference, Figs. 4-22 and 5-37

share the same coordinate system such that the center of the cylinder is to bottom right of the origin given by green asterisk. The SI flow field velocity was essentially limited to the second quadrant which was the global reaction progression direction. This demonstrates that the in-cylinder flow field at the combustion front was driven by the pressure equilibrating across the combustion front, which is why the constant pressure assumption was applied to the thermometry calculations. The stochastic HCCI combustion front locations, on the other hand, resulted in random flow field velocities. Their speed (magnitude of the velocity) was less than the SI flow fields due to less heat release resulting in less pressure equilibration.

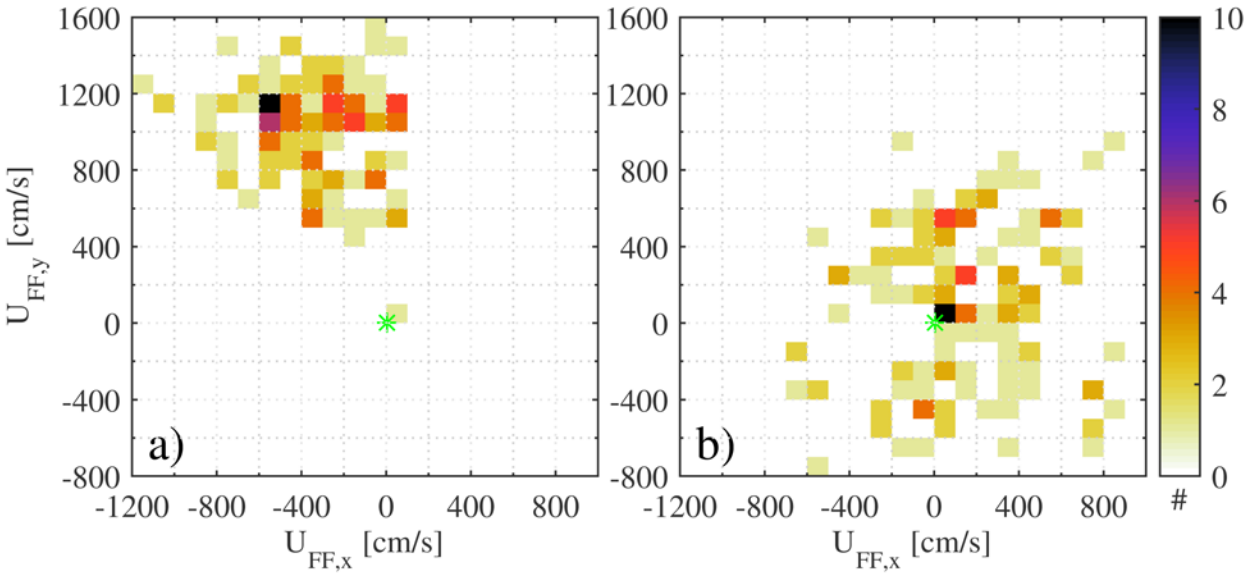

Figure 5-37: Nominal SI (a) and HCCI (b) in-cylinder flow field velocity vectors. The color bar represents the number of contours per bin. The origin (zero flow field velocity) is given by the green asterisk.

The flow field velocities were greater than the resulting combustion propagation speed which makes calculating the combustion speed accurately difficult. The uncertainty associated with the large correction was not accounted for in the uncertainty calculations, which have not been presented due to their nearly single-valued calculation of 4 cm/s. Other methods of calculating the flow field were tested to obtain more accurate correction. The most notable was

tracking the reactants' center of intensity. This method assumed equal burning rates and propagation angles relative to the laser sheet for all combustion fronts. The equal burning rates assumption was likely invalid for the HCCI case, and both SI and HCCI would easily violate the angle of propagation assumption. Typically, though, the reactant masses extended too far to reliable track or did not have trackable features. As a result more erroneous results were acquired than the particle-tracking method.

Because of the large flow field velocities in the SI experiments, it is believed the results were easily skewed by not being able to fully resolve the local flow field around the individual combustion fronts. This led to the high variability of the measured laminar flame speed in Fig. 5-33. The HCCI data had smaller flow field velocities which gave more confidence in the HCCI combustion speeds since the flow field term was a smaller portion of the total combustion front movement.

5.8 Combustion Propagation Mechanism

Sections 5.6 and 5.7 demonstrated substantial issues with the temperature gradient and combustion speed measurements. Those issues made classification of the HCCI combustion mode per the Chen et al. [49] proposal difficult. Figure 5-38 shows the measured HCCI combustion speed as a function of the temperature gradient. For reference, the same plot from Chen's 2-D DNS simulations is shown below in the inset plot. The measurements do not show the same inverse relationship that the simulations do. In reality, the variability in the measurements obscured any trend that did exist. The majority of the measurements are concentrated in the region with temperature gradients between 1 and 5 K/μm and combustion speeds between 100 and 400 cm/s.

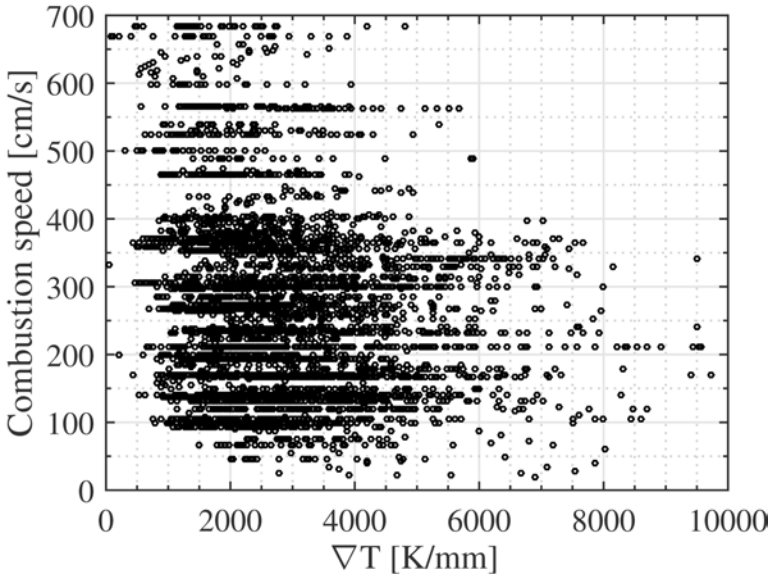

Figure 5-38: HCCI combustion speed as a function of the temperature gradient.

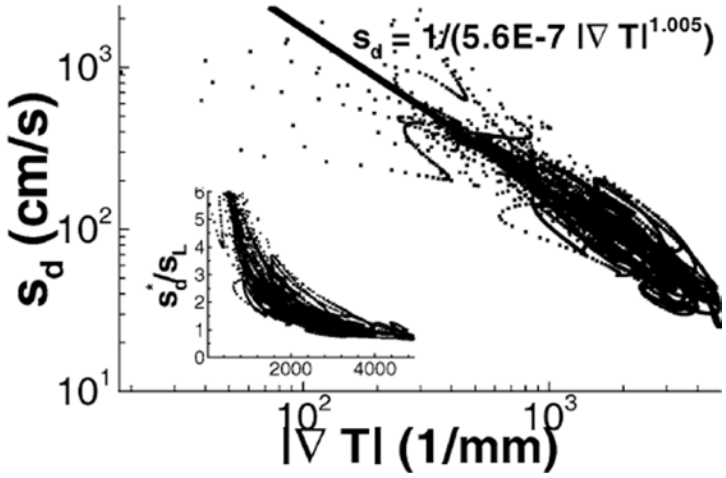

Combustion speed vs. temperature gradient extracted from 2-D DNS simulations. Adapted from Chen et al. [49].

To understand if any evidence of flame propagation existed in the HCCI measurements, the data were fit using Eqn. (2-2) repeated here.

$$s_{ig} = \left|\frac{d\tau}{dT}\right|^{-1}\left|\frac{1}{\nabla T}\right|$$

For comparison to Chen's plot, Fig. 5-39 shows a log-log plot of Fig. 5-38 where two nonlinear least-squares regressions were calculated. The first fit (black line) forced the inverse temperature gradient scaling and calculated the ignition delay temperature sensitivity term. Undoubtedly the data is not modeled well by Eqn. (2-2). The second fit (red line) allowed the fitting function to solve for both $d\tau/dT$ and the temperature gradient dependence. The second curve fit is more appropriate, but the widely varying data suggests a curve fit is not appropriate to begin with.

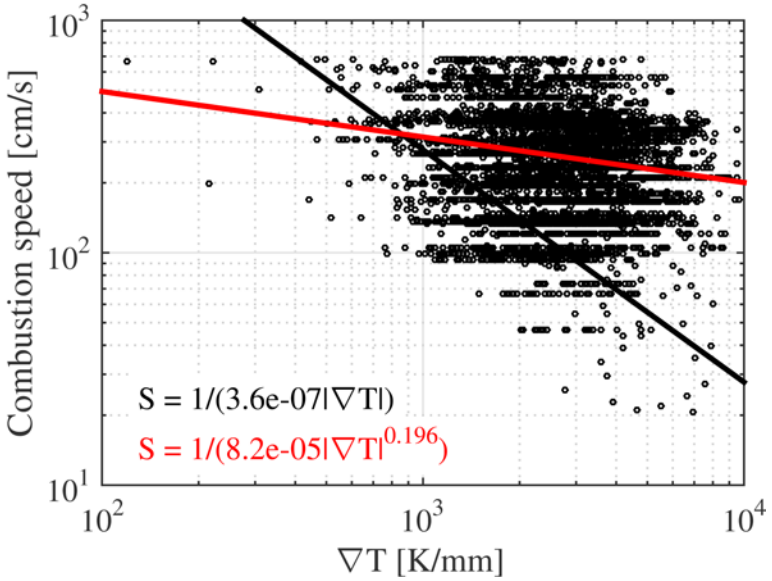

Figure 5-39: Log-log plot of the HCCI combustion speed as a function of the temperature gradient. Two nonlinear least-squares curve fits (black and red lines) were applied to the data.

The curve fits provided two different ignition delay temperature sensitivities: 3.6e-7 and 8.2e-5 s/K. The fitted sensitivities were approximately an order of magnitude different than from the sensitives calculated using the ignition delay simulations, as shown in Fig. 5-40; the single- and dual-image distributions have a mean of 8.5e-6 and 8.6e-6 s/K. Because the curve fits in Fig. 5-39 were impractical, and the ignition delay simulations were shown to agree well with experiments, the sensitivity distributions in Fig. 5-40 were taken as the correct values. Using the temperature gradient and $d\tau/dT$ distributions in Eqn. (2-2) yields the predicted successive

autoignition front propagation speeds shown in Fig. 5-41. The predicted speeds are quite low, but only two factors affect the speed: $d\tau/dT$ and the temperature gradient. If the curve fit sensitivity of 3.6e-7 s/K was used, the mean speed would increase from 6 to 143 cm/s which is still on the low end of the measured propagation speeds but greater than the calculated laminar flame speeds for the HCCI mixture (see Fig. 4-14). Smaller temperature gradients would be required to increase the calculated speed. It was discussed in Section 5.6 that the measured gradient values are smaller than if the calculated temperatures had reached the adiabatic flame temperature, which suggests the gradients are under-calculated. Therefore increasing the temperature gradient would further decrease the calculated propagation speed, making it substantially smaller than the calculated laminar flame speeds. Yoo et al. [53] performed similar 2-D DNS studies as Chen et al. [49] but with lean n-heptane mixtures with initial conditions in NTC regime where $d\tau/dT$ is small, similar to this study. Deflagrations were identified in the combustion fronts, but comparisons were not made with calculations using Eqn. (2-2). Therefore, it is a possibility that the equation breaks down with ignition delays in the NTC regime.

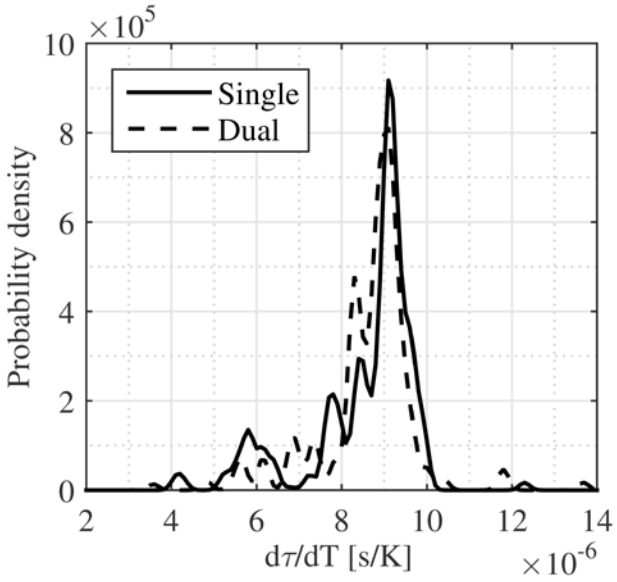

Figure 5-40: Ignition delay temperature sensitivity distributions of the single- and dual-image HCCI data.

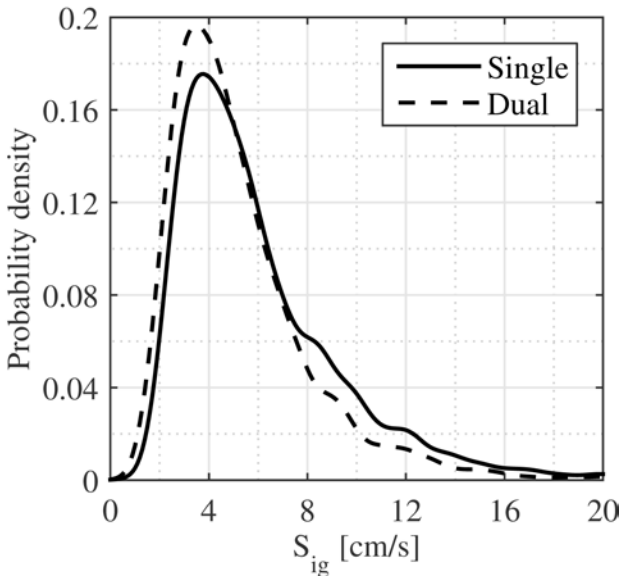

Figure 5-41: Calculated HCCI combustion speed via Eqn. (2-2).

A transition between successive autoignition and flame propagation was not seen in Fig. 5-39, but this does not signify that flame propagation did not occur, it merely did not reject the null hypothesis that flame propagation does not occur in HCCI combustion. The uncertainties associated with the speed measurements were unfortunately too high to conclusively complete the analysis. Additionally, Zeldovich's [48] proposal expanded to include the temperature gradient may fail under certain conditions as it has not been validated across a range of engine-like conditions. Although flame propagation was not explicitly observed, the minimum measured combustion front thicknesses were very close to the measured spark-ignition measurements. If the laminar flame speed is scaled as $S_L = 2\alpha/\delta$ where α is the thermal diffusivity, the relative flame speeds can be calculated. Evaluating the thermal diffusivity at an average temperature of the reactants and the adiabatic flame temperature results in HCCI having a 44% slower laminar flame speed. This could assist in the classification of the propagation mode, but accurate combustion speed measurements of both SI and HCCI are still required to make the comparison.

Chapter 6 - Conclusions

6.1 Summary

The combustion propagation mechanism of homogeneous charge compression ignition combustion was investigated using planar laser Rayleigh scattering thermometry. The experiments were performed in a small-bore, high-speed engine with Bowditch-style optical access. An Nd:YAG laser operated at 532 nm provided the excitation source for the measurements. The laser sheet, formed with a single cylindrical lens, entered the engine offset horizontally from the center to avoid the central spark plug/injector hole and at an axial position that should be unaffected by the thermal boundary layers of the cylinder head and piston surfaces. The scattered light was collected through a window mounted in the piston crown, and was imaged with either a non-intensified or an intensified interline transfer CCD camera.

The sensitivity of Rayleigh scattering measurements to elastically scattered stray light required extensive preventative measures to ensure the success of the measurements. All metallic engine components were painted with high-temperature, low-emissivity matte black paint. The laser entrance window had a small aperture to prevent scattered light from the sheet forming optics entering the engine; the chamber side of the window holder had another aperture to reduce the amount of light scattered from the entrance window. The laser-exit window was oriented at Brewster's angle to minimize the amount of reflected light. A window mounted in the cylinder head provided the lowest background level for the measurements. Ethylene and gaseous dimethyl ether were introduced in the intake system to ensure no liquid droplets (potential scatterers) entered the engine; additionally, the two fuels provided the smallest Rayleigh

scattering cross sectional change across the combustion front for given operating condition requirements.

An in-depth development of the image- and data-processing techniques, as well as all associated uncertainties, was presented. Image processing was seriously hindered by striations induced by beam steering, which made image processing difficult; whole data sets of high-pressure HCCI were rendered unusable. The HCCI images were analyzed for sharp intensity gradients that would provide the highest chance of seeing evidence of flame propagation. The HCCI measurements yielded temperatures lower than a comparable spark ignition (SI) condition, and the resulting temperature gradients had values up to 8 K/μm. The HCCI combustion front thicknesses ranged as low as 80 μm, which were comparable with the SI flame front thickness, to several millimeters (although these regions were not quantitatively investigated). The combustion front propagation speed was estimated for SI and HCCI conditions by acquiring two images spaced closely in time. The measurements relied on the presence of small particles in the field to correct for the chamber fluid motion; the combustion-induced in-cylinder flow field was quite significant, and the combustion front speed measurements were, therefore, unreliable.

Three spark-ignition operating conditions provided baseline measurements to assess the measurement technique's ability to replicate physical trends. In addition to a nominal stoichiometric case, a stoichiometric lower-pressure case and a lean case matching the nominal pressure were tested. The temperature results, already known to be imprecise, were not able to capture the trends expected for adiabatic combustion. The flame thickness measurements did not reproduce the laminar flame thickness scaling laws, but the differences predicted by laminar flame calculations were approximately equal to the uncertainty of the measurements.

Image analysis showed that the flare correction heavily influenced the temperature calculation; a wide range of temperatures (realistic or not) could be achieved. When using the nominally detected flare correction values, the higher signal-to-noise ratio single-image measurements nominally had temperature uncertainties of ~60 K (8%) in the reactants and 150-400 K (15%) in the products. The temperature gradient uncertainty was, on average, 10% (0.7 K/μm for SI and 0.3 for HCCI). The density measurements had the same uncertainty as the temperature due to their common terms, but the thickness measurements were not affected by the flare correction. The temperature-based thickness was 8% and 2% smaller than the density-based thickness with uncertainty that was 36% greater for SI and 31% for HCCI, respectively. Density-based thickness measurements had an absolute uncertainty of 0.7 and 0.3 K/μm for SI and HCCI, respectively.

The HCCI measurements yielded temperatures lower than the nominal SI condition as was expected. The product temperatures were even lower than their respective adiabatic temperatures by a larger amount than was observed in the SI data. The HCCI images showed the possibility of partial combustion where the products were at an intermediate state between reactants and adiabatic flame condition, thus giving a lower temperature. The resulting temperature gradients had values up to 8 K/μm in spite of the low post-reaction temperatures. The combustion front thicknesses ranged down to as low as 80 μm, a thickness that was consistent the value measured for the SI flame front thickness. The combustion speed measurements for SI and HCCI were subject to high levels of uncertainty as a result of the combustion-induced in-cylinder flow field correction. Particles were tracked in the laser sheet to resolve the flow field, but high amounts of variability were still observed in all measurements.

The greatest spread was seen with the SI measurements which should have been nearly single-valued, which signifies the speed measurements were unreliable.

A transition between successive autoignition and flame propagation was not observed when investigating the dependency between the combustion speed and the temperature gradient as had been suggested in the literature, but the uncertainties in the measured temperature gradient and, especially, the combustion speeds did not permit a conclusive determination about the role of flame propagation in HCCI. Based on the fact that HCCI combustion front thicknesses comparable to those for SI combustion were observed, however, it can be concluded that the presence of flame propagation in HCCI combustion is a very real possibility.

6.2 Future Work

The current study showed that flame propagation cannot be definitely ruled out of HCCI combustion. Future work can further the investigation by overcoming the speed measurement limitations. Additionally, a mixed mode spark-assisted HCCI regime can be utilized to produce flame propagation and HCCI results with the same air/fuel mixture. This would eliminate the fuel influence of the results, but the operating conditions must be chosen carefully, though, to minimize beam steering. Finally, research addressing the connection between the thickness and the combustion propagation mechanism would prove useful given the robustness of the thickness measurements, especially if the temperature and combustion speed accuracy issues persist.

Chapter 7 - Abbreviations

CARS	Coherent Anti-Stokes Raman Scattering
CDC	Conventional Diesel Combustion
CO	Carbon Monoxide
CO_2	Carbon Dioxide
DC	Dark Current
DI	Direct-injection
DPF	Diesel Particulate Filter
EGR	Exhaust Gas Recirculation
EOI	End of Injection
FOV	Field of View
FWHM	Full Width at Half Maximum
HCCI	Homogeneous Charge Compression Ignition
HRR	Heat Release Rate
IMEP	Indicated Mean Effective Pressure
IR	Infrared
LF	Laser Flare
LII	Laser Induced Incandescence
LSF	Line Spread Function
LTC	Low-Temperature Combustion
LTO	Low-Temperature Oxidation
MCP	Microchannel Plate
MTF	Modulation Transfer Function
NOx	Oxides of Nitrogen
NTC	Negative Temperature Coefficient
PFI	Port Fuel Injection
PLIF	Planar Laser-Induced Fluorescence
PPC	Partially Premixed Charge
PPCI	Partially Premixed Compression Ignition
RCCI	Reactivity Controlled Compression Ignition
RCM	Rapid Compression Machine
Re	Reynolds number
ROI	Rate of Injection
SCR	Selective Catalytic Reduction
SI	Spark-ignition
SNR	Signal-to-Noise Ratio
SOI	Start of Injection
SRF	Step Response Function
STP	Standard Temperature and Pressure
TDC	Top Dead Center
UHC	Unburned Hydrocarbon
UV	Ultraviolet

Chapter 8 - References

1. Zhao, F., Lai, M.C. and Harrington, D.L., "Automotive spark-ignited direct-injection gasoline engines," Prog. Energy Combust. Sci., 25, pp. 437-562, 1999.
2. Drake, M.C., Fansler, T.D. and Lippert, A.M., "Stratified-charge combustion: modeling and imaging of a spray-guided direct-injection spark-ignition engine," Proc. Combust. Inst., 30, pp. 2683-2691, 2005.
3. Heywood, J.B, *Internal Combustion Engine Fundamentals*, New York: McGraw-Hill, 1988.
4. Dec, J.E., "A conceptual model of di diesel combustion based on laser-sheet imaging," SAE Technical Paper 970873, 1997.
5. Christensen, M., Johansson, B., Amnéus, P. and Mauss, F., "Supercharged homogeneous charge compression ignition," SAE Technical Paper 980787, 1998.
6. Ra, Y., Loeper, P., Reitz, R., Andrie, M., Krieger, R., Foster, D., Durrett, R., Gopalakrishnan, V., Plazas, A., Peterson, R. and Szymkowicz, P., "Study of high speed gasoline direct injection compression ignition (GDICI) engine operation in the LTC regime," SAE Technical Paper 2011-01-1182, 2011.
7. Kokjohn, S.L., Hanson, R.M., Splitter, D.A. and Reitz, R.D., "Experiments and modeling of dual fuel HCCI and PCCI combustion using in-cylinder fuel blending," SAE Technical Paper 2009-01-2647, 2009.
8. Smith, J.R., "Turbulent flame structure in a homogeneous-charge engine," SAE Technical Paper 820043, 1982.
9. Dec, J.E. and Coy, E.B., "OH radical imaging in a DI diesel engine and the structure of the early diffusion flame," SAE Technical Paper 960831, 1996.
10. Turns, S.R., *An Introduction to Combustion: Concepts and Applications*, McGraw-Hill, 2000.
11. Daniel, W.A., "Flame quenching at the walls of an internal combustion engine," Symp. (Int.) Combust., 6, pp. 886-894, 1957.
12. Bradley, D. and Kalgatghi, G.T., "Influence of autoignition delay time characteristics of different fuels on pressure waves and knock in reciprocating engines," Combust. and Flame, 156, pp. 2307-2318, 2009.
13. Bradley, D., Morley, C., Gu, X.J. and Emerson, D.R., "Amplified pressure waves during autoignition: relevance to CAI engines," SAE Technical Paper 2002-01-2868, 2002.
14. Onishi, S., Jo, S.H., Shoda, K., Jo, P.D. and Kata, S., "Active thermo-atmosphere combustion (ATAC) – A new combustion process for internal combustion engines," SAE Technical Paper 790501, 1979.
15. Najt, P.M and Foster, D.E., "Compression-ignited homogeneous charge combustion," SAE Technical Paper 830264, 1983.
16. Zhao, F., Asmus, T.W., Assanis, D.N., Dec, J.E., Eng, J.A. and Najt, P.M., *Homogeneous Charge Compression Ignition (HCCI) Engines – Key Research and Development Issues*, Warrendale, PA: Society of Automotive Engineers, Inc., 2003.
17. Epping, K., Aceves, S., Bechtold, R. and Dec, J., "The potential of HCCI combustion for high efficiency and low emissions," SAE Technical Paper 2002-01-1923, 2002.

18. Hultqvist, A., Christensen, M., Johansson, B., Franke, A., Richter, M. and Aldén, M., "A study of the homogeneous charge compression ignition combustion process by chemiluminescence imaging," SAE Technical Paper 1999-01-3680, 1999.
19. Dec, J.E., Hwang, W. and Sjöberg, M., "An investigation of thermal stratification in HCCI engines using chemiluminescence imaging," SAE Technical Paper 2006-01-1518, 2006.
20. Aceves, S.M., Smith, J.R., Westbrook, C. and Pitz, W., "Compression Ratio effect on methane HCCI combustion," ASME J. of Eng. Gas Turbines and Power, 121, pp. 569-574, 1999.
21. Iverson, R.J., Herold, R.E., Augusta, R., Foster, D.E., Ghandhi, J.B., Eng, J.A. and Najt, P.M., "The effects of intake charge preheating in a gasoline-fueled HCCI engine," SAE Technical Paper 2005-01-3742, 2005.
22. Martinez-Frias, J., Aceves, S.M., Flowers, D., Smith, J.R. and Dibble, R., "HCCI engine control by thermal management," SAE Technical Paper 2000-01-2869, 2000.
23. Aceves, S., Flowers, D.L., Westbrook, C.K., Smith, J.R., Pitz, W., Dibble, R.W., Christensen, M. and Johansson, B., "A multi-zone model for prediction of HCCI combustion and emissions," SAE Technical Paper 2000-01-0327, 2000.
24. Hasegawa, R., Sakata, I., Yanagihara, H., Aldén, M. and Johansson, B., "Quantitative analysis of the relation between flame structure and turbulence in HCCI combustion by two-dimensional temperature measurement," SAE Technical Paper 2008-01-0061, 2008.
25. Hyvönen, J., Haraldsson, G. and Johansson, B., "Operating conditions using spark assisted HCCI combustion during combustion mode transfer to SI in a multi-cylinder VCR-HCCI engine," SAE Technical Paper 2005-01-0109, 2005.
26. Kaiser, E.W., Yang, J., Culp, T., Xu, N. and Maricq, M.M., "Homogeneous charge compression ignition engine-out emissions– Does flame propagation occur in homogeneous charge compression ignition?," Int. J. Engine Res., 3, pp. 185-195, 2002.
27. Roberts, C.E., Matthews, R.D. and Leppard, W.R., "Development of a semi-detailed kinetics mechanism for the autoignition of iso-octane." SAE Technical Paper 962107, 1996.
28. Kamimoto, T. and Bae, M-H., "High combustion temperature for the reduction of particulate in diesel engines," SAE Technical Paper 880423, 1988.
29. Siebers, D., Higgins, B. and Pickett, L., "Flame lift-off on direct-injection diesel fuel jets: oxygen concentration effects," SAE Technical Paper 2002-01-0890, 2002.
30. Street, J.C. and Thomas, A., "Carbon formation in pre-mixed flames," Fuel, 34, pp. 4-36, 1955.
31. Homann, K.H., "Carbon formation in premixed flames," Combust. and Flame, 11, pp. 265-287, 1967.
32. Kalghatgi, G.T., Risberg, P. and Angstrom, H-E, "Advantages of fuels with high resistance to auto-ignition in late-injection, low-temperature, compression ignition combustion," SAE Technical Paper 2006-01-3385, 2006.
33. Dec, J.E., Yang, Y. and Dronniou, N., "Boosted HCCI – controlling pressure-rise rates for performance improvements using partial fuel stratification with conventional gasoline," SAE Technical Paper 2011-01-0897, 2011.
34. Manente, V., Johansson, B. and Tunestal, P., "Partially premixed combustion at high load using gasoline and ethanol, a comparison with diesel," SAE Technical Paper 2009-01-0944, 2009.

35. Schmid, M., Kaiser, M., Koch, P., Wensing, M. and Leipertz, A., “Optical investigations on partially premixed diesel combustion for different operating parameters,” SAE Technical Paper 2008-01-0041, 2008.
36. Inagaki, K., Fuyuto, T., Nishikawa, K., Nakakita, K. and Sakata, I., “Dual-fuel PCI combustion controlled by in-cylinder stratification of ignitability,” SAE Technical Paper 2006-01-0028, 2006.
37. Hanson, R.M., Splitter, D.A., Kokjohn, S.L. and Reitz, R. D., “An experimental investigation of fuel reactivity controlled PCCI combustion in a heavy-duty engine,” SAE Technical Paper 2010-01-0864, 2010.
38. Splitter, D.A., Kokjohn, S.L., Rein, K.D., Hanson, R.M., Sanders, S.T. and Reitz, R.D., “An optical investigation of ignition processes in fuel reactivity controlled PCCI combustion,” SAE Technical Paper 2010-01-0345, 2010.
39. Curran, S., Prikhodko, V., Cho, K., Sluder, C., Parks, J., Wagner, R., Kokjohn, S. and Reitz, R., “In-cylinder fuel blending of gasoline/diesel for improved efficiency and lowest possible emissions on a multi-cylinder light duty diesel engine,” SAE Technical Paper 2010-01-2206, 2010.
40. Prikhodko, V.Y., Curran, S.J., Barone, T.L., Lewis, S.A., Storey, J.M., Cho, K., Wagner, R.M. and Parks, J. E., “Emission characteristics of a diesel engine operating with in-cylinder gasoline and diesel fuel blending,” SAE Technical Paper 2010-01-2266, 2010.
41. Splitter, D.A., Hanson, R.M., Kokjohn, S.L. and Reitz, R.D., “Reactivity controlled compression ignition (RCCI) heavy-duty engine operation at mid-and high-loads with conventional and alternative fuels,” SAE Technical Paper 2011-01-0363, 2011.
42. Blessinger, M.K. and Ghandhi, J.B., “Initial optical investigation of reactivity controlled combustion in an HSDI engine,” *Seventh US National Technical Meeting*, The Combustion Institute, Atlanta, GA, 2011.
43. Kokjohn, S.L., Reitz, R.D. and Musculus, M.P.B., “Chemiluminescence and fuel PLIF imaging of reactivity controlled compression ignition (RCCI) combustion,” *Twenty-third Annual Conference on Liquid Atomization and Spray Systems*, ILASS Americas, Ventura, CA, 2011.
44. Blessinger, M., Stein, J. and Ghandhi, J., “An optical investigation of fuel composition effects in a reactivity controlled HSDI engine,” SAE Int. J. Engines, 5, 2012.
45. Karim, G.A., “A review of combustion processes in the dual fuel engine – the gas diesel engine,” Prog. Energy Combust. Sci., 6, pp. 277-285, 1980.
46. Kokjohn, S.L., “Reactivity controlled compression ignition,” Ph.D. Thesis, University of Wisconsin, Madison, WI, 2012.
47. Singh, S., Reitz, R.D., Wickman, D., Stanton D. and Tan, Z., “Development of a hybrid, auto-ignition/flame-propagation model and validation against engine experiments and flame liftoff,” SAE Technical Paper 2007-01-0171, 2007.
48. Zeldovich, Y.B., “Regime classification for an exothermic reaction with nonuniform initial conditions,” Combust. and Flame, 39, pp. 211-214, 1980.
49. Chen, J.H., Hawkes, E.R., Sankaran, R., Mason, S.D. and Im, H.G., “Direct numerical simulation of ignition front propagation in a constant volume with temperature inhomogeneities – i. fundamental analysis and diagnostics” Combust. and Flame, 145, pp. 128–144, 2006.

50. Hawkes, E.R., Sankaran, R., Pébay, P.P. and Chen, J.H., "Direct numerical simulation of ignition front propagation in a constant volume with temperature inhomogeneities – ii. parametric study," Combust. and Flame, 145, pp. 145–159, 2006.
51. Sankaran, R., Im, H.G., Hawkes, E.R. and Chen, J.H., "The effects of non-uniform temperature distribution on the ignition of a lean homogeneous hydrogen-air mixture," Proc. Combust. Inst., 30, pp. 875–882, 2005.
52. Bansal, G. and Im, H., "Autoignition and front propagation in low temperature combustion engine environments," Combust. and Flame, 158, pp. 2105-2112, 2011.
53. Yoo, C.S., Lu, T., Chen, J.H. and Law, C.K., "Direct numerical simulations of ignition of a lean n-heptane / air mixture with temperature inhomogeneities at constant volume: parametric study," Combust. and Flame, 158, pp. 1727-1741, 2011.
54. Martz, J.B., Kwak, H., Im, H.G., Lavoie, G.A. and Assanis, D.N., "Combustion regime of a reacting front propagating into an auto-igniting mixture," Proc. Combust. Inst., 33, pp. 3001-3006, 2011.
55. Heim, D.M. and Ghandhi, J.B., "A detailed study of in-cylinder flow and turbulence using PIV," SAE Technical Paper 2011-01-1287, 2011.
56. Rothamer, D.A. and Ghandhi, J.B., "Determination of flame-front equivalence ratio during stratified combustion," SAE Technical Paper 2003-01-0069, 2003.
57. Arnold, A., Buschmann, A., Cousyn, B., Decker, M., Vannobel, F., Sick, V. and Wolfrum, J., "Simultaneous imaging of fuel and hydroxyl radicals in an in-line four cylinder si engine," SAE Technical Paper 932696, 1993.
58. Neij, H., Johansson, B. and Alden, M., "Development and demonstration of 2D-LIF for studies of mixture preparation in SI engines," Combust. and Flame, 99, pp. 449-457, 1994.
59. Felton, P.G., Mantzaras, J., Bomse, D.S. and Woodin, R.L., "Initial two-dimensional laser induced fluorescence measurements of OH radicals in an internal combustion engine," SAE Technical Paper 881633, 1988.
60. zur Loye, A.O. and Bracco, F.V., "Two-dimensional visualization of ignition kernels in an IC engine," Combust. and Flame, 69, pp. 59-69, 1987.
61. Mantzaras, J., Felton,,P.G. and Bracco, F.V., "3-D visualization of premixed-charge engine flames: islands of reactants and products; fractal dimension; and homogeneity," SAE Technical Paper 881635, 1988.
62. Koban, W., Koch, J.D., Sick, V., Wermuth, N., Hanson, R.K. and Schulz, C., "Predicting LIF signal strength for toluene and 3-pentanone under engine-related temperature and pressure conditions," Proc. Combust. Inst., 30, pp. 1545-1553, 2005.
63. Burton, C.S. and Noyes, W.A., "Electronic energy relaxation in toluene vapor," J. Chem. Phys., 49, pp. 1705-1714, 1968.
64. Nguyen, Q.-V. and Paul, P.H., "The time evolution of a vortex-flame interaction observed via planar imaging of CH and OH," Twenty-Sixth Symp. (Int.) on Combust., The Combust. Inst., pp. 357–364, 1996.
65. Schrewe, M.R. and Ghandhi, J.B., "Near-wall formaldehyde planar laser-induced fluorescence measurements during HCCI combustion," Proc. Combust. Inst., 31, pp. 2871-2878, 2007.
66. Bijjula, K. and Kyritsis, D.C., "Experimental evaluation of flame observables for simplified scalar dissipation rate measurements in laminar diffusion flamelets," Proc. Combust. Inst., 30, pp. 493-500, 2005.

67. Kim, T. and Ghandhi, J.B., “Investigation of light load HCCI combustion using formaldehyde planar laser-induced fluorescence,” Proc. Combust. Inst., 30, pp. 2675-2682, 2004.
68. Najm, H.B., Paul, P.H., Mueller, C.J. and Wyckoff, P.S., “On the adequacy of certain experimental observables as measurements of flame burning rate,” Combust. and Flame, 113, pp. 312-332, 1998.
69. Bruneaux, G., “Liquid and vapor spray structure in high-pressure common rail diesel injection,” At. Sprays, 11, pp. 533-556, 2001.
70. Xu, H., Chen, X., Ouyang, S., Kako, T. and Ye. J., “Size-dependent Mie’s scattering effect on TiO2 spheres for the superior photoactivity of H2 evolution.” J. Phys. Chem., 116, pp. 3833-3839, 2012.
71. Einecke S., Schulz C., and Sick V., “Measurement of temperature, fuel concentration and equivalence ratio fields using tracer LIF in IC engine combustion.” Appl. Phys. B-Lasers and Optics, 71, pp. 717-723, 2000.
72. Rothamer, D.A., Snyder, J., Hanson, R.K. and Steeper, R.R., “Two-wavelength PLIF diagnostic for temperature and composition,” SAE Technical Paper 2008-01-1067, 2008.
73. Dec, J.E. and Hwang, W., “Characterizing the development of thermal stratification in an HCCI engine using planar-imaging thermometry,” SAE Technical Paper 2009-01-0650, 2009.
74. Seitzman, J.M., Hanson, R.K., DeBarber, P.A. and Hess C.F., “Application of quantitative two-line OH Planar laser-induced fluorescence for temporally resolved planar thermometry in reacting flows,” Appl. Optics, 33, pp. 4000-4012, 1994.
75. Eckbreth, A.C., Bonczyk, P.A. and Verdieck, J.F., “Laser raman and fluorescence techniques for practical combustion diagnostics,” Prog. Energy Combust. Sci., 5, pp. 253-322, 1979.
76. Dibble, R.W., Masri, A.R. and Bilger, R.W., “The spontaneous Raman scattering technique applied to nonpremixed flames of methane,” Combust. and Flame, 67, pp. 189-206, 1987.
77. Stenhouse, I.A., Williams, D.R., Cole, J.B. and Swords M.D., “CARS measurements in an internal combustion engine,” Appl. Opt., 18, pp. 3819-3825, 1979.
78. Hall, R.J., “CARS spectra of combustion gases,” Combust. and Flame, 35, pp. 47-60, 1979.
79. Hall, R.J. and Eckbreth, A.C, “Combustion diagnosis by coherent anti-stokes Raman spectroscopy (CARS),” Opt. Eng., 20, pp. 494-500, 1981.
80. Rothamer, D.A. and Jordan, J., "Planar imaging thermometry in gaseous flows using upconversion excitation of thermographic phosphors," Appl. Phys. B: Lasers and Opt., 106, pp. 435-444, 2011.
81. Jordan, J. and Rothamer, D.A., “Pr:YAG temperature imaging in gas-phase flows,” Appl. Phys. B: Lasers and Opt., 110, pp. 285-291, 2013.
82. Espey, C., Dec, J.E., Litzinger, T.A. and Santavicca, D.A., “Planar laser Rayleigh scattering for quantitative vapor-fuel imaging in a diesel jet,” Combust. and Flame, 109, pp. 65-86, 1997.
83. Arcoumanis, C., Green, H.G. and Whitelaw, J.H., “The application of laser Rayleigh scattering to a reciprocating model engine,” SAE Technical Paper 840376, 1984.
84. Lee, K.-H. and Foster, D.E., “Cycle-by-cycle variations in combustion and mixture concentration in the vicinity of the spark plug gap,” SAE Technical Paper 950814, 1995.

85. Zhao, F.Q. and Hiroyasu, H., "The applications of laser Rayleigh scattering to combustion diagnostics," Prog. Energy Combust. Sci., 19, pp. 447-485, 1993.
86. Strutt, J.W. (Lord Rayleigh), "On the transmission of light through an atmosphere containing small particles in suspension and on the origin of the blue of the sky," Philos. Mag., XLVII, pp. 375-384, 1899.
87. McCartney, E.J., *Optics of the Atmosphere (Scattering by Molecules and Particles)*, New York: John Wiley & Sons, 1976.
88. van de Hulst, H.C., *Light Scattering by Small Particles*, New York: John Wiley & Sons, 1957.
89. Kerker, M., *The Scattering of Light and Other Electromagnetic Radiation*, New York: Academic Press, 1969.
90. Robben, F., "Comparison of density and temperature measurements using Raman scattering and Rayleigh scattering," *Combustion Measurements: Modern Techniques and Instrumentation*, Proceedings of the SQUID Workshop, West Lafayette, IN, 1975.
91. Raman Spectroscopy – Electrochemical Techniques, Gamry Instruments, accessed Feb. 9 2015. <http://www.gamry.com/application-notes/raman-spectroelectrochemistry/>
92. Miles, R.B., Lempert, W.R. and Forkey, J.N., "Laser Rayleigh scattering," Meas. Sci. Technol., 12, pp. R33-R51, 2001.
93. DeKock, R.L. and Gray, H.B., *Chemical Structure and Bonding*, University Science Books, 1989.
94. Born, M. and Wolf, E., *Principles of Optics: Electromagnetic Theory of Propagation, Interference and Diffraction of Light*, Cambridge University Press, 1980.
95. Rothamer, D.A. and Ghandhi, J.B., "On the calibration of single-shot planar laser imaging techniques in engines," SAE Technical Paper 2002-01-0748, 2002.
96. Dibble, R.W. and Hollenbach, R.E., "Laser Rayleigh thermometry in turbulent flames," Eighteenth Symp. (Int.) on Combust., The Combust. Inst., pp. 1489–1499, 1981.
97. Namer, I. and Schefer, R.W., "Error estimates for Rayleigh scattering density and temperature measurements in premixed flames," Exp. in Fluids, 3, pp. 1-9, 1985.
98. Sneep, M. and Ubachs, W., "Direct measurement of the Rayleigh scattering cross section in various gases," J. Quant. Spectrosc. Radiat. Transf., 92, pp. 293-310, 2005.
99. Sutton, J.A. and Driscoll, J.F., "Rayleigh scattering cross sections of combustion species at 266, 355, and 532 nm for thermometry applications," Opt. Letts., 29, pp. 2620-2622, 2004.
100. Smith, J.R., "Rayleigh temperature profiles in a hydrogen diffusion flame," Proc. of SPIE, 158, pp. 84-90, 1978.
101. Gouldin, F.C. and Halthrone, R.N., "Rayleigh scattering for density measurements in premixed flames," Exp. in Fluids, 4, pp. 269-278, 1986.
102. Renou, Y.L, Cabot, G. and Boukhalfa, M., "Experimental determination of laminar flame thickness for CO_2 and H_2 diluted methane/air flames," Proc. Eur. Combust. Meet., 2007.
103. Gardiner, W.C., Hidaka, JR.Y. and Tanzawa, T. "Refractivity of combustion gases," Combust. and Flame, 40, pp. 213-219, 1981.
104. Fuest, F., Barlow, R.S., Chen, J-Y and Dreizler, A., "Raman/Rayleigh scattering and CO-LIF measurements in laminar and turbulent jet flames of dimethyl ether," Combust. and Flame, 159, pp. 2533-2562, 2012.

105. Murphy, W.F., “The Rayleigh depolarization ratio and rotational Raman spectrum of water vapor and the polarizability components for the water molecule,” J. Chem. Phys., 67, pp. 5877-5882, 1977.
106. Bogaard, M.P., Buckingham, A.D., Pierens, R.K. and White, A.H., “Rayleigh scattering depolarization ratio and molecular polarizability anisotropy for gases,” J. Chem. Soc., Faraday Trans. 1, 74, pp. 3008-3015, 1978.
107. Bacskay, G.B., Saebø, S. and Taylor, P.R., “On the calculation of dipole moment and polarizability derivatives by the analytical energy gradient method: application to the formaldehyde molecule,” Chem. Phys., 90, pp. 215-224, 1984.
108. Jenkins, F.A. and White, H.E., *Fundamentals of Optics*, 2nd ed., New York: McGraw-Hill, 1950.
109. Sellmeier, M., “Zur erklärung der abnormen farbenfolge im spectrum einiger substanzen,” Annalen der Physik und Chemie, 219, pp. 272-282, 1871.
110. Graham, S.C., Grant, A.J. and Jones, J.M., “Transient molecular concentration measurements in turbulent flows using Rayleigh light scattering,” Am. Inst. Aeronaut. Astronaut., 12, pp. 1140-1142, 1974.
111. Fielding, J., Frank, J.H., Kaiser S.A., Smooke, M.D. and Long, M.B., “Polarized/depolarized Rayleigh scattering for determining fuel concentrations in flames,” Proc. Combust. Inst., 29, pp. 2703-2709, 2002.
112. Forkey, J.N., “Development and demonstration of filtered Rayleigh scattering – a laser-based flow diagnostic for planar measurement of velocity, temperature and pressure,” PhD Thesis, Princeton University, Princeton, NJ, 1996.
113. Idicheria, C.A. and Pickett, L.M., “quantitative mixing measurements in a vaporizing diesel spray by Rayleigh scattering,” SAE Technical Paper 2007-01-0647, 2007.
114. Blessinger, M., Manin, J., Skeen, S.A., Meijer, M., Parrish, S. and Pickett L.M., “Quantitative mixing measurements and stochastic variability of a vaporizing gasoline direct-injection spray,” Int. J. Engine Res., 16, pp. 238-252, 2015.
115. Espey, C., Dec, J.E., Litzinger, T.A. and Santavicca, D.A., “Quantitative 2-D fuel vapor concentration imaging in a firing D.I. diesel engine using planar laser-induced Rayleigh scattering,” SAE Technical Paper 940682, 1994.
116. Bowditch, F.W., “A new tool for combustion research – A quartz piston engine,” SAE Trans., 69, pp. 17-23, 1961.
117. Lacoste, J., “Characteristics of diesel sprays at high temperatures and pressures,” Ph.D. Thesis, University of Brighton, Brighton, England, 2006.
118. Zhang, J., Yao, S., Himesh, P. and Fang., T., “An experimental study of gasoline direct-injection spray and atomization characteristics of alcohol fuels and isooctane,” Atomization Spray, 21, pp. 363-374, 2011.
119. Kim, B., Kaneko, M., Ikeda, Y. and Nakajima, T., “Detailed spectral analysis of the process of HCCI combustion,” Proc. Combust. Inst., 29, pp. 671-677, 2002.
120. Augusta, R., Foster, D.E., Ghandhi, J.B., Eng, J. and Najt, P.M., “Chemiluminescence measurements of homogeneous charge compression ignition (HCCI) combustion,” SAE Technical Paper 2006-01-1520, 2006.
121. Obertacke, R., Wintrich, H., Wintrich, F. and Leipertz, A., “A new sensor system for industrial combustion monitoring and control using UV emission spectroscopy and tomography,” Combust. Sci. Tech., 121, pp. 133-151, 1996.

122. Kokjohn, S., Hanson, R., Splitter, D., Kaddatz, J. and Reitz, R., "Fuel reactivity controlled compression ignition (RCCI) combustion in light- and heavy-duty engines," SAE Int. J. Engines, 4, pp. 360-374, 2011.
123. Verma, N.K., Khanna, S.K. and Kapila, B, *Comprehensive Chemistry XI*, Laxmi Publications, 2008.
124. Arcoumanis, C., Bae Choongsik, B., Crookes, R. and Kinoshita, E., "The potential of di-methyl ether (DME) as an alternative fuel for compression-ignition engines: A review," Fuel, 87, pp. 1014-1030, 2008.
125. Sorenson, S.C. and Mikkelsen, S.-E., "Performance and emissions of a 0.273 liter direct injection diesel engine fuelled with neat dimethyl ether," SAE Technical Paper 950064, 1995.
126. Longbao, Z., Hewu, W., Deming, J. and Zuohua, H., "Study of performance and combustion characteristics of a DME-fueled light-duty direct-injection diesel engine," SAE Technical Paper 1999-01-3669, 1999.
127. Kumar, K., Mittal, G., Sung, C.J. and Law, C.K., "An experimental investigation of ethylene/O_2/diluent mixtures: laminar flame speeds with preheat and ignition delays at high pressures," Combust. Flame, 153, pp. 343-354, 2008.
128. Kukkadapu, G., Kumar, K., Sung, C.J., Mehl, M. and Pitz, W.J., "Autoignition of gasoline and its surrogates in a rapid compression machine," Proc. Combust. Inst., 34, pp. 345-352, 2013.
129. He, X., Donovan, M.T., Zigler, B.T., Palmer, T.R., Walton, S.M., Wooldridge, M.S. and Atreya, A., "An experimental and modeling study of iso-octane ignition delay times under homogeneous charge compression ignition conditions," Combust. Flame, 142, pp. 266-275, 2005.
130. Fieweger, K., Blumenthal, R. and Adomeit, G., "Self-ignition of S.I. engine model fuels: a shock tube investigation at high pressure," Combust. Flame, 109, pp. 599-619, 1997.
131. Saxena, S., Kahandawala, M.S.P. and Sidhu, S.S., "A shock tube study of ignition delay in the combustion of ethylene," Combust. Flame, 158, pp. 1019-1031, 2011.
132. Pfahl, U., Fieweger, K. and Adomeit, G., "Self-ignition of diesel-relevant hydrocarbon-air mixtures under engine condition," Symp. (Int.) Combust., 26, pp. 781-789, 1996.
133. Ciezki, H.K. and Adomeit, G., "Shock-tube investigation of self-ignition of n-heptane-air mixtures under engine relevant conditions," Combust. Flame, 93, pp. 421-433, 1993.
134. Wakai, K., Nishida, K., Yoshizaki, T. and Hiroyashu, H., "Spray and ignition characteristics of dimethyl ether injected by a D.I. diesel injector," The Fourth International Symposium COMODIA, 1998.
135. Yao, M., Zheng, Z., Xu, S. and Fu, M., "Experimental study on the combustion process of dimethyl ether (DME)," SAE Technical Paper 2003-01-3194, 2003.
136. Tess, M.J., "Size- and speed-scaling of turbulent premixed combustion in a spark-ignition engine," Ph.D. Thesis, University of Wisconsin, Madison, WI, 2014.
137. Hecht, E., *Optics*, Reading, MA: Addison-Wesley, 2002.
138. Brewster, D., "On the laws which regulate the polarisation of light by reflection from transparent bodies," Phil. Trans. R. Soc. Lond., 105, pp. 125-159, 1815.
139. ESCO Optics, Material Data, <www.escooptics.com/material-data/>, 6/24/2013.

140. Musculus, M.P.B. and Pickett, L.M., “Diagnostic considerations for optical laser-extinction measurements of soot in high-pressure transient combustion environments,” Combust. and Flame, 141, pp. 371-391, 2005.
141. Pickett, L.M., Manin, J., Genzale, C.L., Siebers, D., Musculus, M.P.B. and Idicheria, C.A. "Relationship between diesel fuel spray vapor penetration/dispersion and local fuel mixture fraction," SAE Int. J. Engines, 4, pp. 764-799, 2011.
142. Koechner, W. and Bass, M., *Solid-State Lasers: A Graduate Text*, New York, NY: Springer, 2003.
143. Princeton Instruments Imaging Group, MicroMAX System Manual, <ftp://ftp.piacton.com/public/Manuals/Princeton Instruments/Archived Manuals/MicroMAX System Manual.pdf>, 6/7/2013.
144. Princeton Instruments Imaging Group, PI-MAX 4:1024i Datasheet, <http://www.princetoninstruments.com/Uploads/Princeton/Documents/Datasheets/PIMAX 4/Princeton_Instruments_PI-MAX4_1024i_rev_N1_8.30.12.pdf>, 6/28/2013.
145. Wang, G.H. and Clemens, N.T., “Effects of imaging system blur on measurements of flow scalars and scalar gradients,” Exp. Fluid, 37, pp. 194-205, 2004.
146. Mechanical and Aerospace Engineering (Combustion Research), “Chemical-kinetic mechanisms for combustion applications,” University of California - San Diego, <http://web.eng.ucsd.edu/mae/groups/combustion/mechanism.html>, 6/17/2015.
147. Wang, H., You, X., Joshi, A.V., Davis, S.G., Laskin, A., Egolfopoulos, F. and Law, C.K., “USC Mech version II. High-temperature combustion reaction model of H2/CO/C1-C4 Compounds,” <http://ignis.usc.edu/Mechanisms/USC-Mech II/USC_Mech II.htm>, 6/17/2015.
148. Luo, Z., Yoo, C.S., Richardson, E.S., Chen, J.H. Law, C.K. and Lu, T., “Chemical explosive mode analysis for a turbulent lifted ethylene jet flame in highly-heated coflow,” Combust. Flame, 159, pp. 265-274, 2012.
149. Jomaas, G., Zheng, X.L., Zhu, D.L. and Law, C.K., “Experimental determination of counterflow ignition temperatures and laminar flame speeds of C2-C3 hydrocarbons at atmospheric and elevated pressures,” Proc. Combust. Inst., 30, pp. 193-200, 2005.
150. Burke, U., Somers, K.P., O’Toole, P., Zinner, C.M., Marquet, N., et al., “An ignition delay and kinetic modeling study of methane, dimetyhl ether, and their mixtures at high pressures,” Combust. Flame, 162, pp. 315-330, 2015.
151. Li, Z., Wang. W., Huang, Z. and Oehlschlaeger, M.A. “Dimethyl ether autoignition at engine-relevant conditions,” Energy Fuels, 27, pp. 2811-2817, 2013.
152. de Vries, J., Lowry, W.B., Serinyel, Z., Curran, H.J. and Petersen, E.L., “Laminar flame speed measurements of dimethyl ether in air at pressures up to 10 atm,” Fuel, 90, pp. 331-338, 2011.
153. Fischer, S.L., Dryer, F.L. and Curran, H.J., "The reaction kinetics of dimethyl ether. i: high temperature pyrolysis and oxidation in flow reactors," Int. J. Chem. Kinet., 32, pp. 713–740, 2000.
154. Curran, H.J., Fischer, S.L. and Dryer, F.L., "The reaction kinetics of dimethyl ether. ii: low temperature pyrolysis and oxidation in flow reactors," Int. J. Chem. Kinet., 32, pp. 741–759, 2000.

155. Kaiser, E.W., Wallington, T.J., Hurley, M.D., Platz, J., Curran, H.J., Pitz, W.J. and Westbrook, C.K., "Experimental and modeling study of premixed atmospheric-pressure dimethyl ether-air flames," J. of Phys. Chem., 104, pp. 8194-8206, 2000.
156. Zhao, Z. Chaos, M., Kazakov, A. and Dryer, F.L., "Thermal decomposition reaction and a comprehensive kinetic model of dimethyl ether," Int. J. Chem. Kinet., 40, pp.1-18, 2008.
157. Qin, X. and Ju, Y., "Measurements of burning velocities of dimethyl ether and air premixed flames at elevated pressures," Proc. Combust. Inst., 30, pp. 233-240, 2005.
158. Goodwin, D.G., Moffat, H.K. and Speth, R.L., "Cantera: An object-oriented software toolkit for chemical kinetics, thermodynamics, and transport processes," <http://www.cantera.org>, 2014. Version 2.1.2.
159. CHEMKIN 10112, Reaction Design: San Diego, 2011.
160. Yamada, H., Goto, Y. and Tezaki, A., "Analysis of reaction mechanisms controlling cool and thermal flame with dme fueled HCCI engines," SAE Technical Paper 2006-01-3299, 2006.
161. Miles, P.C., "Raman line imaging for spatially and temporally resolved mole fraction measurements in internal combustion engines," App. Opts., 38, pp. 1714-1732, 1999.
162. Ghandhi, J.B., "Spatial resolution and noise considerations in determining scalar dissipation rate from passive scalar image data," Exp. Fluid, 40, pp. 577-588, 2006.
163. Moffat, R.J., "Describing the uncertainties in experimental results," Exp. Therm. Fluid Sci., 1, pp. 3-17, 1988.
164. Dussault, D. and Hoess, P., "Noise performance comparison of ICCD with CCD and EMCCD cameras," Proc. of SPIE, 5563, pp. 195-204, 2004.
165. Rothamer, D.A. and Ghandhi, J.B., "On the calibration of single-shot planar laser imaging techniques in engines," SAE Technical Paper 2002-01-0748, 2002.
166. Kline, S.J. and McClintock, F.A., "Describing uncertainties in single sample experiments," Mech. Eng., pp. 3-8, 1953.